Undercooling-Mediated Growth Transitions in Rapidly Solidified Cu-Ni Alloys

Towards the elucidation of the fundamental mechanism behind 'spontaneous grain refinement' in undercooled metallic melts

Elinor Grace Castle

Submitted in accordance with the requirements for the degree of Doctor of Philosophy

The University of Leeds

School of Process, Environmental and Materials Engineering

March 2014

The candidate confirms that the work submitted is her own, except where work which has formed part of jointly-authored publications has been included. The contribution of the candidate and the other authors to this work has been explicitly indicated below. The candidate confirms that appropriate credit has been given within the thesis where reference has been made to the work of others.

Elements of the work presented in Chapter 5.4.1 of the thesis have appeared in two publications as follows:

Evidence for an extensive, undercooling-mediated transition in growth orientation, and novel dendritic seaweed microstructures in Cu–8.9 wt.% Ni, Acta Materialia, Volume 66, Pages 378-387, March 2014, Elinor G. Castle, Andrew M. Mullis, Robert F. Cochrane

and:

Evidence for an extended transition in growth orientation and novel dendritic seaweed structures in undercooled Cu–8.9 wt%Ni, Journal of Alloys and Compounds, In Press, available online 15 December 2013, Elinor G. Castle, Andrew M. Mullis, Robert F. Cochrane

I was responsible for all experimental data collection, and for the writing of both papers. The contribution of the other authors was to provide help in the interpretation of results and to review the paper scripts prior to submission for publication.

Acknowledgements

The work presented in this thesis would not have been possible without the help and support of a number of people. Firstly, I would like to express my deepest gratitude to my primary supervisor, Professor Andy Mullis, whose skilfully tailored levels of advice and support have been vital to my development as a researcher. Andy has always found the time to help me when I needed it, whether it was: advising on and reviewing papers and thesis chapters, providing impromptu career advice, patiently explaining various concepts with unrivalled clarity and even acting additionally as a mentor to my teaching studies... the list goes on and I cannot thank him enough. I am equally grateful to my secondary supervisor, the walking fountain of materials knowledge known as Dr Bob Cochrane. There is no question he does not know the answer to (and then some!), and no problem he cannot solve. Having him as a supervisor has therefore been invaluable throughout my research degree. As the course leader for my undergraduate materials studies, I have also experienced Bob's teaching from both the student and demonstrator point of view and am sincerely thankful for his immense effort and dedication; without which I might not have had the confidence to tackle a PhD in metallurgy in the first place.

Special thanks also go to both Diane Cochrane and Rob Simpson, the lab technicians who have provided endless practical support to this "thermocouple destroyer extraordinaire". Without their technical wisdom I would probably still be in various labs burning my way through arc-melter shields, wondering why I can't see anything down the microscope and putting nice big scratches into my polished samples. I would like to extend further gratitude to Dr Tim Comyn for all the time he spent in helping me to understand, obtain and interpret XRD results. His expertise was crucial to the success of this work and I greatly appreciate all of his efforts. Additionally, I would also like to thank Dr Mike Keeble at Buehler for the one-to-one support he provided in trying to polish my problematic samples to a state fit for EBSD. Following this, I should also extend some gratitude to the EBSD technician, Dr Richard Walshaw, for putting up with the results of the trials prior to receiving said help!

To my colleagues, Leigang and Caroline; all past and present co-inhabitants of office 1.19; and to all my friends, including: my oldest and dearest friends, Hannah and Emma; my five lovely Leeds ladies; our dependable Mr Mosby (Ben); and worthy pub debate opponent, Deeney (*et al.* of course) – thank you all for the light relief and emotional support. Thank you to all of my family, particularly my parents for supporting me in everything I have ever decided to do, and to my sister for providing fits of giggles incomprehensible to everyone else! Finally - to Christian, who has supported me always through the good times and the bad - ta duck.

Abstract

Within the context of the rapid solidification of metals, an experimental investigation has been undertaken in order to elucidate the fundamental mechanism behind the 'spontaneous grain refinement' phenomenon; in which abrupt transitions between coarse columnar and fine equiaxed grain structures are observed with increasing solidification velocity. A melt fluxing technique has been employed to undercool and rapidly solidify a Cu-8.9 wt.% Ni alloy and a Cu-3.98 wt.% Ni alloy. This method permits *in situ* high-speed imaging of the recalescence front, allowing the solidification velocity to be calculated and studied as a function of undercooling. A B_2O_3 + Na_2SiO_3 glass flux has been identified as the optimal composition for use in the melt fluxing of Cu-Ni alloys, and undercoolings of up to 240 K have subsequently been achieved. Light microscopy, SEM, EBSD and XRD pole figure analysis has been performed on the as-solidified samples in order to study the evolution of microstructure and texture with increased undercooling/solidification velocity. An extended transition in growth orientation, from <100>-oriented at low undercooling to <111>-oriented at high undercooling, has been observed in both alloys. At intermediate undercooling, competitions between the two growth orientations are observed to give rise to mixed-orientation microstructures, a novel form of the dendritic seaweed structure and multiple twinning. In the high-Ni alloy, this mixed-orientation regime appears to coincide with the low undercooling grain refinement transition, subsequently driving a recrystallisation and recovery process. In the low-Ni alloy, however, the mixed-orientation regime does not coincide with the grain refinement region, and grain refinement in this instance occurs via a dendrite fragmentation mechanism. Dendrite fragmentation is also observed to drive spontaneous grain refinement at high undercooling in this alloy. By contrast, at the largest undercooling achieved in the high-Ni alloy, a partially-grain refined sample has been obtained, in which the majority of the substructure consists of dendritic seaweed – suggesting that seaweed is the most likely precursor to spontaneous grain refinement in this case. Thus, three separate grain refinement mechanisms have been identified in the two closely-related alloys; the selection of which appears to be dependent upon the original growth structures present, which are in turn determined by the closeness of the competitions between differently-directed anisotropies. It is suggested that the addition of Ni to Cu either increases the strength of the kinetic anisotropy, or decreases the strength of the capillary anisotropy (or both); leading to a closer competition between the two at higher Ni concentrations, thereby accounting for the differences in microstructure and subsequent grain refinement mechanisms.

Table of Contents

List of Figures

List of Tables

List of Symbols

Symbols	*Definitions*	*Units*
A	Surface area	m^2
C_0	Initial solute concentration (alloy composition)	wt.%
C_L	Concentration of liquid at solid-liquid interface	wt.%
C_S	Concentration of solid at solid-liquid interface	wt.%
C	Specific heat capacity of the system	J mol^{-1} K^{-1}
C_p	Specific heat capacity (constant pressure)	J mol^{-1} K^{-1}
C_V	Specific heat capacity (constant volume)	J mol^{-1} K^{-1}
D	Solute diffusivity	m^2 s^{-1}
D_i	Interface diffusion coefficient	m^2 s^{-1}
E	Internal energy of system	J
f_S	Volume fraction of solid	-
G_1	Gibbs free energy of initial state	J mol^{-1}
G_2	Gibbs free energy of final state	J mol^{-1}
H	Enthalpy	J mol^{-1}
H_f	Enthalpy of fusion	J m^{-3}
I	Nucleation rate	s^{-1}
I_0	Pre-exponential factor rate	s^{-1}
I_V	Ivantsov function	-
k_B	Boltzmann constant	J K^{-1}
k	Partition coefficient	-
k_E	Equilibrium partition coefficient	-
k_V	Velocity-dependent partition coefficient	-
m	Slope of liquidus line	K wt.%$^{-1}$
m'	Velocity-dependent slope of liquidus line	K wt.%$^{-1}$

N_L	Number of atoms in liquid	-
N_n	Number of atoms in crystalline cluster	-
P	Péclet number	-
P_C	Solute Péclet number	-
P_t	Thermal Péclet number	-
P_i	Interface Péclet number	-
r	Radius of atom cluster / spherical cap	m
r^*	Radius of critical size nucleus	m
S	Entropy	J mol^{-1}
$S(\Theta)$	Shape factor	-
T	Absolute temperature	K
T_F	Freezing temperature	K
T_L	Liquidus temperature	K
T_M	Melting temperature	K
T_S	Solidus temperature	K
T_q	Local temperature	K
T^i	Temperature at solid-liquid interface	K
T_e	Eutectic temperature	K
T_0	Temperature at which free energy of solid and liquid states are equal	K
T_C	Critical temperature	K
T_g	Glass transition temperature	K
t_m	Minimum time required for nucleation	s
V	Volume	m^3
V_{FS}	Volume fraction of solid	-
v	Solidification velocity	m s^{-1}
ν_0	Atomic vibration frequency	s^{-1}

v^*	Critical growth velocity	m s^{-1}
Δ_C	Critical undercooling for symmetry-broken (SB) fingers	K
ΔG	Overall Gibbs free energy of system	J mol^{-1}
ΔG^a	Gibbs activation energy barrier	J mol^{-1}
ΔG_d	Activation energy of atom transfer through solid-liquid interface	J mol^{-1}
ΔG_i	Solid-liquid interfacial energy	J mol^{-1}
ΔG_V	Volume free energy	J m^{-3}
ΔG^*	Critical excess free energy barrier	J
ΔG_{hom}	Gibbs free energy change during homogeneous nucleation	J
ΔG_{het}	Gibbs free energy change during heterogeneous nucleation	J
ΔG^*_{hom}	Critical excess free energy barrier for homogeneous nucleation	J
ΔG^*_{het}	Critical excess free energy barrier for heterogeneous nucleation	J
ΔG_{iML}	Interfacial energy between mould and liquid	J m^{-2}
ΔG_{iSM}	Interfacial energy between solid and mould	J m^{-2}
ΔG_{iSL}	Interfacial energy between solid and liquid	J m^{-2}
ΔT	Undercooling	K
ΔT_2^*	Critical undercooling for onset of spontaneous grain refinement	K
ΔT_h	Hypercooling limit	K
ΔT_T	Thermal undercooling	K
ΔT_C	Constitutional undercooling	K
ΔT_R	Curvature undercooling	K
ΔT_K	Kinetic undercooling	K
ΔS_f	Entropy of fusion	J mol^{-1} K^{-1}

α	Thermal diffusivity in the liquid	$m^2\ s^{-1}$
ε	Anisotropy	$J\ m^{-3}$
ε_C	Capillary anisotropy	$J\ m^{-3}$
σ^*	Stability constant	-
δ_i	Characteristic interface width	m
ρ	Dendrite tip radius	m
μ	Kinetic coefficient	$m\ s.K^{-1}$
λ_t	Scaling factor	-

1. INTRODUCTION

Rapid solidification processes have attracted a great deal of attention from the metallurgical community, since they provide access to alternative metastable phases and other metastable phenomena. Interest in these techniques dates back to 1960, when Duwez *et al*. demonstrated that, with sufficiently rapid quenching from the melt, metals could be solidified into new, non-equilibrium crystalline states and non-crystalline (glassy) solids, and that large extensions in solid solubility were possible. Each one of the metastable phenomena offers its own set of potential engineering advantages. For example; metallic glasses offer superior low-temperature strength, hardness, toughness and yield strength in comparison to crystalline metals; whilst supersaturated solid solutions offer enhanced age hardening ability and solid solution strengthening.

Rapid solidification can be achieved via one of two main processes. Industrially, most techniques involve rapid quenching from the melt, with cooling rates between 10^2 and 10^6 K s^{-1}. These techniques include melt spinning and splat quenching, in which thin layers of melt are spread over a chilled material of high conductivity, resulting in extremely rapid heat removal from a small depth of melt. Rapid quenching allows the liquid state to be retained below the equilibrium melting temperature (referred to as 'undercooling') through the kinetic avoidance of nucleation. This bypasses the nucleation of competitive equilibrium phases and thus permits the formation of alternative metastable phenomena. Whilst a number of novel metallic products have been achieved via this route, control over processing parameters is limited and a direct analysis of the resulting solidification processes is not possible. Such techniques are therefore mostly unsuitable in the study of thermodynamics, nucleation and crystal growth processes (Herlach et al., 1993).

In order to better understand the fundamental science behind the formation of metastable phases and other rapid solidification phenomena, a rapid solidification method which offers greater control and closer monitoring of process parameters is required. As such, most research into this area utilises containerless processing techniques. By reducing the number of heterogeneous nucleants present through the avoidance of contact with crucible/mould walls, a large degree of undercooling can be achieved under controlled, slow-cooling conditions. The driving force for rapid solidification then arises from the difference in the Gibbs free energy between the undercooled and the solid state, and the solidification velocity is thus directly related to the degree of undercooling achieved. Many containerless techniques, such as melt fluxing or electromagnetic levitation, also have the added advantage of permitting *in situ*

observations of the solidification process, facilitating accurate calculation of solidification velocities and analysis of the solid-liquid interface morphology.

In the present work, the rapid solidification phenomenon known as 'spontaneous grain refinement' will be investigated. First reported by Walker (1959), spontaneous grain refinement refers to an abrupt transition between a course columnar and a fine equiaxed grain structure with increasing undercooling/solidification velocity. In general, pure metals undergo one spontaneous grain refinement transition at high undercooling, whilst alloys are observed to undergo a second region of refinement at low undercooling. Fine grained metals are desirable in many applications, due to their increased yield strength, hardness and toughness; and are conventionally produced extrinsically via chemical or mechanical manipulation. By contrast, spontaneous grain refinement is intrinsic to the solidification process itself, and may therefore offer an improved alternative to traditional processing routes. However, studies into this phenomenon are mostly driven by the desire to understand and accurately model dendrite growth. Such models would facilitate the development and refinement of many industrial processes, such as casting. However, since spontaneous grain refinement leads to alterations in the original growth structure, continuous measurements of dendritic length scales as a function of growth velocity cannot be made. Mathematical models are therefore limited by the effect, since there is thus a lack of data on which to base and test them. An understanding of the fundamental mechanism behind spontaneous grain refinement would therefore offer a valuable insight into dendrite growth and would subsequently lead to dendrite growth models of much greater accuracy. However, no one model has been able to account for the variety of conflicting evidence obtained. Proposed mechanisms range through; cavitation in the melt (Walker, 1959), recrystallisation (Powell and Hogan, 1969), dendrite fragmentation (Kattamis and Flemings, 1966) and the development of growth instabilities (Mullis et al., 2004b). In many cases the evidence presented for each mechanism is strong, leading to an unresolved debate on the matter which has lasted several decades.

In the present work, a systematic and detailed study of the development of microstructure and texture with increasing undercooling will be undertaken, using the containerless processing technique of melt fluxing. The solidification velocity vs. undercooling relationship will also be studied, with solidification velocity obtained from the high speed imaging of the recalescence front. The study will focus on the Cu-Ni system, with two compositions (Cu-8.9 wt.% Ni and Cu-3.98 wt.% Ni) investigated in order to determine the effect of Ni concentration on microstructural development. The analysis will provide further insight into the fundamental mechanism behind spontaneous grain refinement.

2. LITERATURE REVIEW

2.1. Introduction

This chapter will introduce the essential fundamental science, theories and concepts required in order to comprehend the significance of the work undertaken in this study. The thermodynamics and kinetics of nucleation and grain growth under non-equilibrium solidification conditions will be presented, followed by an overview of some of the key experimental techniques used in studying the rapid solidification of undercooled metallic melts. The main non-equilibrium solid states investigated using such rapid solidification techniques will then be discussed, followed by an extensive literature review of the spontaneous grain refinement phenomenon, which constitutes the main focus of this work.

2.2. Non-equilibrium solidification of undercooled metallic melts

During equilibrium solidification, solid growth occurs following the formation of crystalline nuclei in the melt. Nucleation of the solid phase occurs heterogeneously at the container walls or on impurities and solid particles in the melt. In this case, only a small departure from equilibrium is required to form nuclei, since heterogeneous nucleants provide preferable surfaces on which new crystals can grow from the liquid (Kurz, 1989). However, substantial departures from equilibrium are possible if either the number of heterogeneous nucleants is significantly reduced, or if nucleation is kinetically avoided by rapid cooling. The melt will now retain its liquid state below its equilibrium melting temperature, T_m, referred to as 'undercooling' (ΔT, K). Metallic melts can be undercooled by considerable amounts of up to several hundred Kelvin below T_m. As a result, large driving forces for solidification are generated; leading to rapid solidification and a steep rise in temperature, as stored latent heat is released upon the creation of new solid. This initial 'recalescence' stage of solidification will terminate either when the specimen temperature has risen back to the equilibrium liquidus temperature, or when solidification is complete (should this occur first). For transformation to a metastable phase, sufficient undercooling must be achieved such that the latent heat released upon solidification does not raise the temperature of the sample above the melting point of the desired phase (Jones, 1982). Undercooling is therefore an essential requirement for the formation of metastable phenomena via rapid solidification. An understanding of the thermodynamics and kinetics involved in solidification from the undercooled melt is thus crucial to the analysis and development of such techniques. This section will therefore discuss the relevant fundamental science required for the present study.

2.2.1. Definition of thermodynamic parameters

Thermodynamics plays an important role in the solidification of metals from their undercooled melts. The balance of each of the thermodynamic quantities with respect to one another significantly influences nucleation and the progression of solidification. An understanding of each of these is therefore necessary for the analysis of such processes. This section will therefore provide definitions of the key thermodynamic quantities associated with a solidifying melt.

2.2.1.1. Enthalpy and specific heat

The enthalpy, H, of a system is a measure of its heat content, which is given by:

$$H = E + PV \tag{1.0}$$

where P is the pressure, V is the volume and E is the internal energy of the system, derived from the total kinetic and potential energies of the atoms within it. In the case of solid and liquid states, any change in PV is small in comparison to E, leading to the common approximation $H \approx E$.

The rate of change of enthalpy with temperature, corresponds to the specific heat of the system, C, which is the quantity of heat required to raise the temperature of one mole of substance by one Kelvin. It may be defined with constant pressure, C_P, or with constant volume, C_V. On solidification, an enthalpy change takes place given by Porter and Easterling (1992) as:

$$\Delta H = \int C_p dT \tag{1.1}$$

2.2.1.2. Entropy

Entropy, S, is defined as 'the randomness of the system' (Porter and Easterling, 1992) and describes the heat exchanges which take place on transformation. Heat must be extracted from the system for solidification to occur, and the exchange of heat between the system and its surroundings is denoted ΔQ. At constant pressure, the heat exchange is equal to ΔH, and thus entropy can be given by:

$$dS = \frac{\Delta Q}{dT} = \frac{\Delta H}{dT} = \frac{C_P dT}{T} \tag{2.0}$$

where T is the absolute temperature at which heat exchange takes place. The entropy change associated with solidification is given by:

$$\Delta S = S_S - S_L \tag{2.1}$$

where S_S and S_L are the individual entropies of the solid and the liquid phases respectively (Porter and Easterling, 1992).

2.2.1.3. Gibbs free energy

At constant temperature and pressure, the stability of a system can be determined by its Gibbs free energy, G, given by the equation:

$$G = H - TS \tag{3.0}$$

Where H is the enthalpy, T is the absolute temperature and S is the entropy of the system. If a closed system is at its most stable state, it is said to be in equilibrium. At constant temperature and pressure, such a system would have the lowest value of Gibbs free energy possible and would also satisfy the criterion:

$$dG = 0 \tag{3.1}$$

where, dG is the overall Gibbs free energy of the system for that particular atomic configuration. Note that, whilst this is a necessary condition for the formation of an equilibrium state, it is not sufficient, since many metastable states may also be possible at higher values of Gibbs free energy, whereby dG is also equal to 0. This is best illustrated by, **Figure 1** showing two local minima in the Gibbs free energy of a system (Porter and Easterling, 1992).

Any transformation resulting in a decrease in Gibbs free energy is favoured, and therefore a necessary condition for any phase transformation is:

$$\Delta G = G_2 - G_1 < 0 \tag{3.2}$$

where G_1 and G_2 are the Gibbs free energies of the initial and final states, respectively, and ΔG is the overall change in the Gibbs free energy. In transition from one state to another, the atoms must first break from their initial configuration and rearrange to form the final configuration. There is therefore an associated energy barrier to state transformations known as the 'Gibbs activation energy (ΔG^a) barrier'. This must be overcome before a phase change

can occur, indicated by the 'hump' between configurations A and B in **Figure 1** (Porter and Easterling, 1992).

It is the difference in Gibbs free energy between the solid and liquid states which drives the solidification process in undercooled metallic melts, with the heat released upon recalescence represented by the enthalpy difference between the liquid and solid phases.

2.2.2. Nucleation

Before solidification can proceed, a process known as nucleation must occur. Here, small crystalline 'nuclei' form in the melt and trigger subsequent grain growth. Two types of nucleation may be distinguished – homogeneous and heterogeneous. This section describes the processes and thermodynamics relating to both types of nucleation event according to classical nucleation theory as proposed by Volmer and Weber (1926) and Becker and Doring (1935).

2.2.2.1. Homogeneous Nucleation

Below the equilibrium melting temperature, T_m, a driving force exists for solidification, which is approximately proportionate to the degree of undercooling, ΔT. A system will always strive to reach thermodynamic equilibrium. Therefore, if a liquid is at a temperature whereby its solid state is the stable equilibrium phase, then solidification will be favoured. This driving force is the difference in the Gibbs free energy, ΔG, between the solid and the liquid states (Kurz, 1989).

As a liquid metal is cooled below T_m, thermal fluctuations encourage small clusters of crystallised solid to form within the melt. The creation of a solid fraction lowers the free energy of the system, promoting solidification. However, this is opposed by an increase in energy associated with the creation of a new solid-liquid interface. The volume free energy, ΔG_V, associated with the creation of a solid cluster is proportional to its volume, and thus varies with r^3, where r is the cluster radius. Similarly, the free energy change associated with the creation of a new interface, ΔG_i, is proportional to the surface area of the interface created, and therefore varies with r^2 (Kurz, 1989). The outcome of these relationships is summarised in **Figure 2**.

If it is assumed that the shape of the solid clusters is spherical, then it is clear from **Figure 2** that, for small clusters, the surface-to-volume ratio is very large. Therefore, for a small cluster,

the interfacial energy is relatively large in comparison to the associated reduction in ΔG_v, rendering it unstable. More volume (and therefore surface area) added to this cluster would cause a further increase in the total free energy, ΔG, which would be thermodynamically unfavourable. In this case the cluster will undergo dissolution in order to return ΔG to a lower value, and solidification will not be nucleated.

For a larger cluster, if the volume of solid is sufficient to support the creation of a new interface, it will be thermodynamically stable. In this instance, solidification has been nucleated and the 'nucleus' will continue to grow, since more atoms added to the surface will further lower ΔG, bringing the system back to equilibrium.

The equation used to describe this relationship is given as follows:

$$\Delta G = \Delta G_v . V + \Delta G_i . A = \left\{\Delta G_v . \frac{4}{3}\pi r^3\right\} + \{\Delta G_i . 4\pi r^2\} \quad (4.0)$$

Where; V is the volume of the sphere and A is the surface area of the sphere. Note that ΔG_v is always negative below T_m, as the liquid is metastable (Kurz, 1989).

It is clear from **Figure 2** that a critical-size nucleus, of radius r^*, is required to spontaneously form in order to overcome a critical excess free energy barrier, ΔG^*, and thus nucleate solidification. By differentiating equation 4.0 with respect to r and setting this equal to 0 (since the combined ΔG_V and ΔG_i, terms lead to a ΔG gradient of 0 when $r = r^*$) and rearranging for r^*, it can be shown that:

$$r^* = \frac{2(\Delta G_i)}{-\Delta G_v} \quad (4.1)$$

substituting this into equation 4.0 gives:

$$\Delta G^* = \left(\frac{16\pi \Delta G_i^3}{3(\Delta G_v)^2}\right) \quad (4.2)$$

ΔG_v is related to the latent heat of fusion, H_f, and the degree of undercooling, ΔT, by the following equation (4.3):

$$\Delta G_v \approx \frac{H_f \Delta T}{T_m} . \quad (4.3)$$

Note that, in the derivation of this equation (Porter and Easterling, 1992), the difference between the specific heats of the liquid and the solid phase is assumed to be negligible for

small undercoolings, since the bonding structure of the two phases is not substantially different.

By substituting equation 4.3, into 4.1 and 4.2, the relationships between the degree of undercooling and the values of ΔG^* and r^* can be ascertained:

$$r^* = \left(\frac{2\Delta G_i T_m}{H_f}\right)\frac{1}{\Delta T} \tag{4.4}$$

and

$$\Delta G^* = \left(\frac{16\pi\Delta G_i T_m^2}{3H_f^2}\right)\frac{1}{(\Delta T)^2} \tag{4.5}$$

Equations 4.4 and 4.5 show that activation energy and critical nucleus size decrease with ΔT, thus proving that the tendency to nucleate increases with increasing undercooling (Porter and Easterling, 1992).

This model represents homogeneous nucleation – the simplest representation of a pure metal undergoing solidification. It assumes that nucleation will occur only as a result of random cluster formation, with no heterogeneous stimulation. However, homogeneous nucleation is an extremely rare occurrence, since most systems involve the presence of heterogeneous nucleants, such as mould walls and impurity inclusions (Porter and Easterling, 1992).

2.2.2.2. Heterogeneous Nucleation

If a melt is contained within a crystalline mould, or if it contains solid particles, then the activation energy required to nucleate solidification is decreased. This is termed 'heterogeneous nucleation'.

Preferential nucleation occurs at mould walls and on impurities, requiring much smaller values of ΔT (typically < 1 K for equilibrium solidification). This occurs due to the replacement of part of the solid-liquid interface with a solid-solid interface, leading to a smaller ΔG_i term. For example, consider a solid embryo which has formed in contact with a perfectly flat mould wall (**Figure 3**). Assuming that the solid-liquid interfacial energy is isotropic, it can be shown (Porter and Easterling, 1992) that the total interfacial energy of a system for a given volume of solid will be minimised if the embryo takes the form of a spherical cap with a wetting angle, θ, and with interfacial tensions between the mould and the liquid, the solid and the mould and the

solid and the liquid ($\Delta G_{iML,}$ ΔG_{iSM} and ΔG_{iSL}, respectively) balancing in the plane of the mould wall, i.e.:

$$\Delta G_{iML} = \Delta G_{iSM} + \Delta G_{iSL} cos\,\theta \tag{5.0}$$

or:

$$cos\,\theta = \frac{\Delta G_{iML} - \Delta G_{iSM}}{\Delta G_{iSL}} \tag{5.1}$$

The equation for the Gibbs free energy change of a system undergoing heterogeneous nucleation is much the same as that for homogeneous nucleation, with the exception that it is written in terms of θ and that r denotes the radius of the spherical cap. This is given as:

$$\Delta G_{het} = \left\{-\frac{4}{3}\pi r^3 \Delta G_v + 4\pi r^2 \Delta G_i\right\} S(\theta) \tag{5.2}$$

where $S(\theta)$ is known as the shape factor and is given by:

$$S(\theta) = \frac{(2 + cos\,\theta)(1 - \cos\theta)^2}{4} \tag{5.3}$$

Note that equation 5.3 has a numerical value ≤1 dependent on the wetting angle.

Differentiating equation 5.2 with respect to r (as with homogeneous nucleation) gives the equation for the critical radius, r^*, required for heterogeneous nucleation:

$$r^* = \frac{2\Delta G_i}{\Delta G_v} \tag{5.4}$$

and back-substituting equation (5.4) into (5.2) gives ΔG^* as:

$$\Delta G^* = \left(\frac{16\pi \Delta G_i^3}{3(\Delta G_v)^2}\right) . S(\theta) . \tag{5.5}$$

This shows that the ΔG^*_{het} barrier to nucleation is smaller than the ΔG^*_{hom} barrier by $S(\theta)$, whereas r^* is not affected by the presence of a mould wall and only varies with ΔT. Combining equations 5.5 and 4.2 gives:

$$\Delta G^*_{het} = S(\theta) \Delta G^*_{hom} . \tag{5.6}$$

Hence, the energy barrier for heterogeneous nucleation is always smaller than that for homogeneous nucleation, since $S(\theta)$ is always between 0 and 1. Note that this relationship breaks down at θ = 0 and must, in this case, be modelled differently. The relationship,

however, does confirm that nucleation occurs more readily in heterogeneous systems than in homogeneous systems (Porter and Easterling, 1992).

2.2.2.3. Nucleation rate

The relationship between cluster size and free energy is useful in the estimation of the number of grains nucleated within a given volume of melt and time, referred to as the nucleation rate. In the simplest case, homogeneous nucleation can be considered, wherein an ideal mixture containing a certain number of atoms in the liquid state, N_L, and a variety of small crystalline clusters, each containing n atoms (N_n) exists. Assuming that $N_n << N_L$, if a cluster of atoms is in equilibrium, then the probability that the cluster will gain an atom is equal to the probability that it will lose one. There is therefore an equal probability that the cluster will grow or melt. If clusters of all sizes and structures are assumed to be in steady-state equilibrium, then the equilibrium distribution (solubility) of the clusters can be estimated by:

$$\frac{N_n}{N_L} = exp\left(-\frac{\Delta G_n}{k_B T}\right) \tag{6.0}$$

where ΔG_n is the free energy of a nucleus containing n atoms and k_B is Boltzmann's constant (Kurz, 1989). The number of clusters contained in the melt will therefore increase with decreasing value of ΔG_n. For nucleation to occur, a cluster of critical radius r^* must form (Chapter 2.2.2.1), at which the critical free energy barrier is ΔG^*. There is also an activation barrier associated with the energy required for the diffusion of an atom across the cluster-liquid interface, ΔG_d. The rate of nucleation, I, must therefore take both of these factors into account, via the relationship:

$$I = N_L v_0 \, exp\left(-\frac{\Delta G^*}{k_B T}\right) exp\left(-\frac{\Delta G_d}{k_B T}\right) \tag{6.1}$$

where $N_L v_0 = I_0$ (a pre-exponential factor) and v_0 is the atomic vibration frequency. Equation (4.5) gives ΔG^* as:

$$\Delta G^* = \left(\frac{16\pi \Delta G_i T_m^2}{3H_f^2}\right)\frac{1}{(\Delta T)^2} \tag{4.5}$$

Therefore, as the undercooling is increased, the activation energy barrier to nucleation, ΔG^*, is reduced, increasing the first exponential term in equation (6.1). However, with increasing undercooling (or decreasing T) the rate of diffusion of atoms across the cluster-liquid interface slows, leading to an increase in ΔG_d and an associated increase in the second exponential term

of equation (6.1). The rate of nucleation therefore passes through a maximum at a critical temperature, T_c, somewhere between the melting point and the point of zero thermal activation (at 0 K) (Kurz, 1989). Since the nucleation rate is inversely proportional to time, t, this information can be incorporated into a continuous cooling transformation (CCT) diagram, as shown in **Figure 4**; which represents the overall kinetics of solidification, as influenced by both nucleation and growth rates. This diagram shows that there is a minimum time, t_m, associated with the nucleation and growth of crystalline grains. Under slow cooling conditions, the cooling curve (curve 1) intersects the CCT curve. However, under rapid cooling conditions, the cooling curve (curve 2) may miss the CCT curve completely and solidify into an amorphous/glassy solid through a continuous increase in viscosity (see Section 2.4.5 of this chapter). The addition of heterogeneous nucleants has the effect of decreasing ΔG^* and therefore moves the CCT curve to higher temperatures and shorter times, thereby reducing the likelihood of achieving large undercoolings and forming glassy solids or other metastable states. Note that this CCT diagram only shows the curve for nucleation and growth; at longer times and lower temperatures there are further curves relating to subsequent transformations.

2.2.3. Dendritic solidification in the undercooled melt

2.2.3.1. Introduction

Immediately following nucleation, grain growth will proceed as solidification takes place. The dominant form of single-phase solidification into an undercooled melt is that of dendritic solidification. Dendrites are branched substructures which crystallise into the melt from the mould walls and from any inclusions present (in the case of heterogeneous nucleation), or radially from the stable nuclei formed during homogeneous nucleation. Dendrite growth will proceed following the de-stabilisation of the solid-liquid interface, either due to a negative temperature gradient or a build-up of solute ahead of it. In the case of pure melts, the stability of the interface is determined by temperature gradients only; whilst in alloys, both heat and solute diffusion processes can contribute to the formation of dendrites, with the velocity of the solidification front dictating the balance between the two contributions. The two processes and their relationship with the level of undercooling and solidification velocity thus provide a first basis for elucidating microstructure formation and development mechanisms.

Temperature and solute gradients represent overall departures from equilibrium, since the full system is not at the lowest Gibbs free energy. However the solid-liquid interface might still be

under local equilibrium during the solidification process, allowing the equilibrium phase diagram to be used to determine interfacial values. A ‘true’ departure from equilibrium occurs when local equilibrium at the solid-liquid interface no longer exists, and the temperatures or compositions at the interface cannot be predicted from the equilibrium phase diagram. Such departures are mostly brought about due to the trapping of solute elements in alloys, attachment kinetics of the atoms at the interface and surface energy effects due to the formation of a curved interface. This section will therefore look into the basic theory of dendritic growth and its contributing factors, with a more in-depth analysis of the problem of simulating dendritic growth provided in Chapter 2.4.6.2.

2.2.3.2. Interfacial equilibrium

A significant contribution to the non-equilibrium solidification of metallic melts arises from the development of thermal (in both pure melts and alloys) and/or solutal (in alloys) gradients at the growing solid-liquid interface. Such gradients help to determine whether the growth of an interface perturbation will be promoted or diminished. Perturbations first develop randomly as the result of interactions with insoluble particles, or due to temperature fluctuations in the melt. If the interface is unstable, then the perturbations will be subject to conditions which are more advantageous for growth, and so will grow ahead of the interface and develop into a dendrite. If the interface is stable, then growth of the perturbations will not be favoured and they will subsequently disappear (Kurz, 1989).

For example; consider, in the simplest case, the effect of thermal gradients only. In the directional solidification of a pure melt, the temperature ahead of the interface will increase into the liquid as heat is being withdrawn out through the solid by the cold mould walls. In this instance, a perturbation will be protruding into a higher-temperature region of the liquid, and will therefore tend to re-melt back to the interface. This is a stable interface and dendritic solidification is therefore not favoured. In the case of solid growth into a pure undercooled melt, however, the liberation of the latent heat of fusion upon solidification results in a temperature increase in the newly-formed solid. Since the bulk of the melt is still undercooled and the interface is now at a higher temperature, an interface perturbation will be reaching into much cooler regions whereby further solidification will be favoured. The interface is therefore unstable and the perturbation will continue to grow and develop dendritically (Kurz, 1989).

2.2.3.2.1. Heat and solute redistribution in alloys

Substantial undercooling in a metal is a rare event, and yet dendrites are observed in many different situations. This is because, in impure melts and in alloys, solute 'partitioning' ahead of the interface results in local variations in the equilibrium melting point along the solid-liquid interface. This introduces another decisive factor into the stable/unstable interface behaviour (Kurz, 1989).

Solute will pile up ahead of the solid-liquid interface if it has a greater solubility in the liquid phase than in the solid phase. The tendency of the solute to partition into the liquid under isothermal and isobaric conditions is described by the distribution (partition) coefficient, given by:

$$k = \left(\frac{C_S}{C_L}\right)_{T,P} \tag{7.0}$$

where C_S and C_L are the solid and liquid concentrations (respectively) at the interface, as determined from the equilibrium phase diagram (Kurz, 1989). It follows from equation (7.0) that, if k satisfies the condition $k < 1$, then the solid-liquid interface will reject solute into the liquid. In this case the liquidus slope is negative. For simplicity, theoretical treatment of solute partitioning mechanisms approximate straight liquidus and solidus lines, leading to constant k and m (liquidus slope) values (Kurz, 1989).

A common example which illustrates the influence of solute partitioning on the final microstructure of a product is the steady-state, unidirectional solidification of a column of liquid alloy. Under these conditions, three distinct solute concentration regions are formed (**Figure 5**), the differences in which are known as solute segregation patterns (Kurz, 1989):

- *Region 1.* Upon cooling below the liquidus temperature, solidification is nucleated and the solidification front undergoes a period of growth until a steady-state boundary layer is formed. Within this distance, the solute concentration in the liquid at the interface increases from the original solute concentration, C_0, to the maximum solute concentration C_0/k. The first solid to freeze is therefore of the minimum composition, kC_0, and increases to C_0 as the temperature approaches the solidus temperature, T_S. These are the conditions required for steady-state growth.
- *Region 2*. As the steady-state interface advances, the flux of solute transferring from solid to liquid equals that of the flux diffusing into the liquid due to the concentration gradient existing at the solid-liquid boundary. As a result, the planar solid/liquid interface grows at the solidus temperature corresponding to the alloy composition.

- *Region 3*. Once the remaining liquid region equals the length of the boundary layer, no further solute diffusion can take place, since there can be no concentration gradient at the end of the column. This causes the concentration at the solid-liquid interface to increase above C_0/k, with a corresponding increase in solid concentration above C_0 (Kurz, 1989).

The build-up of solute ahead of a developing solid-liquid interface results in local variations in the equilibrium solidification temperature, T_L , of the liquid. As the liquid concentration decreases into the liquid, T_L increases, as indicated by the phase diagram in **Figure 6**. Hence a region of melt near the interface, containing higher concentrations of solute, would solidify at lower temperatures than regions of melt further away from the interface. However, a temperature gradient existing in the melt due to heat flow during casting imposes a temperature, T_q, on each region of melt ahead of the interface. At the interface this must be equal to or less than the solidus temperature, T_S. If the gradient of T_L is greater than that of T_q then there exists a zone of 'constitutional undercooling' (Rutter and Chalmers, 1953), as illustrated by the shaded region in **Figure 6**. In this case, a perturbation developing at the solid-liquid interface would be growing into a region of undercooled liquid, whereby solidification would be promoted. Subsequent dendritic growth would therefore occur (Kurz, 1989).

At higher solidification velocities, brought about by large values of undercooling, the latent heat released at the interface has less time to diffuse away. In this case, the gradient of T_q therefore increases and will be greater than that of T_L for very high undercoolings. Constitutional undercooling therefore does not occur and any dendritic growth is thus dominated by heat transfer processes (Kurz, 1989). With increasing undercooling (or solidification velocity) a transition between solutally controlled dendritic growth and thermally controlled dendritic growth is therefore observed in alloys.

2.2.3.3. True departure from equilibrium

The concept of constitutional undercooling provides a useful first basis for the estimation of whether a growing alloy interface will remain stable and planar or de-stabilise via the development of perturbations into dendrites. This is based on the assumption that local equilibrium will be established more quickly at the solid-liquid interface than in the bulk phase. However, under certain conditions, such as when the solidification rate becomes large, the interface itself may experience a 'true' departure from equilibrium. Solute trapping in alloys and atomic attachment kinetics in both pure melts and alloys create deviations from

equilibrium at a moving interface; whilst the surface energy effects of a curved interface can contribute to deviations even when the interface is static. Such effects must also be considered when estimating interface stability and will therefore be discussed in the following.

2.2.3.3.1. Solute trapping in alloys

The assumption of local equilibrium at the solid-liquid interface under normal solidification conditions isn't strictly correct, since a small (<1 K) departure from equilibrium is always required to nucleate solidification (Chapter 2.2.2.2) in systems undergoing non-faceted growth (Chapter 2.2.3.3.2). However, this approximation is useful when calculating partition coefficients for alloys when solute diffusion velocities across the interface are far greater than the speed of the growing interface. These equilibrium partition coefficients are therefore commonly given the subscript 'E', i.e. k_E (Kurz, 1989).

If the growth velocity, v, increases to a rate which is greater than the maximum speed with which solute atoms can diffuse across the interface, then solute trapping will occur. In this case there is a departure from local equilibrium at the interface, the degree of which increases with increasing undercooling. The partition coefficient in this case, k_V, is therefore defined as the ratio between the solute concentration in the growing solid and that in the liquid at the interface, and thus increases with growth velocity. In general, it can be stated that $k_E < k_V < 1$, with k_V varying smoothly from k_E to 1 as the growth velocity increases, according to the relationship:

$$k_V = \frac{k_E + \left(\frac{\delta_i v}{D_i}\right)}{1 + \left(\frac{\delta_i v}{D_i}\right)} \qquad (8.0)$$

where $\left(\frac{\delta_i v}{D_i}\right)$ is an interface Péclet number (P_i) in which δ_i is a characteristic interface width and D_i is the interface diffusion coefficient (Aziz, 1982). This behaviour is shown as a function of v in **Figure 7**. Note that, since no compositional dependence has been included in this model, it can only be applicable to dilute alloys.

As the growth velocity tends towards infinity, so the non-equilibrium partition coefficient tends towards 1, as shown in **Figure 7**. If $k_V = 1$, partitionless solidification is possible only if the free energy of the system will be reduced. Thus the temperature of the interface must be below T_0 - the temperature at which both phases have the same free energy. If these

conditions are met, the composition of the forming solid will equal that of the liquid at the interface (Kurz, 1989).

2.2.3.3.2. Atomic attachment kinetics

In the solidification of materials, there can be two types of solid-liquid interface; atomically rough (non-faceted) and atomically smooth (faceted) interfaces. In pure metals and alloys, the structure of the liquid does not differ markedly from that of the solid, since the liquid state is merely a disordered and slightly less dense (by a few percent) form of it. As a result, the transition from liquid to solid occurs over some distance, leading to a diffuse or atomically rough interface which is typically 1-3 nm thick. Such a rough interface offers many sites to be occupied by diffusing atoms, and as such can incorporate them in a continuous manner, with growth equally likely to proceed at any point. The interfacial energy is therefore approximately isotropic, leading (initially) to a spherical equilibrium crystal shape. The diffuse interface at the atomic scale and the equilibrium shape of the crystal are illustrated in **Figure 8**(a) (Dantzig and Rappaz, 2009).

By contrast, atomically smooth or faceted interfaces are observed in systems which consist of complex compounds; such as in semiconductors, oxides, carbides and polymers. In this case the liquid structure differs significantly from the solid structure. Growth is therefore more difficult and requires an additional undercooling, as the interface will only offer a few sites for atoms/molecules to attach to. The solid-liquid interface advances through the lateral growth of rows perpendicular to the apparent growth direction, since such 'ledges' provide a greater incorporation of the molecule into the solid. When a row is completed, the addition of a further molecule to start the next row is required. This may happen via a secondary nucleation process; however this is very unlikely since the Gibbs free energy of a molecule, positioned at a solid surface but mostly surrounded by liquid, is very high. Growth therefore tends to occur through the introduction of defects such as dislocations and twins, as these incorporate atoms more readily. The equilibrium crystal shape resulting from this type of growth is therefore faceted, with the crystal form bound by the slowest growing faces, as illustrated in **Figure 8**(b) (Dantzig and Rappaz, 2009).

In order to predict the type of interface and crystal growth behaviour, Jackson (1958) was able to show that the value for the entropy of fusion, ΔS_f, could be used. For materials with a high ΔS_f, an atomically smooth interface is expected, with sluggish atomic attachment kinetics greatly influencing the solidification morphology. A large kinetic term may therefore be involved in the solidification process. Materials with a low ΔS_f, however, are expected to

exhibit a rough interface, with atom transfer kinetics usually so rapid that they can be neglected. As discussed in the previous section (2.2.3.3.1), however, atomic attachment kinetics may become significant for high solidification velocities. This is usually modelled via the relationship (Herlach et al., 2007):

$$\Delta T_K = v/\mu \tag{9.0}$$

where μ is the kinetic coefficient, which provides a measure of the mobility of the phase boundary.

2.2.3.3.3. Curvature contribution

In both alloys and pure melts, the atoms or molecules present at a diffuse solid-liquid interface do not possess the same molar Gibbs free energy as those in the solid or the liquid. Due to the fact that they have to accommodate the slight structural changes on either side, they possess an excess free energy. This excess free energy, integrated over the thickness of the interface and multiplied by a molar volume gives the solid-liquid interfacial energy, ΔG_i. As the solid is in a crystalline form, the surface energy will be anisotropic – an effect which comes into play during microstructure formation (Chapters 2.2.3.5 & 2.4.6.2). However, initially the diffuse nature of the interface can allow the assumption of an isotropic interface. The surface:volume ratio of a solid particle in a liquid increases with decreasing particle radius (and therefore increasing curvature). This leads to an increase in the total free enthalpy, and therefore free energy of the solid, resulting in a decrease of the equilibrium melting point. The expression relating the melting point of a pure material with a curved surface is the Gibbs-Thomson equation:

$$T_f^R = T_f^\infty - 2\Gamma_{SL}\kappa \tag{10.0}$$

where: T_f^R and T_f^∞ are the melting points of a positively curved surface and a planar surface (respectively), κ is the curvature and Γ_{SL} is the Gibbs-Thomson coefficient – a measure of the energy required to form a new surface or expand an existing one. The Γ_{SL} value for most metals is about 10^{-7} K m. For a small solid particle of radius 10 μm, this gives a decrease in melting point of around 0.02 K. Such small decreases in equilibrium melting point can have a marked impact on microstructure formation. Changes in curvature along the solid-liquid interface lead to local variations in melting point, which in turn lead to heat fluxes across it. For example, if a solid curved particle lies next to a planar interface, heat will be transferred from the flat interface to the particle, causing it to melt. The decrease in melting point associated

with the curvature of the interface is called the curvature undercooling, ΔT_R (Dantzig and Rappaz, 2009).

2.2.3.4. Summary

Local departures from equilibrium at the interface can occur due to a combination of effects, leading to true departures from equilibrium. Under non-equilibrium conditions, these effects contribute to the total undercooling (ΔT), which can therefore be given by the sum of: the thermal undercooling due to heat transport in both pure metals and alloys (ΔT_T); the constitutional undercooling arising in alloys due to the existence of both thermal and solute gradients (ΔT_C); the curvature undercooling arising from changes in the equilibrium melting temperature due to interface curvature (ΔT_R); and the kinetic undercooling arising from atomic mobility at the solid liquid interface (ΔT_K), giving:

$$\Delta T = \Delta T_T + \Delta T_C + \Delta T_R + \Delta T_K \quad (11.0)$$

The forms of ΔT_T and ΔT_C derived from the Ivantsov solution (1947) (see Chapter 2.4.6.2) are given by:

$$\Delta T_T = \frac{H_f}{C_p} 2\lambda_t P_t \quad (11.1)$$

where λ_t is a scaling factor given by the ratio of the thickness of the temperature field in the liquid ahead of the dendrite tip to the dendrite tip radius, and:

$$\Delta T_C = mC_0 \left[1 - \frac{m'/m}{1-(1-k)Iv(P_C)}\right] \quad (11.2)$$

where Iv is the Ivantsov function, P_C is the solute Péclet number and m' is the velocity-dependent liquidus slope.

2.2.3.5. Dendritic growth

The subject of dendrite growth can be divided into two main categories based on the solidification conditions assumed: either free growth or constrained growth. Free growth concerns the unconfined growth of a single spherical nucleus into an infinite undercooled melt, whilst constrained growth concerns the development of many solid structures under an imposed thermal gradient. During the free growth of a spherical solid nucleus, disturbances in the solid-liquid interface lead to the subsequent growth of perturbations ahead of it. At this

point the solid begins to follow preferred growth directions. Under normal solidification conditions, such preferences are dictated by anisotropies in either the surface energy of the solid-liquid interface, ease of atomic attachment to different crystallographic planes, or a combination of both. Such anisotropies arise from the underling crystal structure of the solid, and as such, growth tends to take place along specific crystallographic planes to produce a branched dendrite structure. For example, surface energy anisotropy in a BCC crystal undergoing non-faceted growth, will favour growth along one of the six <100> orientations. In this case the original perturbation will develop into a <100> oriented dendrite trunk and will produce secondary arms just behind the advancing dendrite tip, which grow in each of the four conjugate <100> directions. The result is a structure such as that shown in **Figure 9** - an image of a BCC succinonitrile (SCN) dendrite. SCN has been used extensively in the study of dendritic solidification owing to its metallic-like solidification behaviour and its transparency, allowing the growth of such dendrites to be viewed *in situ.*

As discussed previously (Section 2.2.3.3.2), for most metallic systems growth restriction due to atomic interface attachment kinetics can be assumed to be negligible under normal growth conditions. In this case surface energy anisotropy effects dominate, with preferred growth orientations assumed to arise from the attempt to minimise the area of surfaces with the highest surface energy. As surface energy increases, the dendrite tip subsequently becomes progressively sharper and for very high surface energies, faceted growth takes place.

Free growth can be applied to equiaxed growth in more realistic situations, and offers a useful insight into the factors influencing dendritic growth. The constrained growth of a solid-liquid interface solidifying from a chill surface is a more common occurrence in solidification processing. As demonstrated in Section 2.2.3.2.1, a pure melt solidifying under these conditions will exhibit a stable, planar solidification front due to the positive temperature gradient existing ahead of the interface. For an alloy undergoing constrained growth, the stability of the interface will be dictated by the balance between the thermal and solutal gradients, which may lead to constitutional undercooling and subsequent de-stabilisation of the interface. In this case the velocity of the solidification front plays an important role in microstructure formation. An example of this can be seen in **Figure 10**, showing the differences occurring in the solidification front of an SCN-Salol alloy under varied pulling speeds. At the lowest pulling speed, the interface is planar (not shown). With increasing pulling speed, shallow cells develop at the interface, which are separated by grooves parallel to the temperature gradient. These grooves become deeper as speed is increased and the cell spacing decreases. Such cells are characterised by their large radius of curvature and do not follow any preferred growth orientation. With higher solidification velocities, a gradual

transition to dendrites is seen, characterised by; sharper tips, trunks which follow the preferred growth orientation and side branching. As with free growth, preferred dendrite orientation is determined by anisotropy. In this example, the dendrites are oriented with their <100> preferred growth orientation parallel to the temperature gradient and growth direction. However, in many cases a number of crystal orientations will exist initially, and a competition will take place between them. The more favourably oriented crystals, with preferred growth orientation most closely aligned to the direction of growth, will grow ahead of those which are least favourably oriented. Such off-axis orientations will therefore be eliminated as they impinge upon the faster-growing crystals.

2.2.3.6. Summary

The factors influencing the stability of a developing solid-liquid interface under non-equilibrium solidification conditions have been discussed. The application of these concepts to the basic theory of dendrite growth under free and constrained growth conditions has subsequently been explored. A more advanced insight into the progress and limitations of the modelling and simulation of dendrite growth, and its applicability to rapid solidification, is given in Chapter 2.4.6.2. Such models are supported and challenged by experimental observations of dendrite growth under rapid solidification conditions - achieved through the use of rapid cooling and containerless processing techniques. An up to date literature review of such studies is also provided throughout Sections 2.4.6.2 and 2.4.6.3 in relation to the present investigation.

2.3. Containerless processing techniques

2.3.1. Introduction

In order to investigate the fundamental science behind the formation of metastable phases and other non-equilibrium solidification phenomena (Chapter 2.4), a number of methods are available. Whilst techniques involving the rapid quenching of metallic melts do offer the potential to produce larger volumes of rapidly solidified material, they are mostly unsuitable for the direct analysis of solidification processes and offer limited control over key process parameters. For this reason, containerless solidification techniques are usually favoured, as they permit fine control over processing parameters, such as superheat temperature and cooling rate, and allow *in situ* analysis of the solidification process itself. By significantly reducing the number of potent heterogeneous nucleants in contact with the melt, these

techniques facilitate large degrees of undercooling, subsequently achieving high solidification velocities of up to around 100 m s^{-1}. This chapter will provide an insight into the main containerless techniques employed in rapid solidification research: melt sub-division, drop tube processing, levitation melting and melt fluxing.

2.3.2. Melt Sub-Division

A number of techniques have been developed which involve the division of a bulk melt into smaller, isolated volumes of material. This is based upon the principle that division of the melt will isolate any potent catalytic nucleants present within a droplet minority. If the dispersion is fine enough, then the majority of the material will be nucleant-free and therefore able to achieve large degrees of undercooling.

For example, droplet emulsification is a common sub-division technique concerned with the creation of a dispersion of fine melt droplets within a carrier fluid. A mixture of dispersion fluid and melt is broken into fine (10 – 20 μm) isolated droplets through the use of a shearing blade connected to a high-speed motor. Surface chemistry reactions maintain the droplets separate from one another and certain reactive chemicals can be used to modify the surface oxides on the droplets. Very high levels of undercooling can therefore be achieved, with a proportion of the droplets able to attain maximum levels of undercooling.

The carrier fluid used can be organic if a low melting point (<773 K) metal is being investigated. For higher melting point metals molten salts or inorganic glass slags become necessary. The level of undercooling attainable rises with decreasing droplet size, since the fraction of droplets which don't contain impurity clusters (nucleation motes) increases (Herlach et al., 1993). The largest relative undercooling achieved using this technique was recorded by Perepezko (1984) as 0.58 T_m in Ga.

Melt sub-division can also be associated with small drop tube processing, whereby melts are sprayed down a tube containing an inert atmosphere. This is described in more detail in the following section.

2.3.3. Drop Tube Processing

Drop tube processing is an undercooling method which eliminates contact with mould walls by allowing droplets of molten metal to solidify during free-fall through a vacuum or inert (Ar or He) atmosphere. An Ultra-High-Vacuum (UHV) is most advantageous for undercooling experiments, as this significantly reduces the likelihood of surface contamination of the

droplet, and therefore greatly reduces the number of potential heterogeneous nucleation sites (Herlach, 1991). There are two categories of drop tube – long and short. UHV's are usually used in long drop tubes, which are generally greater than 50 m in height. These exploit the fact that a body undergoing free-fall through a vacuum will experience microgravity conditions (Herlach et al., 1993).

An example of a long drop tube is the 105 m drop tube at the NASA Marshall Space Flight Centre (shown in **Figure 11**). This employs the use of a thin wire to suspend a 5 mm diameter droplet as it is heated via electron beam bombardment. Electromagnetic levitation (EML) (Section 2.3.4) can also be used to produce a droplet. Photodetectors, arranged at various points down the length of the tube, can record the thermal history of the droplet as it falls and releases latent heat upon solidification. Combining calculations of the heat transfer during the fall of the droplet with the time of fall prior to recalescence, allows a direct analysis of the undercooling obtained prior to nucleation (Hofmeister et al., 1989).

Short drop tubes are generally between 1.5 and 6.5 m high. These neither facilitate direct analysis of the thermal history of the falling droplets, nor simulate microgravity conditions. Experiments performed using these tubes rely on post-mortem statistical and microstructure analysis of assortments of droplets containing a range of diameters up to 1 mm (e.g. (Cochrane et al., 1991b, Kim and Koo, 2004, Gao and Wei, 1999, Ozawa and Kuribayashi, 2006)). Here, the material is melted in a crucible at the top of the tube and is then sprayed down it by forcing the metal through a thin nozzle using Ar or He gas pressure (Herlach, 1991). The droplets rapidly solidify as they free fall through an inert gas atmosphere. The resulting powder can then be collected and separated into size fractions, each of which represents a different solidification velocity range. The isolated effects of solidification velocity on microstructure formation can then be inferred, since all other parameters remain identical for each size fraction. This is therefore a useful technique for the collection of a large amount of data at a time and for the study of the formation of metastable phenomena via rapid solidification.

2.3.4. Levitation Techniques

Larger volumes of melt may be undercooled using levitation melting techniques. These techniques also permit in situ observations of undercooling melts, as well as close measurements of undercooling temperatures. There are several ways in which to simultaneously levitate and melt a metallic sample.

Acoustic levitation uses a high-intensity sound field to exert a sufficient amount of steady force on a sample, such that gravitational forces are overcome. In order to levitate a sample in this way, the droplet must be significantly smaller than the wavelength of the sound used. A typical sample for acoustic levitation would be between 1 and 10 mm in diameter, and would be levitated in an inert gas medium using a resonant and interfering field with a frequency between 1 and 100 kHz (Rey et al., 1991, Dragnevski, 2002).

Levitation may also be achieved through the controlled use of high-speed gas nozzles. This is known as aerodynamic levitation. Samples are stabilised through the spreading of the jet of air produced by the carefully engineered nozzles. Nozzle diameter and geometry can greatly influence the stability of the droplet. Droplets are most commonly melted using laser heating (Herlach et al., 1993).

Both acoustic and aerodynamic levitation methods utilise gases, which can compromise the purity of the sample and therefore limit the level of undercooling. Electrostatic levitation can be carried out under vacuum. This is a method which utilises the Coulomb forces acting on charged particles within an electrostatic field in order to levitate and balance a sample. Stability of the small (10-150 μm) particles is provided by a feedback control system. Particles can be levitated under very high temperatures using this method. However, as with acoustic and aerodynamic levitation methods, heat must be provided using an independent heating source (Herlach et al., 1993).

The most commonly used levitation technique for the purposes of metal undercooling experiments is that of electromagnetic levitation. Large samples of 10 to 15 mm diameter can be levitated using this method, which involves passing a high frequency, alternating current through a coil, which surrounds the sample. This produces an electromagnetic field which levitates and inductively heats the electrically conductive materials. Throughout the process the sample can be observed directly, allowing the temperature of recalescence and solidification velocities to be measured (Li et al., 1996). There are however some drawbacks to the EML technique. The strong alternating electromagnetic fields result in the vigorous inductive stirring of the melt, leading to the solidification of samples under forced convective flow in the liquid. This is particularly problematic under terrestrial gravity conditions, since inhomogeneous electromagnetic forces are necessary to counteract gravity; and thus a strong internal fluid flow is induced. Fluid flows of up to 32 cm s^{-1} have been measured in FeCrNi samples (Hyers, 2005) which can have a significant influence over microstructural development, masking the natural solidification processes occurring during rapid solidification and possibly altering the final microstructure (Binder et al., 2014).

2.3.5. Melt Fluxing

Melt fluxing experiments are concerned with the melting, undercooling and solidification of metallic samples which are suspended in an inorganic glass flux. In this way, samples are isolated from solid container walls and the number of potent heterogeneous nucleation sites is significantly reduced.

Melt fluxing methods offer a number of advantages. As well as preventing nucleation on mould walls, the glass also aids in the removal of oxides and impurities from the melt, helping to purify the system and thus obtain appreciably high undercoolings. The technique allows for high-speed imaging of the recalescence front, as well as direct measurement of the temperature of the sample. These methods have therefore generally been useful for investigations into the microstructural development of metallic melts as a function of their undercooling.

It is a versatile technique and therefore the experimental setup varies between research groups. However, the general procedure involves inductively heating the sample and flux within a vacuum or inert atmosphere using a Radio-Frequency (RF) induction coil. The temperature of the droplet can be monitored using either a thermocouple or a two-colour pyrometer, which may be linked to a chart recorder in order to track and record the time-temperature profiles of the experiment (Herlach et al., 1993).

A melt fluxing method has been chosen for the work carried out in this report. More details of the melt fluxing procedure are given in Chapter 4.4.

2.4. Rapid solidification into metastable states

2.4.1. Introduction

Containerless processing techniques offer controlled access to metastable states which lie far from equilibrium – including supersaturated solid solutions, metastable crystalline phases and metallic glasses. Metastable phenomena, such as spontaneous grain refinement, may also arise under the resulting rapid solidification conditions. Each novel phase offers its own particular set of engineering advantages; hence these metastable states have received substantial interest from the metallurgical community. Each of the main metastable states is discussed in this chapter. A comprehensive review of the spontaneous grain refinement phenomenon is also provided, since this represents the main focus of the present work.

2.4.2. Supersaturated solid solutions

As discussed in Section 2.2.3.3.1, if solidification is sufficiently rapid, solute trapping will occur, leading to an extension in the equilibrium solid solubility. The formation of a metastable supersaturated solid solution, and eventually complete solute trapping, is favoured if: the solidification velocity exceeds the atomic diffusive speed, and the temperature of the sample during recalescence remains below the temperature, T_0, at which the free energies for the solid and the liquid states are equal. Above T_0, a finite driving force exists for chemical segregation.

To demonstrate this, an example of the solidification paths possible at different undercoolings during the solidification of an A-B eutectic alloy system, of nominal composition C_0, is shown in **Figure 12**. In order to simplify the case, it can be assumed that there is negligible kinetic undercooling and that the solid-liquid interface is planar – hence the interface temperature, T^i, is equal to T_L and the composition of the liquid at the interface, C_L , is equal to C_0. On cooling from a temperature above T_L, α-phase nuclei of concentration C_s will form between T_L and the eutectic temperature T_e. If the α and β phases have different crystal structures then heterogeneous nucleation of the β-phase on the α nuclei will be difficult and the remaining melt will undercool to a temperature T_1, below T_e. The β-phase can therefore be avoided and the remaining melt will solidify into a supersaturated solid solution, α_{SS}, with a concentration dictated by the metastable extension of the solidus into the undercooled regime. However, as crystallisation takes place, the release of latent heat raises the temperature into the mushy zone (**Figure 12**(b)), in which segregation is permitted. If the cooling rate is not sufficiently rapid, then α_{SS} will transform into a stable α crystallite. In order to fully transform the melt to a metastable supersaturated solid solution and retain the metastable phase, undercooling to temperatures below the point at which the latent heat of fusion is just sufficient to raise the temperature to T_L is therefore required. This temperature is known as the hypercooling limit, ΔT_h. When this occurs, the whole melt solidifies under non-equilibrium conditions and, since atomic diffusion in the solid is much slower than that in the liquid, the metastable supersaturated phase will be 'frozen in' and retained even at moderate cooling rates (Herlach et al., 1993).

Coriell and Turnbull (1982) classified supersaturated solid solutions as an example of compositional metastability. They have been widely researched due to their enhanced properties at ambient temperature and their potential for solid solution strengthening and age hardening. For example, Birol (2007) rapidly solidified Al-12 wt.% Si at cooling rates of up to

10^6 K s^{-1} to achieve a nano-dispersion of Si particles within a supersaturated Al matrix. This microstructural configuration led to a hardness increase of more than double that of the equilibrium alloy. The solid solution could be retained up to a temperature of 523 K, beyond which the precipitation of Si and microstructural coarsening lead subsequently to a substantial decrease in hardness. In order to study the fundamental science behind the formation of supersaturated solid solutions however, such rapid cooling techniques are unsuitable and undercooling methods are preferred. As discussed above however, the release of latent heat upon recalescence can destroy the metastable state and large degrees of undercooling are required in order to retain it. Chen *et al*. (2008b) overcame this problem by using a melt-fluxing and quenching technique. The combination of both undercooling and quenching from a selected point after recalescence allowed the retention of a metastable, single-phase supersaturated solid solution in their immiscible Fe-Cu alloy.

2.4.3. Metastable crystalline phases

Containerless solidification techniques provide a useful way of investigating the formation of metastable crystalline phases. Most research in this area is focused upon determining metastable phase diagrams, understanding phase formation and finding ways to form larger volumes of metastable phases directly from the liquid. In addition to requiring a certain amount of undercooling, the formation of a metastable phase must be kinetically preferred. Kinetic competition between phases (stable and metastable) arises from the influence of nucleation and growth rates, as outlined in the analysis of Turnbull (1987). Nucleation in this case is assumed to occur spontaneously, in either a homogeneous manner or heterogeneously upon substrates which are not specific to the particular phases under competition. However, phase selection can be achieved at a particular undercooling by triggering nucleation and growth using a seed specific to the desired phase. The external triggering of a preselected phase was first demonstrated by Schleip *et al.* (1990) who were able to produce the metastable BCC phase in Fe-Ni alloys by triggering solidification at moderate undercoolings using a BCC Fe-Mo tip. Confirmation of metastable phase formation was obtained through the observation of re-melting at a temperature below the equilibrium melting temperature. The method therefore provided a useful way to obtain experimental data for metastable phase diagram determination.

Occasionally, rapid solidification processing leads to the discovery of new metastable phases and metastable reactions. An example of this comes from the recent work of Cao *et al.* (2013) who investigated a Ni-Si alloy using drop tube processing. The work originated from

investigations into the intermetallic β-Ni_3Si phase, which is of practical interest due to its superior hardness and oxidation resistance at high temperature. However, it is very brittle at ambient temperature, making it unsuitable for most component fabrication techniques. One potential solution to this is to improve ductility using rapid solidification to form a fine grain structure containing anti-phase domains. Towards this, Ahmad *et al.* (2012) attempted to obtain the β-Ni_3Si phase by melt fluxing a Ni-25.2 at.% Si alloy. Despite achieving the required undercooling, a single phase β-Ni_3Si phase was not formed. Instead, a eutectic structure of alternating γ-$Ni_{31}Si_{12}$ and supersaturated α-Ni had developed, with the α-Ni subsequently undergoing a eutectoid transformation to form a mixture of β_1-Ni_3S and α-Ni. A small amount of metastable $Ni_{25}Si_9$ was also observed. Cao *et al.* investigated this observation further by drop tube processing an alloy of a similar composition (Ni-25.3 at.% Si). The resulting analysis revealed the formation of a novel eutectic structure consisting of lamellae of metastable $Ni_{25}Si_9$ and β_1-Ni_3Si, revealing the presence of a eutectic point in the metastable phase diagram between the $Ni_{25}Si_9$ and β_1-Ni_3Si phases.

2.4.4. Quasicrystalline alloys

Quasicrystalline phases are a class of intermetallic compound which have attracted a large degree of intrigue, since their diffraction patterns exhibit symmetries which are 'forbidden' in crystals. In order to fill space in a complete manner, classical crystallographic restriction theorem states that only two, three and four-fold (and higher orders of) rotational symmetry were possible. However , Shechtman *et al.* (1984) reported a 'forbidden' ten-fold diffraction pattern for rapidly quenched Al-14 at.% Mn. It was found that such a structure is possible through the non-periodic ordering of clusters of atoms exhibiting local symmetry, where 'non-periodic' refers to the lack of translational symmetry in two or three dimensions. Two examples of quasicrystalline symmetry are the I-phase and the T-phase quasicrystals. I-phase is the most common form of quasicrystalline symmetry, so-called because of its icosahedral configuration (point group $m\overline{3}5$), which is quasiperiodic in three dimensions. The decagonal T-phase is quasiperiodic in two dimensions and periodic in the third and exhibits point group symmetry 10/mmm (Herlach et al., 1993). The ability to diffract arises from the regular spacing of an indeterminately large number of elements, which can be roughly described as long-range order. Shechtman's discovery of a new principle for the packing of atoms lead to a paradigm shift in chemistry and subsequently won him the Nobel Prize in Chemistry in 2011.

Many other quasicrystalline phases have since been observed, mostly forming via peritectic reactions. Most of these phases are metastable, though some equilibrium quasicrystalline

phases have been observed (Tsai et al., 1987). As the atomic coordination in metallic liquids may be icosahedral, it was suggested that the nucleation of the I-phase may be favoured, since the interfacial energy between this phase and the liquid would be low (Nelson and Spaepen, 1989). Copious homogeneous nucleation of the metastable I-phase was directly observed by Bendersky and Ridder (Bendersky and Ridder, 1986) in Al-14 at.% Mn following electrohydrodynamic atomisation. In addition, I-phase materials are now known to arise from the fine-scale devitrification of glassy alloys (Chapter 2.4.5), which has been attributed to the correlation between the local structure of the glassy phase and the I-phase structure (Köster et al., 1996, Eckert et al., 1998, Saida and Inoue, 2003). The nano-scale dispersion of icosahedral phases within these alloys significantly improves their mechanical strength and ductility in comparison to the corresponding amorphous single-phase alloys (Inoue et al., 2000). Hence, a more comprehensive understanding of the formation of such phases will lead to the better design of future high-performance alloys.

2.4.5. Metallic glasses

Currently, one of the most widely researched metastable metallic structures is that of metallic glass. A glass is formed when crystallisation during cooling is avoided, leading to the continuous and uniform congealment into a solid. As such, the structure of the liquid is essentially frozen into the solid, giving a non-crystalline phase characterised by a complete lack of long-range crystallographic order. In order to avoid crystallisation, a sufficiently rapid cooling rate is required to circumvent the growth of nuclei by reaching the glass transition temperature, T_g, before appreciable crystalline growth can occur. Above T_g, the properties of the liquid (such as volume and viscosity) show a strong temperature dependence, owing to the mobility of the atoms in the melt which allow configurational changes. Below T_g, atomic mobility in the melt becomes so slow that configurational changes are no longer possible and a rigid glass structure is formed. There is therefore little change in the properties of the metal with further cooling. The value of T_g is thus determined entirely from kinetic considerations of atomic mobility, rather than from thermodynamics (Cahn and Greer, 1996). This means that there are a range of structures possible, which can be formed through relaxation processes. The degree of relaxation can be interpreted in terms of the free volume (Taub and Spaepen, 1979) with a rapidly quenched glass possessing an excess free volume which decreases during annealing, or in terms of the local atomic configurations (Dmowski et al., 2007), where more icosahedral order and fewer anomalously long or short interatomic separations lead to a denser and more relaxed glass (Greer, 2009).

Glass forming ability can be enhanced through:

1. The selection of alloying elements which possess a negative heat of mixing, i.e. for a two component A-B alloy, A-B interactions are favoured over A-A or B-B interactions. This raises the energy barrier at the solid liquid interface and decreases atomic diffusivity, lowering the crystal nucleation rate;
2. Multi-component selection, so that the size and complexity of the crystal unit cell is increased to such an extent that the formation of a periodic ordered structure is less energetically favourable;
3. The use of elements with a high atomic radius mismatch, which leads to a higher packing density and smaller free volume in the liquid state. The creation of a crystalline structure will then require a greater volume increase and will be less likely to occur;
4. The use of a composition which is near to a deep eutectic, since the liquidus at this point is closer to T_g, and thus the range of temperatures over which crystallisation can occur is narrower.

Each of these criteria contributes to slower crystallisation kinetics, reducing the cooling rate required for glass formation and increasing the volume of bulk metallic glass (BMG) obtainable. BMGs are highly desirable for their superior low-temperature properties and offer large potential for commercial exploitation. In the dense amorphous structure, crystal defects such as dislocations cannot be accommodated and therefore, under the application of stress, less energy is absorbed and more is elastically rebounded as the material returns to its initial shape. The mechanical properties of glasses and metals therefore combine to give: strengths which are around twice that of steel and yet lighter; good hardness and wear resistance; fracture resistance (toughness), which is greater than ceramics, and; high yield strengths, owing to their elastic properties. At elevated temperatures, metallic glasses exhibit viscous flow, revealing the potential for hot-forming in ways usually restricted to glasses and thermoplastic polymers. Corrosion resistance is also improved in comparison to crystalline metals, due to the inherent lack of grain boundaries. Where glass formers and ferrous magnetic transition metals are combined, soft magnetic properties can also be obtained (Telford, 2004).

Since their discovery by Duwez *et al.* (1960), the achievable casting thickness for BMGs has increased by more than three orders of magnitude, and hundreds of glass compositions have been investigated (Telford, 2004). However, due to the multicomponent nature of BMGs, the number of possible combinations of components becomes inconceivably high and it follows

that only a minute fraction of the compositional space for BMG formers has thus far been explored. To continue investigating one composition of one combination of elements at a time would be inefficient, and is estimated to take several thousands of years at the current rate. In the hunt for optimal BMG forming compositions, Schroers (2013) has therefore developed a technique for creating and assessing 'libraries' comprising of around 800 different compositions at a time. This involves magnetron co-sputtering from three elemental targets which are oriented to create compositional gradients across a substrate. Massively parallel characterisation methods are then employed to determine the solidification temperature, which can be correlated to glass forming ability, and the thermoplastic formability. Using this technique, vast amounts of data can be collected in short periods of time, leading to the rapid identification of promising BMG formers. Over the next few years, potentially huge advances in BMG research are subsequently expected.

2.4.6. Spontaneous grain refinement

2.4.6.1. Introduction

Fine grained metals have long been appreciated for their improved yield strength, hardness and toughness. Smaller grains equate to more grain boundaries per unit volume and therefore more obstacles to dislocation motion. Yield strength subsequently increases with decreasing grain size according to the Hall-Petch relationship (Hall, 1951, Petch, 1953), reaching a maximum at a grain size of approximately 10 nm, beyond which grain boundary sliding results in a decrease in strength. Fine grained metals are conventionally produced via mechanical or chemical means. However, Walker's work (1959) into highly undercooled bulk Ni revealed that an abrupt decrease in grain size occurs beyond a well-defined undercooling, ΔT^*. Since then, a large body of research has shown that a significant number of metallic systems undergo similar transitions (see **Figure 13**). In this case, grain refinement is intrinsic to the solidification process itself, revealing the potential for an attractive alternative to conventional grain refinement processing methods. More crucially, however, the onset of "spontaneous grain refinement" alters or removes the original growth structure; such that continuous measurements of dendrite length scales, as a function of undercooling or growth velocity, cannot be made. There is thus a lack of physical data on which to base and test mathematical models of rapid dendrite growth. As a prevalent structure in solidified materials, which greatly influences the final properties of a component, and as a prime example of spontaneous pattern formation in nature, dendrites have been the centre of much theoretical and practical interest for many

decades. An understanding of the fundamental science behind spontaneous grain refinement would therefore lead to a better understanding of dendrite growth.

Towards the elucidation of the spontaneous grain refinement mechanism, there are therefore two main lines of investigation which have contributed to the spontaneous grain refinement debate – that of the mathematical modelling of dendrite growth and that of gathering physical evidence for the fundamental mechanism behind spontaneous grain refinement, using rapid solidification techniques. To date, however, no one model has been able to completely account for the spontaneous grain refinement behaviour, with the complexity of dendrite growth becoming increasingly more evident as studies progress.

The present report is focused on the collection of physical data for spontaneous grain refinement; however a general awareness of the progress of dendrite growth models and their implications is necessary in order to fully interpret the findings. This section will therefore provide an overview of the on-going 60 year debate behind the simulation of dendritic crystal growth, and will provide an up to date analysis of the main experimental findings and models proposed towards the elucidation of the spontaneous grain refinement mechanism.

2.4.6.2. Simulating dendritic growth

As discussed in Section 2.2.3, when a pure metal or alloy freezes from its undercooled melt, the solid-liquid interface can become unstable and may undergo dendritic growth. The ability to accurately model the process of dendritic solidification would aid in the design of advanced metals and metallic components, and would represent a significant contribution to the wider study of solidification science. As such, a substantial volume of research has been undertaken towards this goal.

Direct observations of dendritic growth in undercooled transparent systems, such as succinonitrile (Corrigan et al., 1999, Li et al., 2000) and xenon (Bisang and Bilgram, 1996, Battersby et al., 1999), provide strong evidence for the self-similar nature of dendrites grown over a range of undercoolings. The radius of the dendrite tip, ρ, thus describes the basic length scale, against which all other length scales of the dendrite may be determined as simple multiples of ρ. Great importance has therefore been placed on the ability to accurately predict ρ, also referred to as the 'operating point' of the dendrite. However, the selection of the correct operating point and morphology of a developing dendrite, with respect to the properties of the system and the solidification conditions, is a long-enduring problem and is far more complex than it first appears.

In 1935, Papapetrou demonstrated, through *in situ* observations of dendritic growth in a number of transparent salts, that the dendrite tip can be closely approximated to a circular paraboloid of revolution, or dendritic 'needle crystal'. Ivantsov's classical theory of 'diffusion-limited' dendritic growth (1947) subsequently confirmed that, for a branchless dendrite growing into an infinite, undercooled, pure melt and whose interface is at local equilibrium, the needle crystal was indeed a shape preserving solution. This was an important finding since the morphology of the tip and the heat and solute rejection rates are greatly influenced by one another. However, rather than directly relating the dendritic growth velocity, v, to the undercooling, Ivantsov's solution uses the Péclet number, P_t, given by:

$$P_t = \frac{v\rho}{2\alpha} \tag{11.0}$$

where α is the thermal diffusivity in the liquid. Hence only the product of the two unknowns, v and ρ, with respect to the degree of undercooling can be determined and the specific v-ρ pair cannot be derived. Experimentally, it is well known that for a given undercooling, a unique tip velocity and radius are selected, revealing the degenerate nature of the Ivantsov solution. As such, the search for an additional mechanism to select the correct operating point of the dendrite began.

Since the Ivantsov solution neglects the presence of a solid-liquid interfacial energy, it falsely allows $\rho \to 0$ as $v \to \infty$. This lead to the introduction of a surface energy term in order to impose a lower limit on ρ, which equates to the critical radius required for nucleation. The idea of the 'extremum condition' was thus born, whereby it was postulated that the dendrite of the highest velocity, with a radius above this limit, would be the one selected (eg. Trivedi and Tiller (1978)). However, Glicksman & Schaefer (1976) showed conclusively through simultaneous measurements of ρ and v, that the correct operating point was not being selected by this method.

Langer and Muller-Krumbhaar (LMK) (1978) among others (Kotler and Tiller, 1968, Oldfield, 1973) thereby shifted the focus to the idea of 'marginal stability', in which the Ivantsov degeneracy is broken by the introduction of capillary forces via:

$$\rho^2 v = \frac{2\alpha d_0}{\sigma^*} \tag{11.1}$$

Where d_0 is a capillary length and σ^* is the 'stability constant', given by Mullins and Sekerka (1964) as $1/4\pi^2 \approx 0.0253$ for a planar interface. This model predicted that an Ivantsov needle would grow at the velocity dictated by the maximum radius permitted against tip-splitting, or

'Mullins-Sekerka' type instability. The LMK model was independently developed into more sophisticated forms by Langer (1980), Lipton, Glicksman & Kurz (LGK) (1984) and Lipton, Kurz & Trivedi (LKT) (1987) which provided good agreement with experimentally determined velocity-undercooling relationships and stability constant data. In particular, the LKT model provided an extension to the case of undercooling and rapid solidification, which gave a reasonable justification for the observed behaviour in the undercooling vs. tip radius relationship. Here, they report that, with increasing undercooling in an alloy system, the dendrite tip radius will first decrease to a local minimum, and then increase to a local maximum, as depicted in **Figure 14**. This behaviour is attributed to the transfer between solutally controlled growth, with high solute Péclet number at low undercooling, to thermally controlled growth, with high thermal Péclet number at high undercooling.

This predicted dependence of ρ upon ΔT has provided a basis for much of rapid solidification theory over the past 20 years (Schwarz et al., 1994), yet experimental evidence in support of a minimum or maximum in tip radius is sparse, owing to the physical difficulties involved in taking *in situ* measurements of ρ. Direct measurements of ρ are possible in transparent dendritic systems, but only for very small undercoolings which are not within the expected range of the local minimum and maximum. For metallic systems, direct measurement is not possible and post-solidification measurements of some characteristic microstructural feature, such as the dendrite trunk radius, are investigated instead; based on the assumption that this scales as some multiple of ρ. To further compound the problem, continuous measurements of such microstructural features across a large range of undercooling are rendered impossible due to spontaneous grain refinement processes, which eradicate the original growth structure (see Section 2.4.6.3). Nevertheless, the theory of a local minimum and maximum in the radius of curvature of the dendrite tip has in fact contributed to one of the more feasible explanations for the spontaneous grain refinement transition itself, which will be covered in more detail in Section 2.4.6.3.

However, the theoretical basis for marginal stability has been widely discredited. Firstly, Langer (1987) demonstrated that the Ivantsov equations have no solution in the absence of crystalline anisotropy, thereby concluding that the apparent agreement with experimental data must be ascribed to coincidence. In addition, the assumption that σ^* is a constant, and therefore independent of ΔT, cannot hold true, since $\rho^2 v$ is proportional to the volume solidification rate, which will vanish as $\Delta T \rightarrow 0$. Thus, σ^* should at least vary with low values of ΔT (Herlach et al., 1993). In fact, there is growing evidence to suggest that, for the case of an alloy system growing under coupled thermo-solutal control, σ^* may vary with undercooling (Ramirez and Beckermann, 2005, Rosam et al., 2008), alloy concentration (Chopra et al., 1988,

Li and Beckermann, 2002, Ramirez and Beckermann, 2005), anisotropy strength, Lewis number (*Le*, equal to the ratio of thermal to solutal diffusivity, α/D) (Ramirez and Beckermann, 2005, Rosam et al., 2009) and Péclet number (Karma and Rappel, 1998, Ramirez and Beckermann, 2005). It may therefore be that the dependence of σ^* on the material (through the anisotropy strength) and on the Péclet number (for pure thermal or pure solutal growth) has facilitated its use as a fitting parameter for the specific material system and local growth conditions being simulated.

As such, marginal stability theory was replaced by microscopic solvability theory, developed by a number of groups (Kessler et al., 1988, Barbieri and Langer, 1989, Ben Amar and Brener, 1993), in which it is shown that an anisotropy in surface tension is necessary to obtain stable dendritic growth. Here, a similar equation to that arising from marginal stability arguments is defined for small Péclet numbers, the key difference being that σ^* is now anisotropy-dependent and, for small Péclet numbers, varies as: $\sigma^*(\varepsilon) \propto \varepsilon^{7/4}$, where ε is a measure of the anisotropy strength. However, the solvability criterion results in a complex equation set which can only be solved for 2-D problems in the limit of low Péclet numbers, the solution to which is similar to that of the more straightforward LKT theory. As such, LKT and other stability models were still in use long after their theoretical basis was shown to be flawed.

More recently, the development of more powerful computing and numerical simulation techniques has driven progress in dendritic growth simulations, the most popular of which are the level set (Osher and Sethian, 1988) and phase-field (Langer, 1986) methods. The level set method has been applied to situations such as the modelling of free dendrite growth into the single-component undercooled parent melt, which has shown good agreement with solvability theory (Kim et al., 2000). However, the complexity of the technique has meant that phase-field methods have overtaken their development in terms of their ability to model multi-component and multi-phase problems. In agreement with solvability theory, phase-field simulations have shown that some degree of crystalline anisotropy is required in order to form dendrites, and that the strength of this anisotropy influences the tip radius, ρ (Wheeler et al., 1993). Most early phase-field methods, however, could only be considered to offer a qualitative analysis in terms of the determination of the characteristic dendritic length scale. It was not until the development of the 'thin-interface' phase-field model by Karma and Rappel (1998, 1996b, 1996a) that quantitatively valid solutions could be obtained through phase-field methods. This model permits quantitative predictions of the dendrite tip radius from the strength of anisotropy, yet only for a single diffusing species. As such, the model can either be applied to the thermal growth of pure elements or the slow solidification of alloys, which can be approximated as isothermal. Hence the ability to quantitatively predict the length scale in

the case of rapid solidification was not advanced much beyond microscopic solvability theory until 2004, when it was shown that the thermal and solutal fields could be coupled within the thin interface model (Ramirez et al., 2004, Ramirez and Beckermann, 2005). From this work it was determined that variations in the selection parameter, σ^*, may be non-monotonic with respect to concentration, for the case of coupled thermo-solutal growth.

These simulations were furthered by Rosam *et al.* (2008, 2009) who applied a selection of advanced numerical techniques in order to extend the case to more realistic Lewis numbers (around 10 000 for metallic systems). Their results exhibited curves akin to the form of LKT theory, undergoing first a local minimum followed by a local maximum; yet in this instance the variations with undercooling are observed in σ^*, rather than in the dendrite tip radius, ρ. Qualitatively, it was further shown that shifts in the position and amplitudes of the LKT curves, due to altered concentration, partition coefficient and Lewis number parameters, were mirrored by those of σ^* within the phase-field model. This confirmed that the apparent parallels between the two models were more than coincidental (Mullis, 2011). Here, it is suggested that the observed parallels arise from the fact that, for a single diffusing species, both σ^* and ρ (within the LKT model) decrease monotonically with increasing undercooling. Thus, since both models rationalise dendrite growth through the effects of competing thermal and solute diffusion, an analogous situation arises. The phase-field model, however, does not reproduce the same relationship between ρ and undercooling as LKT theory. Here, ρ is shown to initially decrease to a local minimum but continues to increase at higher undercoolings, i.e. no local maximum is observed for any of their calculated data sets. Thus, it has been proposed that it is σ^* and not the dendrite tip radius which undergoes the transition through a local minimum and maximum. For lower values of the anisotropy strength, the curve is shifted to lower σ^*, therefore, assuming that $\sigma^*(\varepsilon) \propto \varepsilon^{7/4}$ at low undercooling, it has been suggested (Mullis, 2012) that with increasing undercooling there may be two instances whereby σ^* tends towards 0. If this is the case then it is suggested that as $\sigma^* \rightarrow 0$, the dendritic morphology will become unstable and will undergo tip-splitting to form 'doublons' or 'dendritic seaweed', the implications of which will be discussed in more detail in Section 2.4.6.3. Growth of doublons/seaweed has since been observed in the first instance of $\sigma^* \rightarrow 0$ at sufficiently low anisotropy strength, using further phase-field simulations (Mullis, 2012). However, a second region of unstable dendritic growth was not observed at higher undercoolings, which was attributed to the use of low Lewis numbers (Le = 200). The use of a more realistic Le would be more computationally demanding, and as such further investigation into the possible existence of a second region of unstable growth at high undercooling is required.

2.4.6.3. The spontaneous grain refinement debate

Spontaneous grain refinement can be defined as an abrupt decrease in grain size by 1 to 2 orders of magnitude, which occurs beyond a well-defined undercooling, ΔT^*. It occurs without the need for any external stimulation, since it is intrinsic to the solidification process itself. It is therefore an effect of great interest to the metallurgical community, whereby fine grained metals are conventionally produced extrinsically via one of two methods, either:

1. Mechanically; by fragmentation of the dendritic skeleton during the early stages of solidification, using vigorous stirring (Cheng et al., 1986, Cochrane et al., 2001) or vibration (Mondolfo, 1983), or;
2. Chemically; by the addition of inoculants to encourage copious nucleation throughout the melt (Flemings, 1974).

However, an understanding of the fundamental origins behind the phenomenon is necessary before the full commercial potential of spontaneous grain refinement can be realised. In addition, it transpires from Section 2.4.6.2 that dendrite growth models for rapid solidification are limited by the effect, since spontaneous grain refinement alters the original growth structure in the as-solidified product. As such, continuous measurements of the original dendrite length scale cannot be made as a function of undercooling/solidification velocity, and there is thus a lack of experimental data on which to base and test mathematical models. The subject of the fundamental mechanism behind spontaneous grain refinement has been the centre of debate for a number of decades and, to date, no satisfactory model has been proposed.

Walker (1959), achieved undercoolings of up to 285 K in bulk pure Ni and reported a ΔT^* transition between 140 and 150 K. Here, grain size was observed to decrease monotonically with increasing undercooling to around 20 mm at ΔT^*, beyond which a sharp decrease to a value of around 2 mm was observed. By measuring the pressure pulse created by the solidification of Ni, Walker subsequently found that a maximum in the magnitude of the pulse occurred within the vicinity of ΔT^*. This led him to suggest that grain refinement was due to homogeneous nucleation in the liquid ahead of the solid-liquid interface, induced by a momentary local elevation in melting temperature as a result of the pressure pulse. Walker subsequently performed split crucible experiments in support of this theory, in which he showed that nucleation in the melt on one side of a dividing wall lead to nucleation on the other side of the wall, only beyond undercoolings of ΔT^*. Calculations by Horvay (1965) further showed that the volume change upon solidification may produce negative pressures and result in cavitation ahead of the interface. When such cavities collapse, a sufficient

positive pressure could induce copious nucleation. However, such a mechanism may be expected to produce fine equiaxed grains, whereas at all undercoolings Walker had observed columnar growth from the mould walls into the centre of the sample. Glicksman (1965) subsequently suggested that cavitation at the melt/crucible interface may be responsible for enhanced nucleation in these areas. Most subsequent studies into grain refinement therefore utilised containerless processing techniques (see Chapter 2.3) in order to both eliminate any influence of the crucible walls upon solidification processes and enhance the level of undercooling obtainable.

Since the pioneering work of Walker, a large number of metallic systems have been shown to undergo spontaneous grain refinement transitions, examples of which are summarised in **Figure 13**. The idea of enhanced nucleation due to a solidification-induced pressure pulse has however been discredited, since the measurement of a maximum in the pressure pulse in the vicinity of ΔT^* could not be replicated (Colligan et al., 1961) and neither could the split crucible experiments (Powell and Hogan, 1969). As such, a number of alternative mechanisms have been suggested, including effects arising from the influence of solute upon the melt. Experiments by Jones and Weston (1970) into the Cu-O system, demonstrated that the presence of even small amounts of solute had a profound influence over grain refinement, with oxygen concentrations as low as 150 ppm leading to a measured ΔT^* of only 100 K. The strong influence of O solute upon spontaneous grain refinement was subsequently confirmed in Ag (Powell and Hogan, 1969) and in Ni (Jones and Weston, 1970). Since Walker had doped his Ni with Ag in order to preserve the grain structure, it was suggested that he had in fact observed grain refinement in a dilute alloy, rather than a pure melt, prompting the question of whether grain refinement occurred at all in pure metals. Further experiments into fluxed and levitated pure Ni produced conflicting results in regards to this issue. Ovsiyenko *et al*. (1976) found a columnar dendritic structure up to an undercooling of 140 K, fine equiaxed grains in the region $140\ K < \Delta T < 160\ K$ and a duplex structure at greater undercoolings. Amaya *et al*. (1983) however, observed equiaxed grains at all undercoolings, which gradually reduced in size up to an undercooling of $\Delta T > 225$ K, beyond which a duplex structure containing recrystallisation twins was found. Hence, spontaneous grain refinement in its accepted form – a transition from a coarse columnar to a fine equiaxed grain structure – was not considered to have occurred.

In addition to post-solidification microstructural analysis, further indications as to the physical mechanism behind spontaneous grain refinement have come from examinations of the solidification velocity (v) vs. undercooling relationship. In many cases, a break in the v - ΔT trend is observed to be coincident with the ΔT^* transition, an example of which was observed

by Willnecker *et al*. (1989) (**Figure 15**). Here it was found that, up to ΔT*, the v - ΔT relationship could be closely described by a dendrite growth model based on marginal stability theory (see Chapter 2.4.6.2), which subsequently switched to an approximately linear relationship beyond ΔT*. Similar transitions were observed in Cu-Ni and Cu-Ni-B alloys (Willnecker et al., 1990), with the addition of B concurrently shifting both ΔT* and the v - ΔT break to higher undercoolings. In both cases the velocity at which the ΔT* transition was observed was the same, leading to the concept of a critical growth velocity, v^*, an idea which was supported by a number of other studies (Cochrane et al., 1991a, Evans et al., 1990, Devaud and Turnbull, 1987). Since the critical growth velocity was found to approach the limiting diffusive speed of solute in the liquid, and due to the observed strong influence of solute upon grain refinement, it was subsequently proposed that grain refinement could be linked to the onset of complete solute trapping. However, dilute Ni-C (Eckler et al., 1991b) and Ni-O (Eckler et al., 1991a) systems have been shown to undergo complete solute trapping at velocities well below v^*, which somewhat weighs against this theory.

Another line of enquiry into the spontaneous grain refinement transition surrounded the possible recrystallisation mechanisms occurring either during or immediately following solidification. Powell and Hogan (1969) were the first to suggest that recrystallisation may be driven by dendrite deformation due to a combination of: solidification shrinkage (causing interdendritic fluid flow), evolved oxygen, and pressure pulses leading to cavitation. Evidence in support of this theory came from Ovsiyenko *et al*. (1974), who found that the residual micro-stress in Ni and Ni-3.7wt%Si increased with undercooling, reaching a maximum at 175 K, beyond which recrystallisation resulted in a sharp decrease in micro-stress.

Meanwhile, Kattamis and Flemings (1966) had begun to investigate more concentrated Fe and Ni based alloys. With increasing undercooling they observed a reduction in dendrite side-branching accompanied by a morphological transition to a more cylindrical dendritic form within the coarse columnar grain structure. Beyond the critical undercooling, ΔT*, a transition to a randomly-oriented spherical solute segregation pattern was seen, with each spherical element constituting a single equiaxed grain. Whilst this represented a sharp decrease in grain size, Kattamis and Flemings noted that the 'dendrite element spacing' – taken as the secondary arm spacing below ΔT* and the radius of the spherical elements above ΔT* - decreased monotonically with increasing undercooling. This lead to the suggestion that grain refinement occurs through a combination of two mechanisms:

1. Detachment of the dendrite arms, as observed by Jackson *et al*. (1966) in transparent dendritic systems.

2. Remelting and coarsening of the elongated fragments into spherical elements by mass transport through the interdendritic liquid.

Additional support for this theory, as opposed to recrystallisation or enhanced nucleation mechanisms, has come from an investigation into drop tube processed Cu-Ni and Fe-Ni alloys (Cochrane and Herlach, 1989). The microstructure of large droplets taken from the processed powders was shown to transition from a spherical to a dendritic morphology as solidification proceeded through the droplet. In addition, smaller droplets, whose cooling rate was sufficiently rapid to suppress recrystallisation, still exhibited grain refined microstructures.

Later, Kobayashi and Shingu (1988) published experimental evidence which showed that the coarsening and re-melting of dendrite arms in Cu-O lead to the formation of sub-grains. For higher levels of oxygen supersaturation, they showed that enough excess free energy was therefore present to drive the recrystallisation of these grains into random orientations, with further growth restricted by the pinning of grain boundaries by CuO particles. However, this can only account for grain refinement in systems where the solute has a low solubility in the solid, and not in systems such as Ni-Cu, which undergo spontaneous grain refinement (Xiao et al., 1995, Algoso et al., 2003, Zhang et al., 2010) and yet form a continuous solid solution over the entire compositional range.

Early on, dendrite fragmentation was proposed as a possible mechanism, since such fragments would provide copious heterogeneous nucleation sites for the growth of new grains. This idea was supported by the work of Kattamis and Flemings (1967) who observed branched dendritic fragments in the solute segregation patterns of grain refined alloys, and Schaeffer and Glicksman (1967) who reported that dendrites growing at the surface of Sn–Bi alloys completely fragmented soon after formation. Much later, Cochrane *et al*. (2001) found that both fragmentation and recrystallisation could lead to spontaneous grain refinement in dilute Cu alloys, and that each mechanism might be identified by a distinct signature. Dendrite fragmentation, as was observed in Cu-O (**Figure 16**), may be identified from a discontinuity in the velocity undercooling relationship, along with a more conventional grain refinement transition from a dendritic to a spherical substructure. Recrystallisation, however, does not influence the initial stage of recalescence and should therefore have no impact on the velocity undercooling curve. In this case Cochrane *et al*. demonstrated that, for Cu-Sn (**Figure 17**), the mechanism can be identified from a drop in microhardness beyond ΔT^*. A predominantly dendritic substructure, with curved grain boundaries (indicative of grain boundary migration) and the presence of twins also provide evidence of a recrystallisation and recovery process. Twinned growth was also found to be present at low undercooling, with two sets of poles and

a shared pole (common to both sets) exhibited by the {111} pole figure, relating to the two orientationally-related grains of a sample undercooled by 43 K (**Figure 18**).

Whilst some compelling arguments and evidence had been put forward, no one model for spontaneous grain refinement could provide a complete and satisfactory explanation for the behaviour observed. As more and more studies were undertaken, a general, grain refinement behaviour in alloys began to repeatedly emerge. Whilst pure metals were shown to undergo one grain refinement transition, alloys were shown to undergo two. Many examples of this can be seen in **Figure 13**. Many of the proposed models could not explain the stabilisation of columnar growth at intermediate undercooling with the addition of solute. It was not until the introduction of the Schwarz model (1994) that a feasible explanation for both occurrences of grain refinement was developed. As such, this currently remains the most widely accepted model for spontaneous grain refinement. This theory is based around the marginal stability arguments of LKT theory for dendrite growth (Section 2.4.6.2), in which the radius of the dendrite tip, ρ, is shown to undergo a local minimum followed by a local maximum with increased undercooling as dendrite growth switches from solutal to thermal control. It further draws upon the stability analysis of Karma (1998) who proposed a model for spontaneous grain refinement in which it is shown that the growth of an isolated cylindrical dendrite will develop a Rayleigh-like morphological instability, with wavelength λ , and undergo spheroidisation. Schwarz *et al*. subsequently define two characteristic timescales for dendrite growth from an undercooled melt:

1. τ_{bu} - the breakup time, which is the time required for side branch fragmentation due to Rayleigh instability and which scales with tip radius, ρ.
2. τ_{pl} – the plateau time, which is the time the melt remains close to the melting temperature during recalescence and depends upon the macroscopic heat extraction rate.

When $\tau_{bu} < \tau_{pl}$ grain refinement occurs, since enough time is given for full spheroidisation of the side branches. This therefore corresponds to some critical value of ρ, below which grain refinement occurs (see **Figure 14**), and therefore predicts both grain refinement transitions in alloys as a result of the transfer between solutally and thermally controlled growth with increasing undercooling.

However, in spite of the popularity of the Schwarz model, the theoretical basis for the Karma model was not published until four years later, at which point it was brought into question by Mullis and Cochrane (2000). The Karma model is based upon a simplified view of dendritic growth, considering only a single isolated dendrite, no side-branching activity and a cylindrical

morphology, which is never the case for real dendrites. Since Cline (1971) showed that an array of rod-like eutectics will not spheroidise if the volume fraction of solid, V_{FS}, is greater than ≈25 %, Mullis and Cochrane suggested that the same may be true of an array of dendrites. In which case, the upper ΔT* transition may not be predicted by this theory, as many systems which undergo grain refinement show V_{FS} = 25 % below ΔT*. However Cline only considered solute diffusion, whereas Karma considers the diffusion of both heat and solute. Mullis and Cochrane therefore extended the Karma model to the case of an array of dendrites and found that the wavelength of the spheroidising instability varies as a function of array spacing and becomes infinite above a critical value. This corresponds to a critical undercooling, ΔT^c, above which such instabilities would not grow. By applying this to the Ni-Cu system, they found that ΔT^c exists in the vicinity of the ΔT* transition, casting doubt over whether the Karma model can in fact account for this region of spontaneous grain refinement. Mullis and Cochrane further considered the effect of side branching upon the proposed Rayleigh instabilities and postulated that, if the wavelength of the instability exceeded the secondary dendrite arm spacing, then the instability would be unlikely to grow. Moreover, if grain refinement were due to the proposed remelting mechanism, by definition this must occur post-recalescence and thus cannot account for the apparent coincidence of ΔT* with the break in the velocity undercooling curve.

In addition to the questionability of the Karma model, there is also a concern over the application of LKT theory, which, as discussed in Chapter 2.4.6.2, has largely been discredited. From this however, came the work of Rosam *et al.* (2008, 2009) and Mullis (2012) who demonstrated that it may be the stability parameter, σ^*, and not ρ which undergoes the characteristic local minimum and maximum with increasing undercooling. In this case, there may be two instances whereby σ^*tends to 0 for sufficiently low values of anisotropy, at which point dendrite growth may become unstable, leading to multiple tip splitting and the subsequent transition to dendritic seaweed growth. This theory is supported by the observation of a 'trapped-in' dendritic seaweed structure in samples of highly undercooled 'pure' Cu; where 'pure' is defined as < 200 ppm of oxygen solute (Mullis et al., 2004b) (**Figure 19**).

It is suggested that repeated tip splitting would lead to a delicate and fragile structure with a high degree of crystallographic mismatch, and therefore dislocation density, at the split junctions. As such, it would likely re-melt at these junctions soon after formation, creating numerous solid islands at which fine grains could nucleate. This mechanism is in favourable contrast to conventional dendrite fragmentation, whereby dendrite arms would usually melt off, leaving the primary trunk intact. Since the onset of tip splitting would represent a

transition in growth mode, the model also accounts for the observed break in the v - ΔT trend at ΔT^* (Willnecker et al., 1989, Cochrane et al., 1991a, Evans et al., 1990, Devaud and Turnbull, 1987). It is proposed that the growth front morphology would also change, from a euhedral to a smooth interface as tip splitting took place above ΔT^*, support for which has been observed in levitated Ni droplets (Matson, 1998). However, if seaweed growth is responsible for both grain refinement transitions in alloys, then a break in the v - ΔT relationship and transition in growth front morphology might also be expected for the first grain refinement transition, something which has not yet been reported.

Within the literature, the term 'seaweed' has been used to describe a variety of branched morphologies with varying degrees of deviation from regular dendrites. In general, dendritic seaweed may be defined as a single-crystal growth pattern originating from the repeated tip splitting of a dendrite branch, and which displays a loss of preferred orientation. This results in a structure which does not reflect the symmetry of the underlying crystal. A number of mathematical studies (Ben-Jacob et al., 1983, 1984b, 1984a, Brower et al., 1983, 1984, Kessler et al., 1984) demonstrated that, for diffusion-controlled growth in the absence of sufficient anisotropy to produce stable dendritic growth, repeated tip splitting dominates the interfacial dynamics. The first morphology diagrams for this type of structure were produced using Hele-Shaw (Ben-Jacob et al., 1985) and electrodeposition (Sawada et al., 1986, Grier et al., 1986) experiments, whereby transitions between growth regimes, characterised as 'faceted', 'tip-splitting' or 'dendritic growth', were plotted as a function of the control parameters. Ben-Jacob *et al*. (1986) subsequently went on to perform two-dimensional Hele-Shaw and amorphous annealing experiments, which lead to the identification of a 'dense branching morphology (DBM)', characterised by its smooth circular front maintained by the repeatedly splitting tips. They found that kinetic effects determined the branching rate and that, by including a kinetic term, a good agreement with a linear stability analysis could be made. They postulated that the DBM morphology was distinct from the fractal morphology previously identified (Ben-Jacob et al., 1985, Sander et al., 1985).

Soon after, a number of simulations were carried out (Ihle and Müller-Krumbhaar, 1993, 1994, Brener et al., 1993, 1992, Kupferman et al., 1995) for the two-dimensional free growth of a pure system solidifying in a channel, which identified two types of branch formation. These were classified as 'symmetric fingers', which are symmetric about the axis of the channel, and 'symmetry-broken (SB) fingers' which are not. It was found that the growth of SB-fingers was favoured by a low capillary anisotropy, ε_C, and a high undercooling, i.e. for fixed ε_C, SB-fingers only existed above a critical undercooling, Δ_C, with Δ_C increasing as ε_C increases. Ihle and Muller-Krumbhaar (1994, 1993) further simulated growth in a wide channel, setting $\varepsilon_C = 0$, and

observed the transient growth of a seaweed-like structure. They suggested that the 'building-block' of this structure is a double SB-finger or 'doublon', in which two SB-fingers mirror each other about a narrow 'inner groove' of liquid. This work was supported by Akamatsu *et al*. (1995) who directly observed the growth of a similar morphology in thin films of their transparent FCC analogue system, CBr_4-8mol%C_2Cl_6. Here the growth pattern was investigated as a function of crystal orientation with respect to the directional solidification setup. They found that, in crystals with a {111} plane near-parallel to the plane of the thin film, growth was non-dendritic and exhibited a pattern characteristic of the seaweed morphology. In addition, they found that doublon growth was stabilised at high velocity. A number of important conclusions were subsequently drawn from this work:

1. The capillary anisotropy of the <111> orientation is very weak.
2. Seaweed is formed by the continual creation and elimination of doublons or more complex 'multiplets'.
3. Seaweed can therefore be identified by the presence of 'inner grooves' of constant width.
4. Stable doublon growth obeys selection rules but does not require crystalline anisotropy. No preferred growth orientation is therefore selected for doublon or seaweed growth.
5. Transitions between seaweed growth and a 'degenerate' non-dendritic pattern are observed when two <100> axes are symmetrically tilted at $\pm 45^{o}$ to the pulling axis. These transitions are attributed to the effect of increasing kinetic anisotropy as the pulling velocity increases, since such transitions were not observed for simulations involving purely capillary anisotropy.
6. The characteristic dimensions and tip undercooling of doublons are functions of the growth velocity.

Brener *et al*. (1996), went on to produce a more refined morphology diagram with axes set to the dimensionless undercooling, Δ, and surface tension anisotropy, ε, as shown in **Figure 20**. Here, structures without orientational order are classified as seaweed (S) and structures with orientational order are classified as dendrites (D). Each of these is further sub-categorised into either fractal (F), delineating a pattern with a self-similar internal structure, or compact (C) structures, whereby Ben-Jacob *et al*.'s 'dense branching morphology' is redefined as 'compact seaweed'. It can be seen from **Figure 20** that, in agreement with previous studies, seaweed structures are generally favoured by either a low anisotropy, high undercooling (corresponding to a high growth velocity) or a combination of both. Fractal structures are favoured by low to intermediate anisotropy and/or undercooling, and compact structures are stabilised by high

anisotropy and/or undercooling. They suggest that the noise (e.g. thermodynamic noise), which is always present in a system, plays a large part in the formation of fractal structures, since the strength of the noise both destroys the tips of the dendrites and triggers side-branching. By contrast, the tips of compact structures are stable against noise, yet develop a 'convective' instability which produces side-branches. However, simulations by Bragard *et al*. (2002) into the growth of highly undercooled pure Ni show that, even without the presence of noise, for sufficiently high values of the kinetic anisotropy, tip-splitting may still occur beyond a well-defined level of undercooling, occurring in the vicinity of the ΔT^* grain refinement transition. However, these simulations had been undertaken in order to investigate the possible cause of the commonly observed break in the velocity-undercooling relationship, and the observation of a change in growth front morphology above ΔT^* (Matson, 1998). A break at the 'expected' undercooling was only observed when the kinetic term was set to physically unjustifiable values, leading Bragard *et al*. to suggest that other physical effects may be influencing the interface dynamics at high undercoolings.

Recently, Dantzig *et al.* (2013) have observed both experimentally and computationally the existence of dendritic seaweed structures in FCC Al-Zn alloys. This was in confirmation of similar observations reported by Gonzales and Rappaz (2006, 2008). Here, both groups observe an extended 'dendrite orientation transition (DOT)' with increasing Zn content in Al. For alloys containing less than 25 wt.% Zn, dendrite growth with preferred <100> orientation was observed, whilst for Zn concentrations above 55 wt.%, <110> dendrite growth was found. Between the <100> and <110> regimes at intermediate Zn content, textured seaweed-type structures arise. Dantzig *et al*.'s research was an extension of Haxhimali *et al*.'s model (2006) to the case of binary alloys. Haxhimali *et al*.'s original phase-field simulations were carried out in order to systematically examine the changes in growth orientation as a function of interfacial energy anisotropy, for the equiaxed growth of pure cubic melts at low undercooling. This was carried out alongside experimental investigations into the EBSD-characterised dendrite growth orientations of Al-Zn alloys, as a function of Zn content. It was demonstrated both computationally and experimentally that dendrite growth directions can vary continuously between <100> and <110> as a function of composition-dependent anisotropy parameters. In-between the two regions of well-defined orientation, a region of parameter space was found to exist, in which an extended transition between the two growth directions is observed (see **Figure 21**). Within this parameter space, 'hyperbranched' structures were produced as a result of the competing anisotropies of the growth directions (**Figure 22**). Here, each dendrite initially grew along one of the twelve <110> directions, split into two and then grew towards the <100> direction, resulting in a 24-branched structure. By plotting the positions of several FCC

and BCC metals onto the orientation selection map (**Figure 21**) using anisotropy parameters calculated from molecular dynamics (MD) simulations, it emerged that several FCC metals lie exceptionally close to the <100>-hyperbranched boundary. They therefore suggest that the anisotropy of the solid-liquid interfacial energy can be altered by the addition of solute, leading either to tip-splitting or changes in the preferred growth orientation. It is further postulated that this may account for the many observations of uncharacteristic dendrite growth directions reported in Al and its alloys (Henry et al., 1997, 1998b, 1998a, Sémoroz et al., 2001), since Al has a weak interfacial energy anisotropy which may be altered by the addition of solute with a high interfacial energy anisotropy, such as Zn.

The observations of Haxhimali *et al*., Gonzalez and Rappaz and Dantzig *et al*. have important implications, since they challenge conventional dendrite growth theory. It has generally been accepted that (at least in two dimensions) the preferred dendrite growth orientation will be dictated by the direction in which there is a minimum in capillary pressure, or 'stiffness', which corresponds to a reduction of the melting temperature at the solid/liquid interface. Since differences in capillary pressure arise from the anisotropy of the crystal structure, growth therefore tends to take place along one of the primary crystallographic directions. However, the aforementioned work has shown that other anisotropic parameters can influence the preferred growth orientation. Within the orientation plot of Haxhimali *et al.* (**Figure 21**), Ag, Cu and Ni are all calculated to lie within the hyperbranched regime, just below the <100>-hyperbranched boundary, and yet all of these FCC elements show <100> growth under equilibrium conditions. Since the orientation selection map refers to growth at low undercooling, this suggests that some degree of departure from equilibrium may be required before any alterations in interfacial energy anisotropy become apparent.

In the case of two competing (or oppositely-directed) anisotropies, tip splitting and possible seaweed growth may occur when their strength becomes comparable to one another. In relation to rapid solidification, there is some evidence to suggest that similar competitions in the anisotropies of the growth directions may be occurring as a function of undercooling. In 1986, studies into the anisotropic crystal system of aqueous NH_4Cl demonstrated that undercooling-mediated changes in growth direction were occurring, switching between the <100> and <110> orientations with increasing undercooling (Sawada, 1986). Competitions between the differently-directed anisotropies resulted in the growth of a 'dendrite of oscillatory type' as their relative strengths became comparable. This dendritic structure was characterised by irregularly splitting tips, which do not follow a preferred orientation and whose growth is terminated by impingement on neighbouring branches – indicative of the seaweed morphology. It was concluded that, for a noiseless, anisotropic, 'free' dendrite

system, dendrites may not necessarily grow along crystallographic axes and irregular patterns may form as a result. Further transitions had previously been identified from isothermal studies into the same NH_4Cl-H_2O system (Kahlweit, 1970), wherein NH_4Cl dendrites were shown to transition from slow to fast growth, with growth velocity rapidly increasing by a factor of 10 and the dendrite morphology becoming significantly sharper as undercooling is increased. A detailed analysis of this transition was not carried out until 2001 (Gudgel and Jackson), when the system was subjected to directional solidification experiments and dendrite orientation and morphology was investigated. Oscillations between <100> and <111> oriented growth were observed as solidification progressed, with the growth velocity increasing as the preferred orientation transitioned to the <111> direction. Initially, growth proceeded along a <100> orientation at a speed slower than the imposed drive velocity, thereby leading to a larger undercooling at the dendrite tip. At a critical value of tip undercooling, the morphology of the tip changed such that preferential <111> growth occurred. Due to the smaller tip radius, the growth velocity increased above the drive speed, such that the dendrite grew into warmer liquid and subsequently transitioned back to <100> growth. This process was repeated over the full growth range, confirming that a transition to <111> growth was occurring with increased undercooling.

There have been few studies which have investigated similar transitions in metallic systems as a function of undercooling or growth velocity, with work to this effect mostly restricted to the groups of Henry *et al*. (1998b) and Dragnevski (2004b) and Mullis *et al*. (2004a). These studies were primarily focused on uncovering the mechanism behind the growth of aluminium 'feather' grains, which are highly undesirable structures found in the casting of aluminium alloys and arising from multiply-twinned dendrite growth. Henry *et al*. performed a careful analysis on a range of Al alloys and concluded that the primary dendrite trunks had grown along a <110> orientation, as opposed to the more usual <100> growth direction, and were split at their centre by a {111} twin plane. The switch in growth direction was proposed to be due to the modification of the surface tension anisotropy, owing either to solute addition (a mechanism supported by the aforementioned work of Haxhimali *et al*. (2006)) or due to the solidification conditions - such as a high solidification rate. In order to investigate this further, Dragnevski *et al*. (2004b) performed undercooling experiments on Cu-Sn alloys, with varied Sn contents of 1, 2, 3 and 4 wt.%. Cu-Sn was chosen in preference to an Al alloy, since Al oxides form readily and act as heterogeneous nucleants, preventing large undercoolings from being reached. As feather grain growth had also been observed in some Cu alloys (Kamio, 1989), Cu-Sn was considered to be an appropriate alternative. In all four alloys it was found that, at undercoolings below 90 K, dendrite growth with preferred <111> orientation took place.

Above $\Delta T \approx 90$ K, a transition back to the more usual <100> orientation was observed, accompanied by a distinct break in the v - ΔT relationship (**Figure 23**). Since no transition to <111> growth has ever been reported for pure Cu, it is suggested that there is therefore a minimum solute concentration, which must be less than 1 wt.% Sn, required to induce a change in growth direction with increasing undercooling. For the Cu – 2 and 3 wt.% Sn samples, twinning was also present. Both <111> growth and twinning are restricted to intermediate undercoolings, with the transition back to <100> un-twinned growth above $\Delta T \approx 90$ K attributed to the onset of partitionless growth. This behaviour is compared to that observed by Battersby *et al*. (1999) in the strongly faceting system of Ge-Fe, in which growth along the <111> direction at undercoolings below 150 K switches to a <100> orientation as undercooling is increased. This was coincident with a transition from faceted to continuous growth and was once more identified alongside a large number of growth twins.

2.5. Summary and Aims

Overall, a growing body of work is emerging which is highlighting the extreme complexity of dendrite growth and the large number of competing factors which influence the growth morphology. As prevalent structures in solidified materials, their morphology can have a marked influence on the final properties of solidified components. There is therefore a practical interest in being able to control or even suppress dendrite growth, highlighting the need for more accurate dendrite growth models. It is clear from the literature review that the accurate mathematical modelling of rapid dendrite growth is limited by two principal issues. Firstly, there is currently a lack of sufficient computing power to tackle the multiscale, multicomponent nature of rapid dendrite growth. This is particularly problematic in the case of alloys, where coupled thermo-solutal growth must be considered at realistic length scales; and where it is becoming increasingly clear that solute additions can have a marked impact on the interfacial energy anisotropy and subsequent growth pattern. Secondly, there is a lack of experimental data on which to base and test mathematical models; owing to the removal/alteration of original growth structures by spontaneous grain refinement effects. As such, a better understanding of spontaneous grain refinement would lead to a better understanding of rapid dendrite growth; which represents the main driving force for research into this effect. Experimental investigations into the phenomenon have, however, generated a variety of strong, yet conflicting, evidence as to the fundamental mechanism behind it. As such, there remains a large degree of debate on the subject and, to date, no single model has been able to account for the variety of observations reported.

The present study aims to address the need for more experimental data, with a particular focus on providing a detailed analysis of the character and orientation of the dendrites as a function of solidification velocity. Two compositions of Cu-Ni alloy will be investigated, using the containerless solidification technique of melt-fluxing to undercool and rapidly solidify alloy droplets. The velocity-undercooling data can then be analysed and a range of microstructural and texture analysis applied in order to elucidate the mechanism behind spontaneous grain refinement and the influence of solute concentration upon this. It is hoped that the study will help to illuminate some of the contributing factors to the spontaneous grain refinement mechanism and provide a deeper insight into dendrite development at high growth velocity.

The Cu-Ni system has been relatively well studied within the context of spontaneous grain refinement. This is due mainly to the simplicity of the binary system, since it forms a continuous FCC solid solution over the whole compositional range, thereby simplifying post solidification analysis. In 1989, Willnecker *et al*. used electromagnetic levitation to investigate the microstructure and v-ΔT relationship of a Cu–30 at.% Ni alloy undercooled within the range 100 K < ΔT < 300 K. They reported a transition from a coarse dendritic to a refined spheroidal microstructure at an undercooling of around $\Delta T^* \approx 200$ K. This was found to be coincident with a negative break in the velocity undercooling curve, wherein a transition between a power law and an approximately linear relationship was observed. Grain refinement was attributed to the onset of solute and defect trapping, since the critical velocity of 17.5 m s^{-1} was found to be close to the diffusive speed of solute in the melt. No lower grain refinement transition was reported, most likely because measurements below ΔT = 100 K were not made.

In 1995, Cu–70 at.% Ni was investigated in the undercooling region 120 K < ΔT < 300 K using a melt fluxing technique (Xiao et al., 1995). Here, a drop in grain size by a factor of 10 was observed between 135 K < ΔT < 155 K; hence a ΔT^* value of 145 K is suggested. Microstructures of samples taken from undercoolings just below the ΔT^* transition showed necked and fragmented dendrites (**Figure 24** (left)). EDX analysis of the composition of the dendrites determined that the solute concentration varied across the length of the trunks, leading to the suggestion of a remelting mechanism in which solute-rich areas melt during recalescence to cause a thinning/necking of the dendrite trunk. It is suggested that the necked dendrites subsequently fragment due to mechanical stress; similar to that suggested by Willnecker *et al.* (1989). At undercoolings well above the ΔT^* transition, fine equiaxed grains were observed with an average diameter of around 25 μm (**Figure 24** (right)).

Algoso *et al*. (2003) went on to perform electromagnetic levitation experiments on Ni–5 at.% Cu and Ni-10 at.% Cu. The velocity-undercooling relationship in this case was found to be more complex, initially proceeding via a power law relationship at low undercooling, followed by two plateaus – one at intermediate undercooling and one at high undercooling, separated by a steep increase in velocity, as shown in **Figure 26**. Since similar experiments into pure Ni (Bassler et al., 2003) show that a plateau only exists at high undercoolings, the intermediate plateau is suggested to arise from the addition of Cu solute. The high undercooling plateau is then attributed to the effects of residual oxygen behaving as an additional solute contribution. Within the region between the two plateaus, where the growth velocity increases rapidly with undercooling, a transition between a dendritic and a cellular structure is seen. Here, cell size decreases with increasing undercooling from an average of 61 μm at ΔT = 177 K to an average of 26 μm at ΔT = 233 K; showing a high consistency with studies previously mentioned in spite of the compositional difference. Such plateaus in the v-ΔT relationship have, however, not been reported elsewhere. The mechanism for grain refinement in this case is not explicitly explored, and is loosely attributed to the transfer between solutally and thermally controlled growth.

Similar refined grain sizes have also been observed in a more recent study of Ni–15 at.% Cu (Zhang et al., 2010), with the first grain refinement transition (27 K < ΔT < 84 K) exhibiting equiaxed grains of < 25 μm diameter and the second ($\Delta T^* \approx$ 180 K) leading to grains of around 15 μm. In this case the first grain refinement transition is attributed to the break-up of dendrites upon recalescence, whilst the second is thought to be due to the plastic deformation of dendrites and subsequent recrystallisation.

Norman *et al*. (1998) compiled a comprehensive study of the grain refinement transitions observed in a number of Cu-Ni alloys ranging in composition from 0 to 90 at.% Cu, using electromagnetic levitation. A microstructure-selection map was subsequently compiled as shown in **Figure 25**. Here, microstructures are classified as either grain refined or coarse grained, with the grain refined microstructures again exhibiting an average size of 25 μm. A distinction is made between the low undercooling grain refinement region - whereby a mixture of fine grains, dendrite fragments and a large amount of porosity is observed - and the high undercooling region of grain refinement; which exhibits fine grains separated by high-angle grain boundaries, twins within some of the grains and no porosity. In this case the Schwarz model for grain refinement is suggested to give good qualitative agreement with the grain refinement transitions observed, but as already discussed (Chapter 2.4.6), the basis for this model has been somewhat discredited. In addition, the Schwarz model represents a form of fragmentation mechanism, which may explain the observation of dendrite fragments in the

low undercooling region of grain refinement but may not account for the final microstructure observed in the grain refined samples obtained at high undercooling. Here, the observation of high angle grain boundaries and the presence of twins would be more indicative of a recrystallization mechanism.

A summary of the positions of the grain refinement transitions reported in the literature for the Cu-Ni alloy system is given in **Figure 27**; in which the suggested grain refinement mechanism is indicated. The majority of this data is taken from the microstructure-selection map compiled by Norman *et al.* (1998) and hence, as discussed above, the suggested Schwarz fragmentation mechanism plotted may in fact be fragmentation at low undercooling and recrystallization at high undercooling. This should therefore be kept in mind, as the general mechanism map produced from this (**Figure 28**) would change dramatically if this were the case. This mechanism map shows that, in general, the lower undercooling grain refinement mechanism is reported to occur via dendrite fragmentation. At high undercooling most studies also report a form of fragmentation mechanism; however a handful of these grain refinement transitions are reported to occur via a recrystallisation mechanism. As discussed, the work of Norman *et al.* contributes a large number of points to this map and, due to the ambiguity in the exact grain refinement mechanism, it may be that the majority of this high-ΔT grain refinement transition is actually due to recrystallization. However, to be consistent with the literature, the suggested mechanism has been used. In this case, the handful of recrystallization mechanisms reported occur at slightly higher values of ΔT^* than the general trend observed for fragmentation mechanisms, suggesting that either:

1. Further increases in undercooling may result in a transition from a fragmentation to a recrystallisation mechanism (as indicated by the mechanism map), or;
2. The containerless technique used in the investigations may influence the predominant mechanism. In particular, it may be that the stirring present in the electromagnetic levitation technique employed in most of these studies (including Norman *et al.*) is inducing dendrite fragmentation in place of a natural recrystallisation mechanism. This may also lead to a shift in the apparent grain refinement transition to lower undercooling.

In any case, there is some disagreement between different studies as to the prevailing grain refinement mechanism. In order to investigate this further, the results generated in the present work will be compared against this mechanism map in order to determine if there is good agreement between the present work and that of the literature. It is hoped that a more thorough investigation of dendrite character and texture (using a containerless technique

which induces minimum stirring and convection in the melt), will help to shed some light on the apparent disagreement between mechanisms. The evolution of the mechanism map as a result of the present work can then be deduced for comparison.

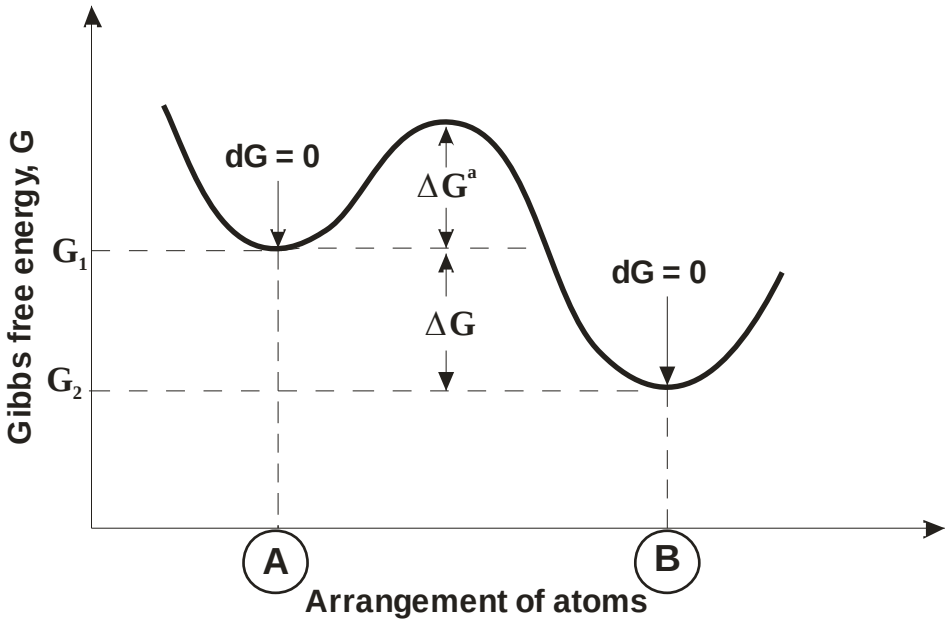

Figure 1 Showing variation in Gibbs' free energy with arrangement of atoms. Since configuration B has the lowest overall free energy, this is the systems' stable equilibrium state. Configuration A is a metastable equilibrium, having ΔG = 0 at higher values of G. Reproduced from (Porter and Easterling, 1992)

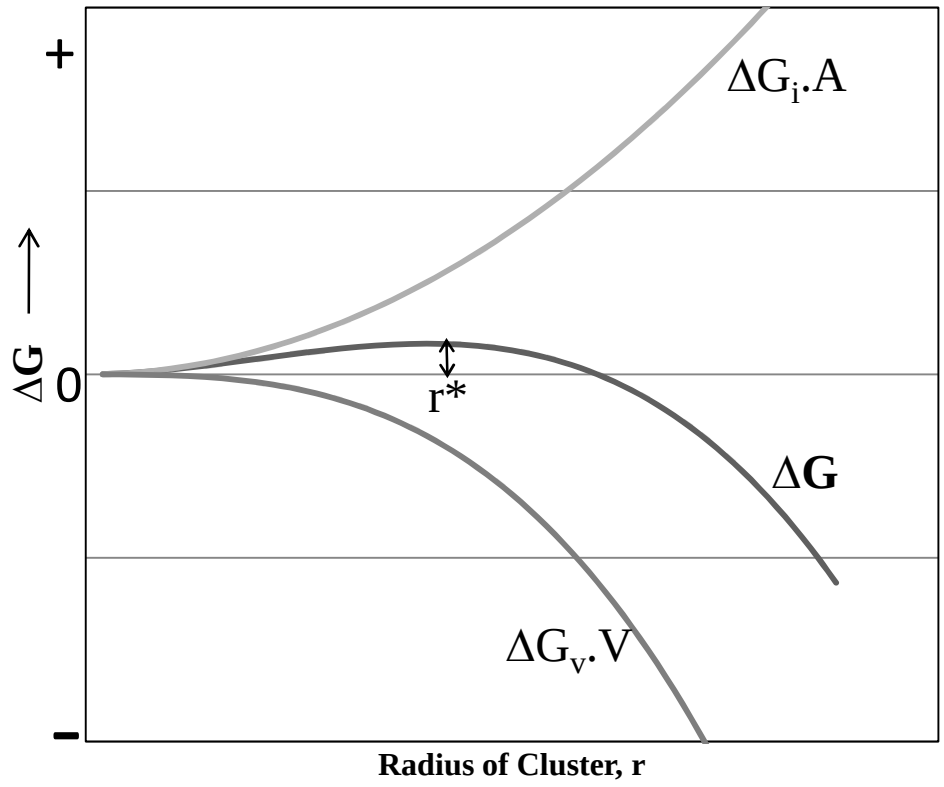

Figure 2 Free energy curve for nucleation at temperatures below T_m, showing the increase in surface energy ($\Delta G_i.A$) and decrease in volume free energy ($\Delta G_v.V$) produced by the formation of a cluster of radius r. The resulting free energy of the system (ΔG) is also illustrated. The critical radius (r*) required for nucleation is highlighted. Reproduced from (Kurz, 1989)

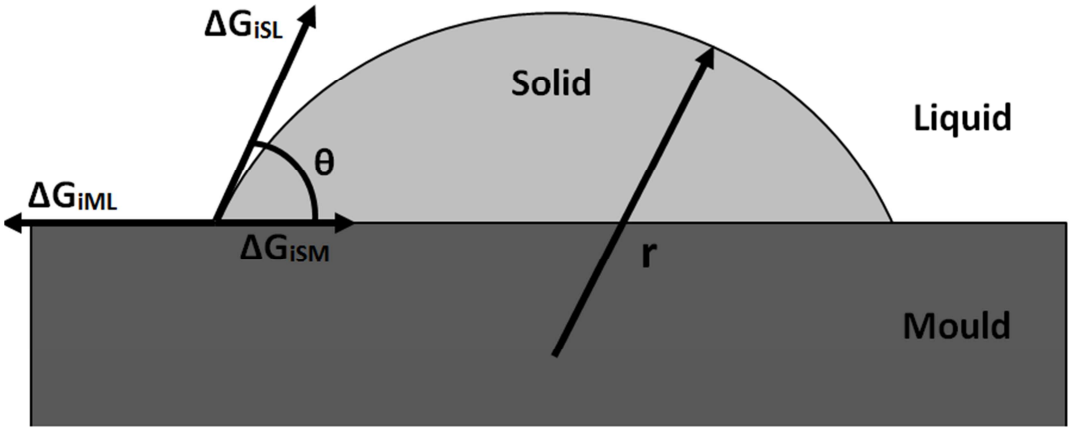

Figure 3 Heterogeneous nucleation of a spherical cap on a flat mould wall. Reproduced from (Porter and Easterling, 1992)

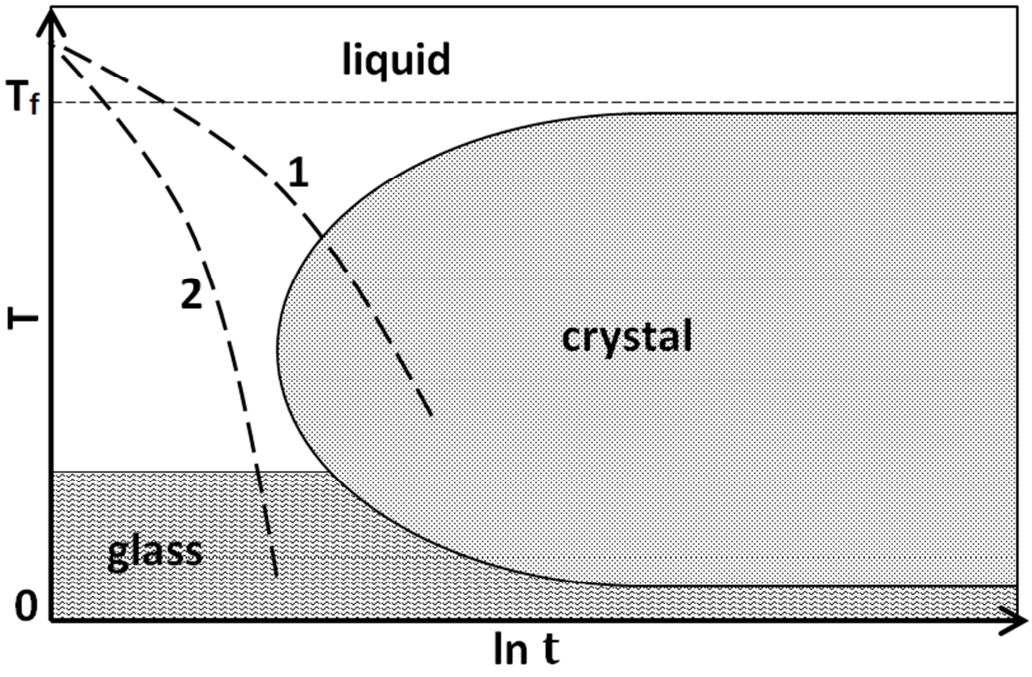

Figure 4 CCT diagram showing the time required for nucleation and growth as a function of absolute temperature. Cooling curve 1 shows nucleation and crystal growth under slow solidification conditions, whilst curve 2 shows that the nucleation of a crystalline phase can be avoided completely upon sufficiently rapid cooling; leading to the formation of an amorphous/glassy solid.

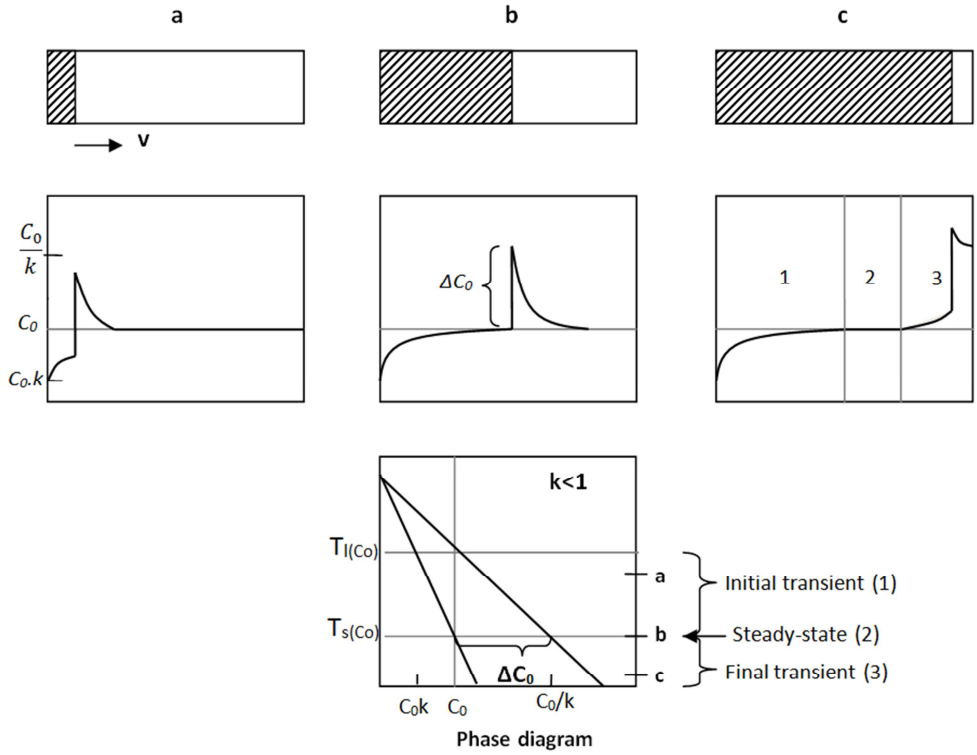

Figure 5 Showing solute pattern formation in a unidirectional (left-right), steady-state, solidifying column of liquid. In this particular case, the temperature at which steady-state growth is occurring is equal to the solidus temperature, since this is a 1D planar front. For dendritic growth, the fraction solidifying will be <1 and thus the steady-state front may be at a temperature anywhere in the range $T_S<T<T_l$. Here, C_s and C_l are given by the intersection of the solidus and liquidus lines at T, and, whilst they depart from C_0, *k* remains constant. Reproduced from (Kurz, 1989)

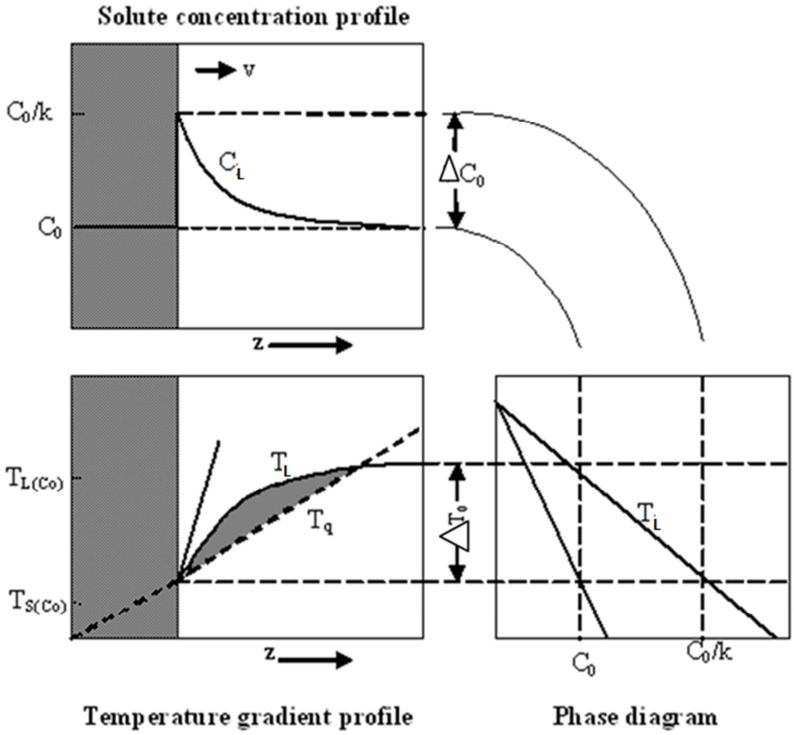

Figure 6 Showing zone of constitutional undercooling in alloys imposed on the melt by solute partitioning mechanisms. Reproduced from (Kurz, 1989)

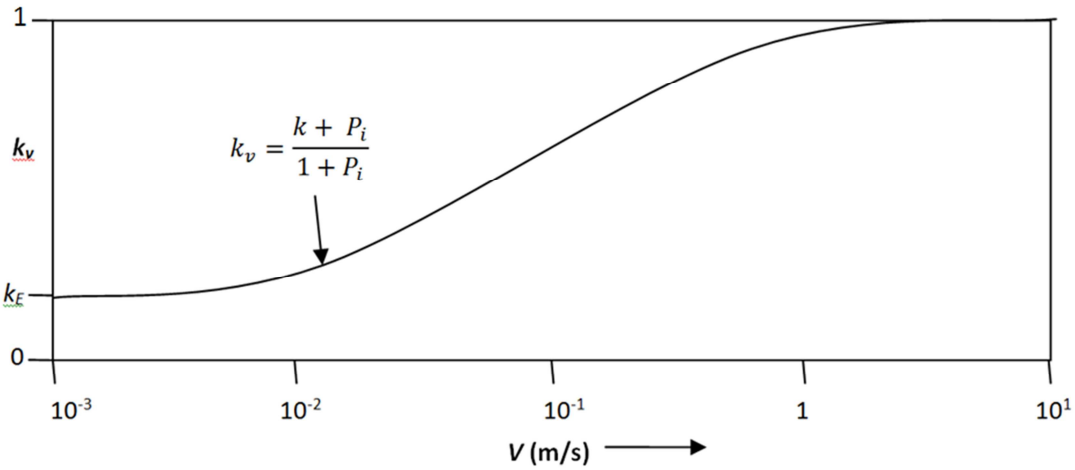

Figure 7 Showing variation in distribution coefficient with growth rate, for k_E =0.1 and D_i / δ_i =3 x 10^{-2} m s^{-1}. Reproduced from (Kurz, 1989)

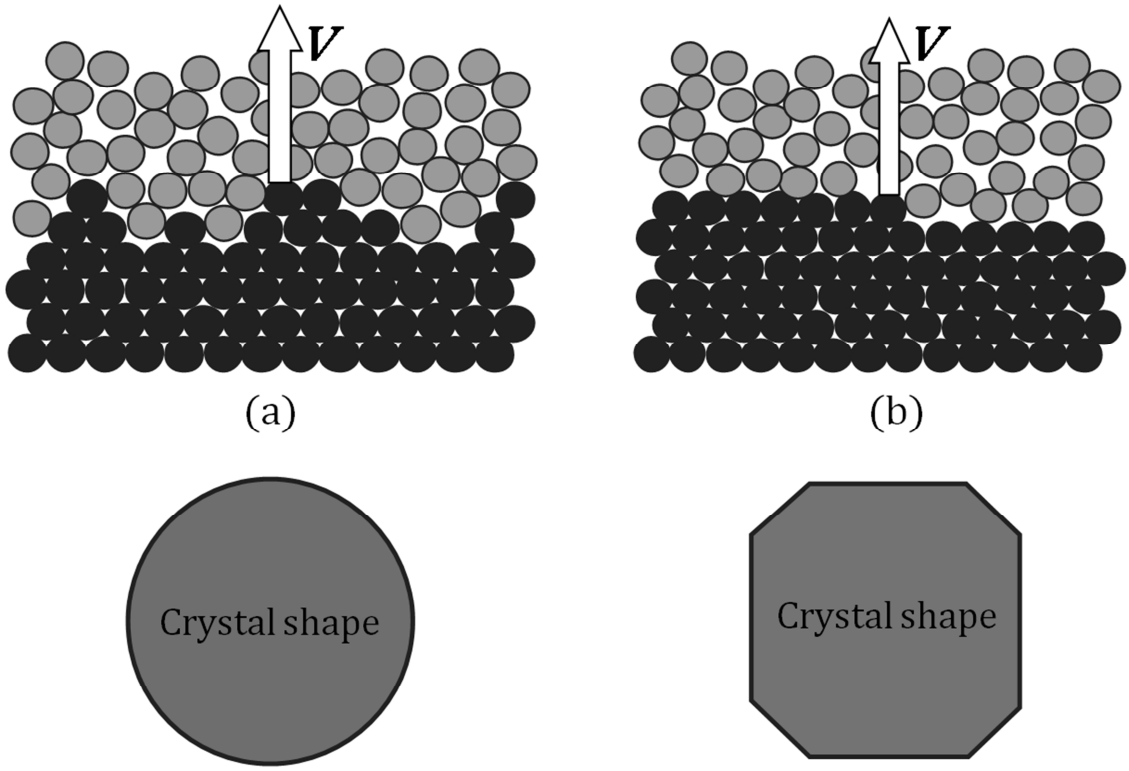

Figure 8 Types of solid-liquid interface encountered in solidification (top) and resulting crystal shapes (bottom) for a) diffuse interfaces typical of metals and b) smooth interfaces typical of faceted materials. Reproduced from (Dantzig and Rappaz, 2009).

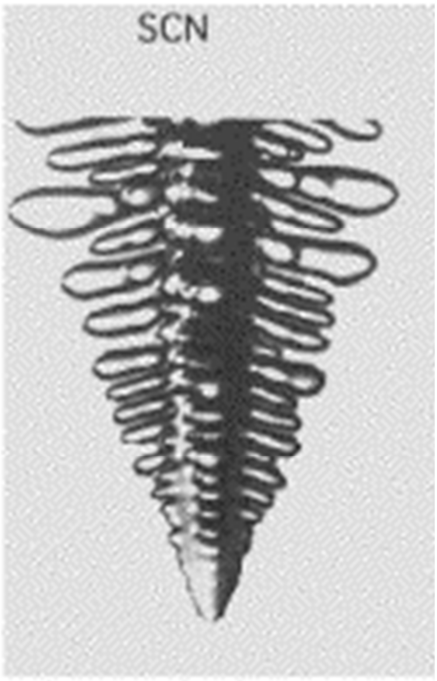

Figure 9 An example of a steady-state BCC succinonitrile (SCN) dendrite grown into a high purity undercooled melt. Obtained from: (Glicksman and Lupulescu, 2004).

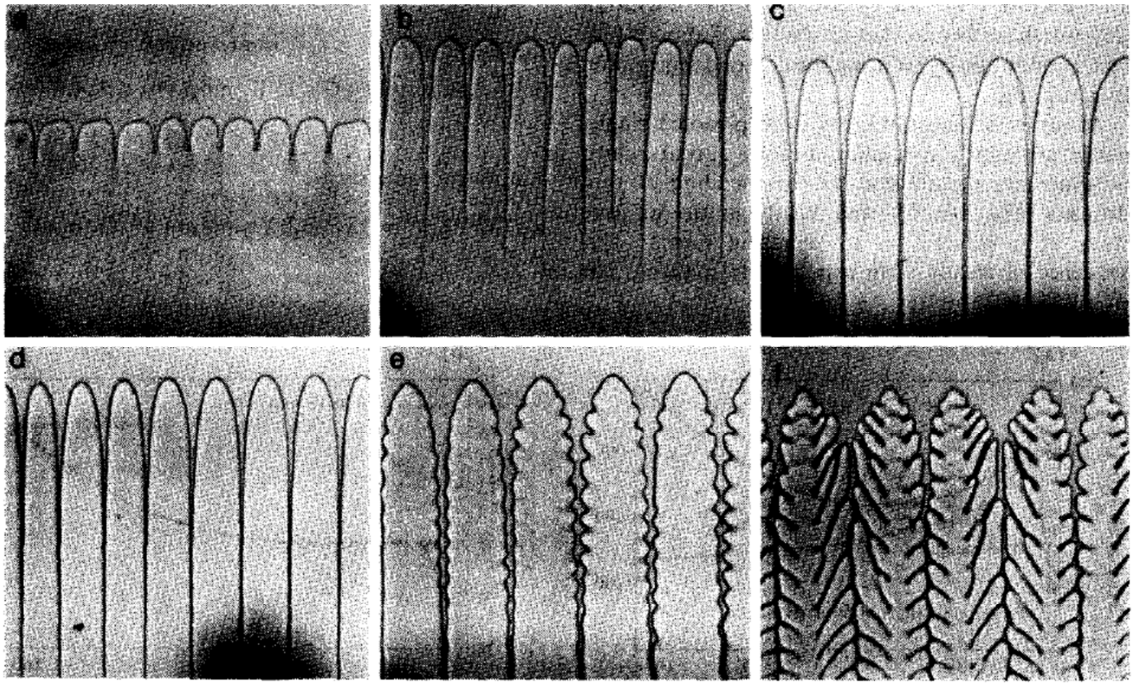

Figure 10 Microstructures observed in an SCN-0.66 wt.% salol alloy, directionally solidified with imposed thermal gradient of 4.5 K mm^{-1} and pulling speeds (in µm s^{-1}) of a) 0.7 b) 0.95 c) 2.0 d) 4.1 and e) 5.7 f) 7.6 (Liu and Kirkaldy, 1995).

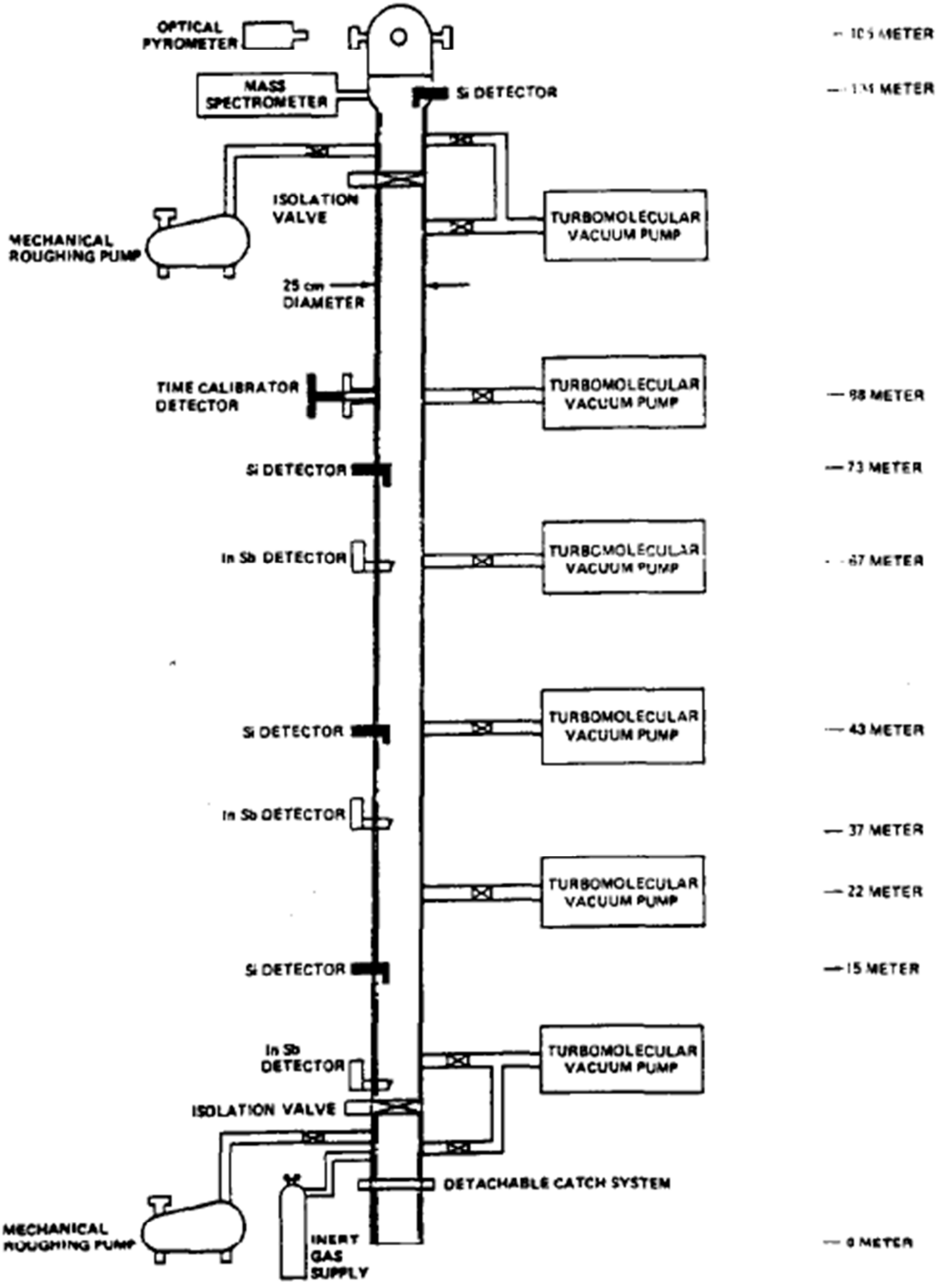

Figure 11 105 m drop tube at NASA Marshall Space Flight Centre (Hofmeister et al., 1989)

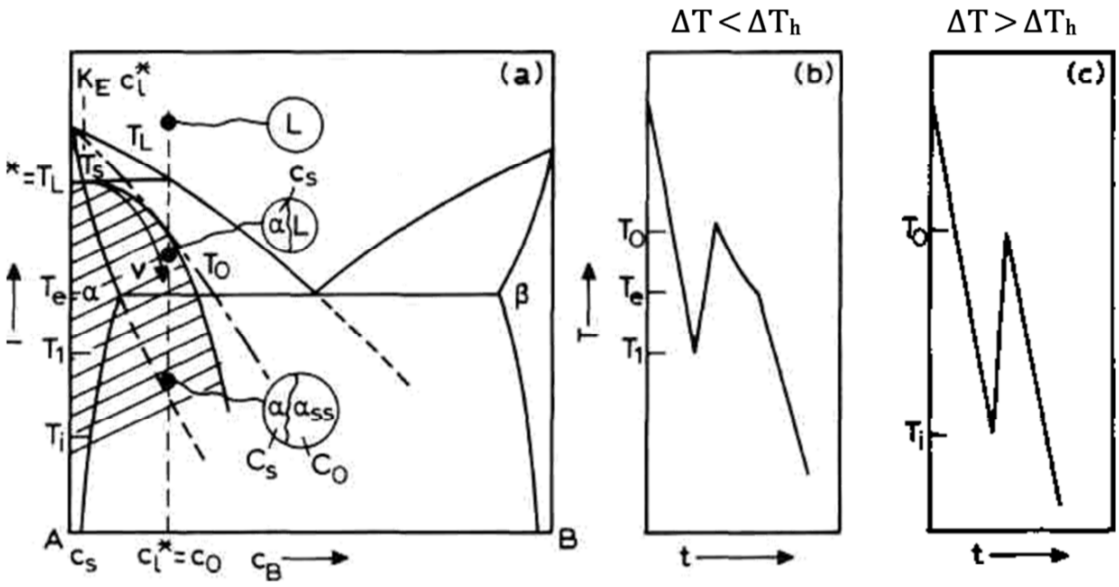

Figure 12 Eutectic phase diagram of A-B alloy showing thermodynamic and kinetic constraints for the formation of a supersaturated solid solution under rapid solidification conditions. a) phase diagram of the system b) temperature-time profile when $\Delta T < \Delta T_{hyp}$ c) temperature-time profile when $\Delta T > \Delta T_{hyp}$ (Herlach et al., 1993).

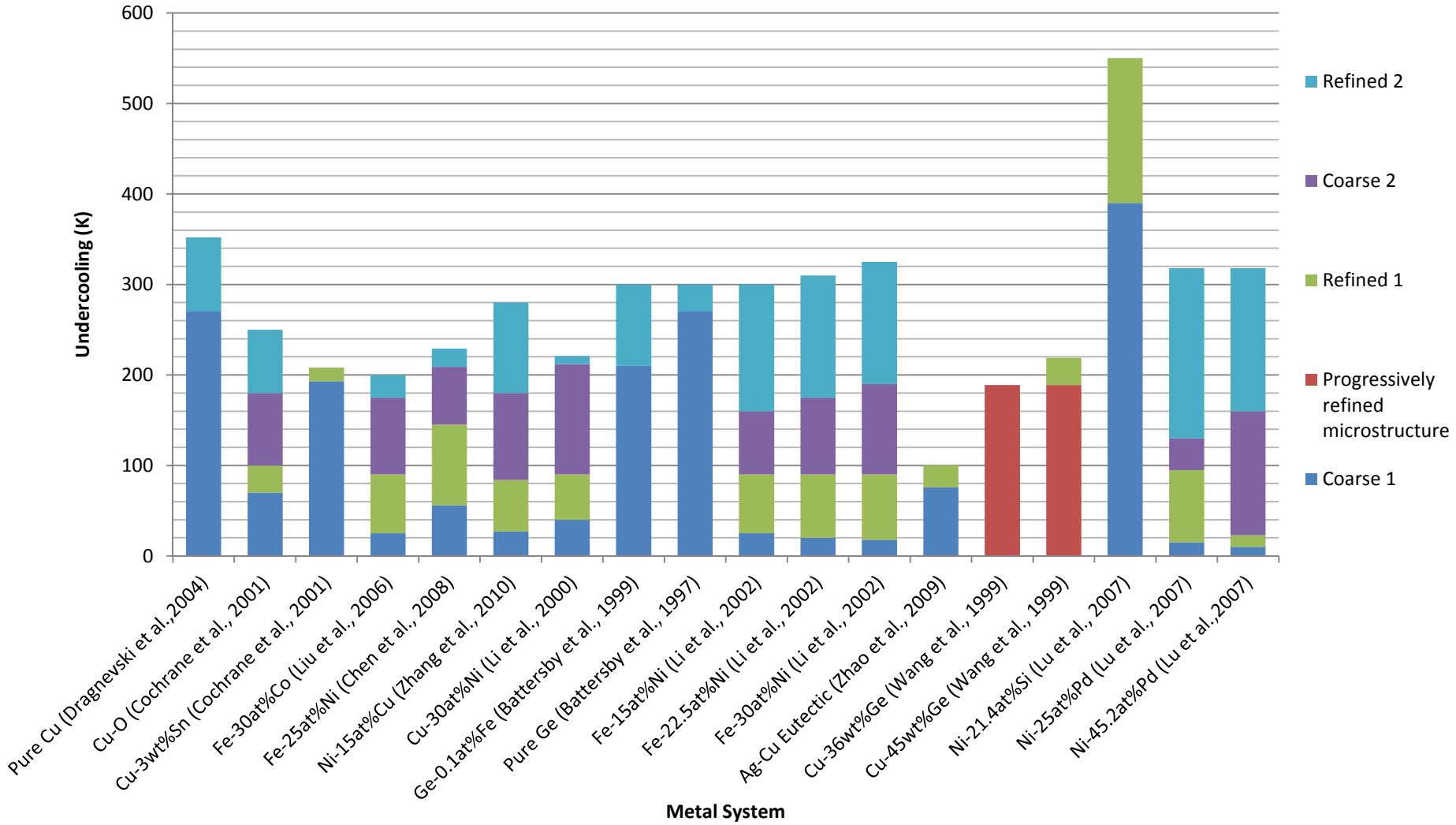

Figure 13 Summary of a number of microstructural transitions observed in many metals with increasing undercooling.

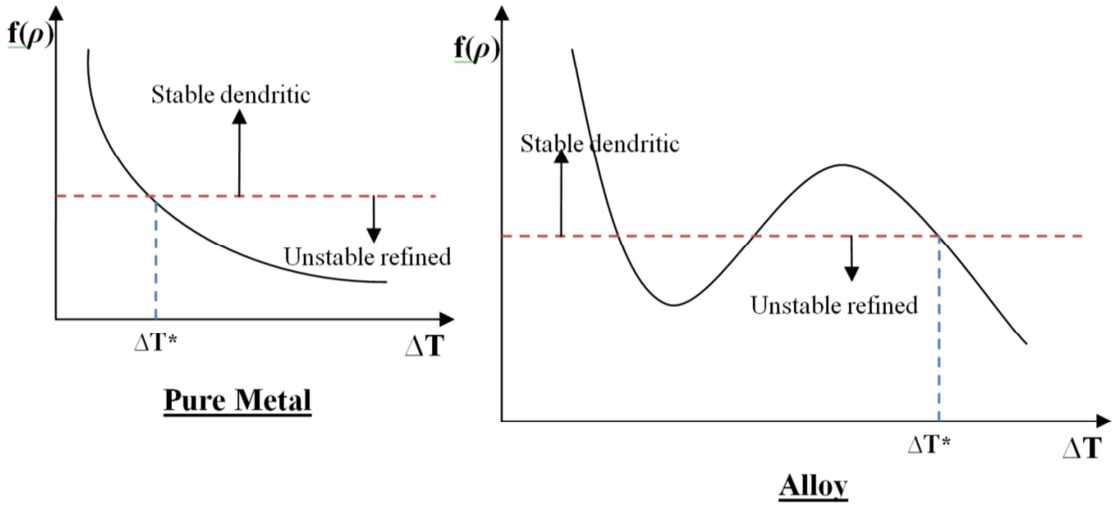

Figure 14 General form of the LKT-predicted ρ-ΔT curves for pure melts and alloys, in conjunction with the grain refinement tendencies as proposed by Schwarz *et. al* (1994).

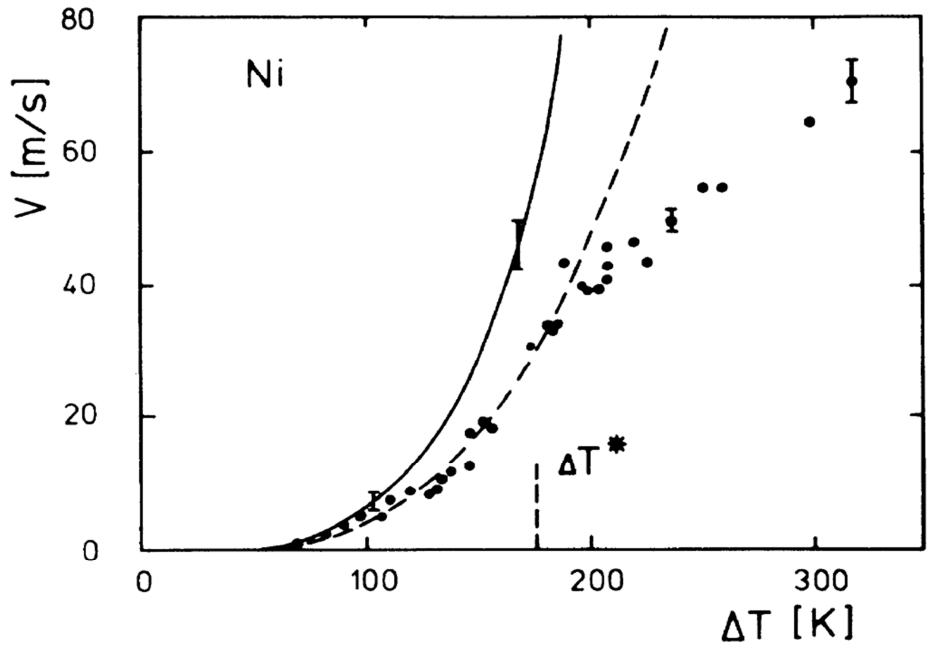

Figure 15 The break in the velocity-undercooling relationship as reported by Willnecker *et al*. (1989) for pure Ni. Dots indicate measured values, solid line indicates the theoretical prediction as based on LKT theory, and dashed line delineates predictions made for nonequilibrium conditions at the interface by including atomic attachment kinetics. The error bar represents the uncertainties present in the material parameters used.

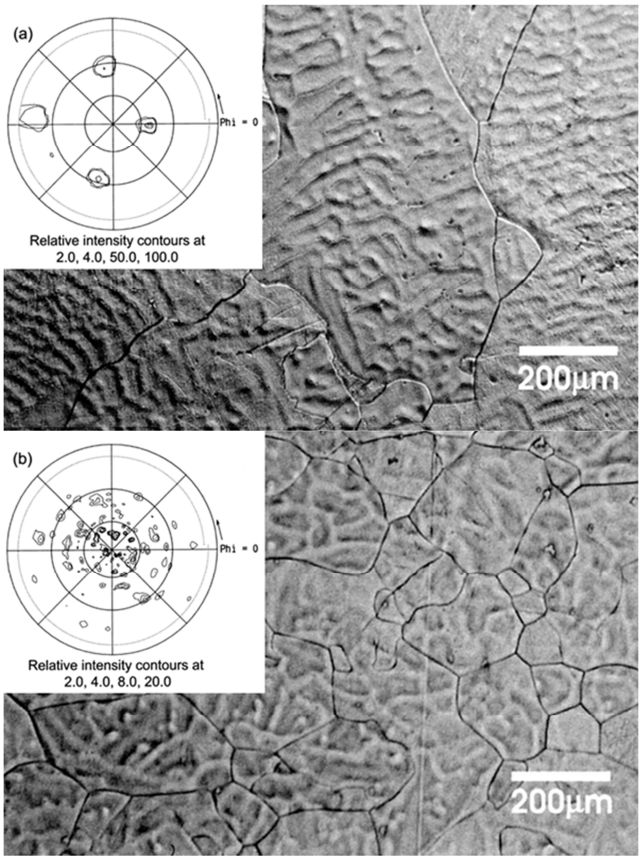

Figure 16 Undercooled Cu-O alloys as reported by Cochrane et al. (2001). (**Top**) Sample undercooled by 160 K exhibiting a dendritic substructure which extends across the grain boundaries, the four poles in the inset pole figure indicating that the substructure is continuous. (**Bottom**) Sample undercooled by 250 K showing refined grains with a spherical substructure containing dendrite fragments, and inset {111} pole figure confirming the random orientation of the grains.

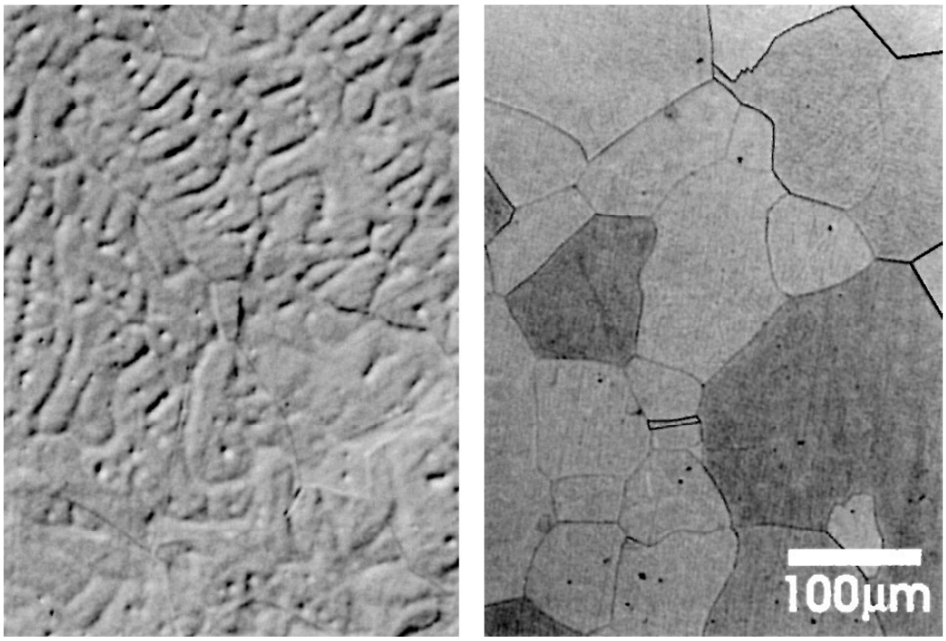

Figure 17 A grain-refined Cu-3wt.%Sn alloy undercooled by 208 K as reported by Cochrane et al. (2001), etched to reveal (**left**) predominantly dendritic substructure and (**right**) curved grain boundaries indicative of grain boundary migration and therefore a recrystallisation and recovery process.

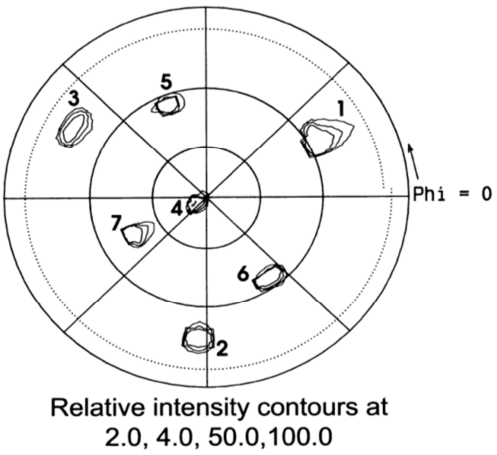

Figure 18 Pole figure of a Cu-3wt.%Sn alloy undercooled by 43 K, with each of the poles 1-6 sharing a common angle of 72°53' or 109°47' with pole 7, indicating growth via a twinned dendrite (Cochrane et al., 2001).

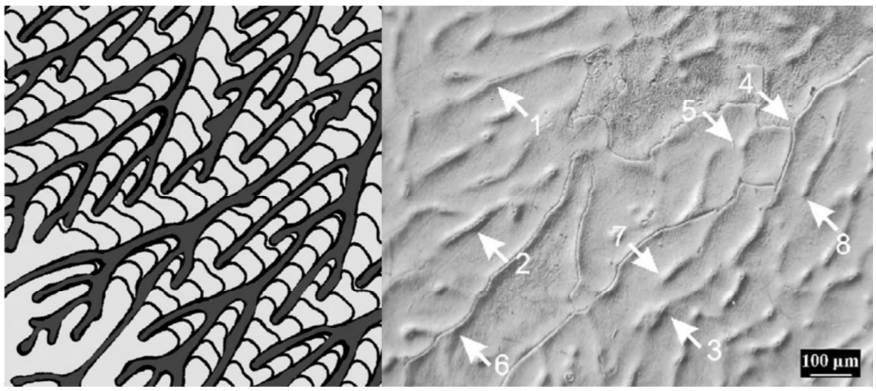

Figure 19 (**Left**) Simulated growth of dendritic seaweed from bottom left to top right and (**right**) microstructure of seaweed observed in highly undercooled 'pure' Cu (where 'pure' is defined as < 200 ppm O – hence the solidification pattern may still be resolved) showing remnant liquid channels which periodically fragment (1-6) or spontaneously appear (7-8), with growth from bottom left to top right (Mullis et al., 2004b).

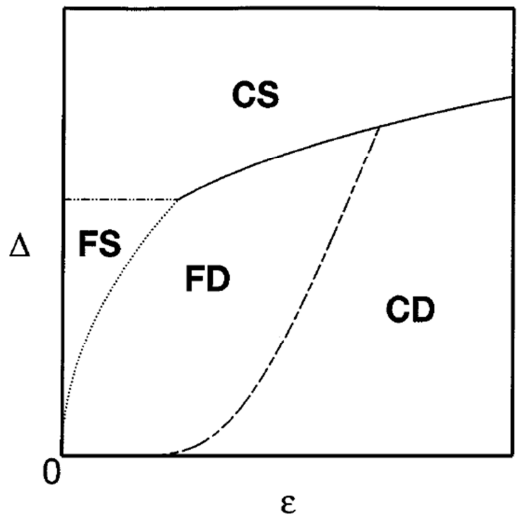

Figure 20 The kinetic phase diagram of Brener *et al*. (1996) delineating the regimes of compact (C) and fractal (F) dendritic (D) and seaweed (S) structures with variation of dimensionless undercooling, Δ, and surface tension anisotropy, ε.

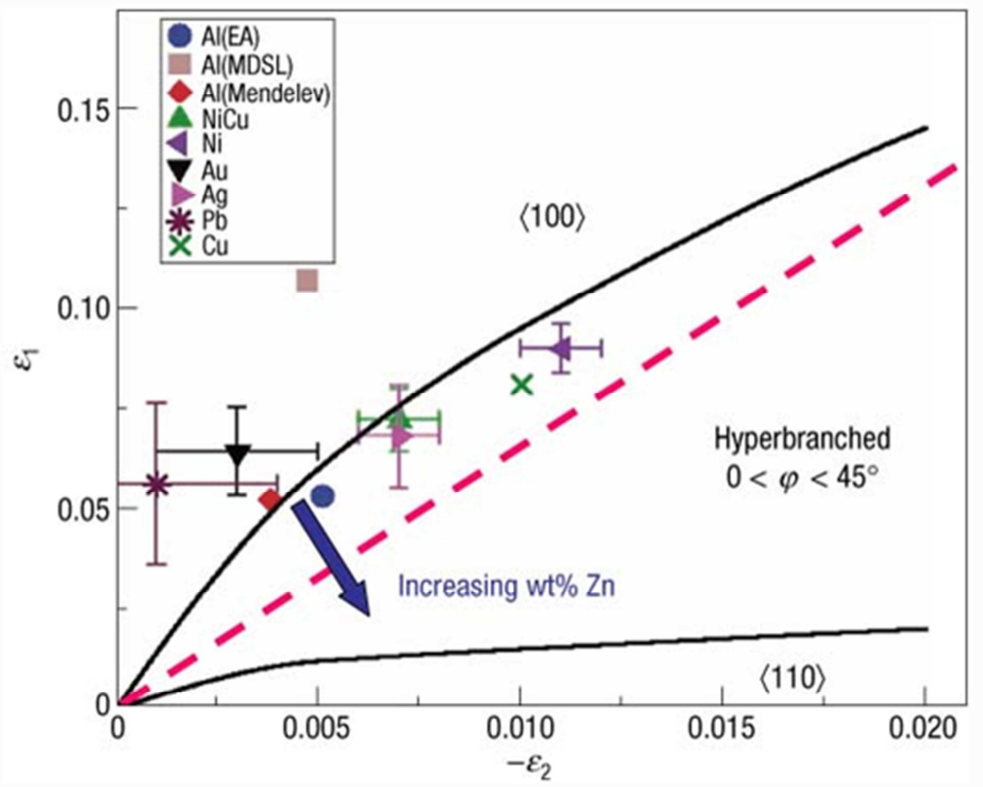

Figure 21 Haxhimali et al.'s (2006) orientation selection map from phase-field simulations, showing the two different regions identified for <100> and <110> growth, above and below the two solid black lines (respectively), and the hyperbranched regime produced in-between. Calculated anisotropy parameters for a range of FCC metals are included, and the blue arrow represents the suggested change of anisotropy with addition of Zn in Al. Interfacial stiffness has minima corresponding to <100> and <110> above and below the dashed red line respectively, with a degeneracy of orientation on this line wherein all directions contained in the {100} planes have equal stiffness minima.

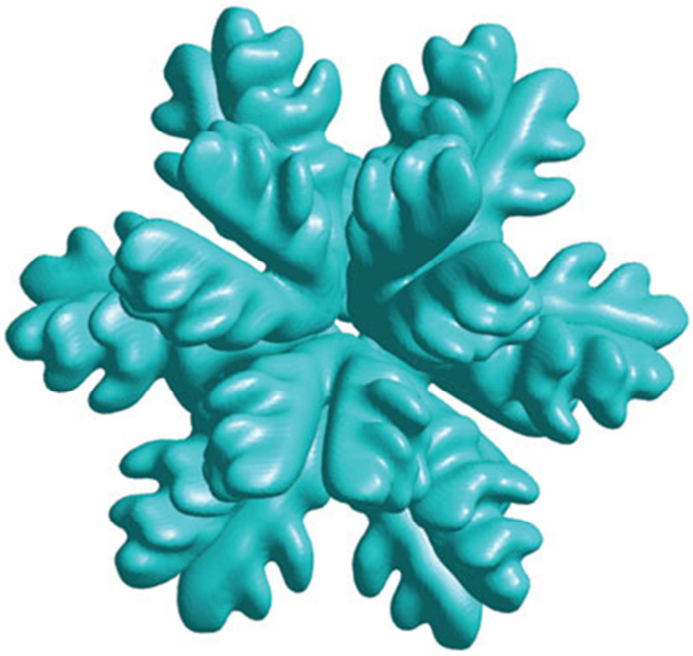

Figure 22 An example of a hyperbranched structure as simulated by Haxhimali et al. (2006).

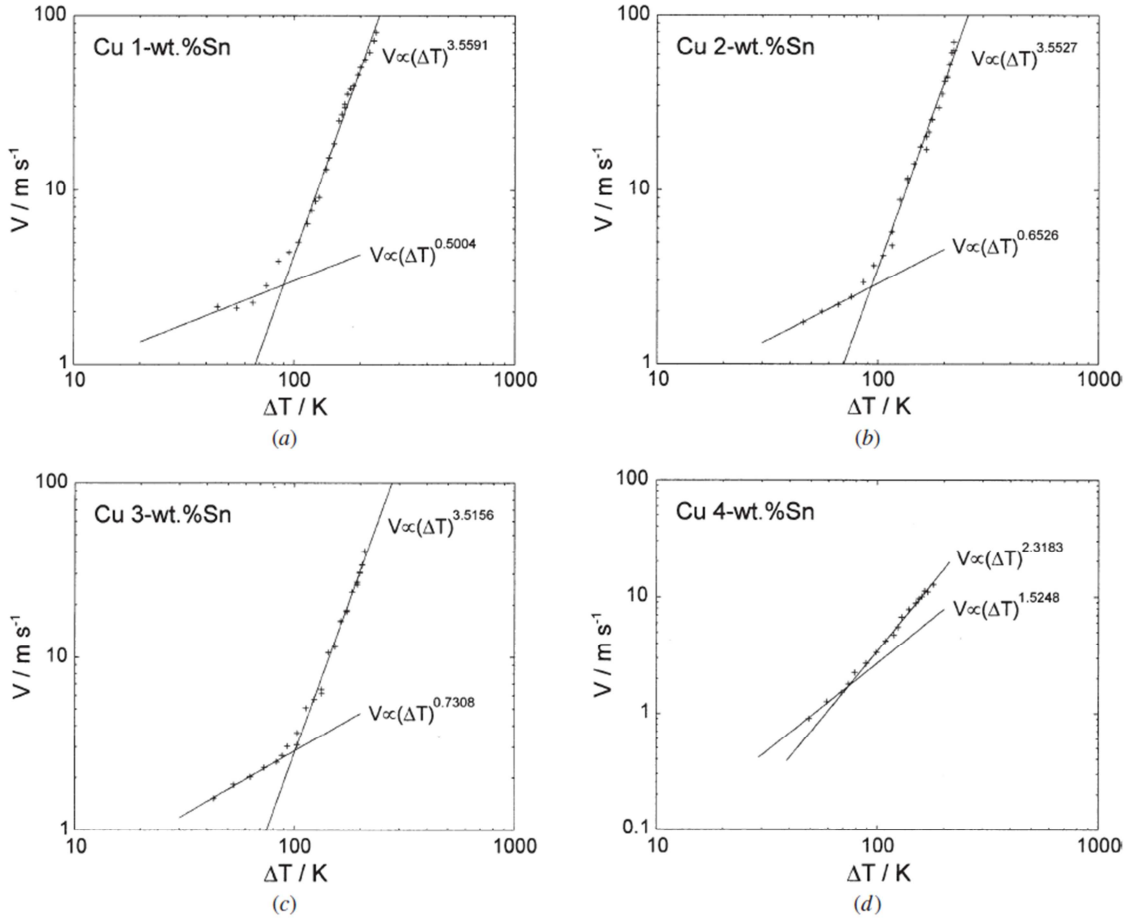

Figure 23 Results of Dragnevski *et al*. (2004) showing breaks in the velocity-undercooling relationship of Cu-Sn alloys, associated with the transition between <111> and <100> growth regimes with increasing undercooling.

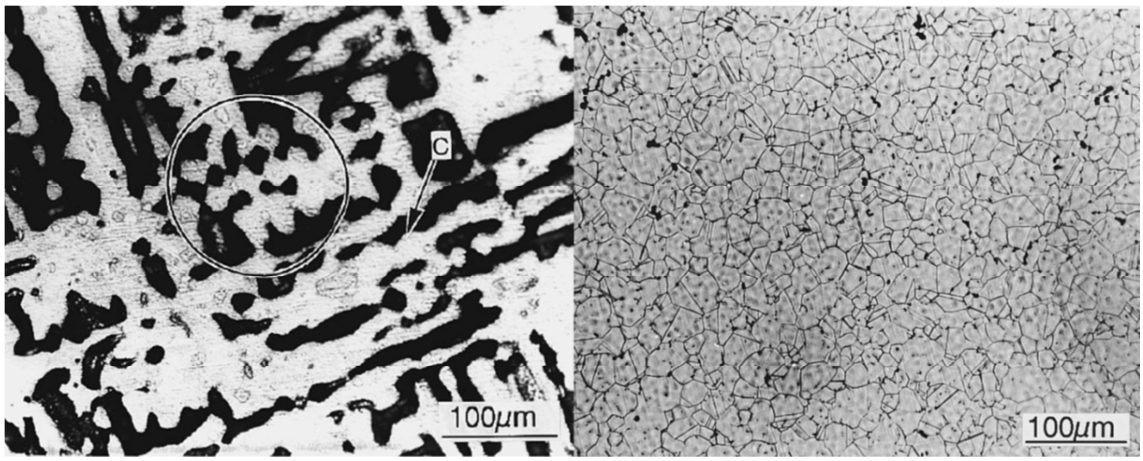

Figure 24 Images reported in the work of Xiao *et al*. (1995) into spontaneous grain refinement in $Cu_{30}Ni_{70}$, showing (**left**) sample undercooled by 138 K (just below the ΔT* transition) exhibiting a porous dendritic structure with necking of the dendrites at certain points (e.g. inside drawn circle), and (**right**) showing refined grains at ΔT = 211 K.

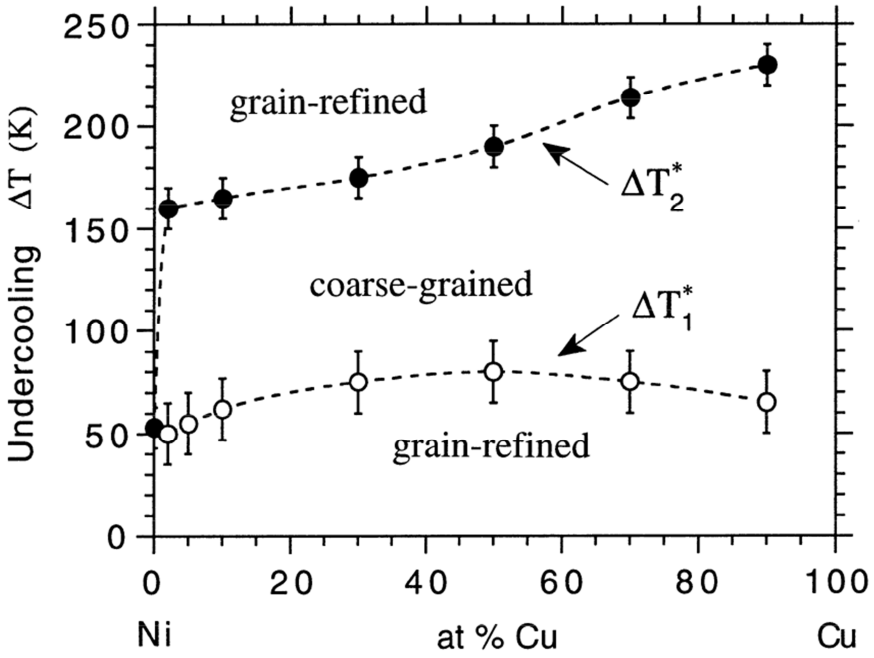

Figure 25 Experimental microstructure selection map of Norman *et al*. (1998) for the Cu-Ni system.

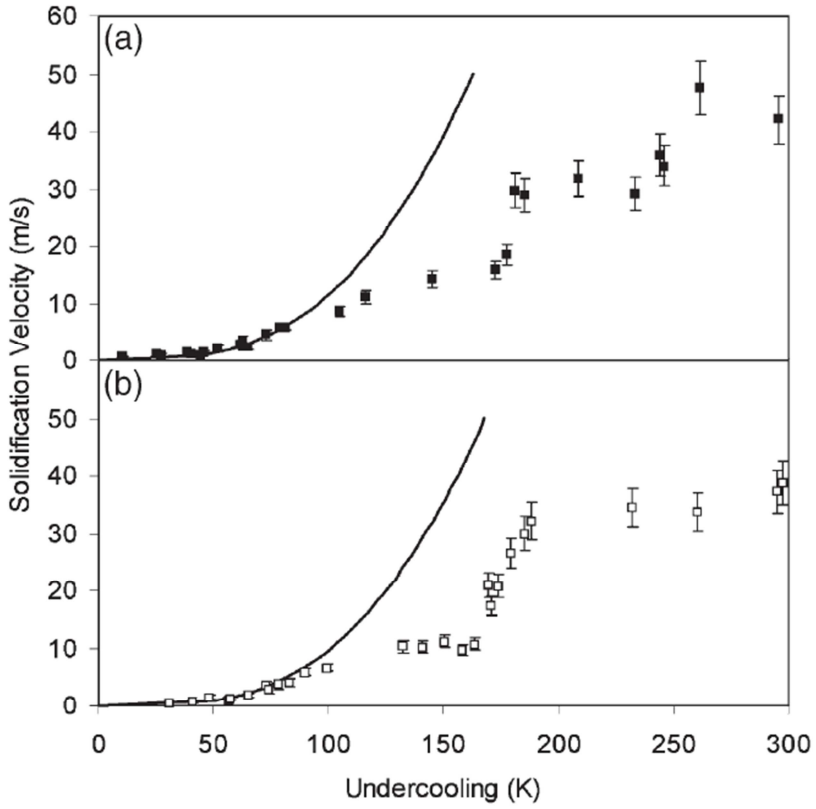

Figure 26 Velocity - undercooling curve for (**a**) Ni-5 at.% Cu and (**b**) Ni-10 at.% Cu as determined by Algoso *et al*. (2003). Solid lines represent predictions by the IMS model.

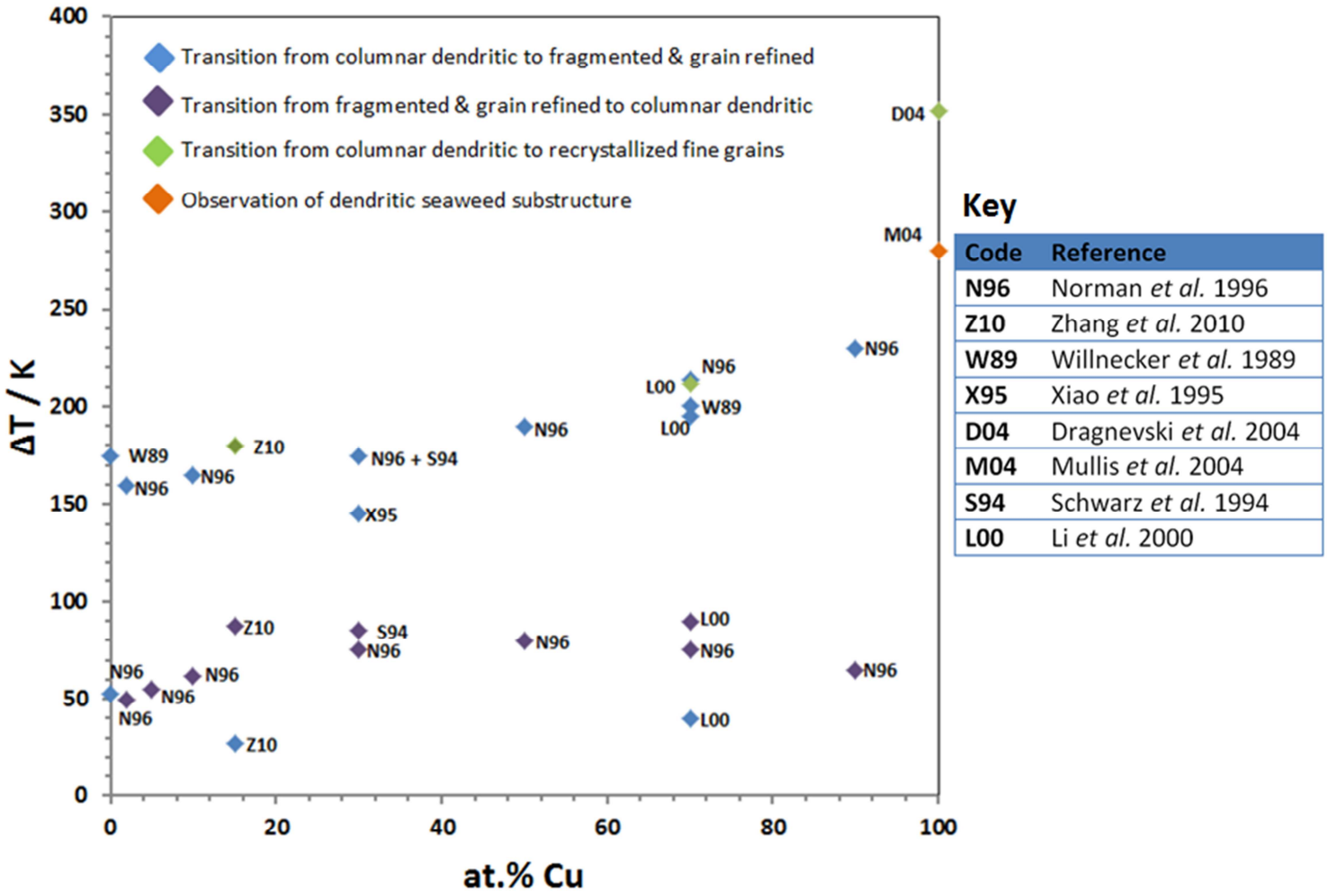

Figure 27 Collection of the spontaneous grain refinement transitions and suggested mechanisms for Cu-Ni alloys, as reported in the literature; plus the observation of a seaweed substructure in pure Cu. References for all points are indicated by the codes of the initial of the first authors' surname and the year of publication, as outlined in the key given.

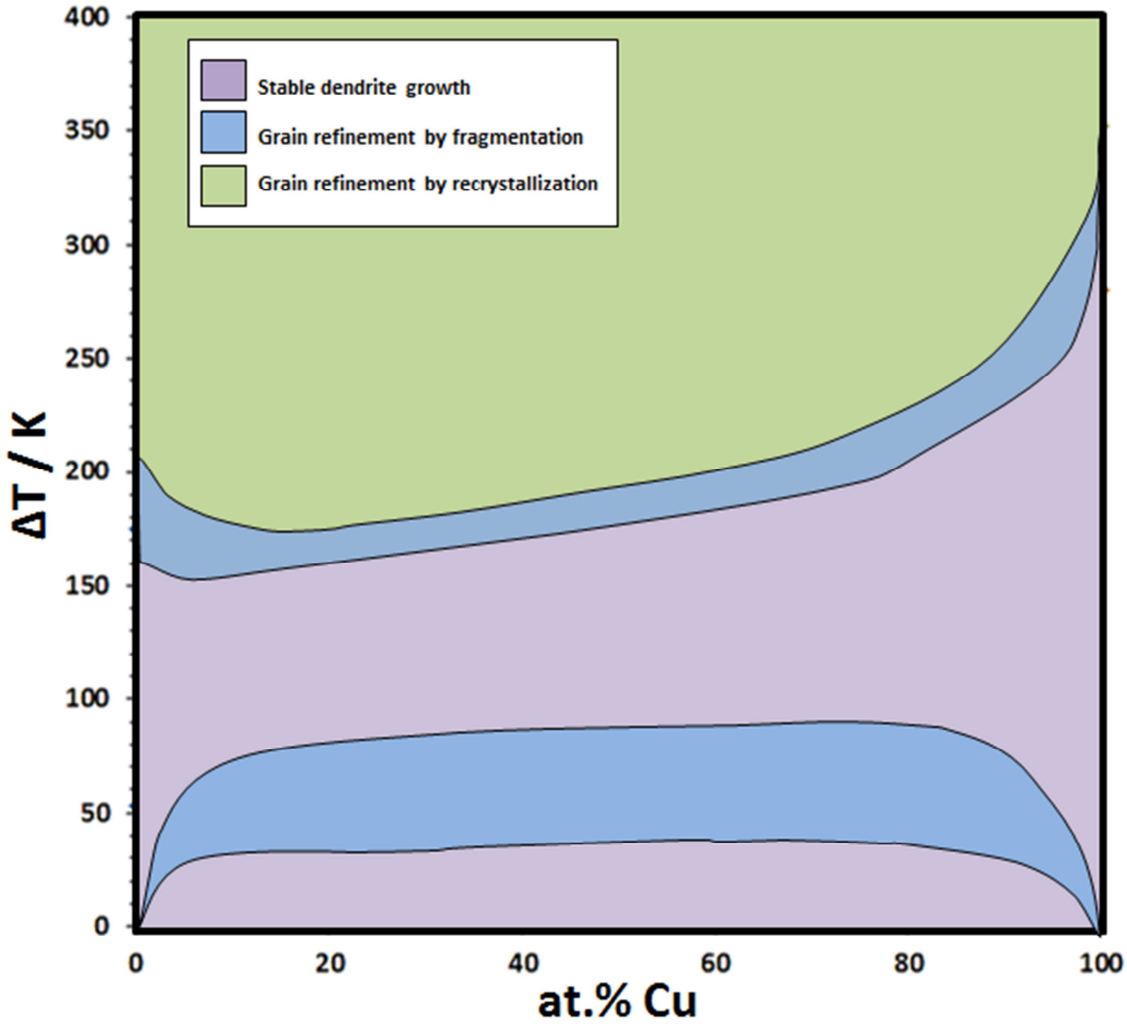

Figure 28 Spontaneous grain refinement mechanism map; as inferred from the collection of observations taken from the literature, which are given in **Figure 27**.

3. EQUIPMENT

3.1. Introduction

The objective of this experimental study is to examine the development of microstructure and texture with increasing undercooling, for different compositions of the chosen Cu-Ni alloy system. From this, any microstructural transitions can be identified, and the critical undercooling for the onset of spontaneous grain refinement (ΔT_2^*) can be measured.

EML (Chapter 2.3.4) is widely used for such studies; however in this case, the low melting temperature and high electrical conductivity of the Cu-Ni alloys could be problematic when using this technique. The containerless solidification technique of melt fluxing has therefore been selected in order to meet the objective, as it permits full control and monitoring of sample temperature and facilitates *in situ* analysis of the solidification velocity via high-speed imaging of the recalescence front. Access to a large range of undercooling is permitted through the use of a molten glass flux. The reason for this is twofold: firstly; the flux isolates sample droplets from the solid crucible walls, reducing the number of potent heterogeneous nucleation sites present and, secondly; sample purity is increased with successive fluxing cycles.

A small RF-induction furnace, contained within a stainless steel vacuum chamber, is employed to heat the sample. The chamber requires evacuation and backfilling with an inert or reducing gas in order to ensure a clean atmosphere during heating. A system of vacuum pumps is therefore required in order to achieve a high vacuum, and a gas inlet valve is necessary for subsequent backfilling. Pressure gauges of varied sensitivities allow the pumping and backfilling process to be monitored, and assist in the identification of leaks.

Accurate solidification velocity measurement and identification of the degree of undercooling necessitates full visibility of the sample throughout the experiment. The apparatus, crucible and flux must therefore be designed and selected with care in order to keep the sample droplet in full view of the high speed camera.

The design and construction of the melt fluxing rig (**Figure 29**) are therefore important factors to the success of the proposed research and will be discussed in detail in this chapter.

3.2. Vacuum System

It is essential that no oxygen, moisture or impurities are present in the atmosphere of the vacuum chamber during fluxing. Such impurities may damage the equipment at high temperatures and would increase the number of potent heterogeneous nucleation sites present, severely restricting the samples range of undercooling. A vacuum system is therefore necessary to remove as much of the atmosphere from the chamber as possible.

A schematic diagram of the vacuum chamber and pumps is shown in **Figure 30**. Prior to pumping, all ports must be firmly sealed and all valves shut, excluding the gate valve which separates the main chamber from the pumps when closed. The chamber is first evacuated down to pressures of around 1 Pa using an oil-sealed rotary vane pump. The rotary pump mechanism involves the movement of a rotor, which is eccentrically mounted inside a cylindrical bore (stator). The rotor contains two spring-loaded blades such that, as it turns, the blades keep constant contact with the stator. This seal is completed through the use of a thin oil film, which is continuously drawn from an oil reservoir. The pump has an inlet, which is connected to the vacuum chamber, and an exhaust.

Figure 31 shows the four stages involved in one revolution of the rotor. During pumping, gas molecules enter the inlet of the pump and pass into the volume of space created by the eccentric mounting of the rotor. As the rotor turns and the blades sweep round, the gas becomes isolated from both the inlet and the exhaust. As the gas is swept into the exhaust it is compressed, forcing the exhaust valve to open and release it, completing the cycle. Note that there are two cycles per revolution (Weissler and Carlson, 1979).

Once the pump has reached pressures below around 10 Pa, it begins to lose suction as the mean free path between air molecules becomes so large that a molecule is more likely to collide with the vacuum vessel walls than with another molecule. Creating a higher vacuum therefore requires the effective withdrawal of the molecules which happen to collide with a particular surface. Therefore, the turbomolecular pump, connected in-line to the rotary, is initiated at this point. This consists of sets of high speed (around 42 000 rpm) rotary blades, separated by stationary vanes, and utilises the effect of the interaction of molecules with moving surfaces. The combination of the lateral movement and incline of the rotary blades increases the probability that an incident molecule will be driven in the direction of the pump exhaust. The stator vanes are pitched such that they will transmit only molecules which are moving in the direction of the exhaust. As a result, there is an overall movement of gas molecules towards the pump exhaust, resulting in evacuation of the chamber to around 10^{-3} Pa. The final pressure obtained is limited by gas adsorption onto the chamber walls and would

require bake-out in order to achieve a higher vacuum, however this is not considered necessary for fluxing under inert atmosphere (Weissler and Carlson, 1979).

The final stage is to isolate the vacuum chamber from the pumps by closing the gate valve. The system can then be backfilled through the gas inlet valve to the required pressure with an inert gas – in this case nitrogen. A clean atmosphere is therefore created in which to carry out the chosen fluxing experiments.

3.3. Pressure Measurement

Accurate pressure measurement is necessary in order to monitor the pressure during pumping and backfilling, and to check for the presence of leaks. Three types of gauge are connected to the vacuum chamber in order to monitor pressure accurately across the full range obtained. These include: a Capacitance manometer, a Pirani gauge and an Ionisation gauge.

The capacitance manometer (**Figure 32**) is used to measure pressures between 10 and 10^5 Pa during rough-pumping and backfilling. This type of gauge employs a diaphragm, which deflects due to a pressure differential created between a sealed volume of known pressure on one side, and the pressure to be measured on the other. The degree of deflection, proportional to the pressure in the chamber, is sensed through a change in capacitance between the diaphragm and an electrode (or electrodes). The higher the vacuum in the chamber, the farther it will pull the diaphragm from the electrodes. Capacitance manometers are typically accurate to between 0.25 % and 0.5 % of the reading, owing to their sensitivity to extremely small diaphragm movements (OMEGA, 2003). Once pressures in the system fall to less than 10 Pa, the capacitance manometer begins to lose sensitivity. At this stage, it is therefore necessary to use a Pirani gauge.

The Pirani gauge can accurately register pressures between 1000 and 10^{-2} Pa, making it ideal for measuring intermediate pressures as the rotary pump loses suction and the turbomolecular pump takes over (Edwards, 2013). This type of gauge employs the principle that the ability of a gas to remove heat from an electrically heated filament is proportional to its pressure. If the pressure is high, heat removal from the filament via collisions with gas molecules will be relatively large (OMEGA, 2003). The fluxing system uses an Edwards APG-L-NW16. In this instrument the pressure of the gas is determined through the change in resistance with temperature of a gold-coated tungsten filament at constant current. It is important to take into account the gas being measured since the thermal conductivity of each

gas is different. The Pirani gauge used is calibrated for nitrogen, but will read correctly for dry air, oxygen and carbon monoxide, with a typical accuracy of +/- 15 % (Edwards, 2013).

Below 10^{-2} Pa, the Pirani gauge loses sensitivity as the thermal conductivity principle breaks down. Beyond this point, the most effective way to measure high vacuums is to ionize the remaining gas molecules, collect them and measure the resulting current. This is the basic principle of the hot cathode Ionisation gauge used to monitor pressures during the final stages of turbo-pumping. It consists of a heated tungsten filament (the cathode), used to produce a constant current of low energy electrons via thermionic emission, which are attracted to a nearby positive electrode in the form of a cylindrical grid. This grid is sufficiently coarse, such that the majority of electrons pass through it and are attracted back. The resultant oscillating motion ensures that the path length of the electrons is maximised before they are captured by the grid, thus increasing the probability that a gas molecule will be ionised by collision with an electron. Ionization can therefore proceed at very high vacuums, giving the ion gauge a total measurement range of between 0.1 and 10^{-9} Pa. In order to measure the ionization current produced, the positive ions are attracted towards a 'collector' anode, which is positioned at the centre of the grid (Lafferty, 1998). The resulting current is a measure of the number density of the gas molecules, rather than pressure. The gauge must therefore be calibrated for the gas being measured in order to finally convert this to a pressure (Reid, 2007).

3.4. Vacuum Chamber Design

As well as providing a convenient connection/disconnection to the pumps through the use of a gate valve, the stainless steel vacuum chamber (**Figure 29** & **Figure 30**) also fulfils several other criteria. The chamber employs the use of three main ports, each of which is sealed by a con-flat (CF) style flange with a copper O-ring gasket, ensuring that system leaks are kept to a minimum. At the rear of the apparatus, one port allows a feed-through of the RF-coil, consisting of a copper tube which is connected to the RF generator. Cooling water is pumped through the copper tube in order to mitigate the effects of RF heating of the coil due to the 'skin effect' concentrating current at its surface. At the front of the chamber another port contains a glass window to allow visibility of the sample during fluxing, and a thermocouple is connected through a third port in the bottom of the chamber, which allows it to be positioned close to the sample.

Since the chamber is designed for use under high vacuum, it is important that it does not become over pressurised due to e.g. expansion of gases during heating. As discussed (Section 3.3), an additional port provides a connection to the pressure gauges so that pressure can be

carefully monitored during pumping and fluxing. In addition, a burst disc consisting of a thin metal membrane has also been fitted to this port, which will fail in the event of overpressure, allowing the chamber pressure to fall back to atmospheric levels.

Other safety features include a copper braid connecting the chamber to earth in the unlikely event that it becomes live, as well as a plastic guard which has been put in place around the exposed portion of the RF-coil which runs between the chamber and the generator.

3.5. Furnace Design

Figure 33 shows a schematic cross-section of the furnace design. The furnace components are designed to fit within the water-cooled RF-coil and are arranged such that the sample is visible, supported and has good thermal contact with the thermocouple.

An RF-coil is used to inductively heat both the metallic sample and a cylindrical graphite susceptor (33 mm outer diameter, 28 mm internal diameter, 119 mm height). This surrounds the crucible, improving temperature uniformity and aiding in the melting of the glass flux. Power is supplied to the coil by an Inductalec 15 kW RF-generator, with an operating frequency of 450 kHz. The power output is adjusted manually in order to control the temperature of the furnace. An alumina tube (45 mm outer diameter, 40 mm internal diameter, 168 mm high) is placed around the graphite susceptor to act as a radiation shield and to avoid contact between the coil and the susceptor. In addition, the susceptor stands on a small alumina tube of the same diameter in order to avoid contact with the steel chamber. Both susceptor and shield are machined to have a 10 mm wide slot at the height of the crucible so that it is visible through the viewing window. In addition to this, the RF-coil is wound with sufficiently large gaps between the coils so that viewing is not obstructed by it.

A small alumina tube (outer diameter = 10 mm, inner diameter = 8 mm and height = 200 mm) is positioned in the centre of the furnace arrangement, which provides the stand for the crucible and allows the thermocouple to be fed through from underneath, such that it sits directly below it. The thermocouple wire is protected and supported by a 4-bore alumina tube. This ensures that the two wires are isolated from each other, up to the point where they are welded together at the tip to form the thermocouple bead. The fluxing experiments require temperatures of up to 1573 K, therefore an R-type thermocouple was chosen as the most suitable, having an operating temperature range of up to 1723 K. A process indicator recorder (CR100 from ABB) is calibrated for the R-type thermocouple and provides a digital read out of

the temperature of the crucible. As a continuous-line 100 mm strip chart recorder, it also provides a record of the heating and cooling curves.

Transparent fused silica crucibles have been custom made to suit the requirements of the experiments. **Figure 34** illustrates the dimensions of the crucibles, which incorporate a smaller cylindrical base into which the thermocouple can be positioned. The joint between the two sections is thinned to ensure good thermal contact. The crucibles have an inner diameter of 8 mm, allowing the samples (typically 5 mm diameter) to be positioned away from the solid walls. The softening temperature of fused silica is around 1800 K, so the crucibles are able to withstand the high temperatures reached during fluxing.

3.6. Growth velocity measurement with high-speed camera

By ensuring that the crucible and its contents are visible throughout the experiments, the solidification velocity can be directly measured via high-speed imaging of the recalescence front. Recalescence is the release of the latent heat of fusion, H_f, during transformation from the undercooled liquid state to the solid state. During this transformation, the undercooled liquid ahead of the solid-liquid interface acts as a sink for the liberated heat. The subsequent volume fraction of solid, f_s, formed during the initial recalescence phase, can be estimated as:

$$f_s = \frac{C_p \Delta T}{H_f} \tag{12.0}$$

Where C_p is the specific heat capacity of the liquid at constant pressure. This is also known as the Stefan number and is essentially the ratio of latent to sensible heat in the system (Gill et al., 1981). However, this is only an approximation since it assumes that the density of the solid and the liquid states are equal and that C_p is constant with temperature, which is rarely the case.

Solid growth during the recalescence phase will proceed close to the equilibrium melting temperature. Since the liquid ahead of the growth front remains undercooled, the solid phase will be hotter and will thus appear brighter. During rapid solidification, the thermal boundary layer ahead of the solid-liquid interface is typically very thin (<1 μm), which gives the appearance of a sharp interface moving radially outwards from the nucleation point across the surface of the sample. A linear velocity can therefore be calculated by capturing the progression of this front using a high speed camera.

Two high speed cameras were employed for this purpose - a Kodak EktaPro HS Motion Analyzer model 4540mx, and a Photron Fastcam SA5. The EktaPro is capable of recording

4,500 full frames per second (fps) and up to 40,500 partial fps, ready for immediate playback from electronic memory. Sharp images are produced by a 256 x 256 pixel sensor with 256 grey levels. The Fastcam SA5 camera is capable of recording 7500 fps in mega pixel resolution and up to 1 x 10^6 fps at reduced resolution. The camera is connected through a Gigabit Ethernet connection to a laptop equipped with PFV Version 335 software, which provides all recording, playback and saving options.

For both cameras, 'record' is pressed once and the camera starts to continuously record; storing around 3 seconds worth of images for playback once 'record' is pressed again. The exact number of frames stored is dependent on the frame rate selected. Three modes are available to determine which frames are stored for playback once 'record' is pressed. 'Start' and 'End' retain the images captured after and before pressing 'record' (respectively), and 'Centre' sets a mid-point when record is triggered, with frames held before and after that point for playback. A range of playback speeds from 1 fps to 25 fps were then available for image analysis. In the case of the Fastcam camera, the videos can also be cropped to contain only the relevant frames and stored as either a video file or a series of images for further analysis.

The procedure adapted for both of these cameras was to focus the camera on the sample at maximum magnification through the viewing window. During cooling below the liquidus temperature the camera was set to continuous record with the 'End' option selected. As soon as nucleation spontaneously occurred, the 'record' button was pressed, capturing the recalescence event. The images were then immediately played back and, by calibrating the distance on the screen using the width of the crucible, velocities were calculated from the progression of the recalescence front per frame. The frame rate used was varied between 4500 fps and 22,000 fps dependent on the level of undercooling achieved (and therefore the solidification velocity expected) and the level of light present; which limits the maximum frame rate. An example of a series of images, which have been captured by high speed camera during the solidification of an undercooled droplet, can be seen in **Figure 35**.

3.6.1. Sources of error in velocity measurement

Sources of error in v-ΔT data are dominated by the velocity measurement, since errors in the measured ΔT values arise mostly from the accuracy of the thermocouple; which is around 1 % of the reading. There are a number of sources of error which may contribute to the overall calculated v value, with the main issue being that of the viewing geometry.

Firstly, the angle of view of the droplet must be considered with respect to its geometry. The high speed camera image is essentially a two-dimensional representation of a three-dimensional object; i.e. the near-spherical droplet appears as a circle/oval shape. Thus, the solidification front moves in three-dimensional space, but is projected onto a two-dimensional imaging plane. For a spherical droplet, the apparent velocity then becomes $v.Sin.t$, where t is the angle between the line of sight and the tangential direction of the velocity. As such, at the edge of the droplet the tangential velocity direction will be parallel to the line of sight and the apparent velocity will be 0, clearly introducing significant error to the velocity measurement. The most accurate velocity measurements occur when the tangential direction of the solidification front is perpendicular to the line of sight; usually, but not necessarily, at the perceived centre of the droplet. Thus, in order to minimise the error arising from the angle of view with respect to the droplet geometry, a series of velocity measurements was taken for each recalescence event captured, and the highest recorded velocity was taken as the truest representation of the actual velocity; since this must incorporate the point at which the direction of travel was perpendicular to the line of sight. This ensures greater consistency between measurements, such that a fair evaluation of the v-ΔT relationship can be made.

Another source of error is introduced through the uncertainty in the position of the droplet within the crucible. In using the known crucible width (10 mm) to calibrate the image and measure the distance travelled by the solidification front per frame, an assumption is made that the solidification front is travelling at the centre of the crucible. In reality, it is not possible to fix the position of the droplet; nor is it possible to tell where the droplet is from viewing it *in situ*, since only one line of sight is provided by the experimental set up. As such, the effect of sample position on apparent width must be considered. **Figure 36** shows a schematic consideration of the possible difference in position of a 5 mm diameter droplet within the crucible (8 mm internal diameter). It is clearly shown that, if the droplet is positioned to the very back of the crucible, the point at which the velocity should be measured (as discussed above) is 1 mm in front of the plane of calibration; representing the source of minimum error present. Likewise, it is shown that if the droplet lies at the very front of the crucible, the point of velocity measurement clearly lies 4 mm in front of the plane of calibration; representing the source of maximum error.

In order to quantify these errors in terms of the percentage overestimation of width, **Figure 37** and **Figure 38** have been provided in consideration. **Figure 37** shows how the width of an object (assigned an arbitrary width of 10 mm) may be overestimated if it lies in front of the plane of calibration; with the error increasing as distance ahead of the calibration plane increases. This is shown by the projection from the camera, through the ends of the object and

on to the calibration plane; with the distance between the two points of intersection with the calibration plane representing the overestimated width of the object. Distances of 1 mm and 4 mm (not to scale so that the effect of object position can be clearly seen) have been used to reflect the estimated minimum and maximum errors arising from sample position; and a camera distance of 300 mm from the plane of calibration has been chosen, since this represents the average working distance of the camera from the crucible centre employed in practice. Simple trigonometry can then be used to estimate the percentage overestimation of width. **Figure 38** shows the known angles and distances for the case of the point of measurement being 1 mm in front of the plane of calibration. Here, the 'opposite' in the right-angled triangle formed between the object and the camera is known to be 5 mm (since object was assigned a width of 10 mm) and the 'adjacent' is known to be 299 mm (since the object lies 1 mm in front of the plane of calibration). The half-angle of view, θ, can then be given as:

$$\theta = Tan^{-1}\left(\frac{5}{299}\right) \tag{13.0}$$

Taking angle θ and considering the same angle of view, projected onto the plane of calibration to give the apparent object width, o?, (i.e. recalculating the 'opposite' for an 'adjacent' of 300 mm instead of 299 mm), gives:

$$Tan\theta = \left(\frac{o?}{300}\right) \tag{13.1}$$

Hence equations 13.0 and 13.1 can be combined to give o?:

$$\left(\frac{5}{299}\right) \mathrm{x}300 = \mathrm{o?} \tag{13.2}$$

This gives an apparent object width of 5.0167 mm, which leads to a minimum velocity measurement error of +0.33 %. Likewise, substituting the relevant figures into equation 13.2 yields a maximum error in velocity measurement of +1.35 %, when the point of velocity measurement lies 4 mm in front of the plane of calibration. Hence, the error introduced to the measurements through the uncertainty in droplet position is relatively low.

The effect of nucleus location on the velocity measurement must then be considered. Within this study, the sample was left to spontaneously nucleate and, as such, the position of the point of nucleation could not be controlled. If solidification nucleated at the front of the droplet (with respect to the angle of view), then the solidification front observed would be a true representation of the actual progression of the solid-liquid interface. In this case, the euhedral envelope of the dendrites was usually apparent and velocities were subsequently measured from the progression of the 'tip'. This therefore permits a relatively accurate

velocity to be calculated using the considerations previously described. However, if solidification nucleated at the back of the droplet, the situation is less straightforward. Here, the recalescence 'front' observed from the front of the droplet will actually be a representation of where the dendrites, growing both round the surface and through the bulk, intersect the front side of the droplet surface. In this case, the solid-liquid interface tends to appear as a rapidly-shrinking circle of undercooled liquid. If a velocity were calculated from the progression of this front, it would be significantly overestimated. Therefore, in order to ensure that the effect of nucleus location did not introduce a large error to velocity measurements, velocities were only calculated when solidification was observed to nucleate on the front of the droplet.

Finally, consideration should be given to the effect of temperature variations within the undercooled droplet, and the effect which this has on the solidification pathway. If the surface of the droplet is at a lower temperature than the bulk of the droplet, then solidification will proceed primarily around the surface of it and, using the procedures described above, relatively accurate velocity measurements can be obtained. Conversely, if the bulk of the droplet is at lower undercooling, solidification will preferentially proceed through the bulk. In this case the velocity being measured from the progression of recalescence across the surface of the droplet will not be the true solidification velocity. Since the droplet is mostly heated through the induction heating of a graphite susceptor, which acts as a large blackbody furnace (relative to the sample size); as the experimental temperature is lowered it is most likely that heat loss will occur between the droplet and its surroundings, with the surface of the droplet subsequently cooling first. As such it is likely that solidification will initially proceed across the surface of the sample, leading to more accurate dendrite growth velocity measurements. This is supported by the observation of clear euhedral growth fronts at the surface of the sample during recalescence, which suggests that the solidification path is around the surface of the droplet. If growth were to occur primarily through the bulk, it is unlikely that such a sharp dendrite envelope at the surface would be seen. Furthermore, microstructural analysis of solidified droplets (see e.g. **Figure 53** and **Figure 58** in Chapter 5.4.1) reveals that the dendrites have grown around the surface of the droplet. A large amount of porosity is also observed in the centre of the undercooled samples, suggesting that this was the last portion of the droplets to solidify (discussed in more detail in Chapter 5.4.2.1.5). As such, it can be assumed that the error due to temperature variations in the droplet is minimal.

Figure 29 Digital photograph of the fluxing chamber, pumps, RF-generator and vacuum gauges.

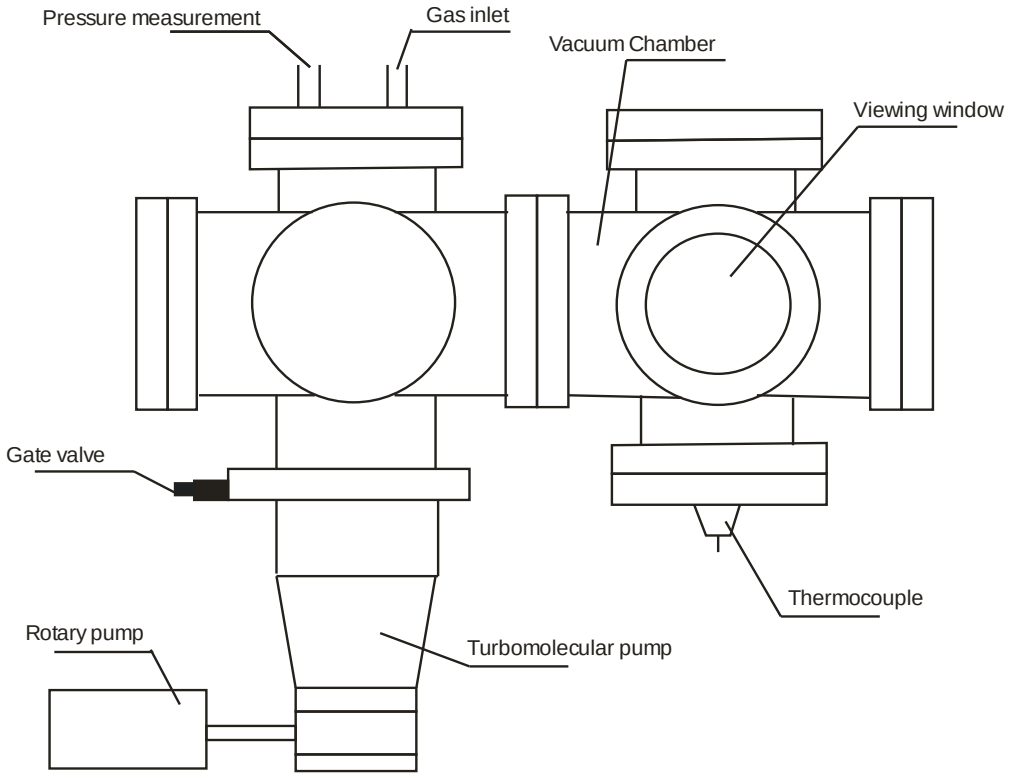

Figure 30 Schematic diagram of the vacuum chamber and pumping elements.

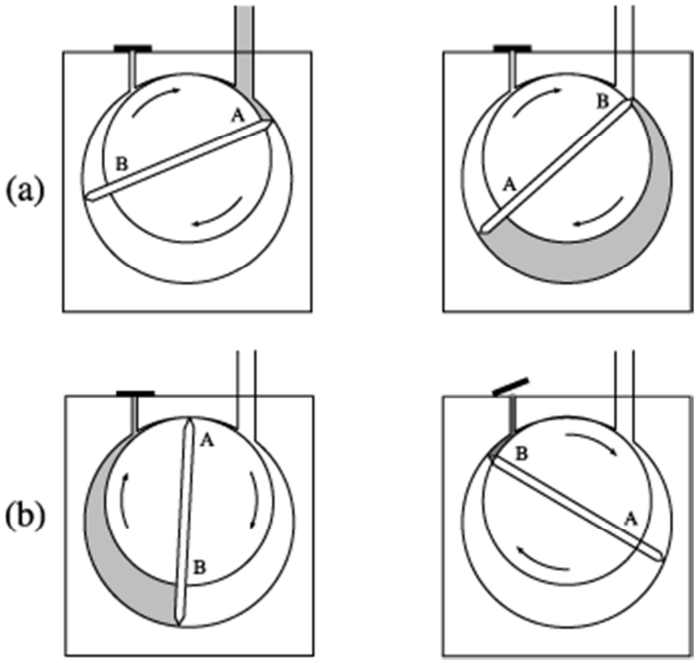

Figure 31 Four pumping phases of a rotary pump. **a**) gas induction (**left**) and isolation (**right**), and **b**) compression (**left**) and exhaust (**right**) (Hofmann, 2013).

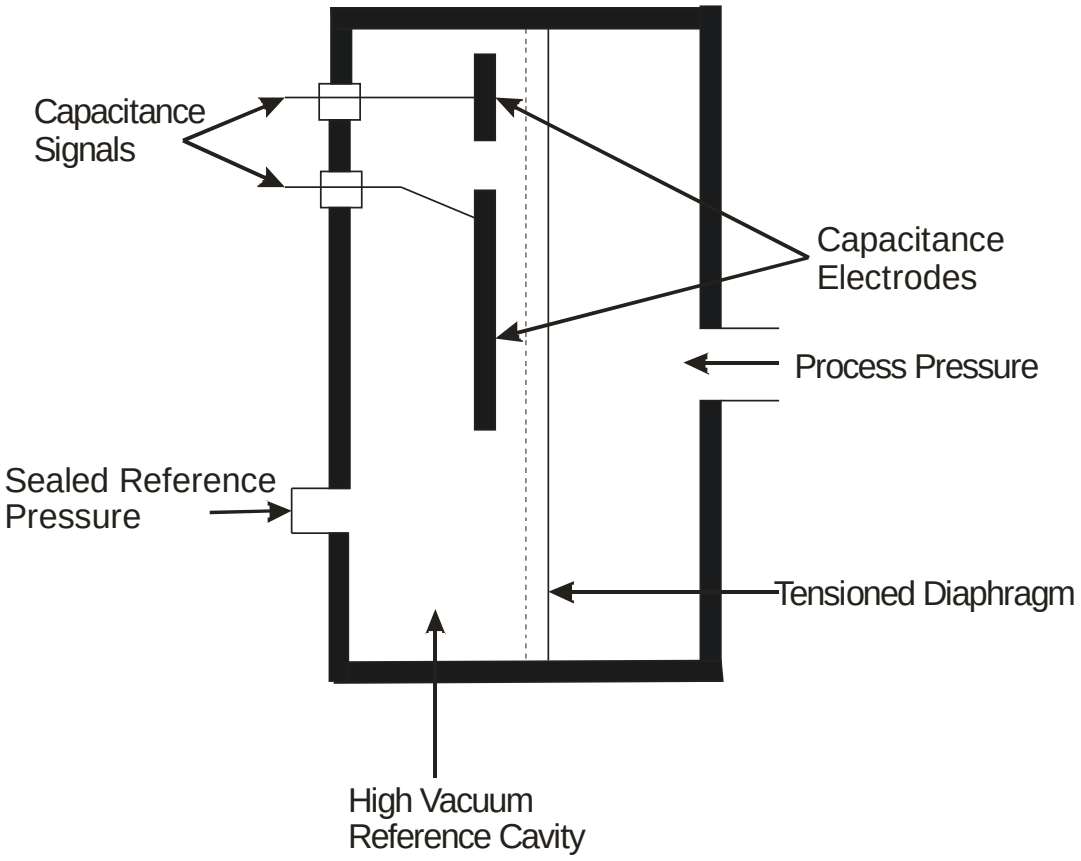

Figure 32 Schematic diagram of a basic capacitance manometer (reproduced from (OMEGA, 2003)).

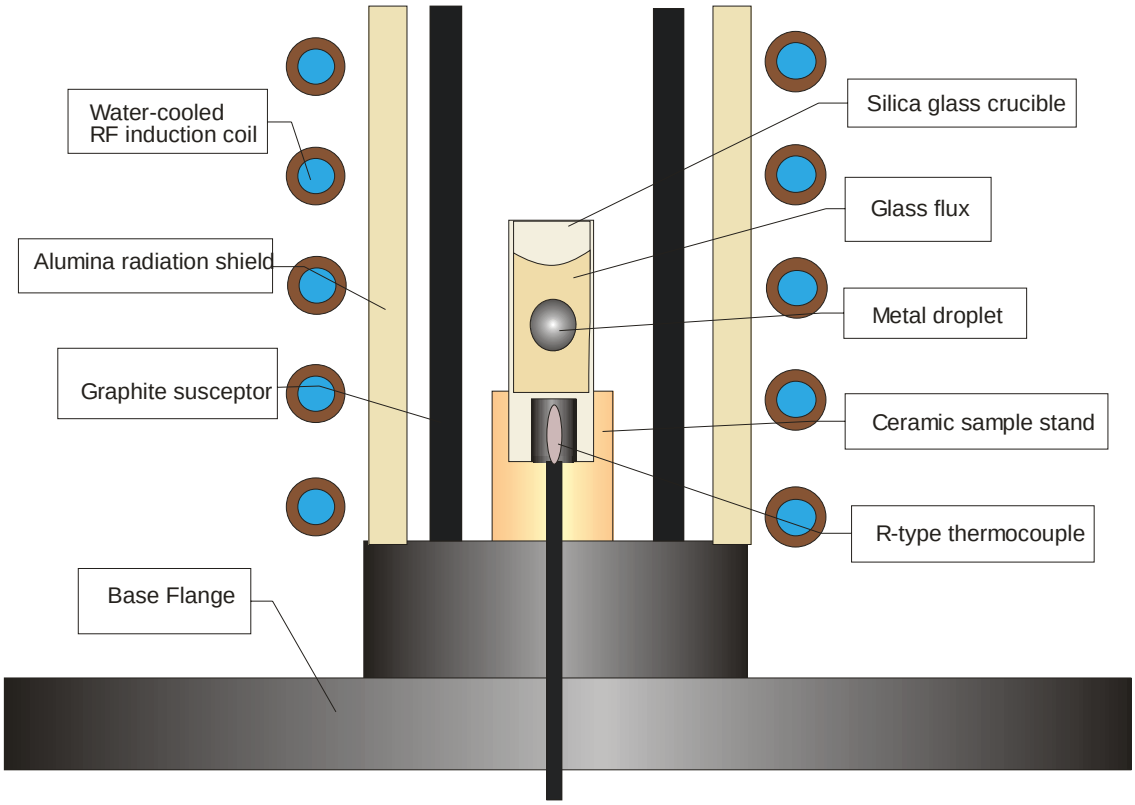

Figure 33 Schematic diagram of furnace and sample arrangement within the vacuum chamber.

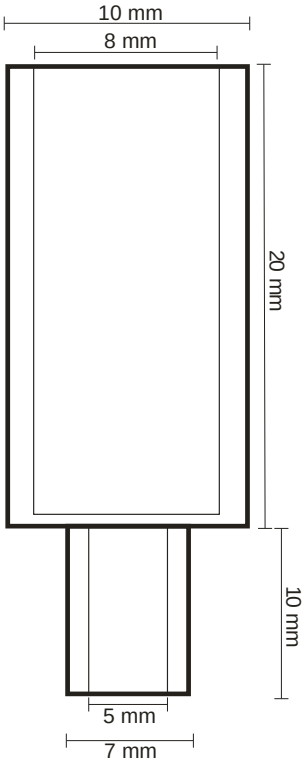

Figure 34 Dimensions of fused silica glass crucibles.

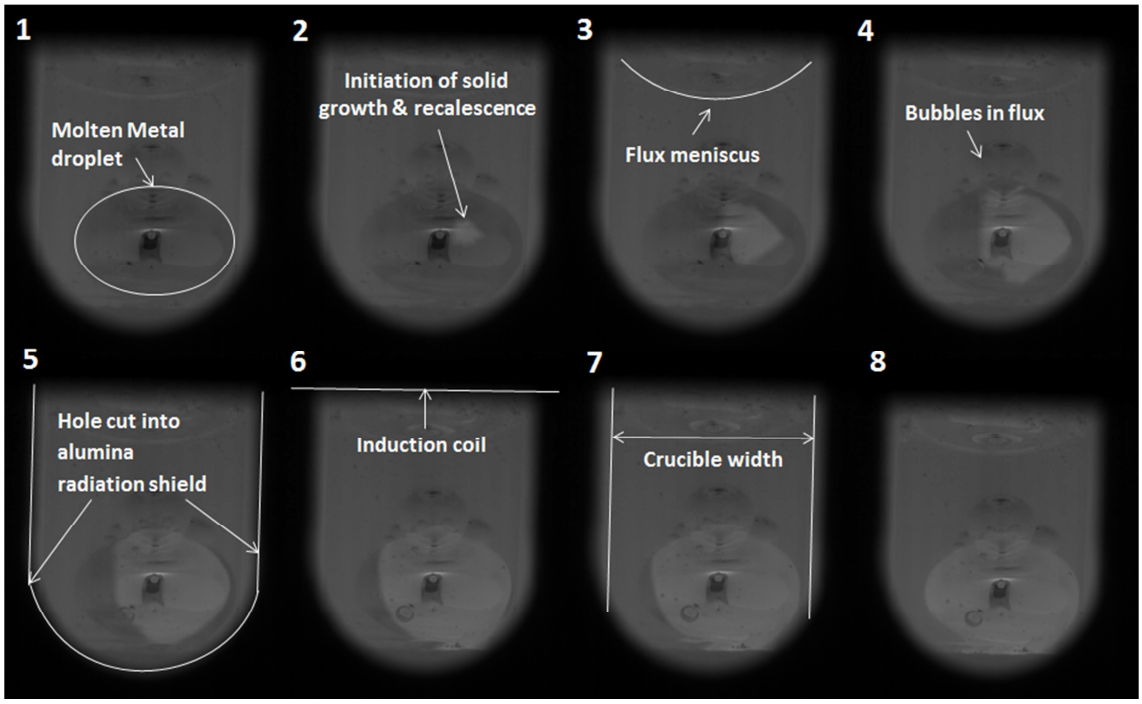

Figure 35 Example of a series of high speed camera images of a solidifying droplet of Cu-8.9 wt.% Ni, undercooled by ΔT = 109 K prior to nucleation. The frame rate in this case is 10 000 fps, with every other frame shown (0.0002 s between frames).

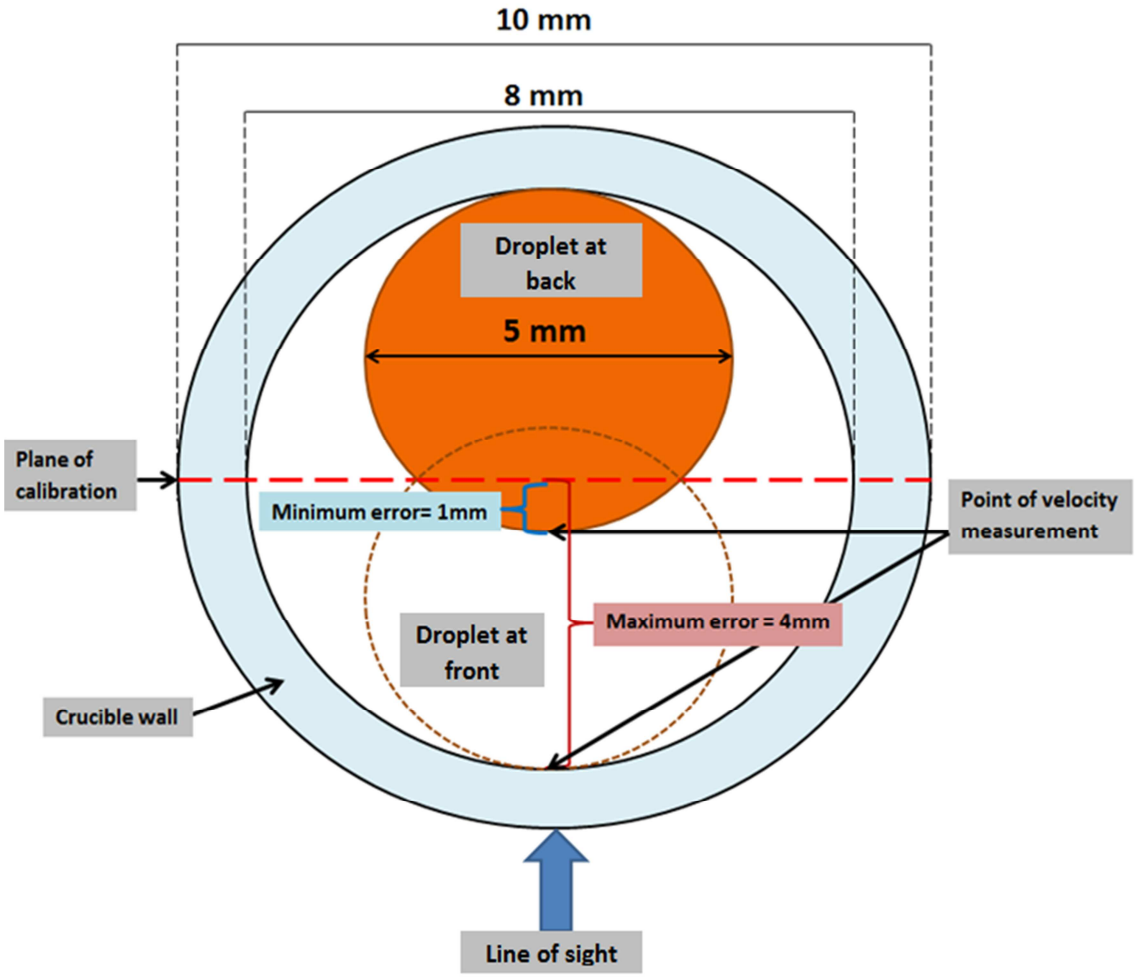

Figure 36 Schematic diagram of crucible and droplet as seen from above with respect to the line of sight. Showing the minimum and maximum possible errors made in assuming that the point of velocity measurement lies at the centre of the crucible; where the known crucible width may be used to calibrate high speed camera images for calculation of the solidification velocity.

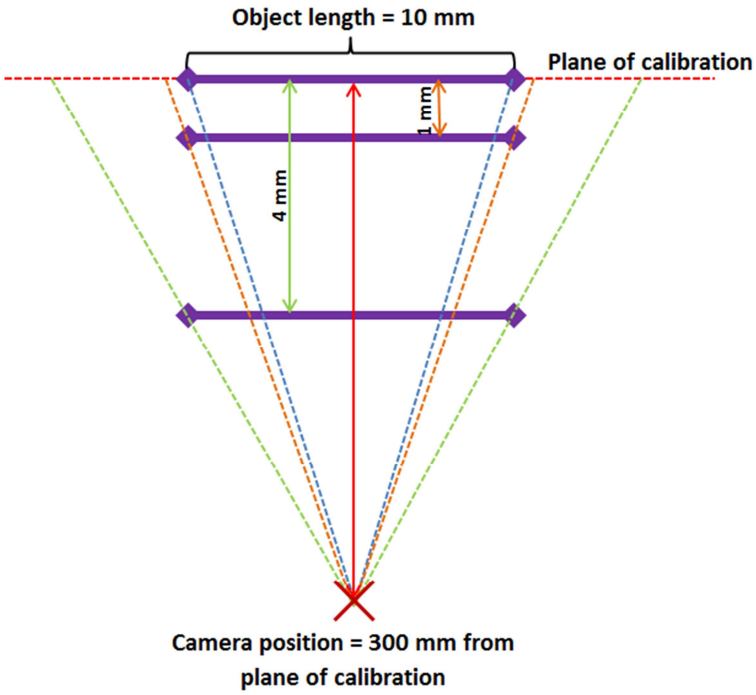

Figure 37 Schematic diagram showing how the measured size of an object (purple line) - or distance, in the case of velocity measurement - is altered as a function of object distance from the plane of calibration. If the image is calibrated in the plane shown, but the object is in front of this plane, the measured object size is overestimated; as shown by the projection from the camera position, back through the ends of the object and onto the plane of calibration. Altered object positions with respect to the plane of calibration are shown as 1 mm and 4 mm (not to scale) to reflect the minimum and maximum estimated errors in droplet position, as shown in Figure 36.

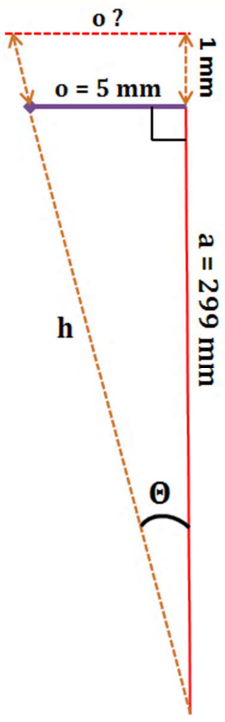

Figure 38 Lengths and angles used to calculate the minimum percentage error in distance measurement due to the point of velocity measurement (purple line 'o') being 1 mm in front of the plane of calibration (dotted red line), with length 'a' representing the distance between the camera and the plane of calibration (as shown in **Figure 36**).

4. METHODOLOGY

4.1. Introduction

This chapter outlines the procedures and techniques undertaken during the experimental part of this project. Firstly, the reasons behind the selection of alloy and flux will be discussed, followed by a description of the methods used in their preparation and characterisation. Following this, the melt fluxing procedure and velocity measurement techniques used in order to obtain undercooled metallic droplets and reliable velocity-undercooling relationships, will be described. Finally, the microstructural characterisation methods used to analyse the undercooled droplets will be discussed, including: light microscopy; X-Ray Diffraction (XRD); Scanning Electron Microscopy (SEM) and Electron Backscattered Diffraction (EBSD) techniques. The overall procedure has been developed in order to produce well-characterised, high purity alloys, which will undercool by a sufficient amount in order to form a broad picture of the solidification velocity vs. undercooling relationship. The final microstructure and texture of the as-solidified droplets could then be used to help identify any developments in microstructural formation or orientation with increasing undercooling/solidification velocity. Such relationships will provide clues as to the fundamental origins behind spontaneous grain refinement.

4.2. Alloy selection and preparation

The following set of criteria was used to select a suitable alloy system to be studied:

1. The system must have an accessible range of undercooling with regards to the fluxing equipment. Specifically, the liquidus temperature of the alloy must not exceed the maximum operating temperature of the fluxing equipment and must also remain well above the melting temperature of the glass flux. This ensures that the sample remains completely encased by molten flux over the full range of undercooling. In addition, a liquidus temperature which is well below the maximum operating temperature of the equipment is desirable, since this allows a greater degree of superheat, increasing the level of undercooling attainable. The alloy system must therefore satisfy the condition 973 K < T_L < 1573 K, where T_L is the liquidus temperature.
2. A higher T_L alloy is preferable, as this will result in a brighter recalescence front. This will make imaging easier and will therefore yield more reliable solidification velocities.

3. The alloy system should preferably have a simple phase diagram. This would allow a more accurate interpretation of results, as judgement would not be confused by the possible existence of many complex phases.

After inspection of all available binary phase diagrams it was decided that the Cu-Ni alloy system would be the most appropriate. Most of the alloys which were within the appropriate liquidus window were Cu-based, and the simplest system of these was Cu-Ni. Within this system, a single FCC solid solution is formed over the full range of composition, making post-solidification analysis as clear and as simple as possible.

The limitations of the equipment mean that the composition of the alloys to be used are restricted to the Cu-rich end. It was therefore decided to compare Cu-10at.%Ni with Cu-5at.%Ni. A Cu-Ni equilibrium phase diagram (**Figure 39**) has been constructed using MTData thermodynamic calculation software, which indicates the presence of a miscibility gap. The CALPHAD method used to calculate this phase diagram is known to produce artificial miscibility gaps. However, for the Cu-Ni system a gap is known to exist at low temperatures (< 595 K) which is asymmetrically centred at around Cu-78 at.% Ni (Hong et al., 1984). If the alloys underwent spinodal decomposition, during or after their fabrication, then their homogeneity would be compromised and smaller samples taken from the same slug of alloy may not be of comparable composition. However, a further advantage of the chosen compositions is that the Cu-5 at.% Ni alloy avoids the miscibility gap completely and, at a 10 at.% Ni concentration, the miscibility gap exists at such low temperatures (<323 K) that Ni solute would not possess sufficient mobility for interdiffusion.

Whilst many studies into the undercooling and rapid solidification of Cu-Ni alloys have been undertaken, these are mostly focused on the Ni-rich end of the composition spectrum as this is better suited to the EML technique (Willnecker et al., 1989, Zhang et al., 2010, Li et al., 2000). A Cu-10 at.% Ni alloy was investigated by Norman et al. (1998) using electromagnetic levitation as part of a study attempting to form a microstructure selection map across the full compositional range. Droplets were characterised as either grain refined or coarse grained for this purpose and microstructural analysis did not progress much deeper than this. The presented study is distinct from their work because it will look in detail at the development of microstructure and texture with increasing undercooling for both alloys, forming a comparison between them.

High purity 99.999 % (metals basis) Cu and Ni powders, of 100 and 120 mesh respectively, were purchased from Alfa Aesar. These were weighed, mixed and compacted into 2 cm diameter pellets before being arc-melted under inert argon atmosphere. In this way, a

minimum number of re-melts (three in total) was required in order to produce alloys to a high degree of homogeneity without compromising purity. Previous attempts at producing alloys from Cu and Ni shot were unsuccessful in achieving sufficient mixing, and the high numbers of re-melts required were introducing excess impurities and making undercooling unobtainable.

Samples were weighed before and after compaction and arc melting in order to account for any difference in composition of the final products to the initial starting materials. Both alloys were then characterised for homogeneity using XRD (see Section 4.5.3), and samples of each were sent to LSM Analytical Services for final Cu and Ni compositional analysis, using Inductively Coupled Plasma - Optical Emission Spectrometry (ICP-OES), and residual oxygen concentration, using Light Element Combustion (LECO®) analysis. The presence of trace impurities in the final alloy is highly undesirable. Firstly, trace elements may react with the main alloy components to produce high melting point particles such as oxides or intermetallics. These would remain solid throughout the experimental temperature range and subsequently act as potent heterogeneous nucleation sites; both limiting the degree of undercooling obtainable and possibly catalysing the growth of metastable phases, which would confuse post-solidification analysis. Secondly, as discussed in the literature review (Chapter 2.2.3), the partitioning of solute and impurities during solid growth has a marked influence on the development of solidification morphology. Therefore, in order to accurately interpret the development of microstructure as a function of undercooling, a sufficient degree of purity must be achieved. However, a full compositional assay is expensive and, in the present case, it is considered that the potential for the introduction of trace impurities during processing is very low; hence only the final Cu and Ni content and residual oxygen content have been analysed for.

4.2.1. Inductively Coupled Plasma - Optical Emission Spectrometry (ICP-OES)

The ICP-OES technique (**Figure 40**) quantitatively measures the amount of metallic elements present in a sample solution, with moderate to low detection limits of 0.2 to 100 ppb. An acid dissolution technique was used to prepare the Cu-Ni alloys for ICP-OES. This involves the drilling, crushing or milling of the bulk metal to produce uniform flakes which can be accurately weighed and completely and quickly dissolved in acid. The solution is then diluted to a known volume ready for introduction to the ICP (LSM-Analytical-Services, 2013b). A peristaltic pump and nebuliser arrangement converts the sample to an aerosol and introduces it to the core of the inductively coupled argon plasma, which generates temperatures of around 8273-10273 K.

The high energy of the plasma excites all elements present to different atomic and/or ionic states and the subsequent relaxations of these occur via the emission of optical radiation. Since each element has a characteristic set of electronic states, the wavelengths of the emitted radiation are characteristic to that element. The optical emissions are therefore separated based on their wavelength and their intensities measured by the spectrometer. The intensities are directly proportional to the concentrations of the elements in the sample and are quantified by comparison with a standard sample of known concentration. The main source of error in this technique comes from possible inter-element interferences which can occur if the wavelength of the elements being measured are close to one another (University-of-Wisconsin, 2005). However, the accuracy of this technique is more than sufficient for determination of the composition of the Cu-Ni alloys and therefore the liquidus temperatures to be used in determination of the degree of undercooling.

4.2.2. Light Element Combustion (LECO®) analysis

In order to determine the residual oxygen concentration of the prepared alloys, LSM Analytical Services performed LECO® analysis, which is an inert gas fusion technique. This employs a high temperature furnace in which the metallic samples are fused under inert atmosphere at around 3273 K within a high purity graphite crucible. Any oxygen present in the sample will react with the carbon in the crucible and emerge as CO gas, which is subsequently converted by reaction with a catalyst into CO_2. The emerging gases are then analysed for CO_2 content by an infrared cell, from which a value of the weight% O present in the sample can be calculated. The instrument is calibrated using a sample of known oxygen concentration in order to cancel out contributions to the CO_2 reading from impurities contained within the crucible and the inert gas used in the furnace. As such, a general detection limit down to 5 ppm can be achieved, which is sufficiently accurate for a general determination of oxygen levels introduced by the arc melting method (LSM-Analytical-Services, 2013a). Since the fluxing method is designed such that oxide impurities are dissolved in the flux as the metallic samples solidify (see Section 4.3), oxygen content is only considered a major concern if it is substantial.

4.2.3. Sample preparation for melt fluxing

Prior to melt fluxing, small (4-7 mm diameter) pieces of alloy were cut from the arc-melted slug, using a Struers Discotom-2 abrasive cutting machine fitted with a 36-TRE resin bonded silicon carbide abrasive wheel. Any oxides apparent on the surface of the specimen were ground off manually using 220-grit silicon carbide paper. The sample was then ultrasonically

cleaned in a warm aqueous solution of ammonium peroxodisulphate for several minutes, followed by rinsing with water, detergent, water and then methanol and finally drying using a specimen dryer. This ensured the sample was as free from surface contamination as possible in preparation for melt fluxing.

4.3. Flux selection

In addition to producing a high-purity alloy, the next crucial step in achieving large degrees of undercooling is to optimise the composition of the glass flux used during melt fluxing. The glass flux is required to support the molten sample and hold it in isolation from the solid crucible walls. In this way, the number of potent heterogeneous nucleation sites is minimised and, since oxides partition out ahead of the solid-liquid interface and into the flux during solidification, sample purity will improve with successive fluxing cycles.

The ideal flux should have a viscosity which is high enough to support the molten sample, yet low enough to encase it with sufficient wettability in order to aid in the dissolution of oxides from the specimen. A low vapour pressure is also desirable to ensure that the flux does not evaporate during the experiment, keeping the sample fully enclosed and out of contact with the surrounding atmosphere. However, in order to ensure full encapsulation of the sample down to the lowest degrees of undercooling obtainable, the flux must have a low melting or softening point and should retain an amorphous structure over a large temperature range. Both low vapour pressure and high viscosity are inconsistent with a low melting point and as such, the ideal flux should represent the best compromise between the three. In addition, it must not decompose or react unfavourably with the molten metal under the high temperatures reached during the experiment. This could have the effect of altering the composition of the sample, introducing chemical contamination or producing potential heterogeneous nucleants.

Fluxes which meet the above criteria and which had previously been used in the fluxing of Cu-based alloys were selected and investigated. These were: soda lime; a 50:50 mixture of soda lime and B_2O_3; 100 % B_2O_3; and various compositions of a B_2O_3:Na_2SiO_3 mix. Any flux containing B_2O_3 required mixing and dewatering by melting at 1173 K for 30 minutes in a high temperature furnace. The compatibility of these fluxes with elemental Cu and Ni over the full temperature range achieved during fluxing was first modelled using MTData thermodynamic modelling software. This software assumes a homogeneous mix of all elements of the alloy and flux and plots the mass of the components formed as a function of temperature for constant pressure and infinite timescale. In other words, it indicates which elements may react

with one another given the most reactive conditions possible, and therefore provides an indication of the likelihood that the Cu-Ni alloys will undergo a chemical reaction with the flux. Following this, fluxing experiments using the high purity Cu-Ni alloys were carried out in each of the fluxes to investigate the undercoolability in each one. The most compatible flux was then used for the melt fluxing experiments undertaken in this work.

4.4. Fluxing procedure

The design of the fluxing rig has been discussed in detail in Chapter 3. After several preliminary experiments, an optimised fluxing procedure was developed as follows.

Firstly, the transparent fused silica crucible was etched in 6% concentration hydrofluoric acid for 45 minutes in order to remove surface defects in the glass, which may act as heterogeneous nucleants if the sample should come into contact with the crucible. After etching, the crucible was washed thoroughly with water and then methanol and dried on a specimen drier. The base of the crucible was then sprayed with boron nitride in order to prevent it from sticking to the ceramic sample stand. The glass flux was then ground into a fine powder using a ceramic pestle and mortar and used to fill the crucible, placing the alloy droplet half way up and out of contact with the crucible walls. The crucible and its contents were then placed into the fluxing chamber, onto the ceramic sample stand with the thermocouple positioned into the hollow base of the crucible. The graphite susceptor and alumina radiation shield were put in place; with the crucible at their centre and the shield between the susceptor and RF-coil. The slots cut into them were aligned such that the crucible was visible through the viewing window and the port was sealed, using a new copper gasket to complete the con-flat style seal every 3 to 4 experiments.

The chamber was then evacuated to around 10^{-3} Pa after around 30 minutes of turbo-pumping, and backfilled to 50 kPa with N_2 gas. The pump for the cooling water which circulates through the hollow RF-coil was then switched on, followed by the RF generator. The voltage to the RF supply was then steadily increased until the temperature reached 100 K above the liquidus temperature of the alloy (100 K superheat). A superheat time of 20 minutes was then allowed to ensure full melting of the sample and removal of bubbles from the glass flux, which both obscure the sample from view and act as heterogeneous nucleants when present. The sample was then slowly cooled at an average rate of 10 K min^{-1} through the liquidus temperature until solidification was spontaneously nucleated. The temperature of solidification was then noted and the recalescence event captured via high speed imaging, where it was analysed to obtain the solidification velocity, as described in Chapter 3.6.

4.5. Microstructural characterisation

Once droplets had been removed from the fluxing rig, they were subjected to microstructural analysis using a number of techniques in order to identify any significant developments in microstructure with increasing undercooling. The structure evident on the sample surface was first investigated using light microscopy and, in some cases, Scanning Electron Microscopy (SEM) in Secondary Electron (SE) mode. Following this, the samples were mounted, sectioned, polished and etched to reveal their interior microstructure, and imaged using bright field (BF), dark field (DF) and Differential Interference Contrast (DIC) modes. Electron Backscattered Diffraction (EBSD) was also employed for orientation mapping of the grain structure.

4.5.1. Optical Microscopy

An Olympus BX51 light microscope, fitted with a Carl Zeiss AxioCam MRc5 camera was used in Bright Field (BF) mode to image any significant features evident on the surface of the sample, including the nucleation points where possible. Since the depth of field of a light microscope is not sufficient to keep the full frame in focus when imaging the spherical sample surfaces, a stack of through-focused images was obtained for each feature and blended together using Adobe® Photoshop® Elements software.

The droplets were then mounted in Bakelite resin and sectioned using the Struers Accutom-5 Automatic precision cut-off machine, fitted with a diamond wafering blade of 0.15 mm thickness to minimise kerf loss. Since growth proceeds radially outwards from the nucleation point, samples with visible nucleation points could be sectioned with a well-defined orientation relative to their growth direction. Samples were then ground with water-lubricated P220 grit silicon carbide paper to remove damage from the saw, followed by successively finer grinding steps of P800, P1200 and then P2400 grit silicon carbide. Once each grinding stage had removed the damage from the previous step, the sample was ultrasonically cleaned in methanol to remove any material which may have smeared into the pores present. If this debris dropped out during polishing at a later stage, it would cause significant surface and sub-surface damage, rendering the sample unsuitable for microstructural analysis. Three polishing stages were employed to produce a flat, damage-free surface on the soft Cu-Ni alloys. Firstly, several minutes were spent on a 3 µm diamond compound stage using a medium-hard woven synthetic cloth (‘TriDent’ from Buehler). In order to maintain good material removal rates, and to keep the cloth well lubricated, fresh, sharp abrasives were introduced by spraying with a 3 µm diamond solution. Then, a further 2-3 minutes was spent on a 1 µm diamond solution stage using Buehler’s ‘Veltex’ - a soft, dense, short-napped cloth. The diamond solution was

sprayed onto the cloth at regular intervals to keep it lubricated and sharp. Finally, Buehler's MasterPrep™ 0.05 µm alumina polishing suspension was used on a soft MasterTex cloth to produce a quality final polish. Again, between polishing stages, samples were ultrasonically cleaned in methanol to remove debris from the pores.

Following etching for 20-30 s with a 323 K solution of aqueous ammonium peroxodisulphate, optical microscopy, in BF and DF modes as necessary, was performed. In some cases it was useful to record the grain structure of the whole droplet, in which case a montage of images was manually constructed using Adobe® Photoshop® Elements software.

4.5.1.1. Reflected Light Differential Interference Contrast (DIC) Microscopy

In order to extract as much information as possible from the microstructure of etched samples, reflected light DIC microscopy was employed. This optical microscopy technique utilises a birefringent 'Nomarski' prism to split polarised incident light into two separate beams travelling at 90° to one another. As these beams hit the surface of the sample, any relief which is present causes a lateral displacement and thus path difference between the two beams. Following their path back through the objective and prism, the now parallel beams are passed through a second polarizer where the path difference between the two beams generates an intermediate grayscale image; which can subsequently be converted into coloured hues through the use of a lambda plate. As such, information about the topography of the sample surface is obtained in a way which is distinct from reflected light microscopy; where any surface relief is represented through shadowing effects. In the case of the metallic samples investigated in the present report, the surface relief present in the sample is due to the differential etching of Ni with respect to Cu; and hence the colour contrast produced is directly related to the solute distribution. In producing DIC images, the Nomarski prism was slowly rotated until maximum contrast was achieved to bring out all microstructural features. This ensured consistency in the interpretation of images taken from different samples, eliminating the effect of any variations in the sample preparation procedure – particularly with regards to etching.

4.5.2. Scanning Electron Microscope (SEM)

A Carl Zeiss EVO® MA 15 SEM, capable of imaging at magnifications up to 1 000 000 X, was used in Secondary Electron (SE) mode with a 20 kV accelerating voltage to obtain high

resolution images with a large depth of field. This was useful in imaging features such as nucleation points on the spherical sample surfaces. In some instances it was necessary to track certain features over a relatively large distance, in which case SmartStitch® acquisition and image stitching software was used to create a high-resolution montage image of the feature. Sample droplets were cleaned in methanol and thoroughly dried before being attached to an aluminium SEM stub via an adhesive carbon disc, and then placed into the SEM chamber.

4.5.3. X-Ray Diffraction (XRD)

XRD techniques centre around the use of Bragg's law of diffraction, i.e. $n\lambda = 2d\sin\theta$, where n is a positive integer, λ is the wavelength of the incident radiation, d is the spacing between the atomic planes in a crystal lattice and θ is the angle between the incident radiation and the atomic planes. When a beam of coherent X-Ray radiation enters a crystalline sample, it will be diffracted by the crystal planes present. If Bragg's law is met, the reflected radiation will exit the sample in phase, constructively interfering to create a signal of high intensity which can be measured by a detector and used for a range of sample analysis.

Two different forms of X-Ray Diffraction (XRD) analysis were performed during the course of this study using a Phillips/PanAlytical diffractometer. As discussed in Section 4.2, XRD was used for chemical analysis of the arc-melted alloys in order to check their homogeneity and purity, and to obtain values of the lattice parameter and space group for each alloy composition in order to aid with EBSD analysis (see Section 4.5.4). Undercooled droplets were then subjected to texture analysis in order to investigate the number of grains present and to identify and characterise the existence of any twinning relationships occurring between them. In cases where the sample could be sectioned with a known orientation relative to the growth direction, texture analysis could also be used to deduce the preferred growth orientation of the sample.

4.5.3.1. XRD for chemical analysis

During chemical analysis, the incident (Cu K_α) radiation forms an angle 2θ with the detector. In the Bragg Brentano goniometer arrangement employed for this work, both radiation source and detector move in an arc, with the radiation focused onto the sample at their origin, to scan through a range of 2θ values. The output is a plot of intensity vs. position (angle 2θ) to give a series of peaks. Each peak corresponds to a set of planes in a material which satisfy Bragg's law at particular 2θ values based on their d-spacings. This 'diffraction pattern' is unique to each

material, allowing identification of the sample constituents by matching peak positions to known diffraction patterns taken from the ICDD (International Centre for Diffraction Data) database. Values for the lattice parameters and symmetry groups of the sample can be deduced from the data, and the shapes and relative heights of the peaks themselves can also reveal information, such as the presence of residual stresses or preferred orientation. However, when performing analysis on flat polished alloy sections - rather than randomised (powder) samples - significant texture effects can contribute to the 2θ plot, so analysis of relative heights requires careful thought.

4.5.3.2. XRD for texture analysis

For samples whose 2θ peak positions are known, texture analysis can be performed. Sectioned undercooled droplets were therefore subjected to texture analysis following a rough 2θ scan to check the peak positions. In this technique the sample is placed into a texture cradle, which allows it to be rotated on the spot through the full 360^{o} 'Phi' (ϕ) range and tilted through 90^{o} 'Psi' (Ψ). In this instance, the angle 2θ is fixed such that Bragg's law can be satisfied for a given set of crystal planes only. As the sample moves, rotating through all ϕ angles for each degree of Ψ, the intensity of the diffracted radiation will increase as the planes of interest move into a position whereby Bragg's law is satisfied. The output is plotted as an intensity contour map for all combinations of ϕ and Ψ onto a 'pole figure'. This is a circular plot on which ϕ increases with distance around the centre of the plot from a given '0' point and Ψ increases with radial distance from the centre. **Figure 41** illustrates the angles 2θ, ϕ and Ψ with respect to the XRD texture arrangement and their relationship to the pole figure. Each 'pole' of increased intensity recorded on the pole figure therefore relates to a particular set of planes. A set of poles (e.g. the {100} pole figure will display (100), (010) and (001) poles) is produced for each crystal present, giving an indication of the number of grains present in the sample. In the instance of a shared pole, a twin relationship can be deduced and in cases where the growth direction of the sample is known, the preferred growth orientation can be obtained.

For both chemical and texture analysis, samples were sectioned, ground and polished to at least a 6 μm finish to ensure the surface was sufficiently flat and strain free. Samples were then mounted into the sample holders, taking care to ensure that their surface was at the exact height required for analysis. Particularly for texture analysis, misalignment of the sample could introduce considerable error into the measurements. In order to mitigate this error, the texture cradle has a positioning needle, the tip of which is at the desired height of the sample to allow correct alignment.

4.5.4. Electron Backscattered Diffraction (EBSD)

In addition to XRD, texture analysis was also performed on selected undercooled sample droplets using Electron Backscattered Diffraction (EBSD). This is a technique which utilises an SEM equipped with an EBSD detector and can provide microscale characterisation of the crystallography and orientation of a sample. In this work an FEI Quanta 650 FEG-ESEM, equipped with an Oxford/HKL Premium Nordlys S EBSD system, was used for high resolution texture mapping over large areas of sectioned and polished samples. Oxford Instruments CHANNEL5 EBSD post-processing software subsequently facilitated the analysis of grain orientation relationships and measurements of grain size.

During EBSD analysis, a beam of electrons is directed at a flat and polished sample surface which is tilted at around 70^{o} towards a phosphor screen (**Figure 42**). As the beam enters the surface of a specimen it generates a large number of scattered electrons, which travel in all directions, but with an overall movement in the direction of the original beam, i.e. they are incoherently but not necessarily inelastically scattered - referred to as 'diffuse scattering' (see **Figure 43** (left)). Some of these electrons will therefore be travelling at such an angle to the lattice planes that the Bragg condition is satisfied, with constructive interference resulting in a stronger beam (see Section 4.5.3). In three-dimensional space, all electron paths which satisfy the Bragg criterion for a particular set of planes radiate outwards in a conical shape, which appears as a parabola when projected onto a flat screen. However, since the phosphor screen is so close to the specimen, the parabola appears as a set of two, bright parallel lines, which form the 'Kikuchi' band for that particular set of lattice planes. Note that, for EBSD, the Kikuchi bands are generated from the backscattered electrons only since specimen thickness is relatively large. This is in contrast to Transmission Electron Microscopy (TEM) where they are formed from scattered electrons which have passed through a thin slice of specimen material. As electrons which have been diffracted from all lattice planes collide with the phosphor screen and cause it to fluoresce, an overall Kikuchi diffraction pattern is built up as shown in **Figure 43** (right) (Herring, 2013).

Each Kikuchi band can therefore be indexed according to its *hkl* origin, and the overall pattern matched with reference patterns generated from the input material parameters – i.e. lattice parameter and space group obtained from XRD analysis (Section 4.5.3), plus atom positions and species. Since the Kikuchi pattern shifts as the orientation of the crystal is changed, the relative orientation of different grains in a sample can be deduced. The crystal structure at each point in the sample can also be identified but, since Cu-Ni is only expected to form an FCC solid solution, this feature was not utilised in this work.

Diffracted electrons can only escape from around the top 10-50 nm of the sample. It was therefore crucial to prepare the sample with an extremely good polish, free of sub-surface deformation, in order to obtain successful EBSD results. The polishing procedure outlined in Section 4.5.1 was followed carefully and the resin coated in graphite dag, making contact with the specimen whilst leaving as much of the surface exposed for analysis as possible. This ensured that electrons were earthed through the SEM sample holder, avoiding charging of the sample. After loading the sample, the chamber was pumped to high vacuum and analysis started. During orientation mapping, a Kikuchi pattern is taken and indexed at each point of a specified area as the beam is scanned across the surface of the specimen. At low magnifications, small areas can be line-scanned, however, for this work larger areas of up to 3 mm^2 were of interest and so a 'stage scan' was used. Here, the area of interest is selected and broken down into a series of smaller areas which are line-scanned one at a time, the motorised sample holder moving accordingly from one to the next. A larger image is then stitched together once data acquisition is completed. Data acquisition was performed with a 30kV accelerating voltage, 15 to 17 mm working distance and a step size of between 12 and 25 µm. The minimum number of 5 Kikuchi bands required for indexing and maximum solution error of 2 degrees was used, as per the default settings of the Oxford Instruments AZtecHKL EBSD software.

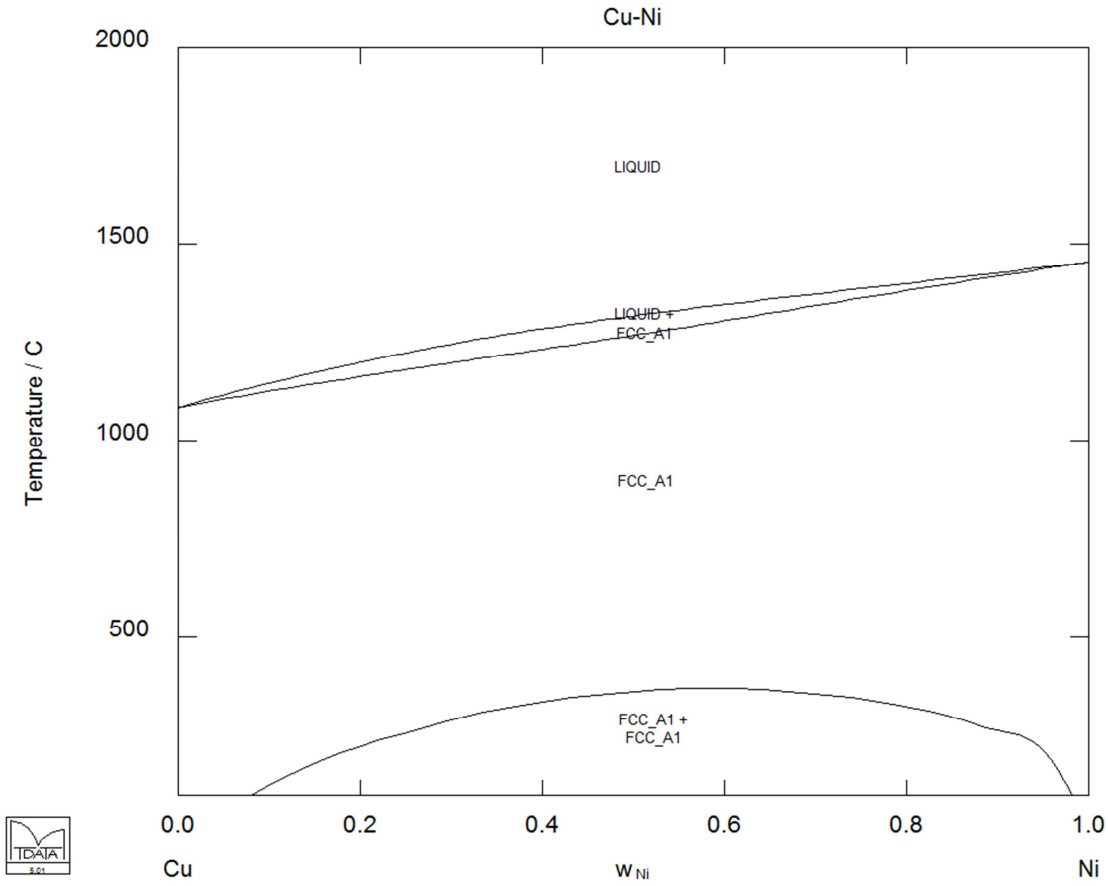

Figure 39 The Cu-Ni equilibrium phase diagram as calculated using MTData software.

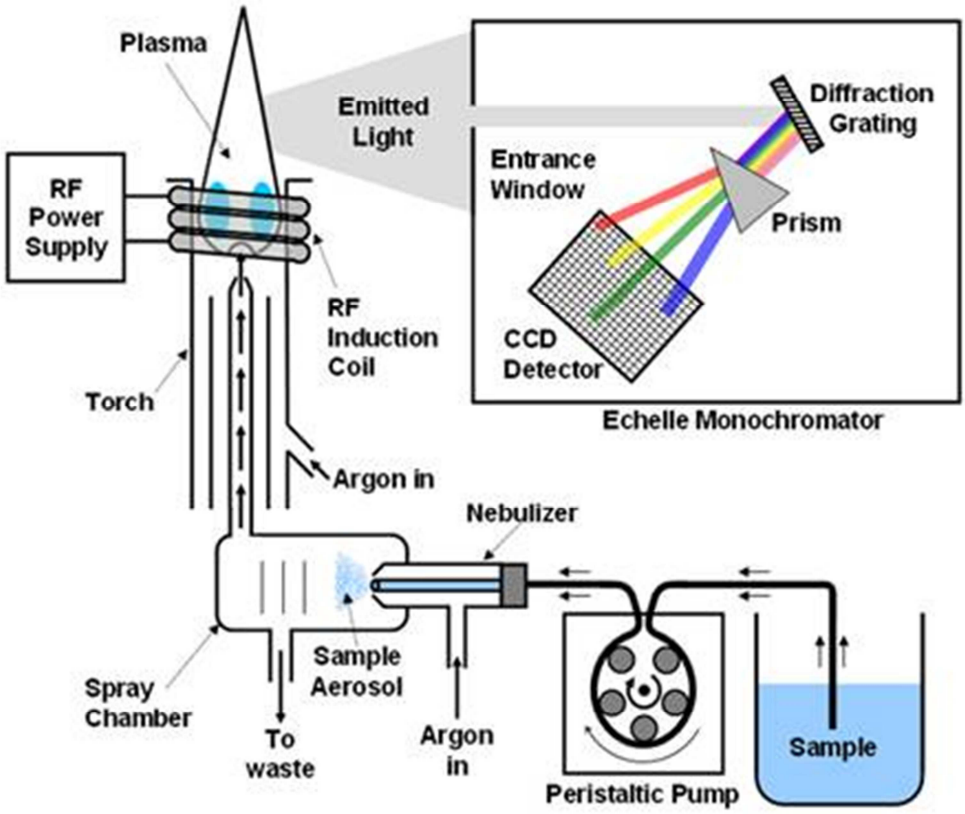

Figure 40 Schematic diagram showing the basic design of an ICP-OES (Concordia-College, 2013).

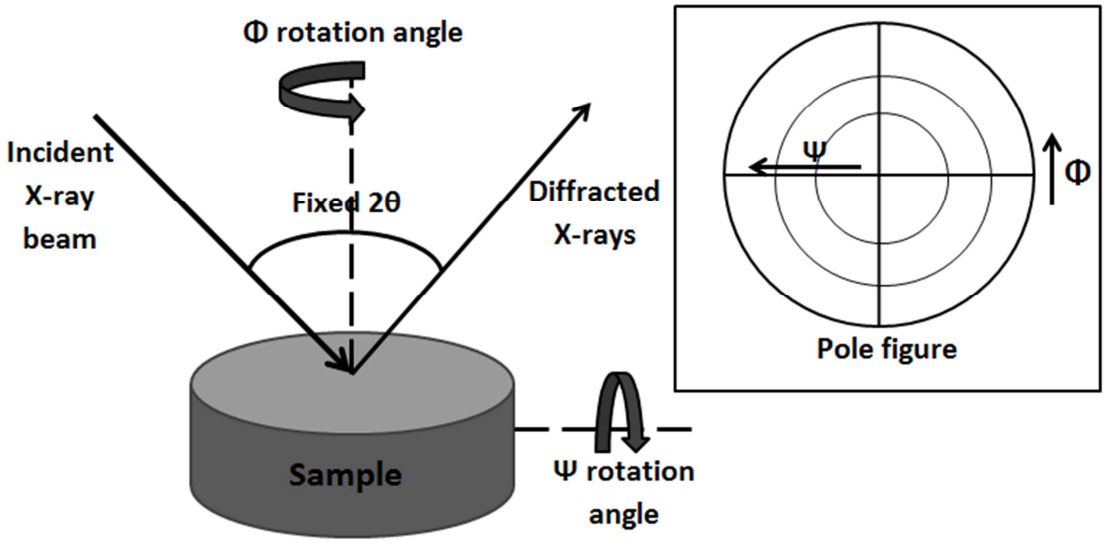

Figure 41 Diagram to show the angles 2θ, Phi (Φ) and Psi (ψ) in relation to the setup of the XRD texture analysis technique and their representation on the associated pole figure.

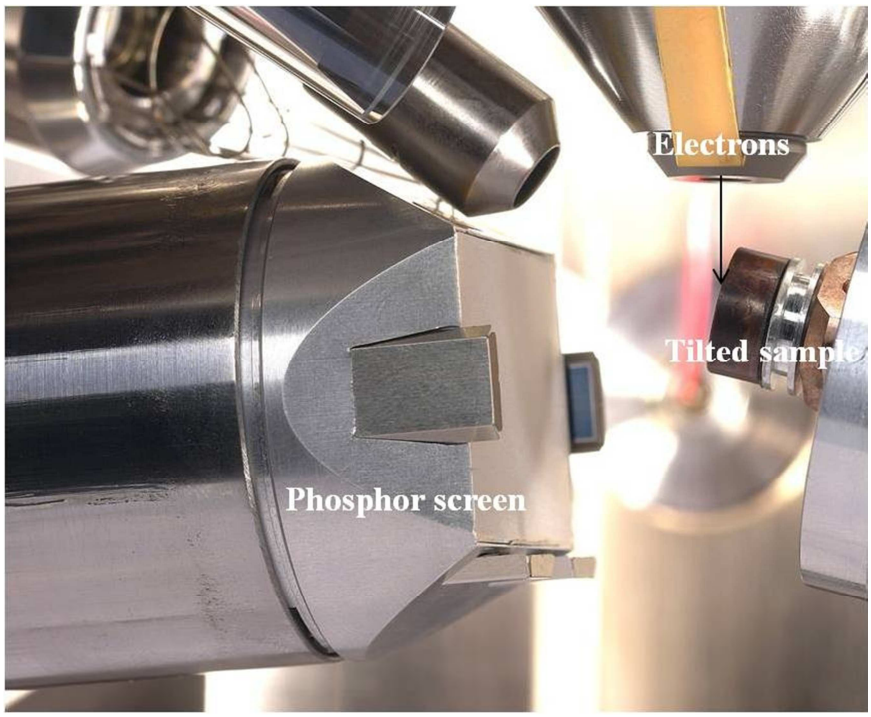

Figure 42 Showing the EBSD arrangement of the Electron gun, sample and Phosphor screen inside the SEM (Oxford-Instruments, 2013).

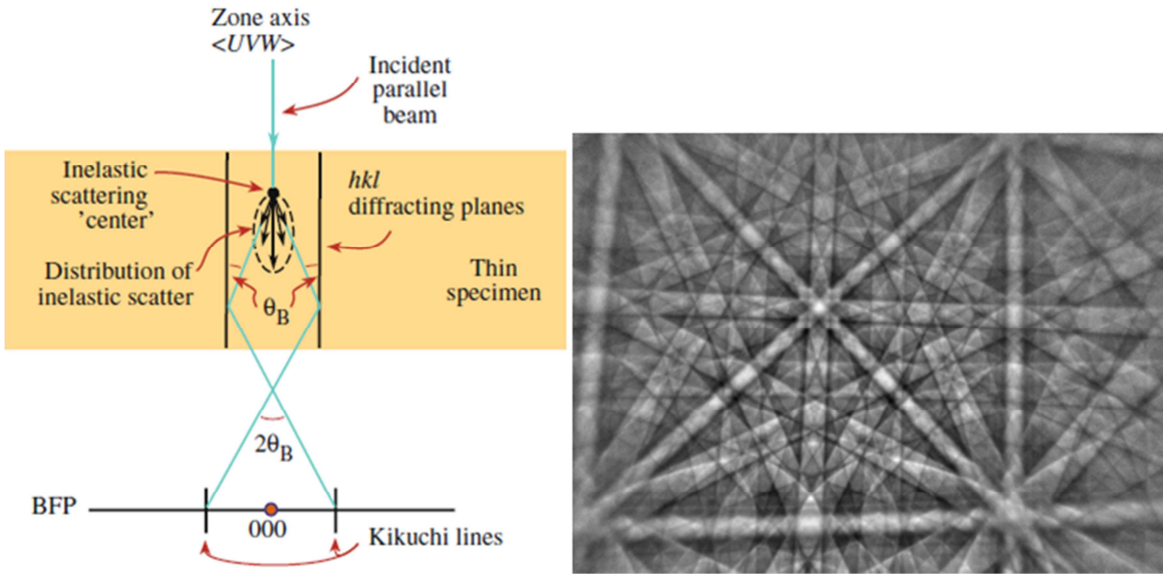

Figure 43 (**left**) schematic representation of the scattering mechanism behind the Kikuchi diffraction patterns obtained during EBSD (Herring, 2013) and (**right**) an example of a Kikuchi diffraction pattern taken from pure nickel (Oxford-Instruments, 2013).

5. RESULTS

5.1. Introduction

The results obtained during the course of this study are presented in this chapter. Firstly, the XRD, ICP-OES and LECO® characterisation of the high purity Cu-Ni alloys prepared for this work will be discussed. Following this, the effect of flux composition on the undercoolability of the alloys will be described. The velocity-undercooling relationship, together with a detailed look at the microstructural and texture evolution with increasing undercooling, will then be presented for the two alloy compositions investigated.

5.2. Characterisation of Alloys

As mentioned in Chapter 4.2, a high purity alloy is required in order to achieve sufficient degrees of undercooling. Characterisation of the final composition is also key to the accurate interpretation of results, since the liquidus temperature and thus the degree of undercooling will be altered if the preferential loss of one of the alloy constituents occurs during fabrication. The residual oxygen concentration is also important to know, as high levels of oxygen will result in the incorrect interpretation of a ternary system as a binary. A small amount of oxygen present in the alloys is less of a concern however, since oxides tend to partition out of the solidifying metal and into the flux. For example, Mullis *et al*. (2004b) measured a decrease in the residual level of oxygen from 600 – 800 ppm (parts-per-million atomic) in the as-received high purity Cu, to less than 60 ppm in deeply undercooled samples. A sufficient degree of homogeneity in the arc-melted slug is also required to ensure that samples taken from different sections of it are of the same composition. This ensures that any identified alterations in the microstructure can be attributed to the solidification conditions only, and not due to variations in solute concentration between specimens.

Table 1 gives the weight change, final composition and residual oxygen concentration of the two arc-melted alloys, which were initially mixed to a Cu–9.31wt.%Ni and Cu–4.63wt.%Ni composition. In both cases material was lost during arc melting, with a 2.045 % weight loss in the Cu–9.31wt.%Ni alloy, and a 1.826 % weight loss in the Cu–4.63wt.%Ni alloy. This could account for the alterations in the final alloy compositions, determined by ICP-OES to be Cu–8.90wt.%Ni and Cu–3.98wt.%Ni. This suggests that the preferential loss of Ni has occurred, which would correspond to 70 % in the high concentration alloy and 86 % in the more dilute alloy. The final compositions correspond to liquidus temperatures of 1423 K and 1385 K (respectively), as calculated by the MTData thermodynamic calculation software. These values

have been used to calculate the degree of undercooling achieved during melt fluxing. Material loss during arc-melting might be expected due to the vigorous, high-energy nature of the process. The preferential loss of Ni may be due to the coarser mesh size of the starting Ni powder. For both alloys the residual oxygen content is just over 0.2 wt.%, which, as discussed, should decrease to much lower levels during successive fluxing cycles.

Figure 44 shows the XRD patterns taken from both of the alloys in comparison to the diffraction pattern of the Si standard, and **Table 2** displays the confirmed lattice parameters and space groups used for EBSD analysis. Diffraction patterns were matched to a paper (Gulyaev and Trusova, 1950) taken from the Landolt-Börnstein Database of Springer Materials. The patterns exhibit sharp peaks, particularly for the more dilute alloy, in which Cu-Kα peak splitting is evident in the shoulders observed at higher angles of 2θ°, relating to the {200} and {220} peaks. An enlarged view of the {220} peak is shown in **Figure 44** to illustrate this effect. This indicates that the peaks are close to the resolution of the instrument. Compared to the Si standard, there is a slight broadening of the peaks for both alloys. This could be due to the fact that the samples will have directionally solidified since, after arc melting, they were left to solidify in the water-cooled hearth of the arc-melter. This directional growth will have taken place dendritically, with solute rejected into the interdendritic liquid. Hence a completely homogeneous mixture of the two elements will never be formed in this manner, which will likely result in a slight peak broadening. This would explain the observation of slightly sharper peaks for the more dilute alloy. In addition, the presence of extra peaks in both of the diffraction patterns indicates the presence of impurities, since only one, FCC phase is expected to form for a Cu-Ni alloy. Based on the results of the compositional analysis, these are likely due to either Cu or Ni oxides. By comparing these extra peaks to the diffraction patterns of the oxides, the impurities have been identified as NiO. These will reduce the homogeneity of the sample and thus contribute to peak broadening. However, in general, the sharpness of the peaks indicates that a sufficient degree of homogeneity has been achieved during arc melting. This is further supported by the presence of a steadily increasing background Cu-fluorescence, since any inhomogeneous, Cu-rich regions might cause an abrupt increase in the fluorescence levels.

In conclusion, the powder compaction and arc melting method for the fabrication of high purity alloys has been successful in producing alloys of sufficient purity and homogeneity for this investigation. The alloys have been characterised in terms of their final composition and residual oxygen concentration to aid in the accurate interpretation of the results obtained in the melt fluxing experiments.

Table 1 Weight change of both Cu-Ni alloys after arc melting, and final composition and residual oxygen content as confirmed by ICP-OES and LECO® analysis.

Notional composition of starting powder prior to compaction and corresponding wt.% values	%Weight loss due to arc melting	Final composition, as confirmed by ICP-OES	Residual oxygen content, as confirmed by LECO®	Liquidus Temp., T_L
Cu-10 at.%Ni = Cu-9.31 wt.%Ni	2.045 %	Cu-8.90 wt.%Ni	0.237 wt.%	1423 K
Cu-5 at.%Ni = Cu-4.63 wt.%Ni	1.826 %	Cu-3.98 wt.%Ni	0.241 wt.%	1385 K

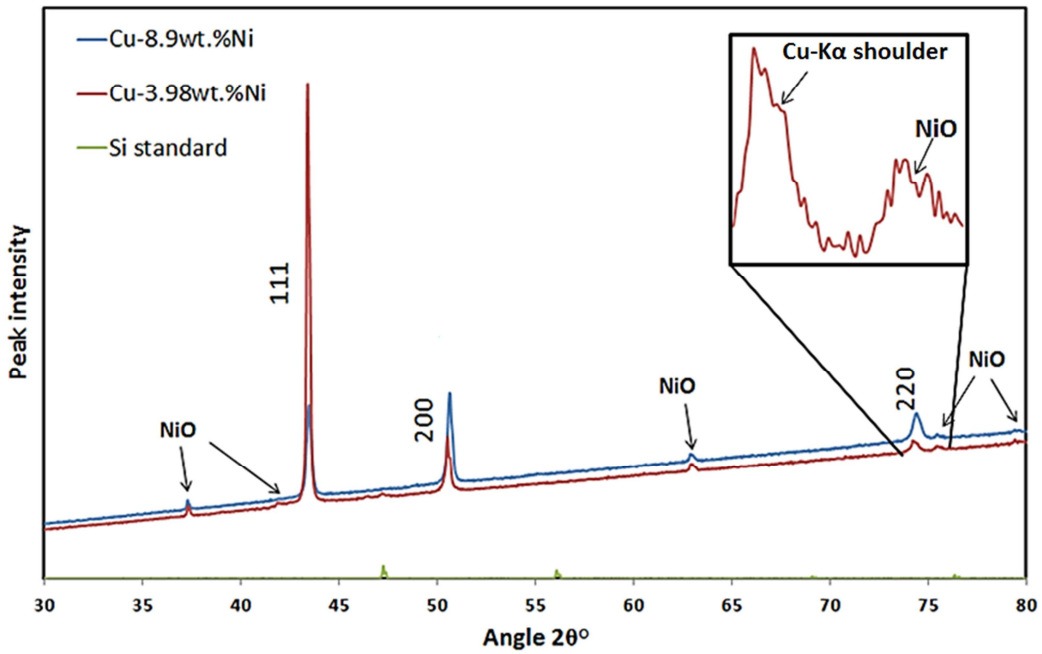

Figure 44 XRD patterns collected for both alloys and for the silicon standard.

Table 2 Calculated lattice parameters and space groups determined from XRD analysis.

Alloy composition	Calculated lattice parameter, Å	Confirmed space group
Cu-8.90 wt.%Ni	3.60892(6)	Fm-3m
Cu-3.98 wt.%Ni	3.61067(3)	Fm-3m

5.3. Flux compatibility

As discussed in Chapter 4.3, a key parameter in the success of the melt fluxing experiments is the composition of the glass flux itself, since its viscosity over the experimental temperature range employed and its reactivity with the Cu-Ni alloys will have a large impact on their undercoolability. Five different fluxes were identified as possible candidates from previous work into the melt fluxing of Cu and its alloys: soda lime; a 50:50 mixture of soda lime:B_2O_3; 100 % B_2O_3; 100 % Na_2SiO_3; and 20:80, 30:70, 50:50 and 60:40 mixtures of B_2O_3:Na_2SiO_3. For each flux investigated, the thermodynamic stability of the components was modelled using the MTData software. The molar quantities of each component present (assuming a full crucible and a spherical sample of 6 mm diameter) was calculated and input alongside the experimental pressure and temperature range employed. This gave an initial indication as to the suitability of each flux and helped to explain the performance of the fluxes during experimental trials. Once a suitable flux had been identified, this was then used to collect the data presented in the rest of this chapter.

5.3.1. Soda lime and Soda lime + B_2O_3

Mullis *et al*. (2004a) used a soda lime flux to undercool Cu-Sn alloys by up to ΔT = 360 K. As dilute Cu-Sn alloys, their melting point was close to that of pure Cu (1358 K), which is < 65 K lower than the melting points of the Cu-Ni alloys employed in this work. Hence, the two alloys would require similar heating ranges during the fluxing experiments, indicating that the viscosity of the soda lime flux may also be compatible with the Cu-Ni alloys. Preliminary fluxing experiments of the high purity Cu–8.9wt.%Ni alloy in a soda lime flux were unsuccessful in achieving any visible degree of undercooling (see **Table 3**). During the experiments, the flux did support the sample but was observed to contain many gas bubbles, obscuring the visibility of the sample and possibly contributing to the number of heterogeneous nucleation sites present. On removing the sample and flux after the experiment, it was found that the flux had turned a murky brownish colour, indicating a possible reaction between flux and sample. Similar observations of a bubbly and discoloured flux were made by Ahmad (2010) when using a soda lime flux to undercool a Ni-Si alloy. In addition, Ahmad observed a cloudy atmosphere within the chamber during the experiments, which left deposits of Na, Si and K on the chamber walls (as determined by EDX analysis of the deposits). Ahmads MTData calculations revealed a significant increase in partial pressure beyond 1593 K due to the formation of gaseous Na, Si and K, which can account for this observation. The fluxing experiments performed with Cu-Ni alloys did not reach temperatures as high as this, hence this effect was not observed.

In spite of the bubbly and gaseous flux, Ahmad achieved undercoolings of up to 379 K in soda lime. Poor visibility and the concern of a possible reaction between the Ni-Si and the soda lime, however, prompted a switch to a B_2O_3 flux. By employing a dewatering technique, a clear and clean atmosphere was maintained during fluxing and the post-experimental flux exhibited no discoloration. Dewatering was necessary in order to suppress the vigorous bubbling of the hydrated B_2O_3 flux, which may result in the sample being pushed out of the crucible. Fluxing of the Cu-Ni alloy was therefore performed using a 50:50 mixture of soda lime and dewatered B_2O_3, in the hope of improving the undercoolability of the sample and its chemical compatibility with the flux. As can be seen from **Table 3**, no undercooling was again observed and the flux became cloudy and discoloured. **Figure 45** and **Figure 46** show the MTData analyses of the chemical compatibility of soda lime and the 50:50 soda lime:B_2O_3 mixture, with Cu and Ni. In both cases, 'gas' is evolved and no elemental Cu or Ni remains, with Ni reacting with O_2 in the flux to form NiO and Cu forming an Al_2CuO_4 compound. This reaction of Ni and Cu with the soda lime elements could account for the lack of undercooling observed, particularly due to the formation of high melting point (2228 K) NiO, which would be solid across the full experimental temperature range and would therefore act as a potent heterogeneous nucleant. In reality, the Cu and Ni elements are alloyed and only the surface of the droplet is exposed to the flux, hence most of the elemental Cu and Ni do still remain. The possibility of a reaction at the surface of the droplet, which may produce heterogeneous nucleants and alter the sample composition, has however been identified, which accounts for the lack of undercooling observed and highlights the unsuitability of soda lime for the present work.

5.3.2. B_2O_3

The MTData analyses of the soda lime and soda lime:B_2O_3 fluxes (**Figure 45** and **Figure 46**) only indicate that chemical reactions will occur with the soda lime components. Hence it was proposed that 100 % B_2O_3 may be a more compatible flux. **Figure 47** shows the MTData analysis of B_2O_3 with Cu and Ni, which indicates complete stability of all components over the full experimental temperature range, since Cu, Ni and B_2O_3 remain as separate components. In addition, there is no evolved 'gas' phase, indicating that the flux will not vaporise during fluxing. Experimentally, the B_2O_3 flux performed much better than the soda lime. The flux did contain bubbles but most of these could be removed during superheating to leave good sample visibility. There was only a faint discoloration of the flux to a purple colour and only during the fluxing of a new piece of alloy, hence this is likely due to the removal of oxides from

the sample. However, whilst the sample did undercool in this flux, the maximum obtained undercooling was only ΔT = 70 K (**Table 3**). Since the sample was observed to sink to the bottom of the crucible during each of the fluxing experiments, it is likely that the viscosity of the B_2O_3 flux is too low to keep the sample isolated from the crucible, thereby limiting the achievable level of undercooling.

5.3.3. B_2O_3 + Na_2SiO_3

Han *et al*. (2001) were able to obtain undercoolings of up to 421 K in Cu-Ni alloys by fluxing with a 70 wt.% Na_2SiO_3 -17.73 wt.% $Na_2B_4O_7$ - 12.27 wt.% B_2O_3 mixture. $Na_2B_4O_7$, or Borax, is an active flux and is thus likely to enhance the dissolution of oxides. However, as a mixture of B_2O_3 (a network-forming oxide) and Na_2O (a non-network forming oxide) it is expected to reduce the viscosity of the B_2O_3 further. Na_2SiO_3, however is a mixture of SiO_3 (a higher-viscosity network-forming oxide than B_2O_3) and Na_2O so may either increase or decrease the viscosity. The measured glass transition temperature (T_g) of B_2O_3 is 580 K (Botta et al., 2008), whilst Avramov *et al*. (2005) state that the dependence of T_g on the silicate composition is given by:

$$T_g(x) = (895 - 626x) \pm 5\% \quad [K] \tag{13.0}$$

where *x* is the molar fraction of the network modifier Na_2O in $(Na_2O)_x(SiO_2)_{1-x}$. This corresponds to a T_g of 686 K ±5%, which is higher than that of B_2O_3, hence it is likely to increase the viscosity of the flux mixture. MTData analysis (**Figure 48** and **Figure 49**) indicates that both a 100 % Na_2SiO_3 and 50:50 B_2O_3:Na_2SiO_3 mixtures are chemically stable in contact with Cu and Ni over the experimental temperature range. As such, various compositions of B_2O_3:Na_2SiO_3 were experimentally tested, with the maximum achieved undercoolings in each flux noted as shown in **Table 3**. Much larger degrees of undercooling were achieved using these fluxes, with a maximum undercooling of 240 K achieved overall. It can be seen that the composition of the flux has little effect on the undercoolability of the Cu-Ni alloy. A 100 % Na_2SiO_3 flux was trialled, but could only achieve up to ΔT = 50 K in pure Cu. All mixtures of the two fluxes were transparent and colourless, and after superheating, were bubble-free at higher temperatures to give extremely clear views of the sharp solidification front. As temperatures were decreased, however, light levels dropped and the flux became slightly murky, leading to a blurring of the solidification front and thus a greater error in velocity measurements at higher undercoolings. As with the B_2O_3 flux, a slight discolouration was only observed for new Cu-Ni samples, indicating reaction only through removal of oxide impurities in the alloy. Undercoolings of up to 240 K for Cu-8.9 wt.% Ni and 216 K for Cu-3.98 wt.% Ni were

achievable. This corresponds to a melt temperature of around 1175 K for both alloys, hence undercooling is probably limited by the higher viscosity of the flux, which must reach some critical viscosity at this temperature.

Overall, good chemical stability and undercoolability has been achieved with the B_2O_3: Na_2SiO_3 flux. Hence, the present work employs the use of a B_2O_3 + Na_2SiO_3 glass flux to undercool the prepared Cu-Ni alloys.

5.3.4. Flux preparation

Both the B_2O_3 and Na_2SiO_3 fluxes require dewatering prior to fluxing. The presence of water in the flux causes it to bubble vigorously, such that both flux and sample can bubble out of the crucible during an experiment. Attempts to dewater B_2O_3 *in situ* by holding the temperature of the melt fluxing equipment at 473 K for 1 hr. were unsuccessful in suppressing the bubbling. In order to investigate this, a sample of B_2O_3 was investigated using Thermogravimetric Analysis (TGA), in which minute fluctuations in sample weight are measured as a function of time during heating. The experiment involved heating the B_2O_3 to 473 K and then holding at this temperature for 10 hrs. The results can be seen in **Figure 50**, showing the percentage decrease in sample weight and the temperature (expressed as a percentage of 473 K) as a function of time. The most significant decrease in sample weight, and therefore water loss, is observed to occur during the initial heating stage, with little excess weight lost once the sample had reached 473 K. This suggests that the temperature of the dewatering process is more critical than the hold time. Han *et al.* (2001) were able to fully dewater and mix their Na_2SiO_3:$Na_2B_4O_7$:B_2O_3 flux by melting the components together at 1173 K. Through following this procedure, a sufficiently dehydrated B_2O_3:Na_2SiO_3 flux was produced, which did not excessively bubble and remained within the crucible throughout the experiment.

5.3.5. Conclusion

Following experimental trials and MTData analysis of the chemical stability of a number of glass fluxes, the B_2O_3 + Na_2SiO_3 system was selected as the most suitable for the melt fluxing of Cu-Ni alloys. This flux is chemically stable with respect to Cu and Ni, does not produce a gaseous phase at high temperature and, experimentally, has been capable of producing undercoolings of up to 240 K. A suitable mixing and dewatering procedure has been identified in order to reduce bubbling in the flux, ensuring that the Cu-Ni specimens are visible throughout the experiments.

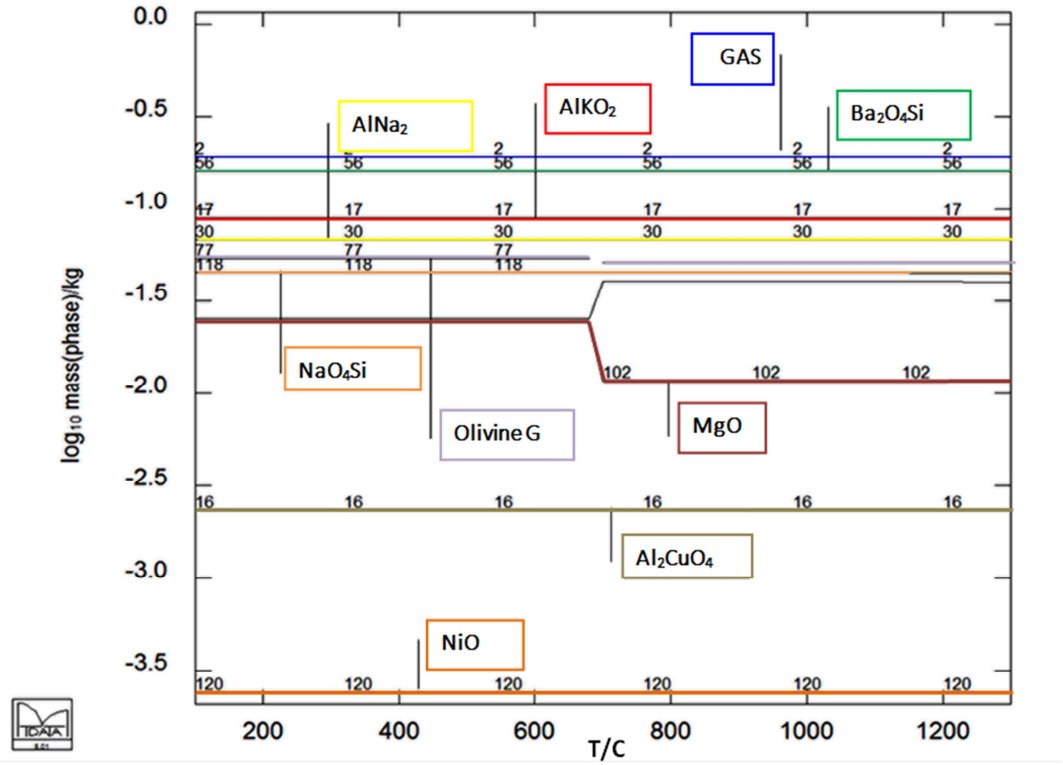

Figure 45 MTData plot of the thermodynamic stability of Cu, Ni and soda lime glass, showing no elemental Ni or Cu left due to reaction with O and Al in the flux (colour coded for better visibility).

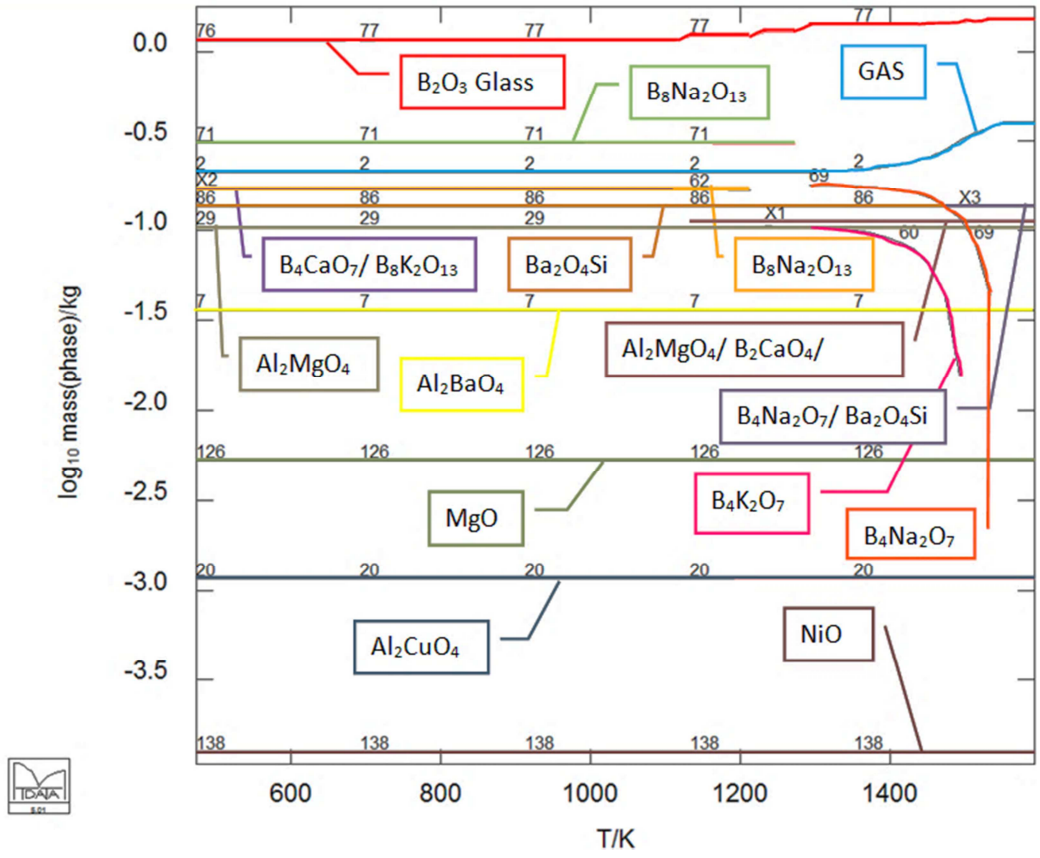

Figure 46 MTData plot of the thermodynamic stability of Cu, Ni, soda lime and B_2O_3 glass showing no elemental Ni or Cu left due to reaction with O and Al in the flux (colour coded for better visibility).

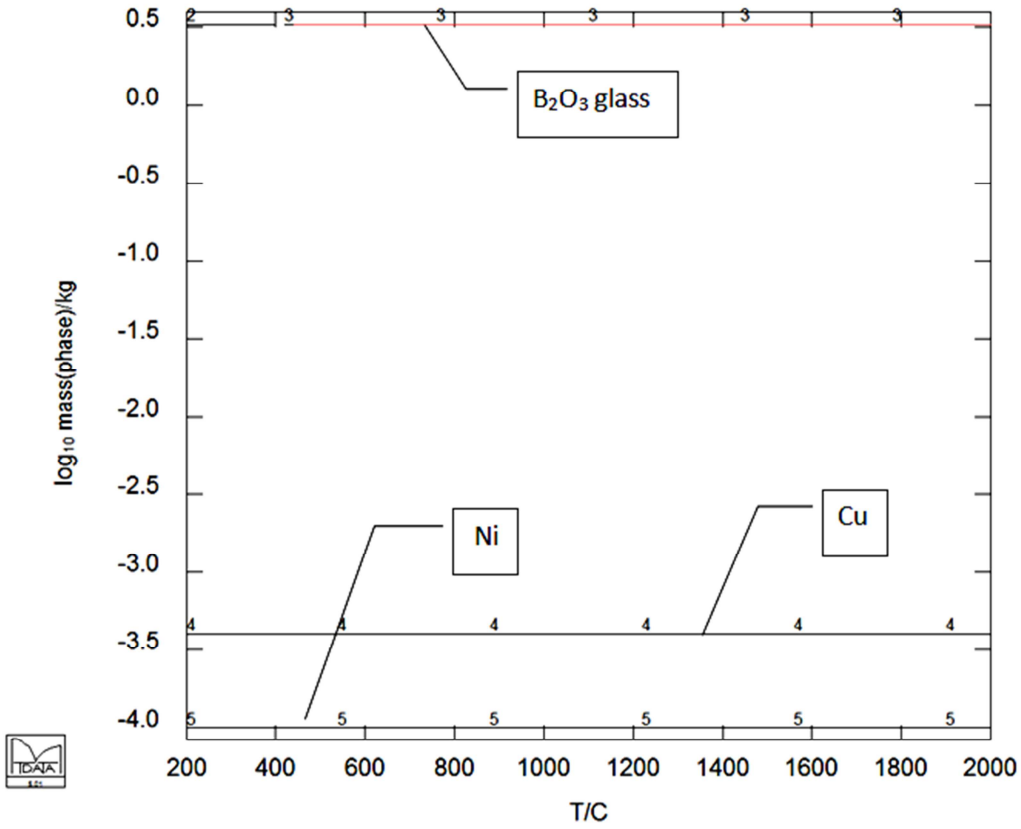

Figure 47 MTData plot of the thermodynamic stability of Cu, Ni and B_2O_3 glass showing no reaction between the elements.

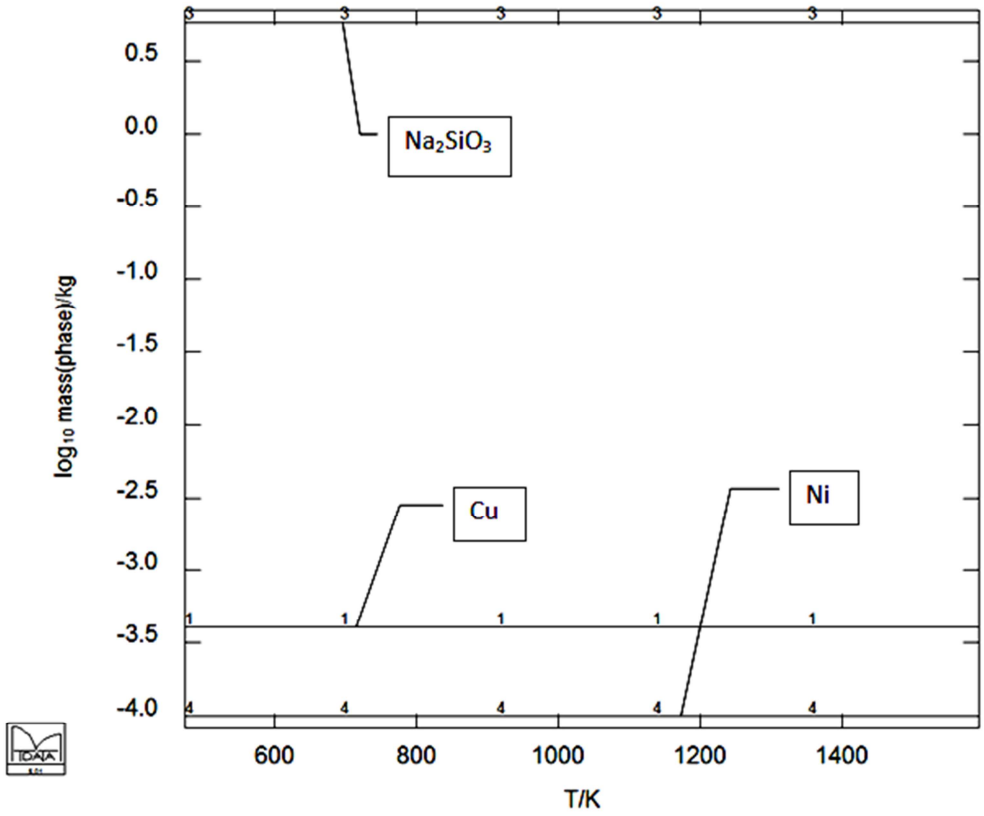

Figure 48 MTData plot of the thermodynamic stability of Cu, Ni and Na_2SiO_3 glass showing no reaction between the elements.

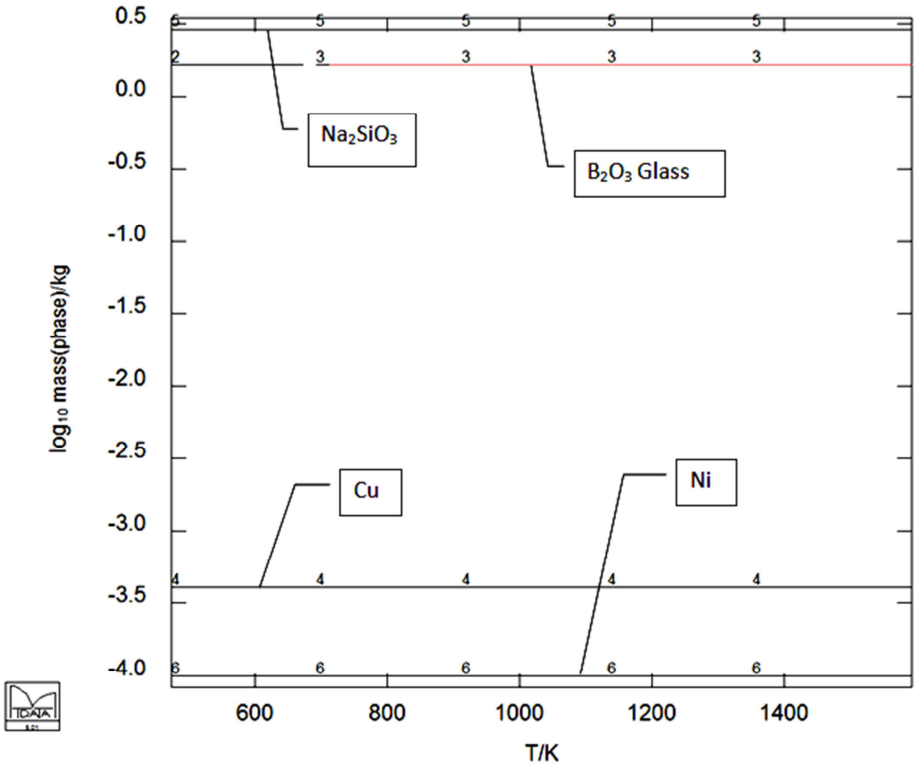

Figure 49 MTData plot of the thermodynamic stability of Cu, Ni, B_2O_3 and Na_2SiO_3 glass showing no reaction between the elements.

Table 3 Showing the maximum undercooling achieved (if any) for each flux investigated.

Flux	Composition	Maximum undercooling achieved
Soda lime	100 %	No undercool observed (Cu-Ni)
Soda lime:B_2O_3	50:50	No undercool observed (Cu-Ni)
B_2O_3	100 %	70 K (Cu-Ni)
Na_2SiO_3	100 %	50 K (Cu)
B_2O_3: Na_2SiO_3	20:80	233 (Cu-Ni)
	30:70	228 (Cu-Ni)
	50:50	232 (Cu-Ni)
	60:40	240 (Cu-Ni)

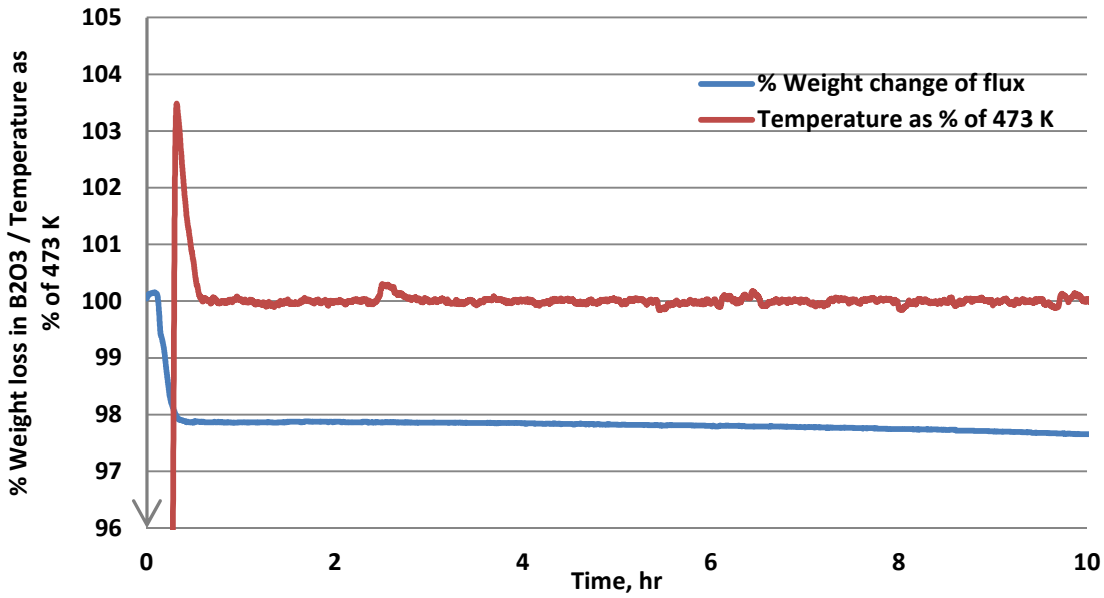

Figure 50 TGA analysis of the dewatering of B_2O_3 flux as it is heated and held at 473 K for 10 hrs., with temperature expressed as a percentage of 473 K.

5.4. Melt fluxing results

Having optimised the flux composition and dewatering procedure, melt fluxing experiments could then be undertaken in order to compile velocity-undercooling relationships for the Cu-8.9 wt.% Ni and Cu-3.98 wt.% Ni alloys. Each successful heating and cooling cycle produced a measured undercooling and corresponding solidification velocity. Up to 7 cycles could be performed per experiment, with each experiment generating an undercooled droplet for microstructural and texture analysis. This section will present the results of these investigations, firstly for the more concentrated alloy and then for the Cu-3.98 wt.% Ni composition.

5.4.1. Cu-8.9 wt.% Ni

5.4.1.1. Velocity-undercooling relationship

The measured velocity-undercooling relationship can be seen in **Figure 51**. Undercoolings of up to 240 K and velocities close to 100 m s^{-1} were achieved. Initially, the growth velocity is observed to increase gradually with increasing undercooling; however, beyond around $\Delta T \approx$ 200 K, a more rapid increase in growth velocity occurs with increased ΔT. This indicates the possibility of a positive break in the curve beyond this point. A log-log plot of the data suggests that this may be the case, with two distinct relationships emerging. However the presence of a break remains inconclusive. Through further manipulation of the data, it can be shown that a good degree of proportionality exists between v and ΔT^2, with a v - ΔT^2 plot exhibiting a more definite break at an undercooling of around $\Delta T \approx$ 207 K, or $v \approx$ 35 m s^{-1} (**Figure 52**).

5.4.1.2. Microstructural and texture evolution with increasing undercooling

The existence of a break in the velocity-undercooling relationship is indicative of a possible transition in growth mode beyond this point. Microstructural and texture analysis of samples solidified over the full range of undercooling reveal the occurrence of a number of growth transitions. These are summarised in relation to both the undercooling and growth velocity in **Figure 51**. This section will therefore present the findings for each defined growth regime in turn.

5.4.1.2.1. Single grain dendritic up to $\Delta T \approx 45$ K

At the smallest undercoolings observed (from ΔT = 30 K), droplets consisted entirely of a single dendritic grain, an example of which is shown in **Figure 53**, showing the droplet surface and interior microstructure of a sample undercooled by ΔT = 35 K. Dendrites observed within this region of undercooling exhibit strong orthogonality, as would be expected from a FCC alloy undergoing preferred growth along the usual <100> direction.

5.4.1.2.2. Equiaxed grains between 45 K $\leq \Delta T \leq$ 85 K

Between undercoolings of approximately 45 K and 85 K, a large equiaxed grain structure is observed, as indicated by the regions of light and dark contrast in **Figure 54** (top): a randomly sectioned and etched sample undercooled by ΔT = 65 K. Sub-grains are present within the parent grains and many of the grain boundaries appear to be curved (as shown by the arrows), indicative of grain boundary migration. A DIC image of the same area (**Figure 54** (bottom)) appears to show an underlying dendritic substructure which extends across the grain boundaries (indicated by the arrows). This is confirmed by the pole figure shown in **Figure 55**, which exhibits only one set of poles and thus confirms the presence of a substructure which is continuous throughout the sample. The above is consistent with recrystallisation, a mechanism commonly associated with the low undercooling region of grain refinement observed in many alloys.

5.4.1.2.3. Eightfold, twinned, mixed-orientation dendritic growth at 85 K $\leq \Delta T \leq$ 155 K

With increasing undercooling, samples underwent a transition back to a large-grained dendritic structure. For nearly all samples within the range 85 K $\leq \Delta T \leq$ 202 K, nucleation points were visible on the droplet surfaces. Within the undercooling range 85 K $\leq \Delta T \leq$ 155 K, nucleation points exhibited near-eightfold symmetry, the growth pattern of which displayed dendrites of mixed growth orientation. For example, **Figure 56** shows the light microscope and SEM images of the nucleation point visible on the surface of a sample undercooled by ΔT = 139 K. The feature labelled as '1' in these images is a split primary dendrite branch, on which secondary arms grow orthogonal to the primary – consistent with <100> oriented growth. However at 90^{o} to this is feature '2', a primary dendrite branch whereby the secondary dendrite arms appear to grow in a more <110> or <111>-like orientation. The interior microstructure of this droplet can be seen in **Figure 56** (bottom), which exhibits a large grain

structure consisting of a mixture of dendritic and seaweed microstructures. The grains are separated by wavy boundaries and a small 'floating' grain can be seen close to one of the boundaries (indicated by the arrow), suggesting significant grain boundary migration. Pole figure plots of the {200}, {220} and {111} projections, taken from a section parallel to the growth direction, are shown in **Figure 57**. Whilst sharp poles can be seen on each of the plots, indicating some preference in preferred growth orientation, the absence of a pole from the centre of each of them renders the preferred growth orientation of the sample difficult to conclude. This could be as a result of slightly off-axis sectioning, preferred growth in another crystallographic direction, or may be due in some way to the apparent competing growth orientations. Each of the pole figures indicates the presence of a strong set of poles and a further weak set of poles, which become more evident when pole intensity is plotted as a log scale. Two groups of poles can be related to one another via common angles of 72° 53′ or 109° 47′, indicating the presence of two large grains. Furthermore, it becomes evident from the log{111} plot that there is a shared pole, indicative of twinning. Since this is not the strongest pole, this suggests that growth was twinned along one of the secondary growth directions.

5.4.1.2.4. Sixfold, twinned, mixed-orientation dendritic growth at 161 K ≤ ΔT ≤ 202 K

The nucleation point of a sample undercooled by ΔT = 159 K appears to have lost any discernable symmetry (**Figure 58**). However, by ΔT = 161 K, a transition to sixfold growth is observed (**Figure 59** (top)). Once more, dendrites of mixed morphology are evident on the surface of samples undercooled in this range. Feature '1' in **Figure 59** (top), for example, is a primary dendrite branch on which well-developed orthogonal branches can be seen, whilst to the left of this branch, a neighbouring primary dendrite displays strong <111> type growth. **Figure 59** (middle) shows the DIC micrograph of some of the interior microstructure of this sample. A large grain structure is observed to exist, consisting of a mixture of dendritic and dendritic seaweed substructures. The grain boundary seen in this image is wavy, and the substructure is observed to extend across it, hence it appears that grain boundary migration has taken place. In the bottom image of this figure a triple junction between three grains is shown close to the surface of the sample. Texture analysis (**Figure 60**) performed on a section taken parallel to the growth direction reveals a strong pole close to the centre of the log{111} plot, indicative of dominant <111>-oriented growth. Seven sharp poles can be seen, which might indicate the presence of two grains which are twinned, however a third grain can clearly be seen in **Figure 59** (bottom), which suggests otherwise. Through careful analysis of the common angles between the poles, it can be seen that there are three grains (indicated by

separate colours) and three shared poles (indicated by yellow circles). Hence there appears to be an unusual 'triple-twin' relationship.

5.4.1.2.5. Dendritic seaweed 'branches' at 161 K ≤ ΔT ≤ 202 K

Throughout the eightfold and sixfold growth regimes, branches of a dendritic seaweed-like microstructure were observed. These can be seen in **Figure 56** (top and middle), labelled as features '3', and in **Figure 59**, labelled as feature '2'. To our knowledge, structures such as these have not previously been reported. In order to inspect these structures more closely, the development of feature '2' in the ΔT = 159 K sample was tracked over the surface of the droplet using montage imaging software on the SEM. The resulting image is shown in **Figure 61**. The sixfold nucleation point can be seen in the bottom right-hand corner of this image, with the seaweed branch extending out to the left. It can be seen from this image that the seaweed branch originates from a primary dendrite branch, which splits soon after formation and diverges. Secondary arms then appear to grow into the split and bend to become near-parallel to the original growth direction of the branch, at which point they undergo repeated tip-splitting to form a seaweed structure which is bound by the two halves of the original dendrite. The growth of the observed seaweed branches are always observed to terminate via the growth of an array of dendrites. In some cases, the seaweed branch exhibits orthogonal outer secondary arms, in which case the seaweed terminates via an array of <100>-type dendrites – as seen on the SEM image. This type of dendrite is labelled as '3.i' on **Figure 56** (top and middle). In other instances, no outer secondary branches are observed, in which case seaweed growth breaks down via the growth of a more <111>-type dendritic array (labelled as features '3.ii.' on **Figure 56**).

Texture analyses, of samples taken from the eightfold and sixfold regimes, appear to indicate which type of seaweed branch (<100> (3.i) or <111> (3.ii.)) is present in each sample. For example, in the pole figures taken from the sample undercooled by ΔT = 139 K (**Figure 57**), additional weak texture can be seen on the log-scale {111} and {200} pole figures, but not on the {220} plot. Both types of seaweed are observed in this sample, hence it is suggested that the additional texture arises from the seaweed structures. Each seaweed branch would have grown in a general crystallographic direction, since it will have originated from an oriented primary dendrite branch, yet would otherwise have developed without any strong preference in growth orientation. Hence, the texture observed in the {111} and {200} pole figures might arise from the seaweed branches, growing with overall <111> or <200> orientations (respectively), but with repeated tip-splitting leading to a relative misorientation of the

respective planes and therefore reflections from a broad range of Φ and Ψ angles. In all samples investigated, where a particular type of seaweed branch is observed to grow from the nucleation point, additional weak texture arises on the corresponding pole figure.

5.4.1.2.6. Coarse dendritic grains at 202 K ≤ ΔT ≤ 220 K

Beyond ΔT = 202 K, a further transition to a large-grained structure is observed, an example of which is shown in **Figure 62**, a sample undercooled by ΔT = 214 K. This transition appears to coincide with the suggested break in the v - ΔT curve. In this case, the dendritic substructure observed is discontinuous between grains, as confirmed by the {111} pole figure, which indicates several sets of poles, sharing no orientational relationship. The surface topography of this sample (**Figure 63**) reveals the coexistence of dendrites of a large variety of morphologies. Both coarse and fine dendrites can be seen, as well as apparent mixed orientations. In some cases, neighbouring secondary dendrite arms appear to have grown with different orientations relative to one another. Since growth will have proceeded from a single nucleation point, which is no longer evident, the original growth structure appears to have been removed or modified by post-solidification processes.

5.4.1.2.7. Partially grain-refined from dendritic seaweed precursor at 220 K ≤ ΔT ≤ 235 K

Up to the highest undercoolings achieved, (ΔT = 235 K), a decrease in grain size is observed above undercoolings of around 220 K. An example of a sample undercooled by ΔT = 220 K is shown in **Figure 64** (top), a dark-field, optical microscopy montage of a full section of the droplet. Within this image, some directionality appears to remain – with the grain structure transitioning from fine equiaxed to large elongated grains from right to left (approximately). This is confirmed by the inset {111} pole figure, containing a large number of poles which are mostly confined to one half of the plot, indicating the presence of a number of individual grains, yet with overall directionality still existing. The region of high reflection in the centre is due to a large amount of porosity present in this region. The underlying substructure of this droplet is mostly dendritic, though some of the small equiaxed grains appear devoid of any substructure. However, the substructure in areas which are not grain refined (where large elongated grains are observed) is distinctly dendritic seaweed-like in certain areas. This substructure is shown in the enhanced DIC micrograph (**Figure 64** (bottom)) of the approximate area outlined in **Figure 64** (top). Since a global transformation to a fine-grained equiaxed structure has not been observed, this is not considered to be a fully grain-refined

sample. However, this droplet may represent some intermediate stage in the spontaneous grain refinement process, in which case it looks like the growth of dendritic seaweed is playing some part.

5.4.1.3. Conclusion

With increasing undercooling (and therefore solidification velocity), a number of microstructural transitions and novel microstructural features have been observed. At the lowest undercoolings, <100>-oriented growth gives rise to single-grain dendritic samples. With increasing undercooling, a transition to a finer, equiaxed grain structure occurs via a recrystallisation mechanism. At intermediate undercoolings, large-grained growth returns, consisting of the twinned and multiply-twinned growth of mixed-orientation (<100> and <111> type) dendrites, and novel dendritic seaweed 'branches'. Within this range, eightfold growth is observed at low undercooling and sixfold growth at high undercooling. Beyond this range a further transition to coarse-grained structures is seen, in which mixed-morphology dendrites exist. This transition appears to be coincident with the suggested positive break in the velocity-undercooling relationship. This indicates a possible transition in growth mode beyond this point, though the original growth structure is no longer present and thus the growth mode cannot be confirmed microstructurally. Finally, at the highest undercoolings achieved, an equiaxed-to-elongated grain microstructure is observed, which may be an intermediate in the spontaneous grain refinement process. Since some of the substructure in the non-grain refined regions appears to consist of dendritic seaweed, it appears that this morphology may be involved in the spontaneous grain refinement phenomenon.

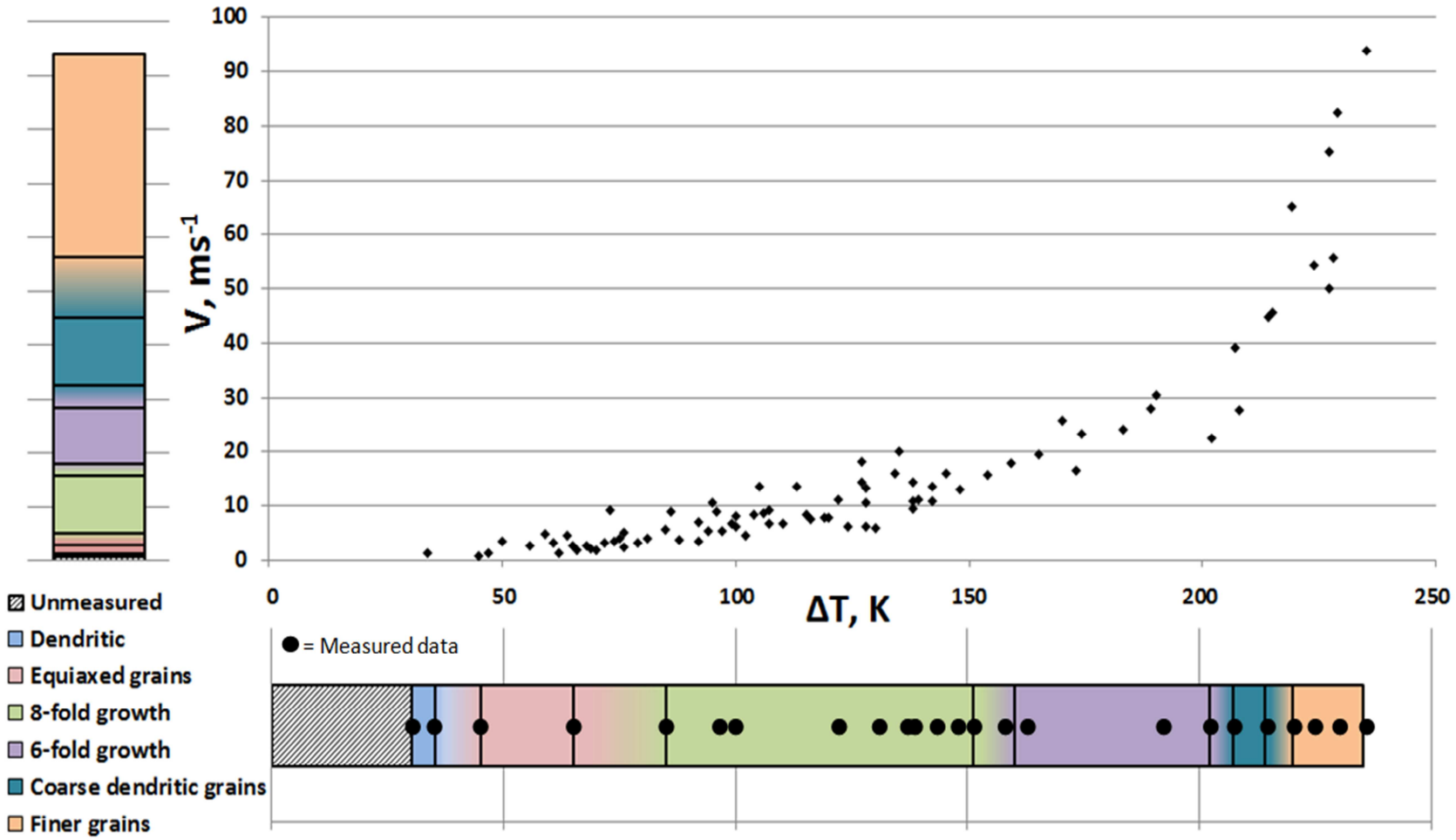

Figure 51 Velocity-undercooling relationship and observed growth transitions with increasing undercooling and growth velocity for the Cu-8.9wt.%Ni alloy. Regions of shaded colour gradients indicate the uncertainty in the positions of the transitions.

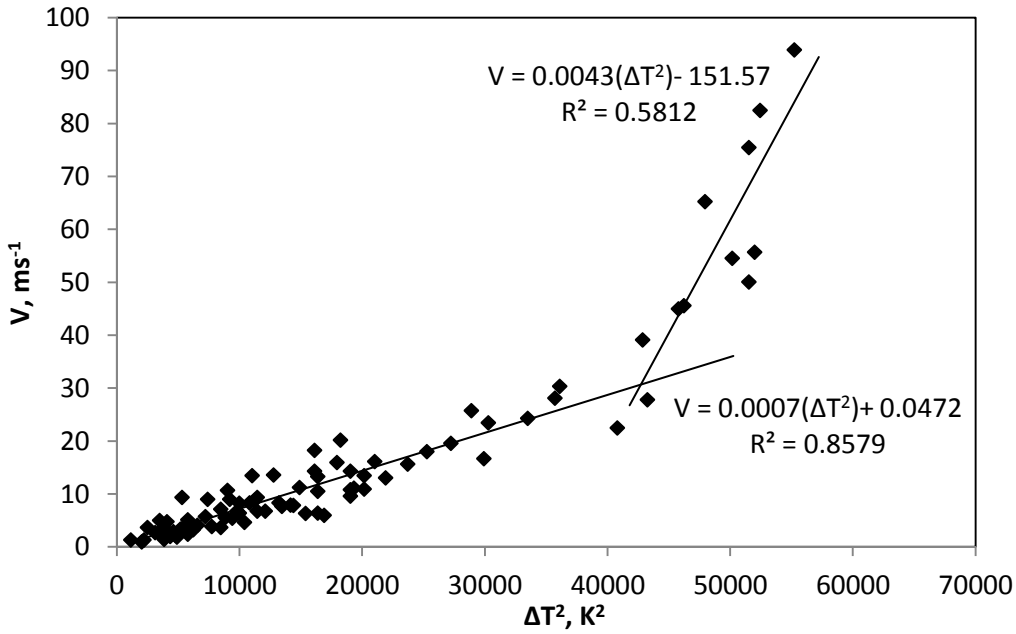

Figure 52 V - ΔT^2 relationship for the Cu-8.9wt.%Ni alloy, showing two distinct regimes with a break occurring at an undercooling of $\Delta T \approx 207$ K.

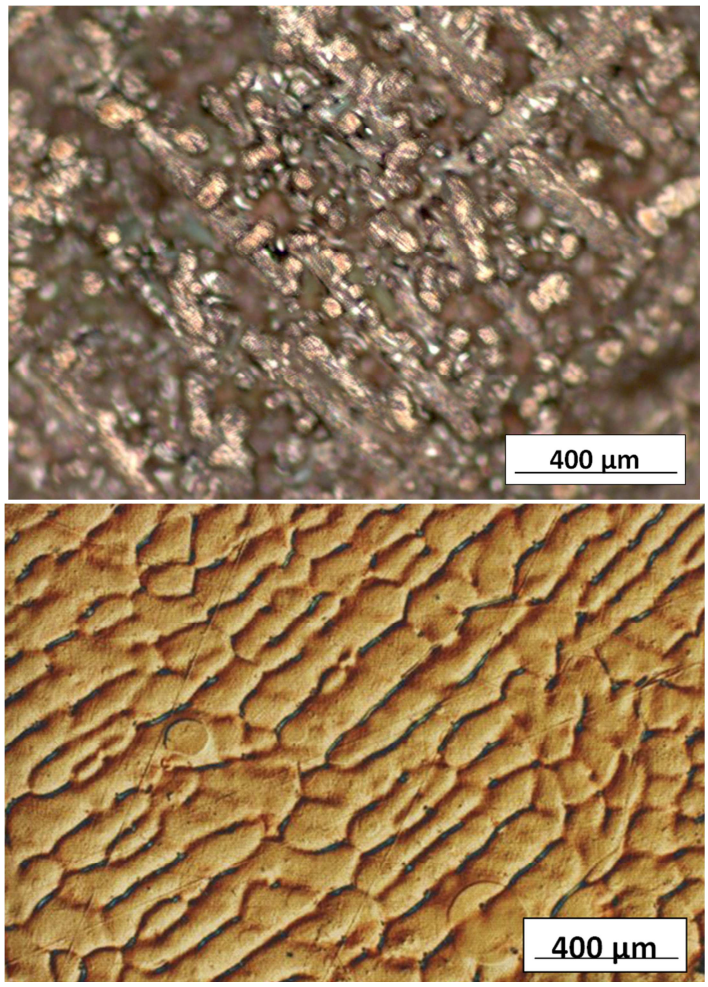

Figure 53 (**Top**) dendrites observed on the droplet surface and (**bottom**) bright field light microscope image of an etched random section taken from a Cu-8.9wt.%Ni droplet undercooled by $\Delta T = 35$ K.

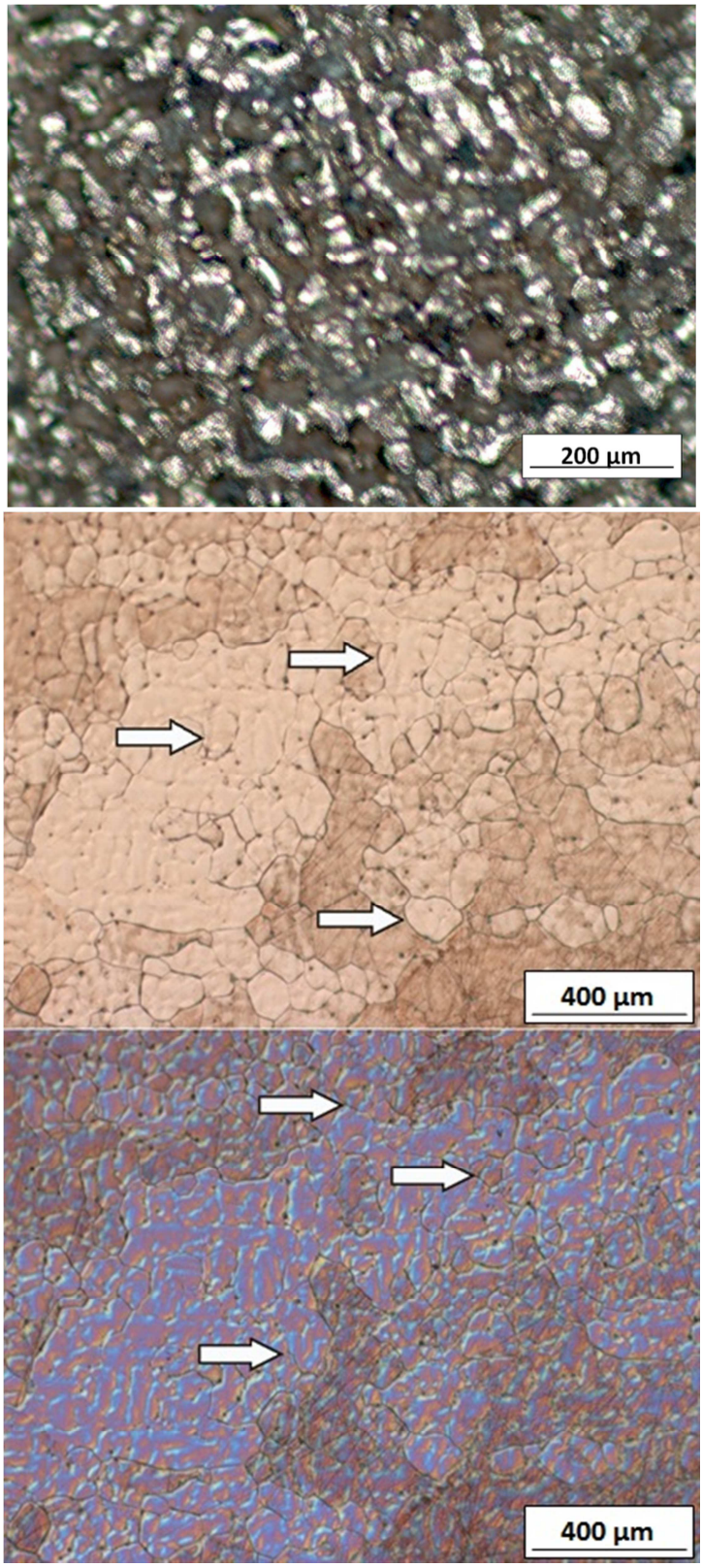

Figure 54 Light microscope images of a randomly sectioned and etched Cu-8.9wt.%Ni sample undercooled by ΔT = 65 K: (**top**) dendritic surface structure **(middle)** bright field image of the grain structure showing large equiaxed grains consisting of smaller subgrains and curved grain boundaries (indicated by the arrows) and **(bottom)** DIC image of the same area showing underlying dendritic substructure which crosses the grain boundaries (as indicated by the arrows).

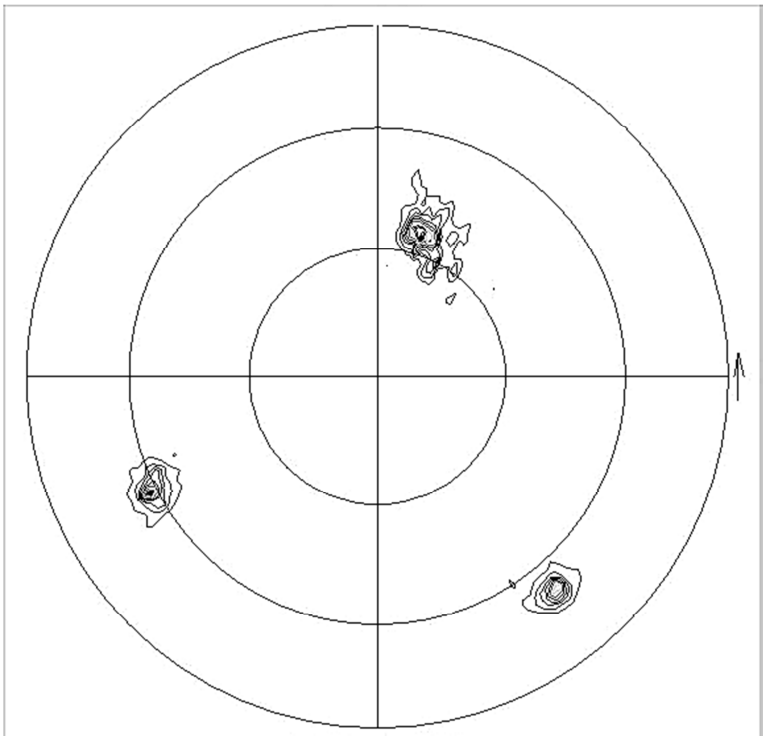

Figure 55 {200} pole figure taken from the ΔT = 65 K, Cu-8.9wt.%Ni droplet (**Figure 54**).

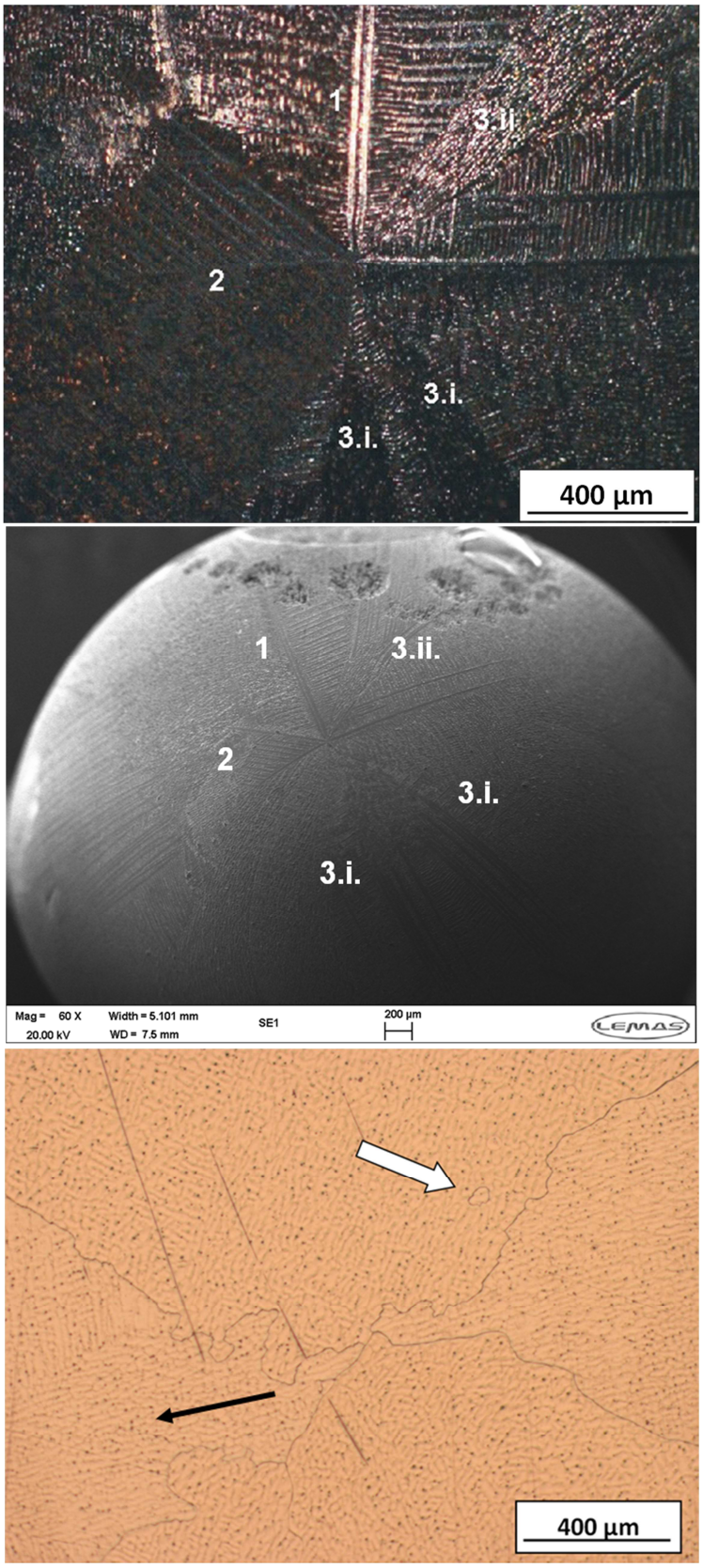

Figure 56 (**Top**)Through-focused light microscope image and (**middle**) SEM secondary electron image of the nucleation point visible on the surface of a Cu-8.9wt.%Ni droplet undercooled by ΔT = 139 K, showing eightfold growth. (**Bottom**) shows large grained interior microstructure consisting of mixed dendrite/seaweed growth, where the black arrow indicates the direction of growth of some of the seaweed microstructure, and wavy grain boundaries. White arrow indicates a 'floating grain'.

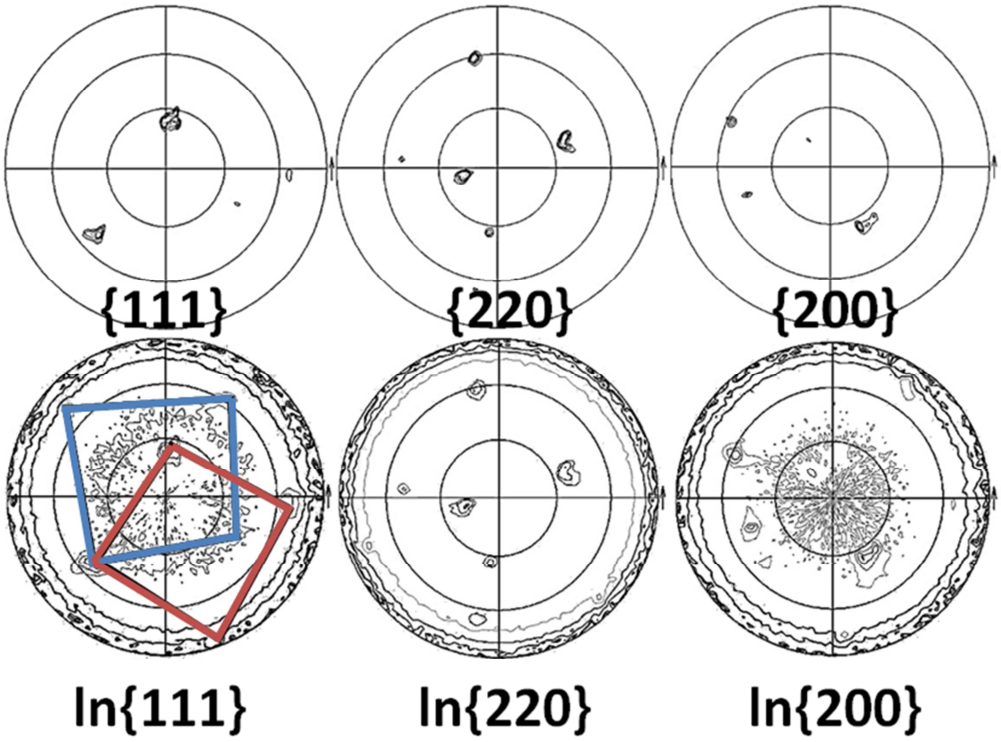

Figure 57 Linear and log-scale pole figures taken from the Cu-8.9wt.%Ni undercooled by ΔT = 139 K (shown in **Figure 56**).

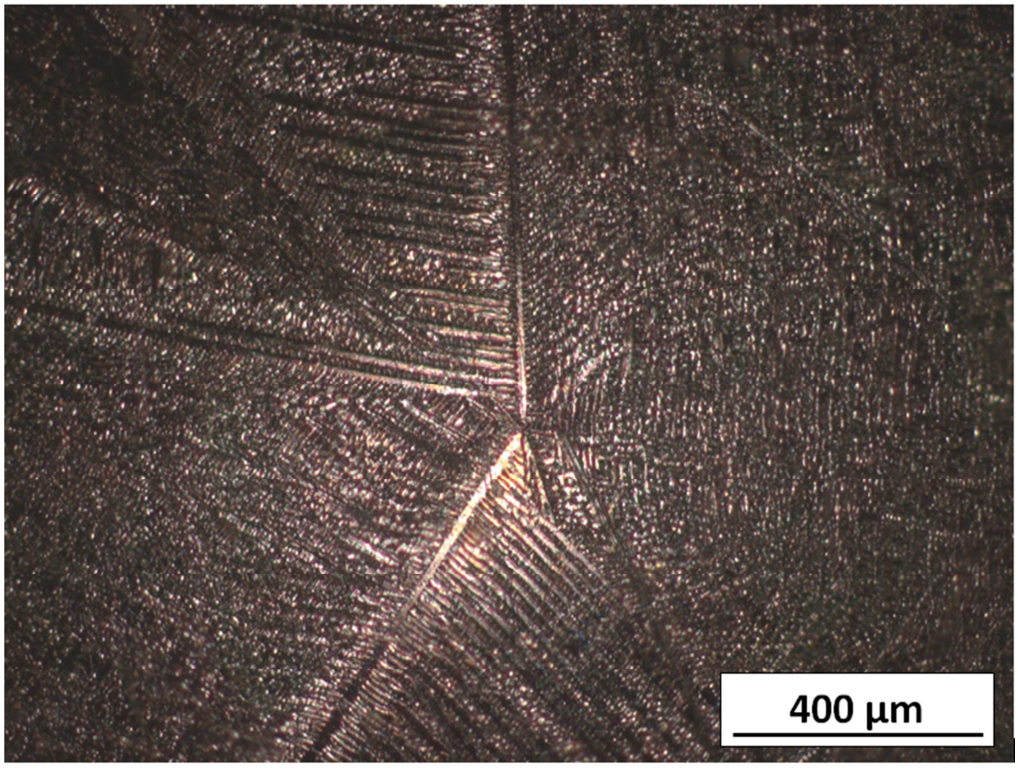

Figure 58 Through-focused light microscope image of the nucleation point observed on the surface of a Cu-8.9wt.%Ni droplet undercooled by ΔT = 159 K.

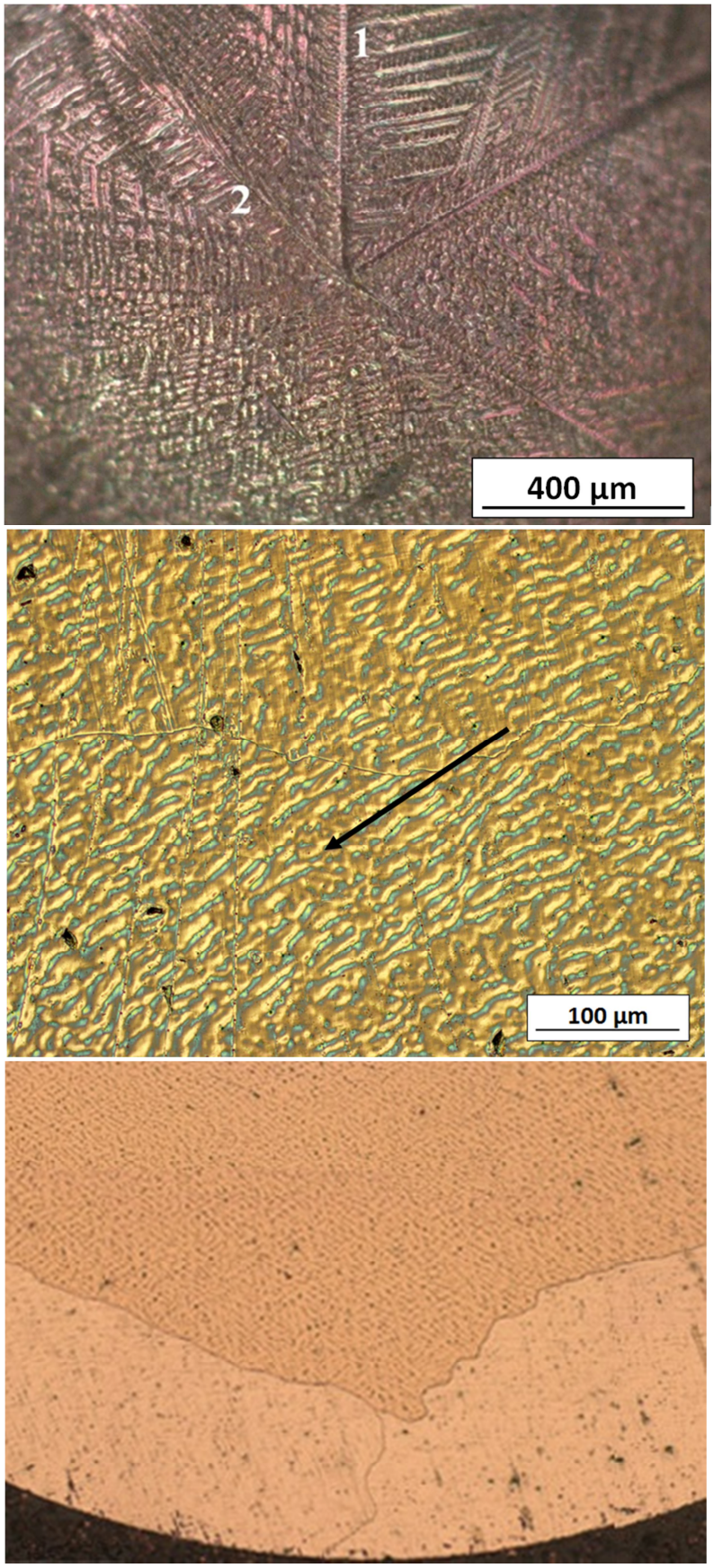

Figure 59 (**Top**) Through-focused light microscope image of the six-fold nucleation point observed on the surface of a Cu-8.9wt.%Ni droplet undercooled by ΔT = 161 K, (**middle**) interior microstructure (DIC image) showing part of a fine wavy grain boundary and dendritic/seaweed substructure which appears to traverse the grain boundary (indicated by the black arrow) and (**bottom**) triple junction between the three grains present.

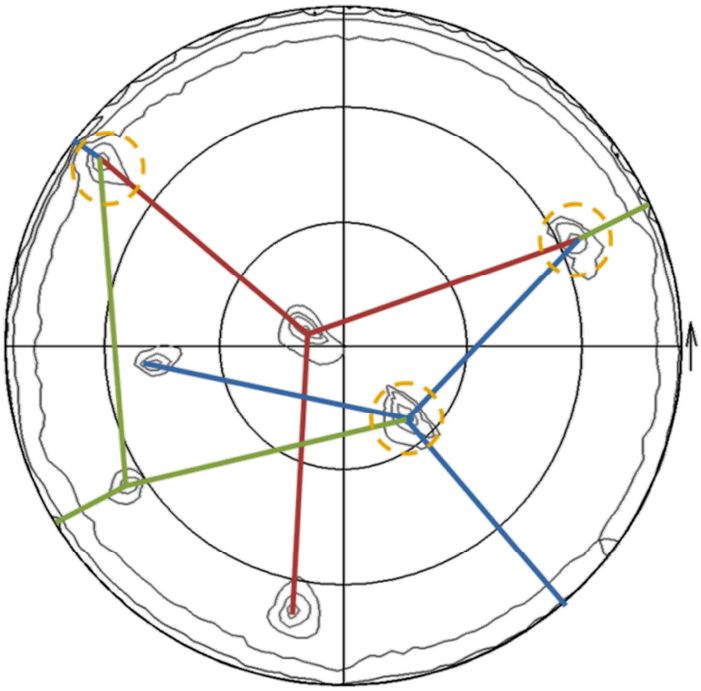

Figure 60 Log{111} pole figure taken from the sixfold sample shown in **Figure 59**, indicating the presence of the grains (three colours) and three shared poles (yellow circles).

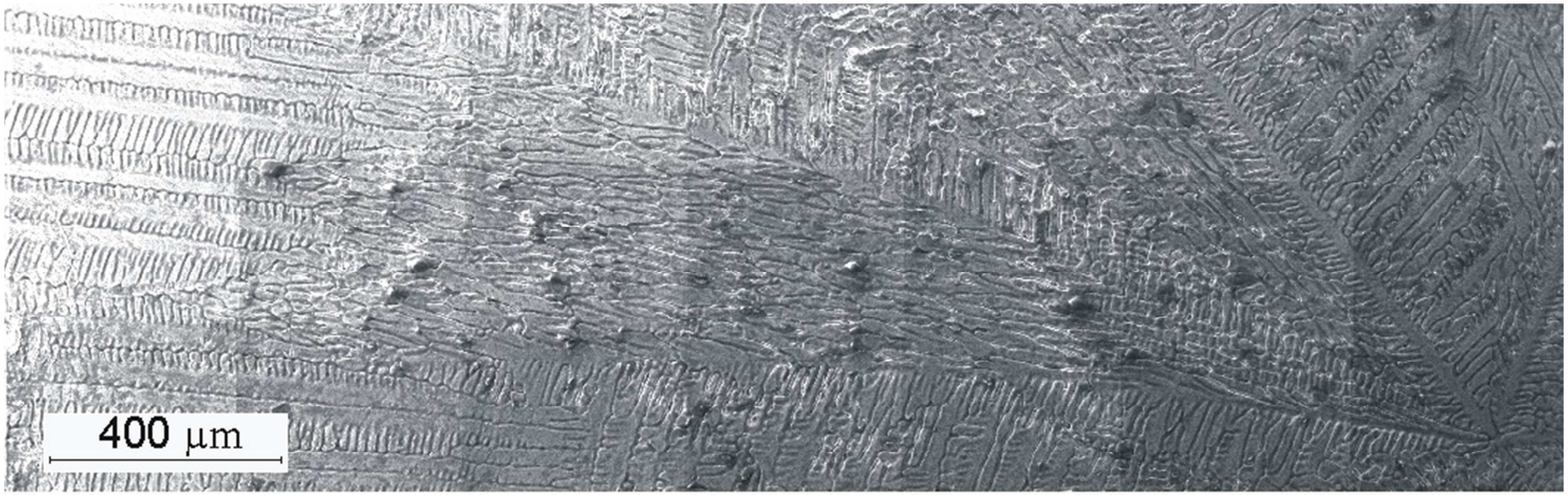

Figure 61 SEM SE montage image of the seaweed branch identified as feature '2' in **Figure 59.**

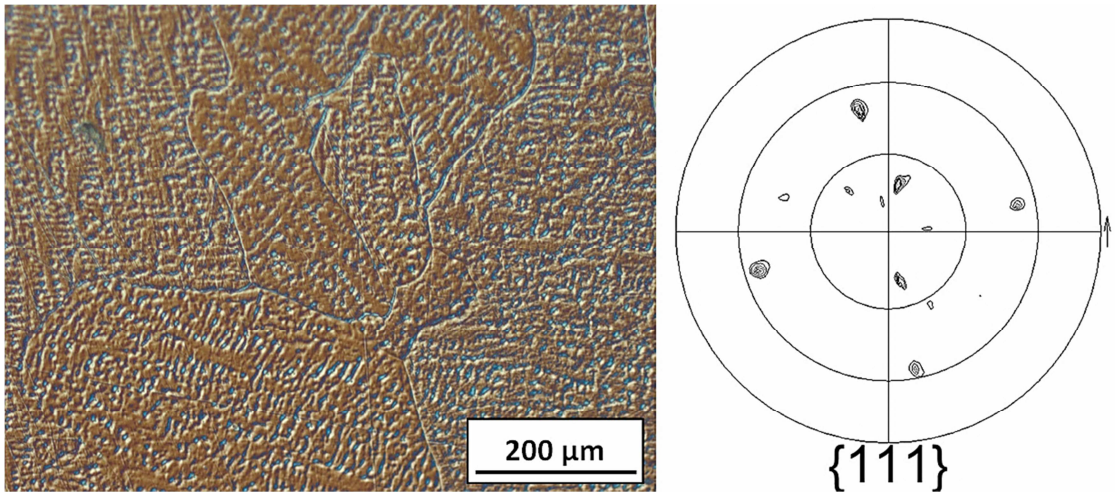

Figure 62 (Left) DIC light microscope image of a randomly sectioned and etched Cu-8.9wt.%Ni droplet undercooled by ΔT = 214 K and **(right)** corresponding {111} pole figure indicating the presence of several unrelated grains.

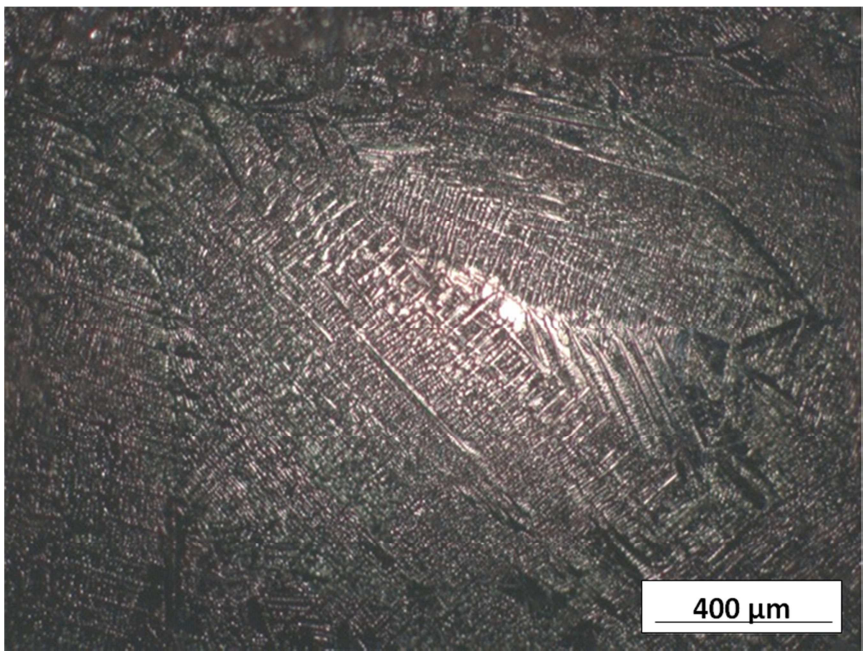

Figure 63 Light microscope image of the dendritic morphologies observed on the surface of a Cu-8.9wt.%Ni sample undercooled by ΔT = 214 K.

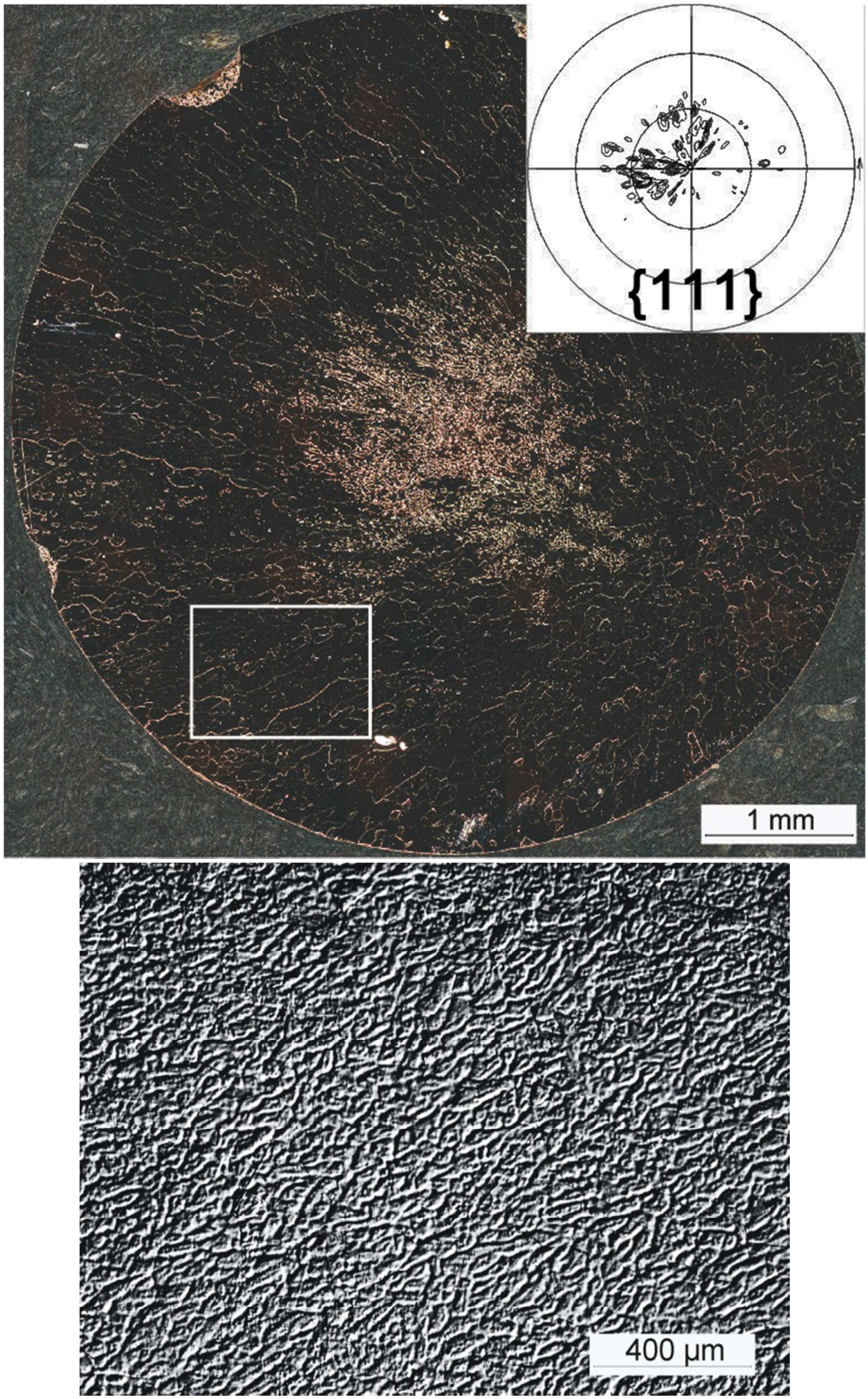

Figure 64 (Top) Dark Field montage micrograph of a randomly sectioned and etched Cu-8.9wt.%Ni droplet undercooled by ΔT = 220 K, with inset {111} pole figure and **(bottom)** enhanced DIC micrograph of the dendritic seaweed substructure observed in the approximate region outlined in the top image.

5.4.2. Cu-3.98 wt% Ni

5.4.2.1.1. Velocity-undercooling relationship

The velocity-undercooling relationship and growth transitions defined for the Cu-3.98 wt.% Ni alloy are shown in **Figure 65**. Maximum undercoolings of up to ΔT = 216 K and velocities up to 93 m s^{-1} were achieved. A power law trend is fitted to the full data set, which represents a good fit to the measured velocity-undercooling relationship up to an undercooling of around $\Delta T \approx 200$ K (or $V \approx 40$ m s^{-1}), beyond which a positive departure of the data occurs. As with the Cu-8.9 wt.% Ni alloy, the V- ΔT^2 plot displays a clear break from the initial trend; with a shift in the trend of the data to lower undercoolings observed with decreasing Ni content (**Figure 66**).

5.4.2.1.2. Microstructural and texture evolution with increasing undercooling

The break in the velocity-undercooling relationship is, again, indicative of some transition in growth mode beyond this point. Microstructural and texture analysis of samples solidified over the full range of undercooling reveal the occurrence of a number of growth transitions, including a spontaneous grain refinement transition which is coincident with the suggested break in the trend. The evolution of microstructure with increasing undercooling will therefore be presented in this section, with reference to each defined growth regime.

5.4.2.1.3. Grain refined from $\Delta T \leq 36$ K to $\Delta T < 53$ K

Undercoolings of less than around ΔT = 36 K did not display any visible recalescence; hence measurements below this point could not be recorded or assessed. A sample undercooled by ΔT = 36 K (**Figure 67**), reveals a (relatively) grain-refined microstructure, indicating that the first region of grain refinement for this alloy occurs at lower undercoolings than for the Cu-8.9 wt.% Ni alloy. In line with the transitions observed in the more concentrated alloy and with that observed for most alloy systems, it may be assumed that stable single or large-grained dendritic growth precedes the grain refinement. The absence of any grain refinement mechanism is almost certainly true for very low undercoolings, however the exact value of undercooling for the onset of the first spontaneous grain refinement transition cannot be confirmed microstructurally.

In this instance, the grain refinement mechanism appears to differ with respect to the recrystallisation process observed in the more concentrated alloy. Within the centre of the

droplet, shown by the bright field image (**Figure 67** (top)), large parent grains containing small subgrains are again present. However, in this case there is no underlying continuous dendritic substructure evident. Instead, there appear to be dendrite 'cores' present within the subgrains, and large dendrite fragments are evident at the surface of the droplet (**Figure 67** (middle)), indicative of a dendrite fragmentation mechanism. The corresponding log-scale {200} pole figure plot (**Figure 67** (bottom)) exhibits at least three sets of unrelated poles, indicating the presence of three or more separate grains and confirming the discontinuity of the substructure between them.

5.4.2.1.4. Single-grained orthogonal dendritic droplets at 53 K ≤ ΔT ≤ 72 K

With increased undercooling, droplets collected at ΔT = 53 and 61 K comprise a single grain and exhibit an orthogonal dendritic substructure, indicative of <100> oriented growth. An example of the microstructure observed in a sample undercooled by ΔT = 53 K is shown in **Figure 68**, along with the corresponding {200} pole figure. Only one set of poles is observed on the pole figure, confirming the presence of a single large grain.

5.4.2.1.5. Large, twinned grains, mixed-orientation dendrites and seaweed branches at 72 K ≤ ΔT ≤ 183 K

A sample undercooled by ΔT = 72 K indicates the presence of a further microstructural transition occurring somewhere between 61 K < ΔT ≤ 72 K. Up to (at least) ΔT = 183 K, nucleation points were evident on the surface of the droplets, and displayed dendrites of mixed-orientation and dendritic seaweed branches - much like the structures observed in the eightfold and sixfold growth regimes of the more concentrated alloy. However, in contrast to the Cu-8.9 wt.% Ni alloy, no distinct eightfold-to-sixfold transition is observed and the symmetry of the growth patterns is much less apparent. **Figure 69** (top) shows the nucleation point observed on the surface of a droplet undercooled by ΔT = 100 K. In this instance, solid growth has nucleated close to the edge of a bubble in the flux, which has left an imprint in the surface of the metal – the edge of which is roughly outlined in white on the image. Dendrites and <100>-type seaweed branches (labelled 1-3) with orthogonal outer secondary branches can be seen emanating from the nucleation point. On sectioning the sample (**Figure 69** (bottom)), there appear to be at least two large grains present, consisting of both dendritic and dendritic seaweed branch substructures. A wavy grain boundary between the two grains suggests that grain boundary migration has taken place. Texture analysis (**Figure 70**) confirms

the presence of at least two grains, with two sets of poles indicated in both the log scale {200} and {111} pole figures. A strong pole is located close to the centre of the {200} plot, indicating a possible dominant {100} growth orientation. However, a shared pole is evident in the {111} pole figure, indicating that the grains are twinned about one of the {111} directions. In spite of the observation of <100>-type seaweed branches in the sample, the weak background texture, which was associated with the two types of seaweed identified in Cu-8.9wt.%Ni (Section 5.4.1.2.5), arises on the {111} pole figure, and not in the {200} in this case.

A sample undercooled by a further 48 K (ΔT = 148 K) is shown in **Figure 71**. Once more, the sample has nucleated close to a bubble (outlined) and the growth symmetry is difficult to determine. Five clear primary dendrite branches, exhibiting secondary branches of contrasting orientation, emanate from the nucleation point. The three top branches have grown close to right-angles to one another, suggesting a fourfold, <100>-dominant orientation, whilst the two lower branches have grown at either 53^{o} or 72^{o} to their neighbouring branches, as indicated on **Figure 71** (top), suggesting a sixfold <111>-dominant orientation. A seaweed branch is observed to be growing out from underneath the top 'fourfold' dendrites (as indicated by the arrow). The interior microstructure of this droplet can be seen in **Figure 71** (middle), once again showing large grains consisting of a mixture of dendritic and seaweed microstructures. The grains are separated by wavy boundaries and a small 'floating' grain can be seen close to one of the boundaries, suggesting significant grain boundary migration. Texture analysis (**Figure 72**) indicates the presence of two grains which are twinned about one of the {111} directions. A strong pole at the centre of the plot indicates a dominant <111> orientation.

Within this range of undercooling there are a couple of re-emerging features which are not present in samples observed within the mixed-orientation range of the Cu-8.9wt.%Ni alloy. One of these features can be seen in **Figure 73**, showing the dendrites evident on the surface of a sample undercooled by ΔT = 117 K. Here, feature 1 indicates a multiply-split primary dendrite branch. This structure appears to originate through a similar mechanism to the seaweed branches, with a diverging split primary dendrite branch in which inner secondaries have grown and become near-parallel to the original growth direction. In this case, multiple tip-splitting has not taken place, resulting in the growth of an array of parallel dendrites. This is in contrast to feature 2, showing a seaweed branch which terminates in a similar array of dendrites. Other recurring features can be seen in **Figure 74**, showing the structures observed in a sample undercooled by ΔT = 119 K. Feature 1 shows a straight diverging split primary branch, in which the inner secondaries have grown orthogonally into the diverging split, this time not becoming parallel to the original growth direction. Feature 2, however, shows another diverging split primary branch, which appears bowed and where inner secondaries

grow non-orthogonal to the primary split branch. This feature displays a greater likeness to the seaweed branches; however multiple tip-splitting is not evident in this case. By contrast to the structures observed in the more concentrated alloy, there therefore appears to be a greater spectrum of dendrite-to-seaweed branch morphologies possible.

There also appears to be a greater amount of porosity present in this alloy. Within both alloys, regions near the centre of the droplet exhibit a large amount of porosity, revealing the skeleton of a dendrite or dendritic-seaweed branch (see e.g. **Figure 71** (bottom)). Since the shape of the pores outline a dendritic skeleton, this suggests that the porosity originates from solidification shrinkage; as opposed to the evolution of gas, where spherical pores might be expected. The position of the regions of porosity suggests that the last region of the droplet to solidify was therefore the droplet centre; leading to the conclusion that dendrite growth initially proceeded at the surface of the droplet, as discussed in Chapter 3.6.1. An analysis of the porosity patterns may help to reveal more detailed information about the solidification sequence, and would be interesting to investigate further in future work.

5.4.2.1.6. Grain refined at $\Delta T > 183$ K

Above an undercooling of $\Delta T \approx 183$ K and by $\Delta T = 201$ K, an abrupt decrease in grain size is observed, coincident with the suggested break in v - ΔT relationship. The surface structure of these samples (**Figure 75** (top)) exhibits fine grains of a fragmented dendrite morphology. The interior microstructure (**Figure 75** (middle)) reveals an average equiaxed grain size of around 200 μm in diameter. The substructure of the grains appears dendritic, but the morphology of the dendrites is unclear. This substructure appears to traverse some, but not all, of the grain boundaries. Texture analysis indicates the loss of any directionality and the presence of a large number of randomly-oriented grains, with a number of poles distributed over the full Φ and Ψ range. In contrast to the high undercooling samples observed in the concentrated alloy, a global transformation to fine equiaxed grains has occurred and this may therefore be classed as spontaneous grain refinement.

5.4.2.2. Conclusion

Once more, a number of microstructural transitions have been observed with increasing undercooling in the Cu-3.98 wt.% Ni. However, there are a few key differences in the transitions and microstructures observed between the Cu-8.9 wt.% Ni and the Cu-3.98 wt.% Ni alloys. Firstly, the observed <100>-oriented growth regime is stable to much higher degrees of undercooling in comparison to the more concentrated alloy, extending beyond the first, low-

undercooling region of grain refinement. Possibly as a result of this, the low-undercooling grain refinement regime appears to have arisen from a dendrite-fragmentation mechanism, in contrast to the recrystallisation mechanism observed in the Cu-8.9 wt.% Ni alloy. With further undercooling, a transition to a large-grained structure containing dendrites of mixed orientation and seaweed branches is observed, akin to the eightfold and sixfold regimes of the more concentrated alloy. However, in this alloy no distinct eightfold-to-sixfold transition in growth symmetry is observed, and the symmetry of the growth patterns is much more ambiguous. An increasing dominance in {111}-oriented growth is, however, indicated by texture analysis whereby a pole is observed central to the {200} plot at low undercooling, whilst at higher undercooling the {111} plot exhibits a strong pole at its centre. In further contrast to the more concentrated alloy, there appears to be a wider spectrum of the 'seaweed branch' morphology present for this alloy. Each structure appears to originate from a diverging split primary dendrite branch initially, before developing inner secondary branches, which range in morphology from dendritic to seaweed. At the highest undercoolings achieved a spontaneous grain refinement transition is observed to be coincident with a possible break in the velocity-undercooling relationship. In contrast to the Cu-8.9 wt.% Ni alloy, a transitional regime of intermediate grain size is not observed in this instance. Grain refined droplets had a fragmented-dendrite structure evident on their surface, suggesting that grain refinement arises from some dendrite fragmentation mechanism.

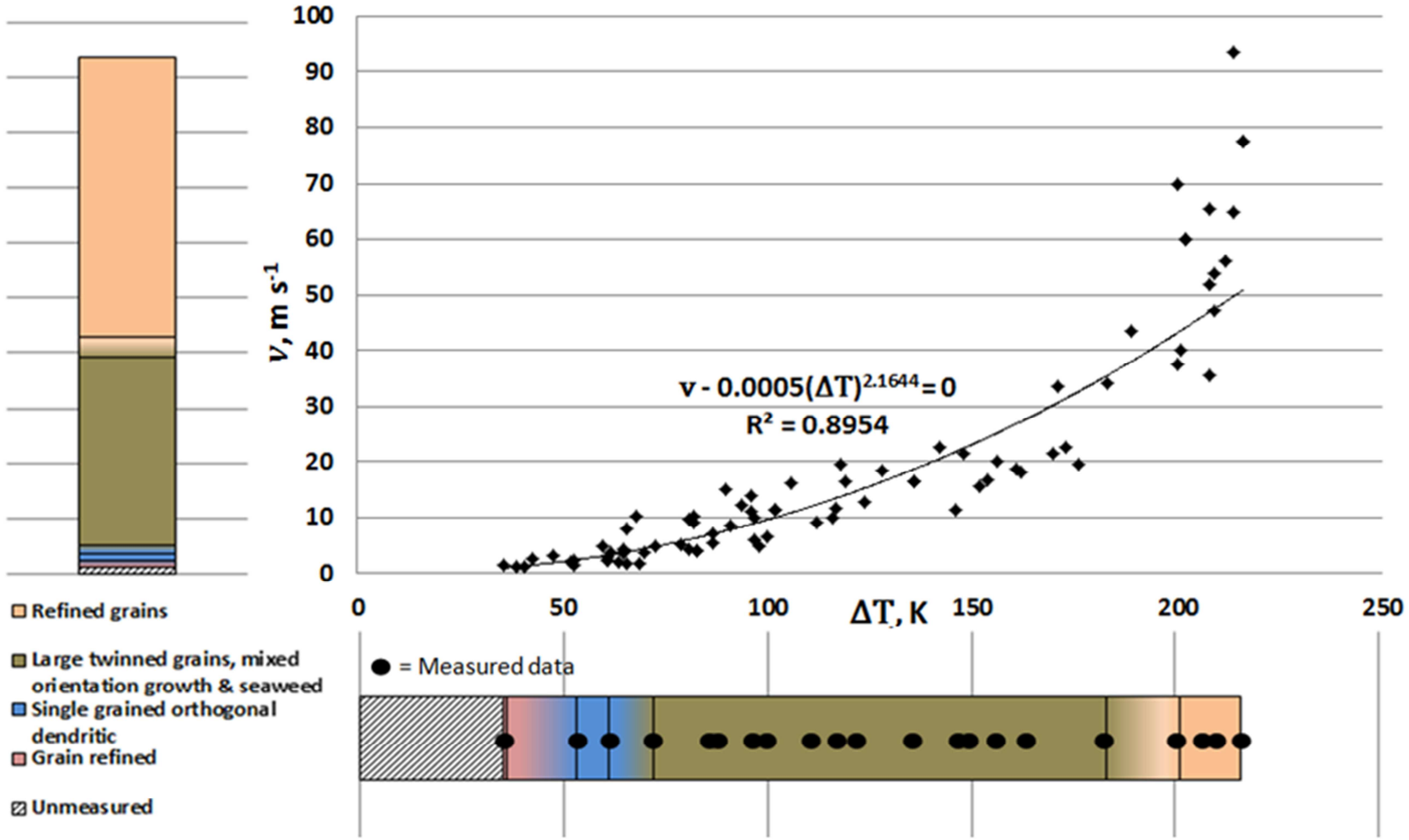

Figure 65 Velocity-undercooling relationship and observed growth transitions with increasing undercooling and growth velocity for the Cu-3.98 wt.% Ni alloy. Regions of shaded colour gradients indicate the uncertainty in the positions of the transitions.

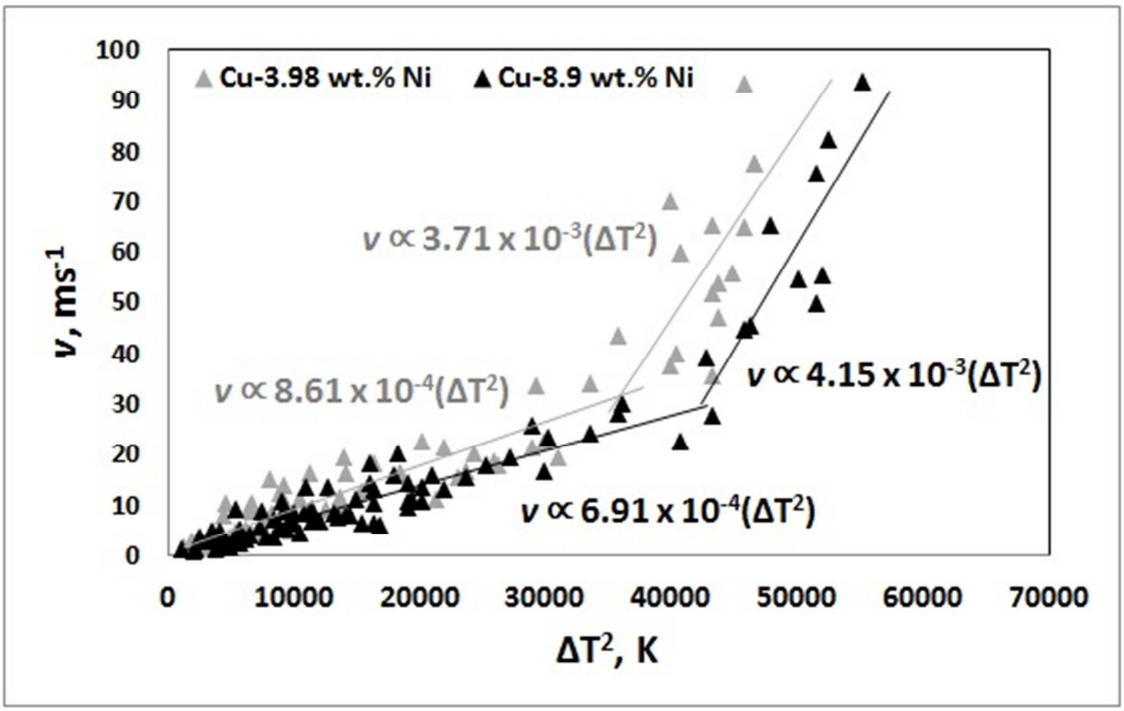

Figure 66 v - ΔT^2 relationship for the Cu-3.98 wt.% Ni alloy in comparison to the Cu-8.9 wt.% Ni alloy; showing the similarity between the two data sets and the shift in the data as a function of Ni concentration.

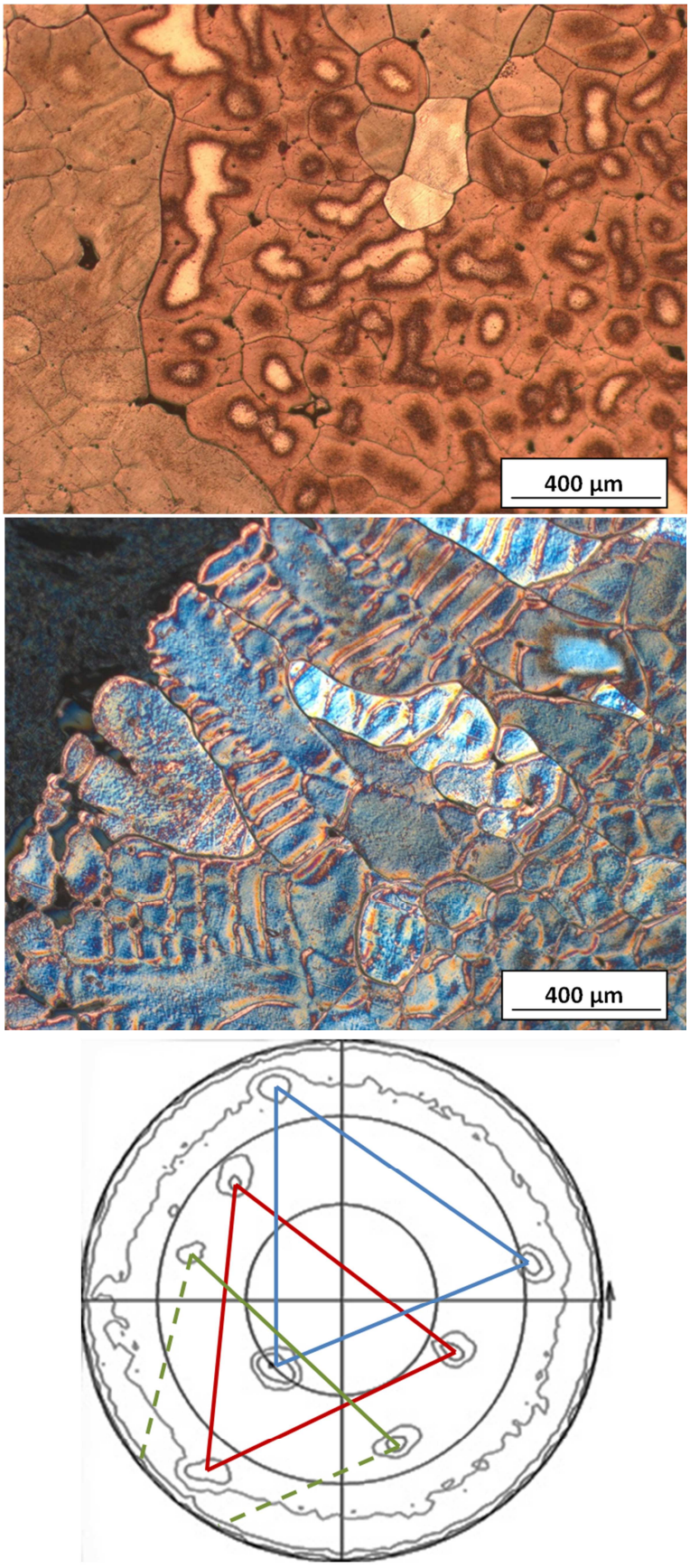

Figure 67 Optical micrographs of a randomly sectioned and etched Cu-3.98 wt.% Ni sample undercooled by ΔT = 36 K. **(Top)** Bright field image of droplet centre, **(middle)** DIC image of droplet edge, **(bottom)** corresponding log-scale {200} pole figure.

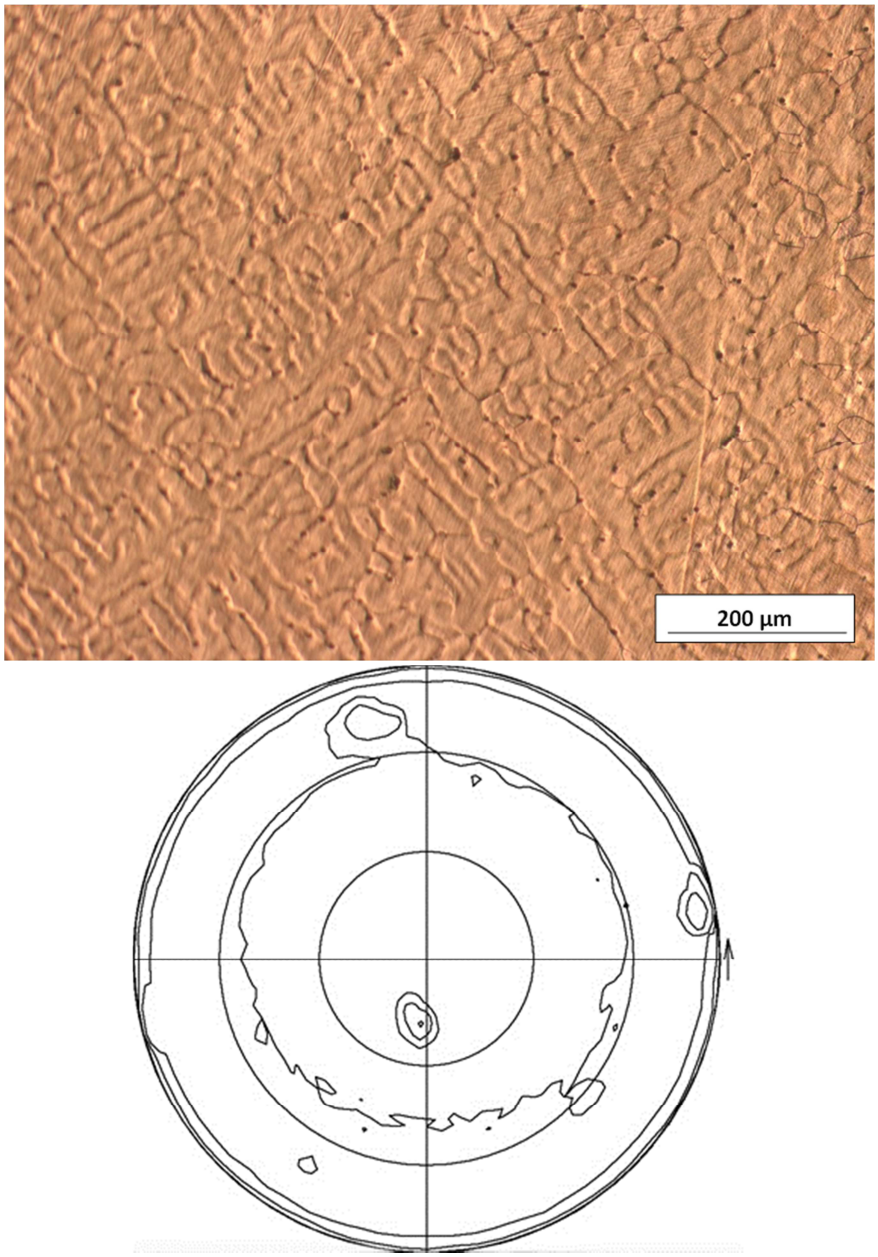

Figure 68 (Top) Optical micrograph of a randomly sectioned and etched Cu-3.98 wt.% Ni sample undercooled by ΔT = 53 K and **(bottom)** corresponding {200} pole figure.

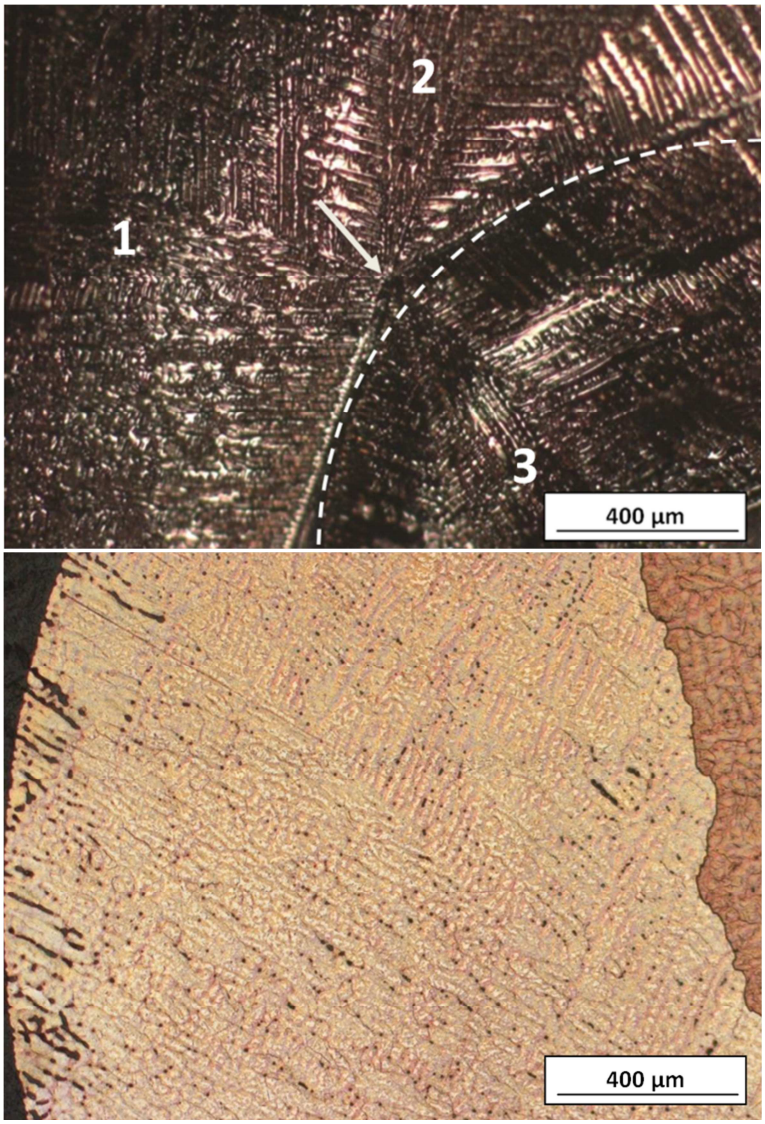

Figure 69 (Top) Light microscope image of the nucleation point (indicated by arrow) observed on the surface of a Cu-3.98 wt.% Ni sample undercooled by ΔT = 100 K, with solid growth nucleated on the edge of a bubble (outlined by white dashed line) and three seaweed branches, labelled 1-3, present. **(Bottom)** Bright field image of the interior microstructure of the droplet, after sectioning parallel to the growth direction and etching.

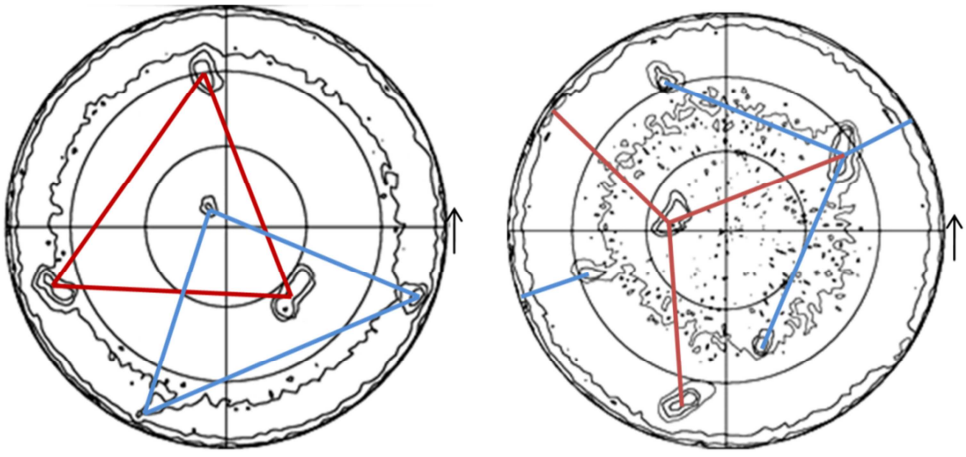

Figure 70 Log-scale {200} **(left)** and {111} **(right)** pole figures corresponding to the ΔT = 100 K sample shown in **Figure 69**, showing the presence of two grains (differentiated in red and blue), which are twinned about one of the {111} planes.

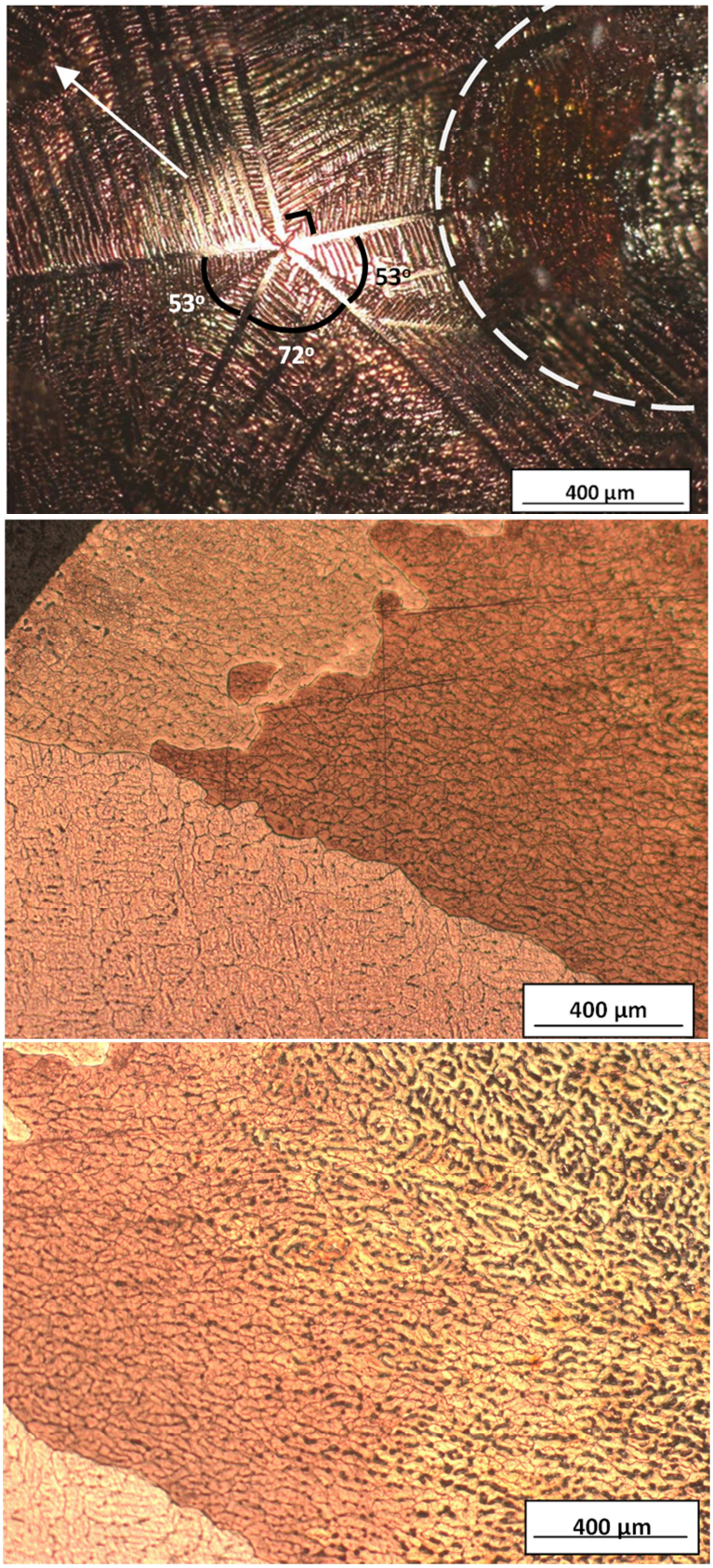

Figure 71 (Top) Light microscope image of the nucleation point observed on the surface of a Cu-3.98 wt.% Ni sample undercooled by ΔT = 148 K with five primary dendrite branches and a seaweed branch (arrow) nucleated close to a bubble (outlined by white dashed line). **(Middle & bottom)** Bright field images of the droplet, sectioned parallel to the growth direction and etched.

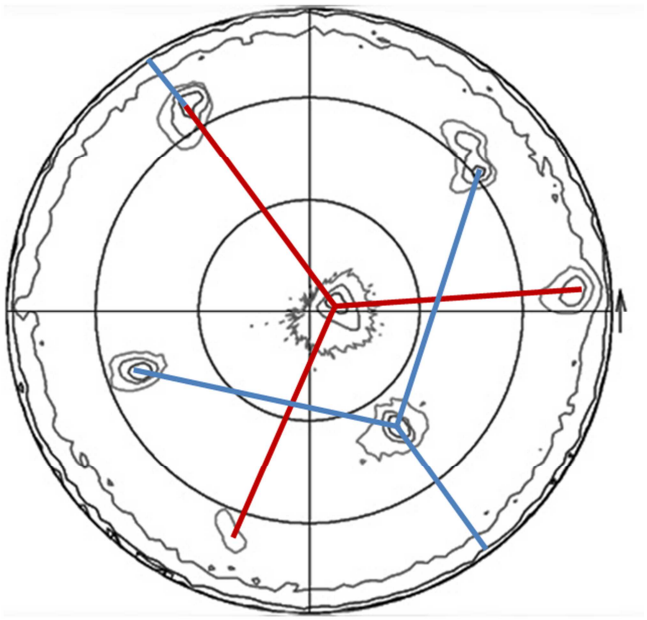

Figure 72 Log-scale {111} pole figure, taken from the Cu-3.98 wt.% Ni sample undercooled by ΔT = 148 K shown in **Figure 71**.

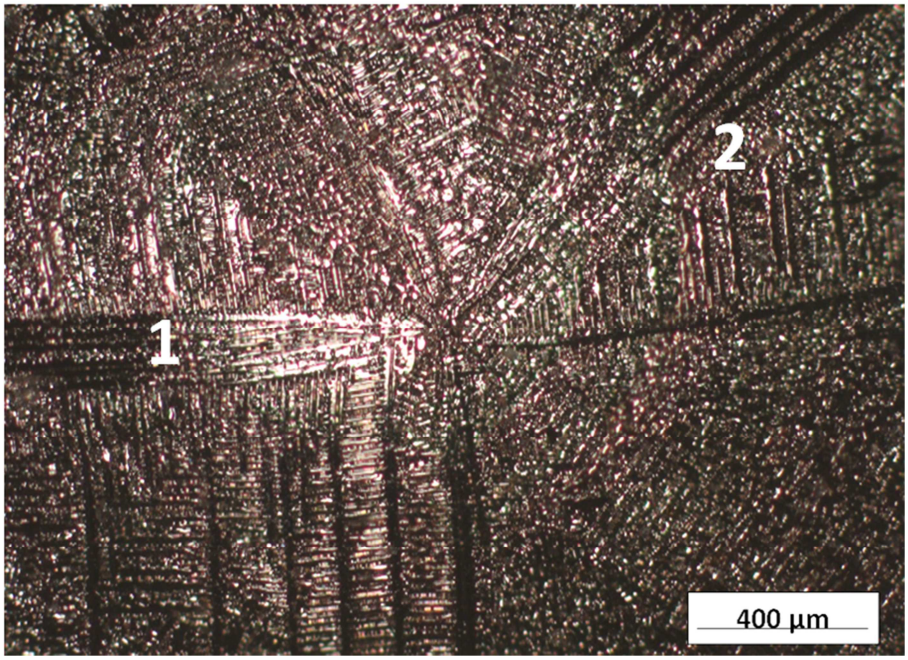

Figure 73 Nucleation point on the surface of a Cu-3.98 wt.% Ni droplet undercooled by ΔT = 117 K, showing a multiply-split primary dendrite branch (feature 1) and a <100>-type seaweed branch (feature 2).

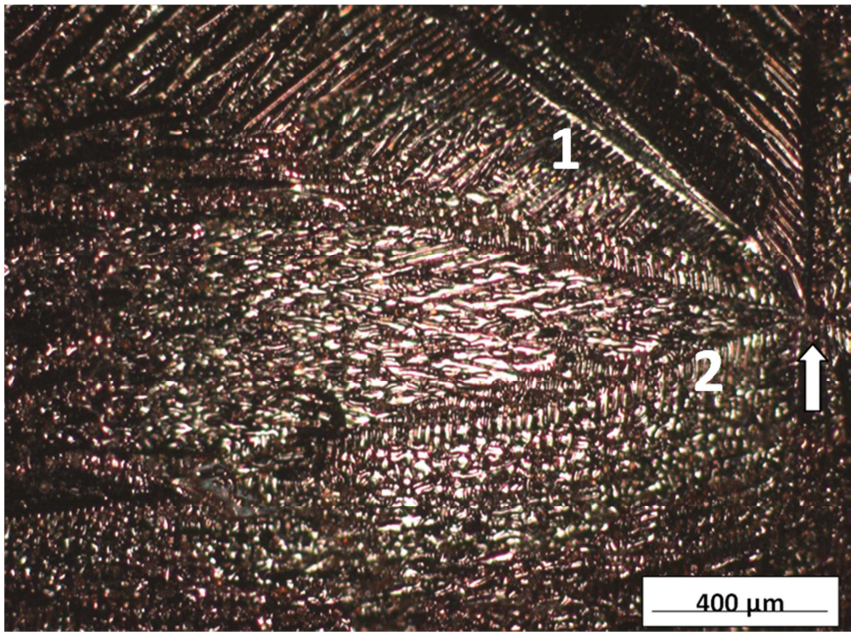

Figure 74 Nucleation point (indicated by arrow) on the surface of a Cu-3.98 wt.% Ni droplet undercooled by ΔT = 119 K, showing two diverging split primary branches (features 1 and 2).

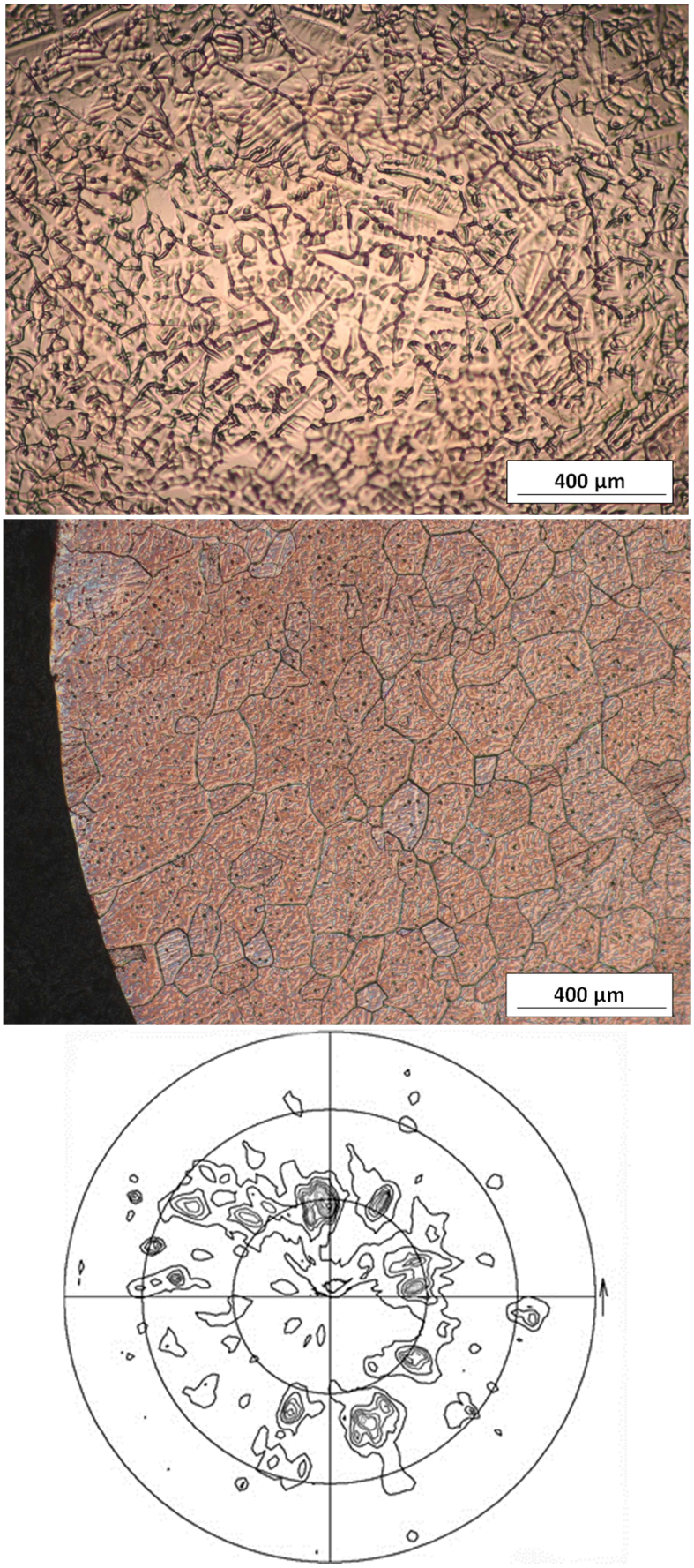

Figure 75 (Top) Light microscope image of the fragmented dendritic structure observed on the surface of a Cu-3.98 wt.% Ni sample undercooled by ΔT = 216 K, **(middle)** DIC image of the droplet grain structure after random sectioning and etching, **(bottom**) corresponding {111} pole figure.

5.5. EBSD analysis

EBSD analysis was performed on a sectioned and polished Cu-8.9 wt.% Ni droplet undercooled by ΔT = 135 K, using an accelerating voltage of 30 kV and a working distance of 17 mm. Prior microstructural analysis indicated the existence of very large grains, hence a stage scanning mode and a large step size of 25 µm were used in order to map the full sample cross-section within a reasonable period of time. A DIC montage image of the droplet microstructure observed over the full cross-section investigated is shown in **Figure 76**. It is evident from inspection of this image that the substructure consists of a mixture of fine dendrites and dendritic seaweed-like microstructures, including the observed seaweed 'branches'. Unlike most of the samples observed within the corresponding 'eightfold' regime for this alloy, no nucleation point was visible on the sample surface. It appears from the DIC image that solidification was nucleated close to the centre of the sample in this instance, and hence grains appear to radiate outwards from a point near the centre.

The resulting EBSD orientation map is shown in **Figure 77**, where different grain orientations are represented by different colours and can be related to the corresponding pole figures shown in **Figure 79**. In this case, the large neighbouring purple and green grains seen radiating from the centre of the droplet indicates that the misorientation between them is large. This is confirmed by the corresponding grain boundary misorientation map shown in **Figure 78**, in which misorientations of over 10 % are plotted and thus the boundaries between the grains constitute high angle grain boundaries (HAGB). These four main grains appear to alternate in orientation around the central nucleation point. XRD pole figures taken from this sample (Figure **80**) indicate the presence of two or three main grain orientations, with four shared poles evident on the log{111} pole figure and one shared pole evident on the log{220} pole figure. There is therefore some form of multiple-twinning occurring in this sample, which will be discussed in more detail in Section 6.3.

Further large misorientations are observed to be present, with further grains (delineated by HAGB in **Figure 78**) appearing at the perimeter of the droplet. In total there appear to be four separate orientations existing in the sample, represented by purple, green, blue and pink. The pole figures obtained during EBSD analysis (**Figure 79**) indicate, from the multi-coloured nature of the poles, that each grain contains a large amount of misorientation within it. This is most notable in the top right grain of **Figure 77**, where there is some degree of misorientation between one side of the grain (of 'green' orientation) and the other side of the grain, shown in blue, without the occurrence of a complete HAGB. There is some crossover between the two

orientations, which interestingly appears to coincide with the site of a seaweed branch – delineated by the two arrows shown in **Figure 76**. The existence of the seaweed branch may therefore be facilitating a large misorientation within the same grain.

The quality of the orientation map is not sufficient to resolve finer details, and a relatively low indexing rate has been achieved. This will be, at least in part, due to the surface polish of the specimen. A high-quality surface finish was difficult to achieve due to the ductile nature of the alloys and the porosity of the samples. During grinding and polishing, this resulted in the smearing of material into the pores, which later dropped out during polishing and produced scratches in the surface. A limited polishing success has been achieved through the use of ultrasonic cleaning in alcohol between each grinding and polishing steps in order to reduce debris drop-out. Low indexing rates could also be due to the existence of dendritic seaweed substructures, since the continual tip-splitting and bending of the branches during growth may result in distortions of the lattice parameter and hence produce difficulty in indexing the diffraction patterns. Sufficient indexing has, however, been achieved in order to confirm the mixed-orientation nature of samples observed within the eightfold regime.

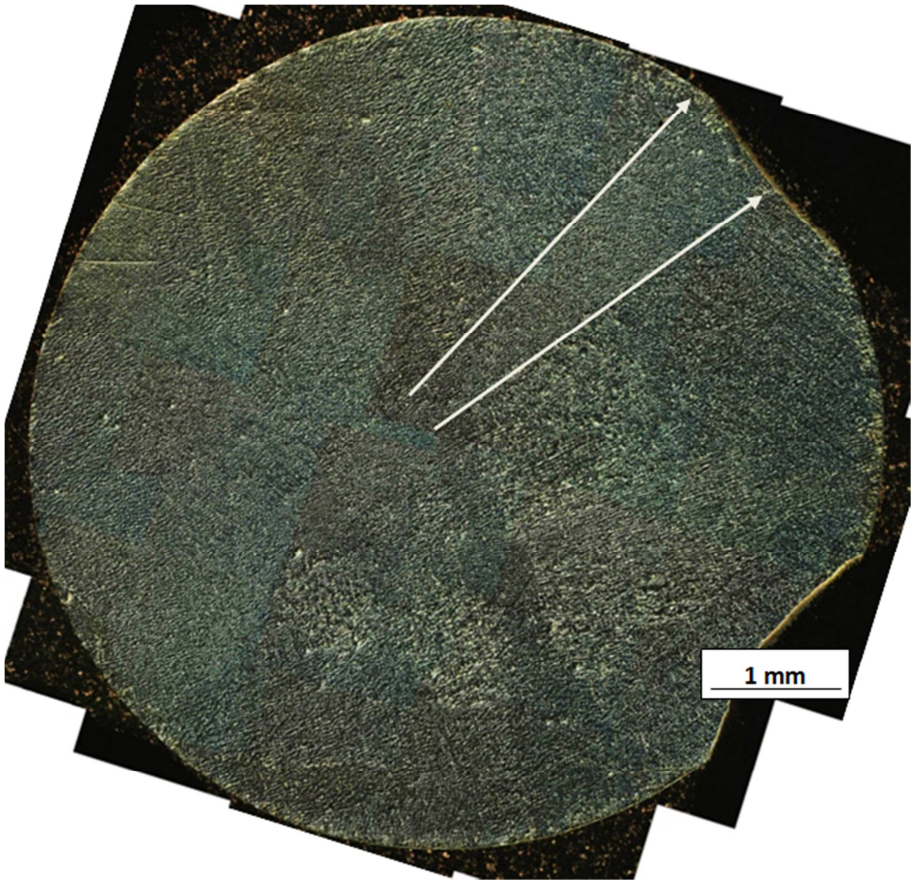

Figure 76 DIC montage image of a randomly sectioned Cu-8.9 wt.% Ni droplet undercooled by ΔT = 135 K, showing the microstructure of the full section investigated using EBSD orientation mapping. Arrows delineate the position of a seaweed branch.

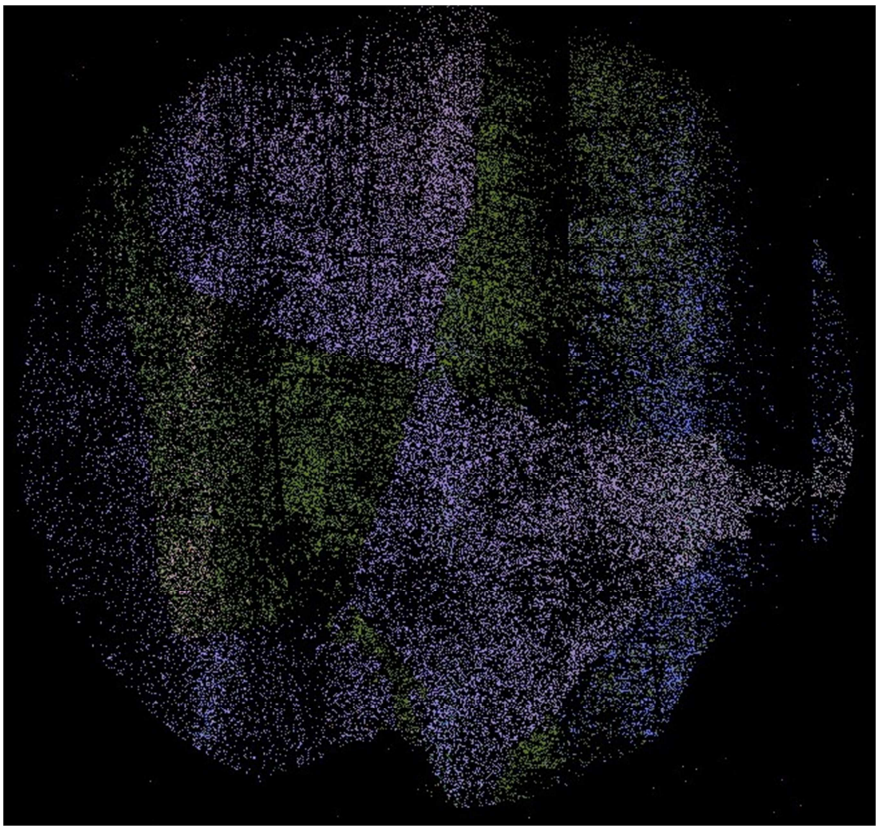

Figure 77 EBSD orientation map obtained from the sample shown in **Figure 76**, Both figures are of the same scale and orientation.

Figure 78 EBSD grain boundary misorientation map obtained from the sample shown in **Figure 76** where misorientations of > 10 % are plotted.

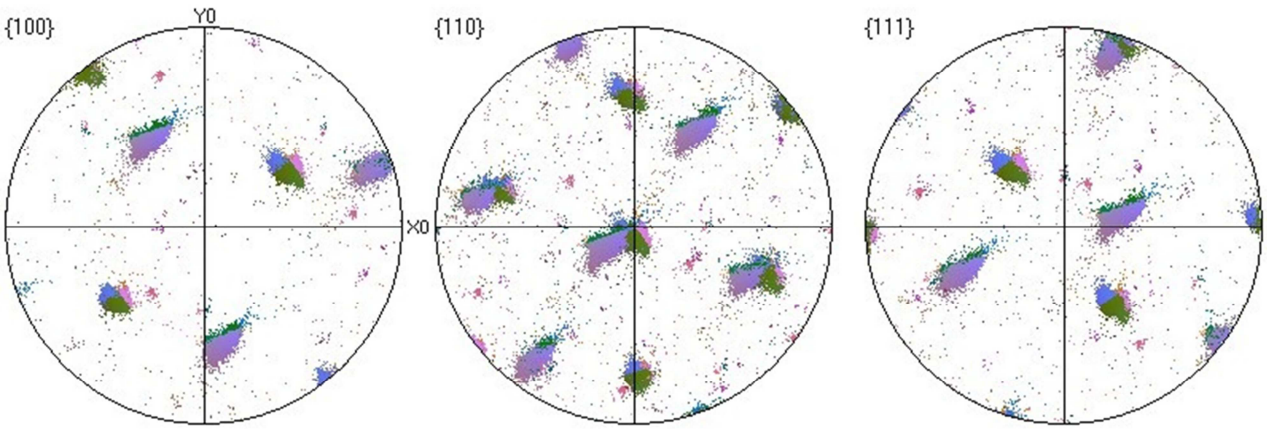

Figure 79 Pole figures obtained during the EBSD analysis of the randomly-sectioned sample shown in **Figure 76**. Equal area projection of the upper hemispheres.

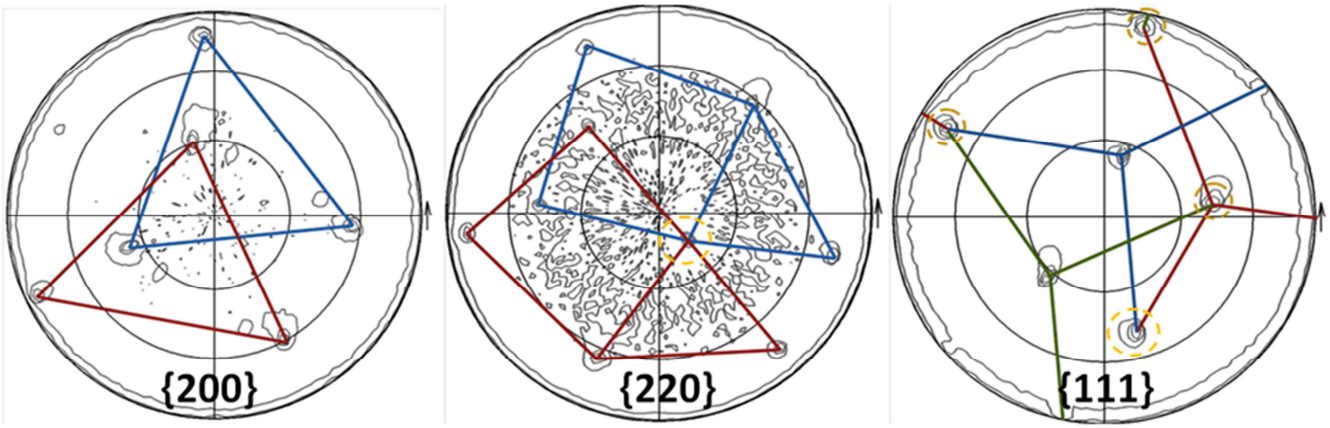

Figure 80 XRD-generated log-scale pole figures obtained for the randomly-sectioned sample shown in **Figure 76**.

6. DISCUSSION

6.1. Introduction

The experimental results of this project uncovered several interesting and novel findings, which will be discussed in this chapter. The compatibility of the various fluxes with the Cu-Ni alloys investigated will first be addressed. An analysis of the evolution of microstructure with increasing undercooling, and the impact that this appears to have on the velocity-undercooling relationship will then be discussed for both alloy compositions. Through comparison of the two alloys, the effect of Ni content on the microstructural evolution of undercooled Cu-Ni will then be proposed. Finally, the implications of these findings will be concluded in relation to conventional dendrite growth theory and spontaneous grain refinement.

6.2. Glass flux selection

The glass flux used in the melt fluxing technique was the key process parameter requiring optimisation for the success of this project. A number of fluxes were trialled in an attempt to find the optimal composition. Soda lime glass was observed to support the sample but contained many bubbles, which were not removed on superheating. No undercooling could be achieved in Cu-Ni using this flux, and the brownish discoloration observed on removal from the fluxing rig indicated that a reaction had occurred between it and the alloy. Similar results were also observed for a 50:50 mixture of dewatered B_2O_3 and soda lime. MTData calculations revealed that the evolution of gas was likely during heating, which can account for the bubbles observed in the flux. It was also confirmed that a reaction between some of the elements in the soda lime flux and elemental Cu/Ni was likely, with elemental Cu reacting to form Al_2CuO_4, and Ni oxidising to NiO. Stoichiometrically correct NiO is green in colour, whilst non-stoichiometric mixtures appear black, due to the resulting difference in oxidation state of the Ni (2^+ and 3^+ respectively) (Sato et al., 1975). At high temperatures (above 1225 K) Al_2CuO_4 has been shown to dissociate into Al_2CuO_2 and α-Al_2O_3 leading to a change from a black to a reddish-brown colour (Yu et al., 1989). The formation of Al_2CuO_4 and NiO may therefore explain the observation of a brownish discolouration of the flux. A lack of undercoolability in this flux is therefore likely to be due the presence of copious heterogeneous nucleants, arising from the formation of bubbles and high T_m NiO at the surface of the droplet during heating.

A 100 % B_2O_3 mix was then trialled, since MTData calculations indicated that this would be stable in contact with Cu and Ni at the temperatures reached during fluxing. Using this flux, a

moderate degree of undercooling could be achieved and bubbles in the flux could be removed during superheating. Discolouration of the flux was much fainter and only occurred during the fluxing of a new sample. This is therefore believed to be due to the initial removal of oxides from the fresh sample during repeated heating and cooling cycles. In spite of the improved chemical compatibility of this flux with the Cu-Ni alloys, the maximum undercooling achieved was only ΔT = 70 K. This is believed to be due to the low viscosity of the flux, which resulted in the loss of isolation of the samples from the crucible walls and the subsequent increase in heterogeneous nucleation sites, limiting the level of undercooling achievable. In order to increase the viscosity of the glass flux, Na_2SiO_3 was added to it in varying compositions. This proved a successful solution and lead to a significant increase in undercoolability of up to ΔT = 240 K and ΔT = 216 K for the Cu-8.9 wt.% Ni and Cu-3.98 wt.% Ni alloys, respectively. Changing the ratio of B_2O_3 to Na_2SiO_3 seemed to have little impact on the undercoolability of the sample. Perhaps this is due to the fact that only a slight increase in viscosity was required to better support and isolate the samples, with increasing additions of Na_2SiO_3 offering little further improvement, yet not increasing the viscosity so much that it became detrimental to the undercoolability. Since neither alloy could be undercooled below an experimental temperature of around 1175 K, it is suggested that the flux must become too viscous beyond this point, leading to heterogeneous nucleation of the sample.

Nevertheless, a sufficient degree of undercooling could be achieved in order to comprehensively study the microstructural evolution of the two Cu-Ni alloys with increasing undercooling. The B_2O_3:Na_2SiO_3 flux was therefore selected as the optimum flux composition for the present study.

6.3. Cu-8.9 wt.% Ni

The microstructural and texture analysis of melt-fluxed Cu-8.9 wt.% Ni has revealed a number of complex growth transitions and unusual microstructural features with increasing undercooling. At the lowest undercoolings observed, droplets consisted of single grains composed of orthogonal dendrites, typical of an FCC system undergoing normal, <100>-oriented growth. As undercooling was increased above $\Delta T \approx 45$ K, this gave way to a microstructure of finer, near-equiaxed grains which consisted of subgrains, curved grain boundaries and a dendritic substructure which is continuous throughout the sample. Each of these features is indicative of grain refinement occurring via a recovery and subsequent recrystallisation mechanism (Doherty et al., 1997). Subgrain boundary formation indicates that the redistribution of line defects in the solid state has occurred, suggesting recovery, whilst the

traversing of grain boundaries by the dendritic substructure and the presence of curved grain boundaries suggests that significant grain coarsening has occurred, indicative of an ensuing recrystallisation process. Similar observations have been made in pure Cu by Dragnevski *et al.* (2004a), who noted that the ΔT^* transition was preceded by recovery processes occurring at intermediate undercooling, evidenced by the observation of well-developed networks of low and high angle subgrain boundaries. Beyond the ΔT^* transition, samples were observed to undergo full recrystallisation into randomly oriented refined grains, accompanied by a reduction in microhardness. Comparable features were also observed at low undercooling in a Cu-O alloy (Cochrane et al., 2001), in which the dendritic substructure was observed to extend across the curved grain boundaries and pole figure plots exhibited only a single set of poles.

Beyond $\Delta T \approx 85$ K, at intermediate undercoolings, a return to large grained microstructures is observed up to an undercooling of $\Delta T \approx 202$ K. Within these "eightfold" and "sixfold" regimes mixed-orientation dendrites and novel dendritic seaweed branches have been observed. These features suggest that competitions in the preferred growth orientation are occurring within this range of undercooling. Since preferred growth takes place along the more usual <100> orientation at the lowest undercoolings observed, it is suggested that this growth mode dominates at lower undercoolings within the intermediate regime. As the undercooling is increased, the switch to a sixfold nucleation pattern and the observation of a sharp pole in the centre of a {111} pole figure suggests that a <111> preferred growth orientation is becoming more dominant. If this is the case, then the transition to faster, fully <111> oriented growth might account for the apparent positive break in the v - ΔT trend and the transition to a finer grain structure at $\Delta T \approx 202$ K. However, since the original growth structure is no longer present within the finer grain structure, this is difficult to confirm microstructurally.

Such an extensive, undercooling-mediated transition in growth orientation has not previously been reported. As discussed in Chapter 2.4.6.3, abrupt switches in preferred growth orientation with increased undercooling have been observed in transparent metal analogue systems (Sawada, 1986, Gudgel and Jackson, 2001) and in Cu-Sn (Dragnevski et al., 2004b), and an extended dendrite orientation transition (DOT) was investigated by Dantzig *et al*. (2013) with increasing Zn content in Al-Zn alloys. However, the DOT reported involved abrupt transitions between fully dendritic and fully seaweed microstructures. By contrast, in the present work, mixed morphology microstructures are observed in the intermediate regime.

Texture analysis of samples taken from the eightfold and sixfold regimes reveals the presence of shared {111} planes between grains, indicating twinned growth. This includes one sample in the sixfold regime which exhibits three sets of poles and three apparent shared poles,

indicating a triple-twin/triplet relationship. Multiple twinning is favoured in FCC or diamond cubic (DC) crystalline materials, where lower twin boundary energies are facilitated and surface energy anisotropies with, for example, $\varepsilon\{111\} < \varepsilon\{100\}$ exist. There are two types of multiple twinning mode:

1. Lamellar twins, formed from repeating parallel contact twins;
2. Cyclic twins, which form from the non-parallel growth of co-planar twin planes and which (usually) enclose a 360^{o} angle in total.

According to the number of twins and the angle between them (120^{o}, 90^{o}, 60^{o} or 45^{o}), cyclic twins may be called “trilling” “fourling” “sixling” or “eightling”, examples of which can be found in many classic minerals such as cassiterite (SnO_2), wurtzite (ZnS), rutile (TiO_2) and chrysoberyl ($BeAl_2O_4$). Some cyclically twinned mineral crystals can be seen in **Figure 81**. Multiple twinning can occur due to the growth of twinned nuclei formed from arrangements of tetrahedral subunits, or through cyclic twinning operations arising from the misstacking of atoms (growth twinning) or mismatch of lattices (deformation twinning) during growth (Hofmeister, 2004).

Cyclic twinning has also been observed in some metals and alloys. A prime example of this was reported by Lehman *et al.* (2010) who observed sixfold cyclic twinning in near-eutectic SnAgCu, Sn-Ag and Sn-Cu solders, which had undercooled by 30 – 80 K prior to solidification. In each system, three orientations of dendritic <100> grains were observed, though the grain morphologies of each were found to differ with the addition of Ag or Cu (**Figure 82**). In image A of **Figure 82** the single grain orientation of pure Sn is shown. In image B the effect of the addition of 1 at.%Ag can be seen. Here, it is suggested that, although a large quantity of grain boundaries are observed, the existence of only three colours under cross-polarised light suggests that only three relative grain orientations are present (subsequently confirmed using EBSD analysis), which is consistent with previous observations of sixfold cyclic twinning. With the addition of 0.1 at.% Cu to Sn, microstructures such as that shown in image C are observed, in which plate-like grains radiate outwards from the nucleation event. Finally, in image D a ‘beach ball’ microstructure is observed when both 3.9 at.% Ag and 0.6 at.% Cu are added. Here, six grains of alternating orientation radiate outwards from the nucleation point, and are bound by sixlings. This structure was first observed by Kara Mather (Lehman et al., 2004) and is hence referred to as “Kara’s beach ball”. Lehman *et al*. proposed a model for the formation of the sixfold {101} twinned beach ball structure (**Figure 83**). Here, a two-layer representation of the Sn unit cell is used to form triangular sections by cutting along two {101} planes. This is then replicated and rotated around the observed central <101> rotational axis to complete the

sixfold twin nucleus, which subsequently undergoes dendritic growth along preferred fast growth orientations (<110> in this instance). Secondary dendrite arms consequently grow perpendicular to the primary dendrites along slower <001> directions towards the neighbouring twins, leading to the interpenetration of neighbouring twins and thus the observed irregular interface. The {101} twin planes form a 57.2^{o} angle to each other, and hence the 60^{o} rotations result in misfits between segments, which they propose accounts for the low angle grain boundaries commonly observed in cyclically twinned solder joints. It is concluded that "the sixfold cyclic twinning event is associated with the nucleation of Sn in a metastable/pseudo-hexagonal structure that defines the basis for further growth".

In the present work, the observation of three grains and three twin planes therefore suggests a similar multiple-twinning occurrence, in this instance trilling. As an FCC metal, the close-packed {111} planes in Cu-Ni favour low energy twinning through greater coherency, accounting for the observation of shared {111} twin planes. Since this droplet was sectioned close to parallel to the growth direction (in order to ascertain the preferred growth orientation), the vast majority of the visible droplet consists of one grain. However, close to the edge, it can be seen (**Figure 60**) that two further grains are present which look to have originated from the same point. If this sample were sectioned perpendicular to the growth direction, a triple-fold symmetry between the three grains might be observed, with a grain structure which resembles the Kara's beach ball morphology. However, insufficient sample remains in order to confirm this.

If the three grains are symmetrical and the twins are of equal length then this would suggest formation from a twinned nucleus as opposed to the development of stacking faults during growth. The 6-fold symmetry of the nucleation point may support the notion of a triple-twinned nucleus, or this could simply be due to a dominance of the <111> preferred growth orientation. The development of growth twins soon after nucleation may also be a likely explanation for multiple twinning, due to the increased influence of atomic attachment kinetics at high solidification velocity and to the competing growth directions present, both of which could lead to increased stacking fault formation. The wavy/stepped grain boundaries observed could have arisen from the interpenetration of secondary arms from neighbouring twins, however the substructure appears to extend some way across the grain boundaries, suggesting that they have migrated. The mobility of the twin boundaries will be enhanced at high temperatures, hence it is suggested that grain boundary migration most likely occurred during cooling from the high temperatures reached during recalescence.

Multiple twinning also appears to be present in the sample undercooled by ΔT = 135 K, which was investigated using EBSD texture mapping and XRD texture analysis. Pole figures taken from this sample during XRD analysis reveal four shared poles in the log{111} pole figure and one shared pole in the log{220} plot (Figure **80**) (Chapter 5.5). The orientation map acquired from a randomly-oriented section of this sample reveals that nucleation occurred from within the droplet, rather than at the surface, allowing a more accurate view of the symmetry of the growth pattern around the nucleation point. The grains in this sample exhibit fourfold symmetry of alternating orientation around the nucleation point, bearing a strong resemblance to the 'Kara's beach ball' structure. The symmetry of these grains and near equal length of the twin boundaries suggests that growth originated either from a twinned nucleus, or from the development of stacking faults very soon after nucleation to produce fourfold twinning along four {111} planes. The alternating grain orientations result in two dominant orientations, which can account for the observation of two/three sets of poles within the pole figures.

In contrast to the beach ball morphology, other regions of misorientation are also present in this sample, sometimes resulting in sharp high angle grain boundaries (HAGBs) (defined as having misorientations of greater than 10°) and sometimes occurring in a diffuse manner within the grains. In instances where diffuse transitions between grain orientations are observed, there appears to be a coincidence with the sites of seaweed branches, as discussed with reference to the top right hand grain seen in **Figure 77** (Chapter 5.5). This might be expected, owing to the lack of preferred growth orientation in dendritic seaweed and due to the constant splitting and bending of the tips, which could lead to slight misorientations within the seaweed structure itself. It therefore appears that the growth of seaweed branch structures facilitate large misorientations within grains, without resulting in sharp HAGBs. With regards to the observed additional HAGBs, their formation could be due to the apparent competing anisotropies in the <100> and <111> preferred growth orientations, which would increase the likelihood of developing further stacking faults and misorientations during growth. Alternatively, the presence of a large volume of dendritic seaweed indicates the likely presence of a high dislocation density, which may subsequently migrate and align in the solid state to produce additional misorientations. At least one of the sharp HAGBs is likely be the remaining {220} twin identified from the pole figures. Overall, the mixed-orientation nature of these samples will inherently give rise to interesting and unusual texture effects, which will require further characterisation in future work.

With increasing undercooling, a further transition to smaller dendritic grains is subsequently observed, which, as discussed, could be coincident with the transition to faster, fully <111>

oriented growth and the suggested break in the $v - \Delta T$ trend. The existence of smaller, individually oriented grains suggests that some post-solidification modifications to the microstructure have occurred, since growth will initially have proceeded from a single point and not from many nucleation sites within the droplet. The sharp increase in growth velocity at this undercooling (as indicated by the $v - \Delta T$ curve) will result in the growth of finer dendrites, which would be more likely to remelt or break up during recalescence. Hence the original growth structure has been replaced by randomly oriented dendritic grains, and the suggested <111>-oriented nature of the original growth structure cannot be confirmed microstructurally. However, if the dendritic nature of the grains is indicative of the original growth structure then it appears growth at this point is fully dendritic, (as opposed to seaweed) in character.

Finally, at the highest undercoolings achieved in this alloy, a droplet consisting of a transitional equiaxed-to-elongated grain structure is observed. It is suggested that, although a globally grain-refined sample hasn't been obtained, this may represent an intermediate structure in the spontaneous grain refinement process. In the non-grain refined portion of the droplet, the substructure is distinctly seaweed-like. Hence it is proposed that this was the original growth structure which led to a partial grain refinement. From the literature review given in Section 2.4.6.3, it appears to be well established that tip-splitting and seaweed growth generally occurs when either the anisotropy is weak or the growth velocity (and therefore the strength of the kinetic anisotropy) is high. From the work of Akamatsu *et al*. (1995) it was established that for an FCC metal analogue system, the anisotropy of the <111> orientation was weak. Hence the transition to this growth orientation, coupled with the high solidification velocities (and therefore kinetic anisotropy) present at high undercooling, may result in a destabilisation of the solid-liquid interface and transition to dendritic seaweed growth. As proposed by Mullis *et al*. (2004b) the inherently unstable seaweed structure would then be likely to rapidly remelt at the split junctions during recalescence, forming numerous solid islands at which new grains could nucleate and leading to spontaneous grain refinement. An investigation of higher undercooling samples would be required in order to investigate if a full spontaneous grain refinement transition would be observed.

6.4. Cu-3.98 wt.% Ni

For the more dilute alloy, similar features and microstructural transitions were observed, with some key differences worth noting. The velocity-undercooling relationship once more appears to deviate from the initial $v \propto \Delta T^2$ trend, exhibiting a positive break at around $\Delta T \approx 190$ K. When compared to the $v \propto \Delta T^2$ data of the Cu-8.9 wt.% Ni alloy it is clear that a very similar

relationship exists, yet with a shift in the trend to lower undercoolings as Ni content is decreased. At the lowest undercoolings obtainable (36 K ≤ $\Delta T < 53$ K), a grain refined structure is seen. It is assumed that at undercoolings below this grain refined region there must also be a region of single-grained growth, in which grain refinement hasn't occurred. This is in line with the typical grain refinement transitions observed in many alloys (including the Cu-8.9 wt.% Ni alloy), and is based on the assumption that, at least for very low undercoolings, dendritic growth will be stable and there will therefore be insufficient driving force to facilitate any grain refinement mechanism.

In contrast to the higher concentration alloy, this low undercooling region of grain refinement appears to involve a dendrite fragmentation mechanism, consistent with that commonly reported (Kattamis and Flemings, 1967, Kattamis, 1976, Chen et al., 2008a, Kobayashi and Shingu, 1988). Whilst large parent grains and a network of subgrains are again observed, there is no continuous dendritic substructure present. This is confirmed through texture analysis, which indicates that at least three unrelated grains are present. Under DIC light microscopy, some of the former Ni-rich dendrite cores can be seen within the substructure of the grains, which appear fragmented. The subgrain boundaries are situated between these fragments and hence it appears that they arise from the slight misorientations of the fragments with respect to one another. Such boundaries must consist of small misorientations, as larger misorientations would give rise to significantly more texture on the associated pole figure. Larger, more intact dendrite fragments are also observed at the surface of this droplet, providing further confirmation of the dendrite fragmentation mechanism, as opposed to recovery or recrystallisation. The orthogonality of the secondary arms observed on these fragments suggests that the original growth structure was that of <100>-oriented dendrites. Hence it is suggested that with increasing undercooling, the combination of increasingly refined dendrites (due to reduced solute diffusion lengths) and larger recalescence temperatures, leads to a partial remelting of the original growth structure – in line with the theory of Schwarz *et al.* (1994). The Ni-rich dendrite cores would exhibit higher melting temperatures and hence would mostly remain solid, with remelting mostly occurring in Cu-rich regions. This leads to dendrite fragments, with slight misorientations between them, situated within the large grains remaining in the sites previously occupied by either individual or arrays of dendrites of the same relative crystallographic orientation. It then seems that as the undercooling is increased further, the transfer between solutally and thermally controlled growth occurs, leading to a coarsening of the dendrites and subsequent stabilisation against grain refinement beyond $\Delta T \approx 53$ K. Single grained droplets consisting of orthogonal, <100>-oriented dendrites are then observed up to $\Delta T \leq 72$ K.

Above $\Delta T \approx 72$ K, a transition to mixed-orientation, twinned droplets is seen, displaying a close likeness to the eightfold-to-sixfold regimes of the more concentrated alloy. Twinning, involving shared {111} twin planes, is observed in all samples subjected to texture analysis, and grain boundaries are again wavy, suggesting significant grain boundary migration in the solid state. However, in contrast to the concentrated alloy:

- no distinct eightfold or sixfold growth patterns are observed;
- no multiple twinning occurrences have been identified;
- there appears to be a much greater degree of porosity within the centre of the samples, revealing a dendritic/dendritic seaweed skeleton;
- a greater spectrum of diverging split primary dendrite branches are observed, ranging from dendritic to seaweed-like in their morphology.

In spite of the lack of an eightfold-to-sixfold transition, an increasing dominance in the anisotropy of the <111> preferred growth orientation is still evident. This is deduced from the mixed morphology and seaweed microstructures, indicating the presence of competing anisotropies, and through the observation of a pole in the centre of the {200} pole figure at low undercooling and a pole in the centre of the {111} plot at high undercooling. However, the later transition to this mixed-orientation regime (with respect to the first region of grain refinement), coupled with the lack of an eightfold-to-sixfold transition and the decreased prominence of split branches of fully seaweed character, suggests that the competition between the two growth directions is not as strong in comparison to the more concentrated alloy.

Beyond $\Delta T \geq 183$ K, and certainly by $\Delta T = 201$ K, a spontaneous grain refinement transition is observed, coinciding with the suggested positive break in the $v - \Delta T$ curve and suggesting again that a transition to faster, fully <111>-oriented growth has taken place. In contrast to the high Ni alloy, no intermediate coarse grained dendritic structure has been observed. However it is possible that such a transition may still exist over the unmeasured range between $183 \text{ K} < \Delta T < 201$ K. The surface structure of the grain refined droplets exhibits a fragmented dendrite structure, with each fragment constituting a single grain of around 200 μm in diameter. In contrast to that proposed for the high Ni alloy, this suggests that grain refinement occurred from the remelting and fragmentation of a dendritic rather than a seaweed precursor.

Figure 81 Example of (**top**) fourlings of celsian (MuseumWales, 2014), (**bottom left**) Chrysoberyl sixlings (Crystal-Treasure.com, 2014) and (**bottom right**) Rutile eightlings (FMF, 2014).

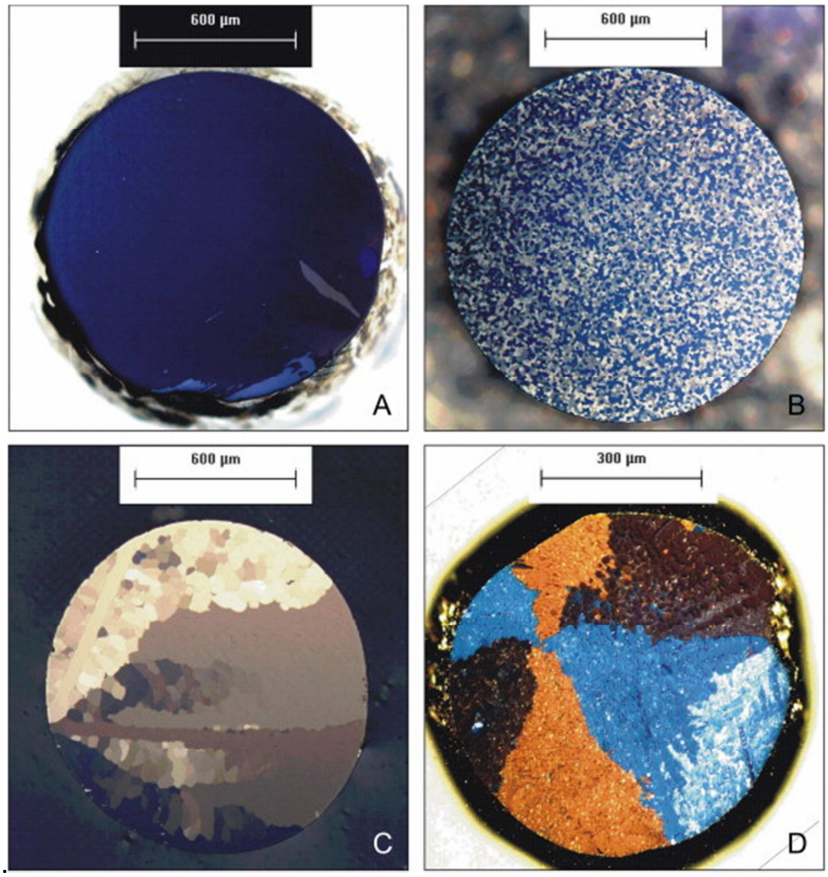

Figure 82 Cross-polarized light micrographs of (**A**) pure Sn cooled from a temperature of 265 °C at a rate 1 °C s^{-1}; (**B**) Sn–1Ag cooled from a temperature of 250 °C at a rate of 0.03 °C s^{-1}; (**C**) Sn–0.1Cu cooled from a temperature of 320 °C at a rate of 0.01 °C s^{-1}; and (**D**) Sn – 3.9Ag – 0.6Cu cooled from a temperature of 250 °C at a rate of 1 °C s^{-1}. Different colours arise from the birefringent properties of Sn and hence each colour represents a particular orientation of the grain (Lehman et al, 2010).

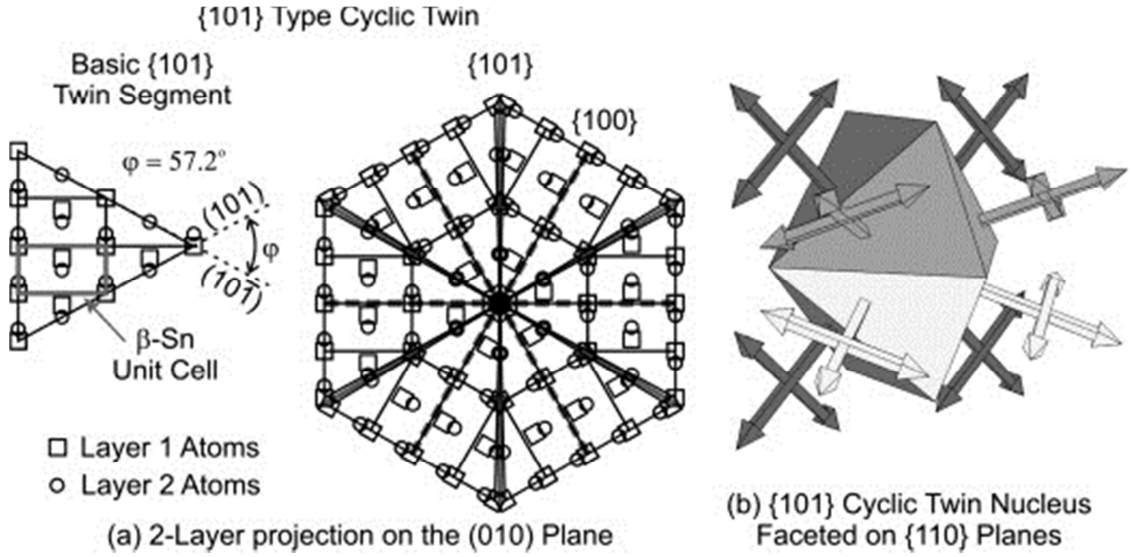

Figure 83 Rudimentary sixfold cyclic twinned ({101} type) multi-crystal model proposed by Lehman *et al.* (2010) (**a**) Projection view of Sn lattice onto the (0 1 0) plane, showing a basic {1 0 1} twin segment and a {1 0 1} cyclic twin nucleus. (**b**) Perspective view of {1 0 1} cyclic twin nucleus faceted on {1 1 0} planes and rendered as planes.

6.5. Effect of Ni content on microstructural evolution

Within both alloys, the evolution of microstructure with increased undercooling/solidification velocity reveals the presence of an extended transition between <100>-oriented growth at low undercooling and <111>-oriented growth at high undercooling. At intermediate undercooling, the competition between the two growth directions appears to be giving rise to mixed-orientation microstructures and the observed seaweed branches. The position of this mixed-orientation regime appears to shift to lower values of undercooling (relative to the first grain refinement transition) with increasing Ni content. For the more concentrated alloy, this leads to a coincidence of the mixed-orientation regime with the low undercooling region of grain refinement. For the less concentrated alloy, fully <100>-oriented growth appears to exist up to undercoolings beyond this grain refinement transition, such that the mixed-orientation regime does not coincide with it. Hence, within this grain refinement transition, there will be a difference in the original growth structures present as a direct result of the Ni concentration.

This would appear to account for the differences in grain refinement mechanisms observed at low undercooling. In the concentrated alloy, the initial growth of mixed-orientation microstructures appears to drive a recovery/recrystallisation process. This is probably due to the presence of a high dislocation density, which might be associated with the accommodation of mixed-orientation growth. For the less concentrated alloy, the initial growth of fully <100>-oriented dendrites results in a more stable and less defect-dense microstructure, and hence there is insufficient driving force for recovery/recrystallisation. Instead, the combination of the progressive refinement of dendrites and greater recalescence temperatures (with increasing undercooling) drives a partial remelting and fragmentation process – as per Schwarz *et al.* (1994).

The identification of two different low-undercooling grain refinement mechanisms, in two closely related alloys, is significant, as it may help to resolve some of the previous debate and confusion over the ‘true’ mechanism for the low undercooling region of spontaneous grain refinement in alloys. In the low Ni alloy, it appears the grain refinement transition is determined by the underlying morphology; whilst, in the high Ni alloy, grain refinement appears independent of, and superimposed upon, the underlying mixed-orientation morphology.

The shift of the mixed orientation regime to lower undercooling with increasing Ni content suggests that some anisotropic property is being influenced by the addition of Ni to Cu, which subsequently leads to a switch in the preferred growth orientation at high undercooling. Since

the capillary stiffness determines the equilibrium/low undercooling growth orientation, another anisotropic parameter (which is independent of this) must gain sufficient strength with increasing Ni content to become competitive with it at intermediate-to-high undercooling. This leads to a consideration of the kinetic anisotropy. With increasing undercooling and solidification velocity, the influence of the kinetic anisotropy will increase as atomic attachment kinetics become more influential. As discussed in Section 2.4.6.3, Akamatsu *et al*. (1995) demonstrated that the capillary and kinetic anisotropies may compete at high (pulling) velocity, leading to transitions between seaweed and degenerate non-dendritic patterns. In addition, the models of Bragard *et al.* (2002) showed that tip-splitting could occur in the vicinity of the ΔT^* transition if the strength of the kinetic anisotropy was sufficiently high. In the present work, the observation of a similar transition to seaweed growth at high undercooling (in the high Ni alloy), indicates the existence of a similarly large kinetic term. However, Bragard *et al*. did note that the tip-splitting transition only occurred for unrealistically high values of the kinetic anisotropy, and thereby concluded that in order to produce such a transition, there must be other contributing factors.

Further to this, an increase in the effect of the kinetic anisotropy with increasing undercooling is true for all metallic systems. Hence, if this alone were responsible for the <100> to <111> transition observed, more frequent reports of such transitions might be expected. Since pure Cu has not been reported to show such a transition, and since the addition of more Ni to Cu shifts the competitive, mixed-orientation region to relatively lower undercoolings, this suggests that the addition of Ni either:

1. increases the strength of the kinetic anisotropy, or;
2. decreases the strength of the capillary anisotropy.

This would therefore lead to a closer competition between the kinetic and capillary anisotropies at high undercooling/growth velocity. In the first case, it could be argued that the kinetic anisotropy would be increased by the need to incorporate more Ni into the growing crystal solid. If this is true, the point at which the kinetic and capillary anisotropies come into approximate balance would be shifted to a lower (and therefore more achievable) undercooling with increasing Ni content. This is supported by the observation of seaweed growth at high undercooling in the high Ni alloy and not in the low Ni alloy. In addition, if the kinetic term is increased as a result of the difficulty associated with the incorporation of more Ni into the growing solid, then this may also result in a higher probability of developing stacking faults during growth; which might account for the occurrence of multiple twinning only in the high Ni alloy.

In the second case, a decrease in the strength of the capillary anisotropy would suggest that the interfacial energy anisotropy is being altered by the addition of Ni. In Section 2.4.6.3 it was shown, through the work of Dantzig *et al.* (2013) and Haxhimali *et al.* (2006), that the anisotropy of the interfacial free energy can be modified by the addition of solute. In fact, both Cu and Ni were identified as being relatively likely to undergo changes in the interfacial energy anisotropy, since they appeared to lie just within the 'hyperbranched' regime outlined by Haxhimali *et al*.; rather than lying fully within the <100>-oriented regime, as would be expected. Hence both options 1 & 2 (or possibly a combination of both) could offer a reasonable explanation for the shift in the observed transitions as a function of Ni concentration.

In both alloys, the subsequent competition between the more equally-matched capillary and kinetic anisotropies therefore appears to produce a region at intermediate undercooling in which neither <100> or <111> growth is strongly favoured. Eventually, the increased effect of the kinetic anisotropy over the capillary anisotropy leads to a switch to fully <111>-oriented growth. This transition is coincident with a sharp increase in growth velocity, which would lead to a more rapid refinement of the dendrites with increasing undercooling, making them more likely to fragment. In the high Ni alloy, this may account for the corresponding transition to a large, randomly-oriented dendritic grain structure. As discussed (Section 6.4), such a transition has not been observed in the low Ni alloy, however it is still possible that this exists over the narrow undercooling range which was not measured.

At the highest undercoolings reached, the seaweed structure observed in the more concentrated alloy most likely arose from the combination of: a sufficiently high kinetic anisotropy, shown by Bragard *et al.* (2002) to give rise to seaweed growth; and the relatively low capillary anisotropy of the <111> growth direction. Higher levels of undercooling would need to be achieved in order to investigate if a transition to full spontaneous grain refinement occurs; however, it would seem that the most likely precursor for grain refinement in this alloy is dendritic seaweed. By contrast, it appears that the reduced Ni content in the low Ni alloy has subsequently shifted the point at which the increased kinetic anisotropy gives rise to seaweed growth to higher undercoolings, out of the achievable range. As such, spontaneous grain refinement in this alloy appears to have arisen from the remelting and fragmentation of a dendritic, rather than seaweed, precursor.

In order to visualise this more clearly, approximate regions of <100>-oriented, mixed-orientation, <111>-oriented and seaweed growth are plotted in the morphology map shown in **Figure 84**, as functions of Cu content and undercooling. This map was drawn based on the

results of the present work and the observations of seaweed substructures at 280 K (Mullis *et al.* (2004)) and grain refinement at 352 K (Dragnevski *et al.* (2004)) in pure Cu; which allow the intercepts of these transitions with the undercooling axis to be determined. The range of undercooling, over which measurements were taken, for both alloys investigated in the present work are indicated. Approximate positions of grain refinement transitions are shown in order to illustrate how the alteration of Ni content may alter the precursor to grain refinement; thereby altering the dominant grain refinement mechanism. It is assumed that the low undercooling region of grain refinement tends to 0 at 100 wt. % Cu, since pure metals undergo only one grain refinement transition at high undercooling. Furthermore, it is assumed that there is no upper limit for the high undercooling region of grain refinement, since a further transition back to stable dendritic growth has never been reported.

Overall, within the two alloys, three different spontaneous grain refinement mechanisms have been identified:

1. Recovery and recrystallisation,
2. Remelting and fragmentation of dendrites due to scale refinement, as per Schwarz *et al.* (1994),
3. Remelting and fragmentation of dendritic seaweed.

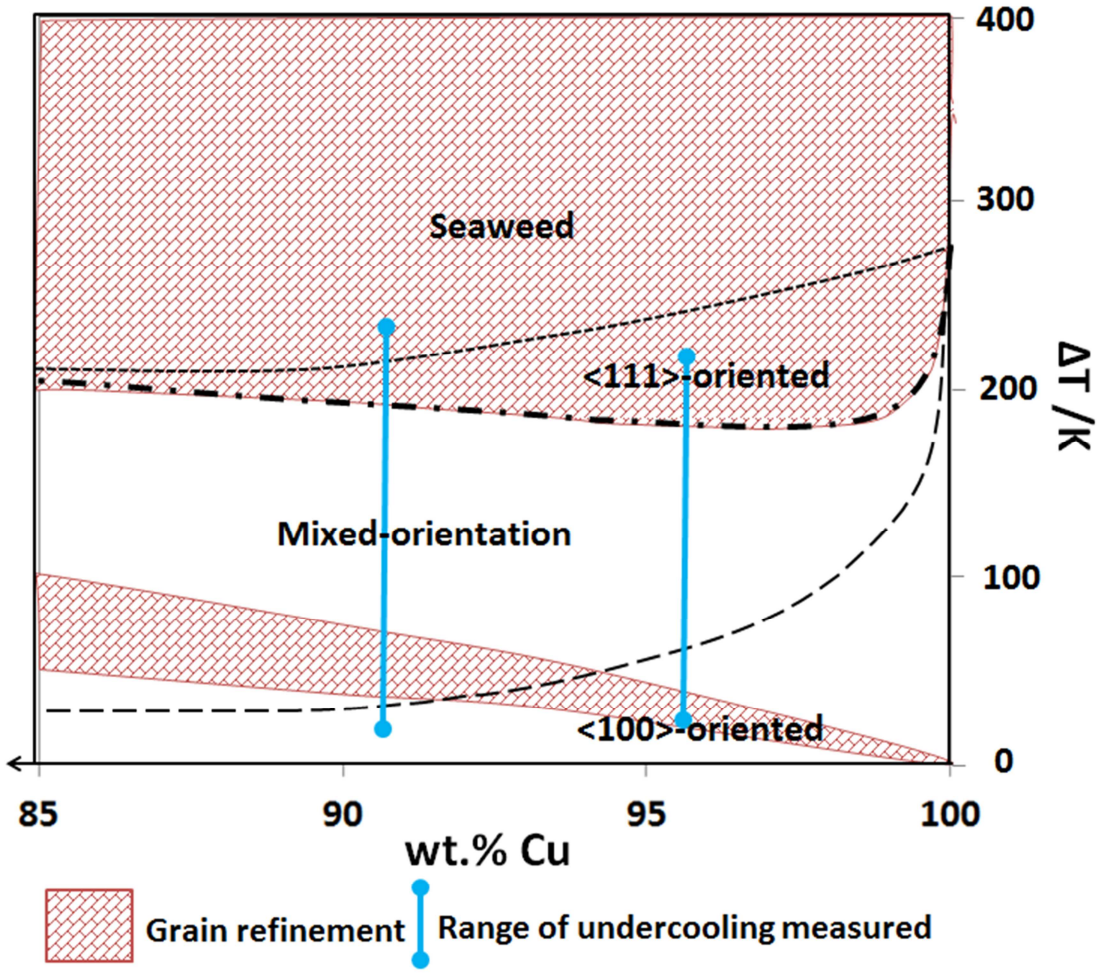

Figure 84 Suggested dendrite morphology map based on the present study; showing transitions between <100>, mixed-orientation, <111> and dendritic seaweed growth, as functions of undercooling and Cu content for the Cu-rich end of the Cu-Ni alloy system. Positions of the observed grain refinement transitions are shown in order to show how Ni content may change the original growth morphology and thus grain refinement mechanism. The range of undercooling measured for the two alloys presently investigated are shown.

6.6. Further discussion & comparison with literature

Whilst such an extensive transition between growth orientations with increasing undercooling has not previously been reported, abrupt switches in preferred growth orientation have been observed in a limited number of metallic systems. For example, Battersby *et al.* (1999) reported a <111> to <100> transition in Ge-Fe, coincident with a transition from faceted to continuous growth and the observation of a large number of growth twins. Conversely, Dragnevski *et al*. (2004b) observed the opposite transition, from abnormal twinned <111> growth to the more usual <100> non-twinned growth, at moderate undercooling in Cu-Sn alloys. Since pure Cu does not show such a transition, Dragnevski *et al.* suggested that a minimum solute concentration is required to induce such a transition, indicating once more the possible influence of solute additions on the anisotropy of the interfacial free energy.

The existence of twinning in both of these cases, as well as in the present work and in reports of abnormally-oriented Al feather grains (Henry et al., 1998b), suggests that this may be an integral part of abnormally-oriented growth. This could be due to an increased likelihood of the development of stacking faults during growth, owing to the competing anisotropies which must be present in order to induce the observed switches in growth direction. However, further studies would be required in order to investigate the twinning mechanisms more closely.

Occurrences of orientation transitions and twinning may be more common than previously reported, since not all studies incorporate a detailed texture analysis of the undercooled samples. It is interesting to return to some of the key pieces of research in this area and re-evaluate the micrographs provided. Kobayashi and Shingu (1988) noted that undercooled Cu-O samples, which were quenched to suppress grain refinement and retain the original growth structure following nucleation, exhibited “radiating fan-shaped grains originating from a single point of nucleation, which are related through twinning operations”. The (albeit grainy) images of these structures can be seen in **Figure 85**, which show both a grain morphology which appears very like the distinct Kara’s beach ball morphology, and a microstructure consisting of what appears to be seaweed/split dendrite branches. Similar morphologies in Cu-Ni alloys were also published by Schwarz *et al.* (1994) (**Figure 86**) when proposing their dendrite break-up model based on the stability analysis of Karma (1998) (discussed in Chapter 2.4.6.3). Hence, whilst the seaweed/split-dendrite branch morphologies and cyclically twinned microstructures appear to have been present, they may have been overlooked in the past.

The proposed transition to fully <111>-oriented growth is supported by the observed positive breaks in the $v - \Delta T$ curves. The work of Gudgel and Jackson (2001) (Section 2.4.6.3) suggests that the transition to <111>-oriented growth results in a sharpening of the dendrite tip and an associated increase in growth velocity. This might therefore account for the observation of a positive break in the curve, rather than the more commonly observed negative break. Positive breaks are not unheard of, however, and have previously been reported (Galenko et al., 2007, Algoso et al., 2003, Liu et al., 2011, Battersby et al., 1999).

The most closely related positive break was reported by Li *et al.* (2000), who studied the solidification behaviour of a Cu-30 at.% Ni alloy using an undercooling and directional solidification technique. Here, the melt was first undercooled within a cylindrical crucible and then solidification triggered at one end. Some parallels can be drawn between the microstructural transitions observed by Li *et al*. (**Figure 87**) and that observed in the present work, particularly for the Cu-8.9 wt.% Ni alloy. Both alloys have been found to transition through: orthogonal dendritic -> grain refined -> single grains in which the dendrites become increasingly misoriented as undercooling is increased -> large, randomly oriented grains coincident with a break in the $v - \Delta T$ relationship -> refined grains. Therefore, in the present work and in that of Li *et al.*, the break in the $v - \Delta T$ relationship appears to be coincident with the transition to large, randomly-oriented grains, rather than the spontaneous grain refinement transition *per se*. A positive break at this point, and the observed increasing misorientation of the dendrites leading up to this break, suggests that there might also be an orientation transition occurring in the study of Li *et al*., though this is not investigated. In the present work and in that of Li *et al*. insufficient data has been collected at higher undercooling to determine if there is a further break in the curve, which is coincident with the spontaneous grain refinement transition. Hence it is still possible that there might be another, more 'classic' break in the trend from a power law relationship to a linear relationship. Since seaweed growth is observed at the highest undercoolings in the concentrated alloy, such a break might be expected in the present work. This is based on the simulations of Mullis *et al.* (Mullis et al., 2004b), which show that seaweed growth occurring at a designated value of undercooling was shown to propagate less rapidly than that of a dendrite growing under the same conditions. However, further data at higher undercoolings would be required in order to confirm the presence of a further break.

The classic, negative power law-to-linear breaks in the $v - \Delta T$ relationships represent quite distinct changes in the trend, and are thus easy to identify. Since positive breaks in the curve are more difficult to identify and justify, it could be that previous work has overlooked these transitions. In order to investigate if this may have been the case, the data of Willnecker *et al.*

(1990) has been reassessed (**Figure 88**), since this was the first observation of a break to a linear relationship, which was coincident with the grain refinement transition in a closely-related Cu-30 at.% Ni alloy. By re-plotting the data on both a double-log and a $v - \Delta T^2$ plot, it can be seen that there does appear to be an additional break in the trend at lower undercooling. Breaks in the trend are most clear from the $v - \Delta T^2$ plot, in which the data closely fit individual linear trends, suggesting that (as with the Cu-Ni alloys investigated in this report) v is proportional to ΔT^2. It is not obvious from Willnecker *et al*.'s linear plot of the data that there is a break in the trend at lower undercooling, and hence such breaks may have been overlooked in other instances as well. Since a break in the trend indicates that some form of growth transition has taken place, this additionally indicates that possible growth orientation transitions have gone unnoticed.

The work of Mullis et al. (2004b) into the relative velocities of dendrites and seaweed suggests that the high undercooling, power law-to-linear ΔT^* transition observed by Willnecker *et al*. may indicate a transition to the seaweed morphology. However, since this coincides with the transition to refined grains, the original growth structure has not been directly observed. In fact, the only experimental observations of a transition to a seaweed morphology in metals at high undercooling have been in the present report, and in that of Mullis *et al*. (2004b). In both cases the exact same melt fluxing apparatus has been employed. Recently, Binder *et al*. (2014) carried out a thorough comparative study of the extent to which different techniques for measuring the $v - \Delta T$ relationship agree. Electromagnetic levitation (under terrestrial and microgravity conditions), melt fluxing (with and without a stabilising magnetic field) and electrostatic levitation, were compared. It was concluded that, to within experimental error, all techniques agree, apart from terrestrial EML; which gave a significantly different set of data owing to the strong electromagnetic stirring of the melt. The work of Willnecker *et al*. was undertaken using an EML technique. If a strong stirring of the melt was present, then this may have led to the remelting/fragmentation of a fragile dendritic/seaweed structure, and hence direct observation of the original growth structure would not be possible.

It could therefore be that the use of the melt fluxing apparatus employed in this work has allowed the original seaweed structure to be retained. Binder *et al.* state that, even within the melt fluxing equipment employed in their work, fluid flow effects are observed due to externally imposed temperature gradients. By contrast, the melt-fluxing equipment employed in the present work should minimise this effect since, in contrast to that employed by Binder *et al*., the sample is fully submerged in flux (whereas the top half of their sample is not) and a graphite susceptor is employed, which will act as a large blackbody furnace (relative to the sample size), creating a very uniform radiation environment. Hence, through the minimisation

of externally induced fluid flow processes, the technique employed in the present work enables a more stable retention of the original growth structures, and subsequently increases the likelihood that delicate seaweed microstructures will be observed.

With this in mind, the Cu-Ni spontaneous grain refinement mechanism map (**Figure 28** produced in Chapter 2.5 from the data and mechanisms reported in the literature) has been revisited and altered (**Figure 89**); based on the present work. It is difficult to project the observations of the present work onto the full mechanism map based on only two sets of data; especially given the apparent disagreement between the different studies, which may be due to the issues discussed above regarding fluid flow and the possible overlooking of orientation transitions etc… As such, the additional mechanisms have been introduced and represented with colour gradients to reflect the uncertainty in the extent of their existence within this parameter space. Further work using identical techniques would be required in order to investigate the full compositional and undercooling range.

Overall, this investigation has highlighted the extreme complexity of dendrite growth under rapid solidification conditions. Based on the findings, it is suggested that future spontaneous grain refinement studies should:

- include more careful considerations of the character of the dendrites,
- be aware of the influence of convective processes in the melt on the final microstructures obtained,
- not rule out a switch in the preferred growth orientation, and;
- analyse the v – ΔT data more closely for the identification of any less-apparent positive breaks in the trend.

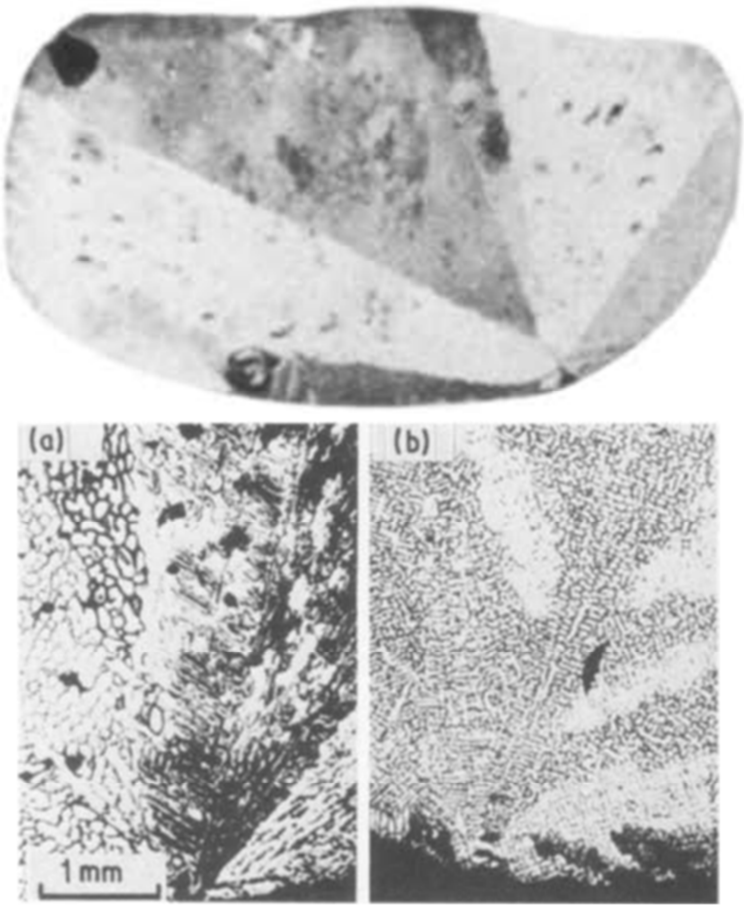

Figure 85 Examples of microstructures previously reported by Kobayashi and Shingu (1988) showing the 'fan-like' grains radiating outward from a single nucleation point and related by twinning operations, which appear much like the cyclically twinned samples observed in this report (**top**) and which contain dendritic structures which look very like the reported seaweed/split dendrite branches (**bottom**).

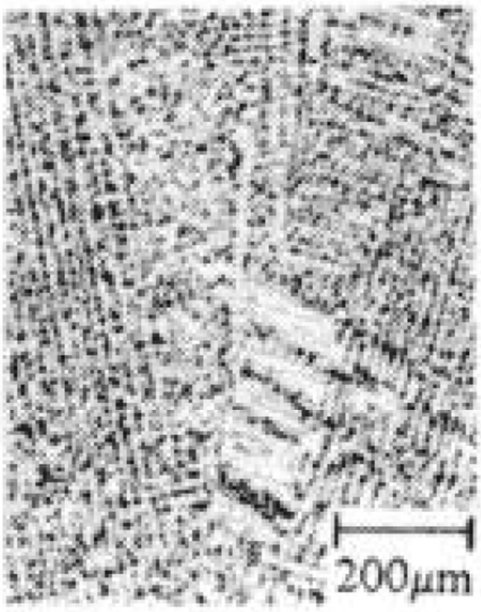

Figure 86 Image of microstructure of a Cu-Ni alloy observed at intermediate undercoolings by Schwarz *et al*. (1994), which appears to show fanned arrays of dendrite/seaweed morphologies similar to that observed in the present work.

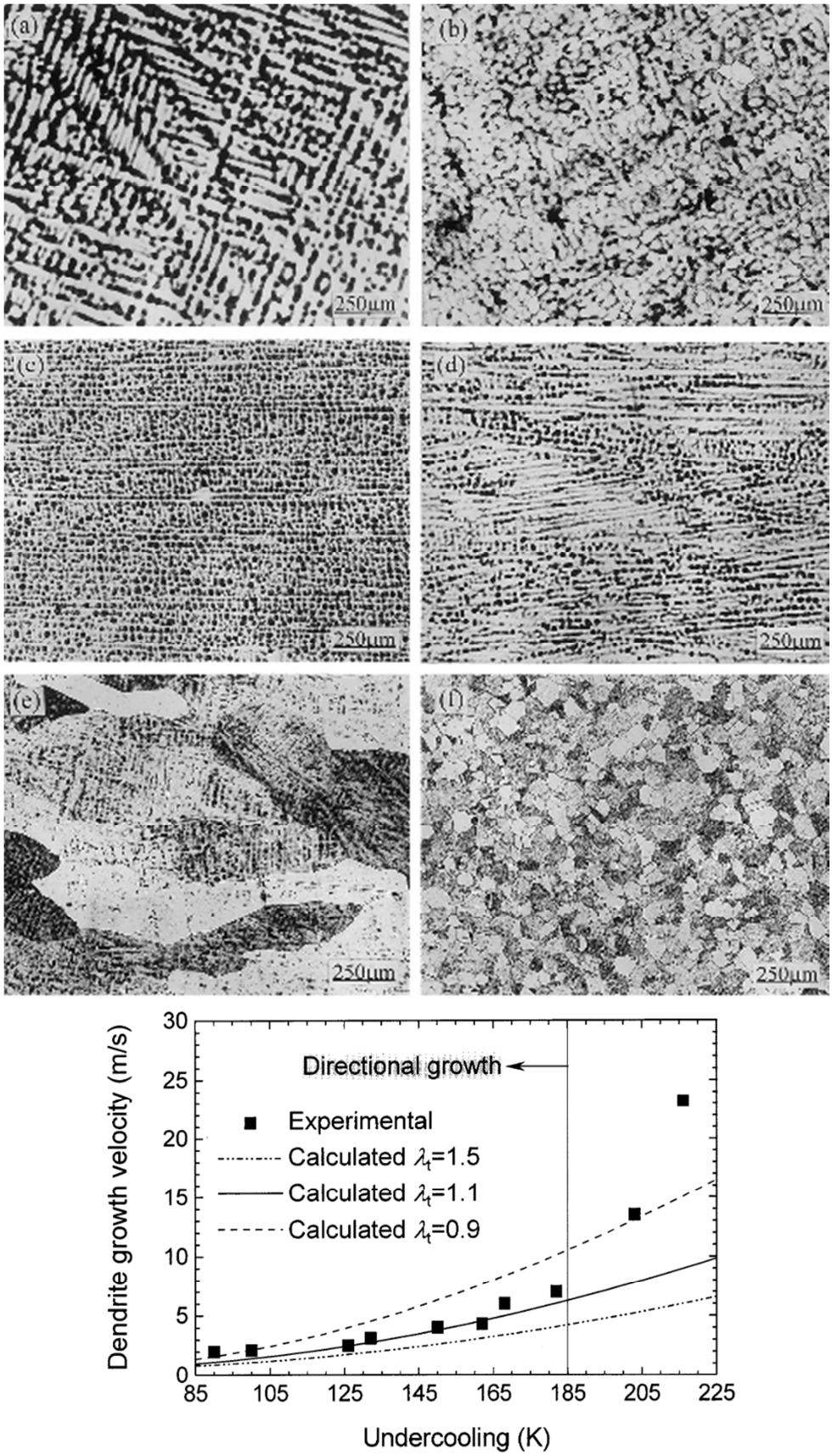

Figure 87 Microstructures (**top**) and *v*-ΔT relationship (**bottom**) observed by Li *et al*. (2000) in a Cu-Ni alloy. Microstructures are observed at undercoolings of a) 10 K b) 65 K c) 160 K d) 180 K e) 195 K f) 221 K. The *v*-ΔT relationship is shown alongside the calculated directional dendrite growth relationships (shown by the plotted lines) for different values of an undetermined scaling factor λ_t.

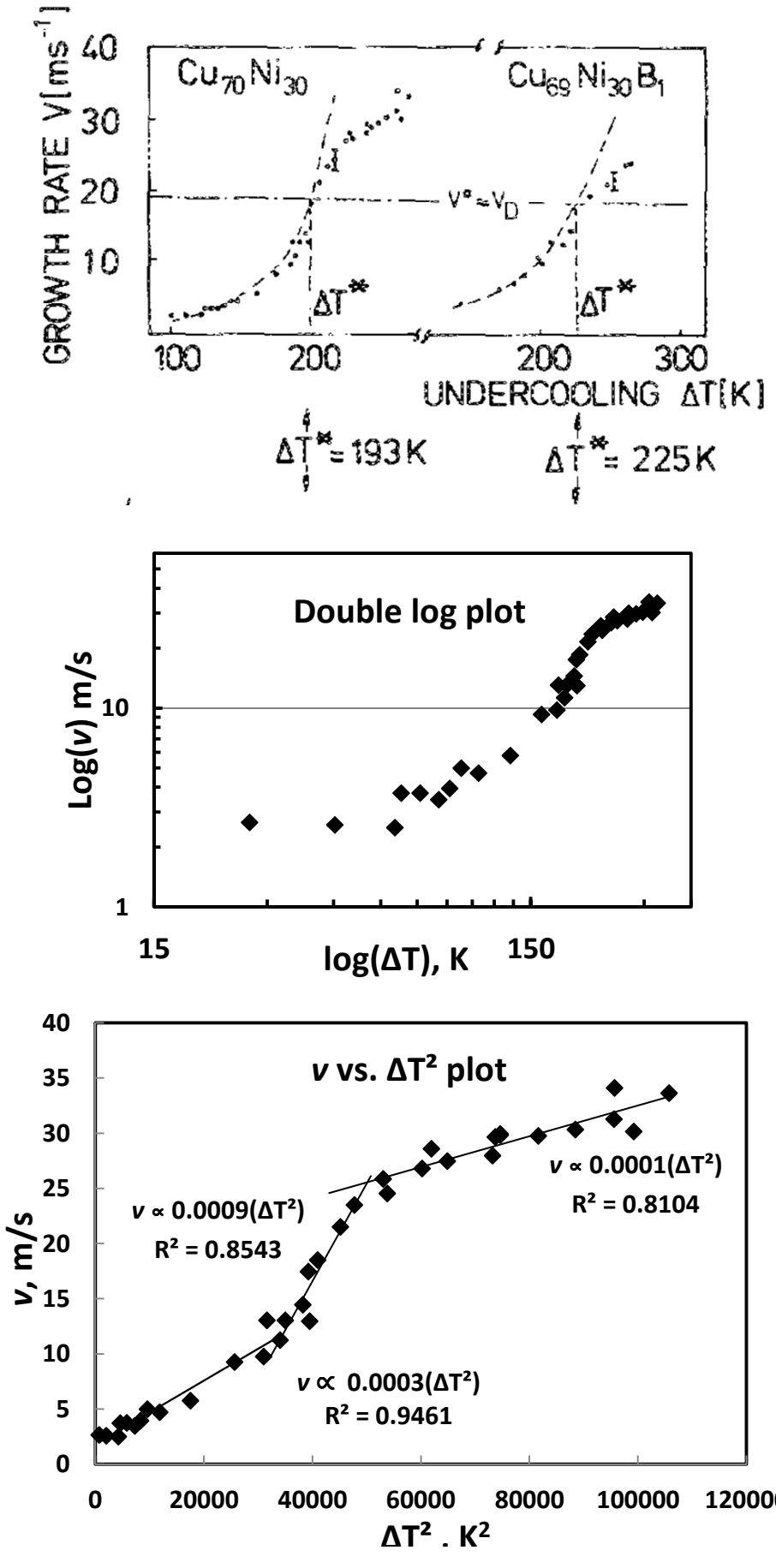

Figure 88 Re-modelling of the $Cu_{70}Ni_{30}$ data of Willnecker *et al.* (1990) (data on left-hand side). (**Top**) original data, (**middle**) double log plot of data, (**bottom**) *v* vs. ΔT^2 plot of data.

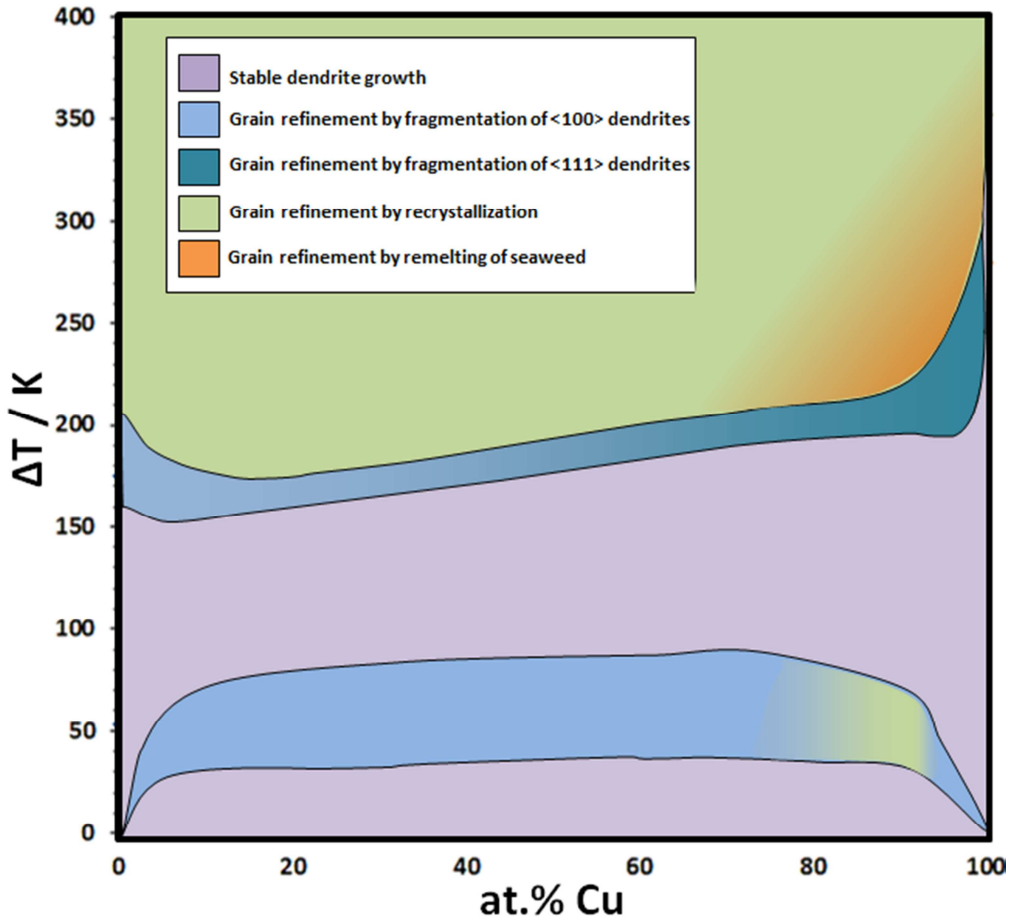

Figure 89 Development of the mechanism map shown in **Figure 28**, based on the results of the present work.

7. CONCLUSIONS

1) It has been shown that a soda lime flux is not chemically compatible with Cu-Ni alloys, and is therefore not suitable for use in the containerless melt fluxing technique. B_2O_3 is chemically compatible, but has a viscosity which is too low to support the sample away from the crucible walls. As such, a mixture of dewatered B_2O_3 and Na_2 SiO_3 has been employed to successfully undercool two compositions of Cu-Ni alloy by up to ΔT = 240 K.
2) Using the optimised melt fluxing procedure, a detailed examination of the texture and microstructural development of both a Cu-8.9 wt.% Ni and a Cu-3.98 wt.% Ni alloy with increasing undercooling has been undertaken. By imaging the nucleation points visible on the surface of the undercooled droplets, and examining their texture and interior microstructure, a number of novel discoveries have been made.
3) It appears that the addition of Ni to Cu leads to either an increase in the strength of the kinetic anisotropy, or a weakening of the capillary anisotropy via modifications to the interfacial free energy. With increasing departure from equilibrium it is then suggested that the effect of the kinetic anisotropy increases to compete with the capillary anisotropy. This leads to an extended transition in preferred dendrite growth orientation, from <100> at low undercooling to <111> at high undercooling, which is observed in both alloys. There is novelty in the extent of this transition, which represents a significant observation since it challenges conventional dendrite growth theory and highlights the importance of the roles of other anisotropies in non-equilibrium solidification processes.
4) In between the two separately-oriented regimes, a transitional, mixed-orientation regime is observed in both alloys, in which the competing kinetic and capillary anisotropies are of comparable strength. This gives rise to dendrites of mixed-orientation and a range of diverging split primary dendrite branches, into which secondary arms of varied morphology (ranging from dendritic to seaweed-like in character) grow. Such microstructures have not previously been reported, however it appears they may have been overlooked in previous studies.
5) The competing anisotropies present at intermediate undercoolings also appear to be giving rise to twinning in both alloys. In the more concentrated alloy, multiple twinning is present in the form of cyclic twinning. It is suggested that the presence of more solute, which has to be incorporated into growing crystal, might increase the likelihood of developing stacking faults during growth; thereby accounting for the observation of

multiple twinning in the high Ni alloy only, and supporting the theory of an increased kinetic anisotropy due to the addition of Ni. Cyclic twinning has not previously been reported within the context of spontaneous grain refinement, but, from a review of previous studies, it appears that such twinning operations may have previously gone unnoticed.

6) Two distinct low-undercooling grain refinement mechanisms have been identified in both alloys. For the less concentrated alloy, the mixed-orientation regime does not coincide with the first region of grain refinement, and hence a fragmentation mechanism is observed. For the more concentrated alloy, the mixed orientation regime does appear to coincide with the grain refinement region, altering the original growth structure present and resulting in a contrasting recovery/recrystallisation mechanism. The unambiguous identification of two separate grain refinement mechanisms in two closely related alloys is significant, since it may help to clear the debate surrounding the 'true' mechanism of grain refinement at low undercooling.
7) Beyond the mixed-orientation regimes, a transition to a finer-grained (but not spontaneously grain refined) microstructure is observed in the high Ni alloy, coincident with a positive break in the $v - \Delta T$ relationship. It is suggested that this occurs due to a transition to faster, fully <111>-oriented dendrite growth, which leads to a rapid refinement of the dendrites and subsequent fragmentation to produce a coarse dendritic grain structure. Such grain structures have not been observed in the low Ni alloy.
8) At $\Delta T = 220$ K a partially grain-refined sample has been obtained for the more concentrated alloy. Since the non-grain refined portion of this sample contains a dendritic seaweed substructure, it is suggested that this was the original growth structure which gave rise to the partial grain refinement through rapid remelting/fragmentation during recalescence. This therefore represents a third overall grain refinement mechanism to have been observed in the two Cu-Ni alloys.
9) Seaweed growth in the concentrated alloy is postulated to arise from the increased kinetic anisotropy (due to higher Ni content), which leads to a shift in the point at which the capillary and kinetic terms balance, to lower, more achievable undercoolings. It may also be due, in part, to the transition to fully <111>-oriented growth, in which the anisotropy is weak.
10) It is suggested that the melt fluxing technique employed in this work has allowed the retention of the delicate seaweed structure, where other undercooling methods may not, owing to the uniform radiation field imposed on the sample and the subsequent reduction in externally-imposed fluid flow.

11) A spontaneous grain refinement transition has been observed in the more dilute alloy above $\Delta T = 185$ K. The refined grains are composed of individual dendrite fragments; suggesting that the precursor structure was dendritic, rather than seaweed, in character and that grain refinement therefore arose from the remelting of dendrites. It is suggested that seaweed growth is not observed in this alloy, since the lower Ni content (and therefore lower kinetic anisotropy) would lead to a shift in the point at which the kinetic and capillary terms balance to higher undercoolings, and therefore out of the achievable undercooling range.
12) The observed positive breaks in the $v - \Delta T$ relationship are difficult to identify in comparison to the more usual negative ΔT^* break. It has been demonstrated through re-evaluation of some previous $v - \Delta T$ data that a positive break has gone unnoticed on at least one occasion, and hence growth orientation transitions may be more common than previously thought.

8. SUGGESTIONS FOR FUTURE WORK

Following the discoveries made in the present report, some suggestions can be made as to the direction of future work in this area.

1) Similar investigations into further compositions of Cu-Ni alloys could be made in order to examine any associated shifts in the microstructural transitions observed in this report. The influence of solute concentration on the solidification of undercooled melts could then be more firmly deduced. In particular, compositions which are intermediate between the two alloys investigated in this report would be interesting in order to investigate the shift in grain refinement mechanism at low undercooling. It would also be interesting to see if the growth orientation transition occurs over the full compositional range of the alloy, and to investigate the impact that this has on the spontaneous grain refinement mechanism at high undercooling. Alternative alloying elements can then be substituted for Ni, and the impact which these have upon the growth transitions can be examined in the same way.
2) A closer look at the exact twinning relationships occurring in cyclically twinned samples would be useful in deducing the twinning mechanism – through a twinned nucleus or from the development of stacking faults during growth? This may reveal more information about the solidification process and whether cyclic twinning is relevant to the spontaneous grain refinement mechanism.
3) A further study into the porosity patterns observed in the rapidly solidified samples may yield some interesting and useful information on the solidification process.
4) In order to examine further the development of dendritic seaweed and whether it can give rise to spontaneous grain refinement, detailed research in which an attempt at forcing seaweed growth in metals would be advantageous. From what we know about dendritic seaweed currently, it appears to arise either when large departures from equilibrium are reached, or when growth is forced in a direction which is largely misoriented with respect to the preferred growth orientation. Hence, a directional solidification setup which utilises high withdrawal speeds, or possibly a supercooling directional solidification (SDS) setup, could be employed. If solidification is then nucleated from a crystalline seed which is misoriented with respect to the preferred growth orientation, then presumably the chances of producing a seaweed structure will be increased. A quenching stage may be required to retain this structure. If this is successful, then the research can focus on how the seaweed is influenced by the growth conditions, more detailed microstructural analysis can be employed and the

physical properties of the seaweed can be measured. Attempts might then be made to induce spontaneous grain refinement by reheating samples to different temperatures for varied hold times. Comparisons between the microstructure of these samples and spontaneously grain refined droplets can then be made and any parallels drawn. The grain refined samples can also be characterised in terms of their physical properties and compared to the properties of the seaweed precursor. If all of this is successful, then this may provide a significant contribution to the future development of industrial scale spontaneous grain refinement techniques.

5) In order to truly get to the bottom of rapid dendrite growth problems; in situ recordings of rapid dendrite growth in three dimensions, using high-speed x-ray tomography at the Diamond Light Source, could be employed. This would allow direct analysis of the character, scale and orientation of the original growth structure; without requiring any post-solidification analysis. Dendrite growth models would then have accurate, contiguous data from which they could be developed and refined.

9. REFERENCES

ABBASCHIAN, G. J. & DAVID, S. A. 1983. Grain refinement in castings and welds : proceedings of a symposium. *In*, Warrendale, Pa.: The Metallurgical Society.

AHMAD, R. 2010. *Rapid Solidification on Intermetallic Compounds by Melt Fluxing.* PhD Thesis, University of Leeds.

AHMAD, R., COCHRANE, R. F. & MULLIS, A. M. 2012. The formation of regular αNi-γ(Ni 31Si 12) eutectic structures from undercooled Ni-25 at.% Si melts. *Intermetallics,* 22**,** 55-61.

AKAMATSU, S., FAIVRE, G. & IHLE, T. 1995. Symmetry-broken double fingers and seaweed patterns in thin-film directional solidification of a nonfaceted cubic crystal. *Physical Review E,* 51**,** 4751-4773.

ALGOSO, P. R., HOFMEISTER, W. H. & BAYUZICK, R. J. 2003. Solidification velocity of undercooled Ni-Cu alloys. *Acta Materialia,* 51**,** 4307-4318.

AVRAMOV, I., VASSILEV, T. & PENKOV, I. 2005. The glass transition temperature of silicate and borate glasses. *Journal of Non-Crystalline Solids,* 351**,** 472-476.

AZIZ, M. J. 1982. Model for solute redistribution during rapid solidification. *Journal of Applied Physics,* 53**,** 1158-1168.

BARBIERI, A. & LANGER, J. S. 1989. Predictions of dendritic growth rates in the linearized solvability theory. *Physical Review A,* 39**,** 5314-5325.

BASSLER, B. T., HOFMEISTER, W. H. & BAYUZICK, R. J. 2003. The solidification velocity of pure nickel. *Materials Science and Engineering: A,* 342**,** 80-92.

BATTERSBY, S. E., COCHRANE, R. F. & MULLIS, A. M. 1999. Growth velocity-undercooling relationships and microstructural evolution in undercooled Ge and dilute Ge-Fe alloys. *Journal of Materials Science,* 34**,** 2049-2056.

BECKER & DORING 1935. *Ann. Phys.,* 24**,** 719.

BEN-JACOB, E., DEUTSCHER, G., GARIK, P., GOLDENFELD, N. D. & LAREAH, Y. 1986. Formation of a Dense Branching Morphology in Interfacial Growth. *Physical Review Letters,* 57**,** 1903-1906.

BEN-JACOB, E., GODBEY, R., GOLDENFELD, N. D., KOPLIK, J., LEVINE, H., MUELLER, T. & SANDER, L. M. 1985. Experimental demonstration of the role of anisotropy in interfacial pattern formation. *Physical Review Letters,* 55**,** 1315-1318.

BEN-JACOB, E., GOLDENFELD, N., KOTLIAR, B. G. & LANGER, J. S. 1984a. Pattern selection in dendritic solidification. *Physical Review Letters,* 53**,** 2110-2113.

BEN-JACOB, E., GOLDENFELD, N., LANGER, J. S. & SCHÖN, G. 1983. Dynamics of interfacial pattern formation. *Physical Review Letters,* 51**,** 1930-1932.

BEN-JACOB, E., GOLDENFELD, N., LANGER, J. S. & SCHÖN, G. 1984b. Boundary-layer model of pattern formation in solidification. *Physical Review A,* 29**,** 330-340.

BEN AMAR, M. & BRENER, E. 1993. Theory of pattern selection in three-dimensional nonaxisymmetric dendritic growth. *Physical Review Letters,* 71**,** 589-592.

BENDERSKY, L. A. & RIDDER, S. D. 1986. Nucleation behavior of Al-Mn icosahedral phase. *Journal of Materials Research,* 1**,** 405-414.

BINDER, S., GALENKO, P. K. & HERLACH, D. M. 2014. The effect of fluid flow on the solidification of Ni_2B from the undercooled melt. In Press.

BIROL, Y. 2007. Microstructural evolution during annealing of a rapidly solidified Al–12Si alloy. *Journal of Alloys and Compounds,* 439**,** 81-86.

BISANG, U. & BILGRAM, J. H. 1996. Shape of the tip and the formation of sidebranches of xenon dendrites. *Physical Review E,* 54**,** 5309.

BOTTA, W. J., OTA, K., HAJLAOUI, K., VAUGHAN, G. & YAVARI, A. R. 2008. Glass transition, thermal expansion and relaxation in B2O3 glass measured by time-resolved X-ray diffraction. *Journal of Non-Crystalline Solids,* 354**,** 325-327.

BRAGARD, J., KARMA, A., LEE, Y. & PLAPP, M. 2002. Linking Phase-Field and Atomistic Simulations to Model Dendritic Solidification in Highly Undercooled Melts. *Interface Science,* 10**,** 121-136.

BRENER, E., MÜLLER-KRUMBHAAR, H., SAITO, Y. & TEMKIN, D. 1993. Crystal growth in a channel: Numerical study of the one-sided model. *Physical Review E,* 47**,** 1151-1155.

BRENER, E., MÜLLER-KRUMBHAAR, H. & TEMKIN, D. 1992. Kinetic phase diagram and scaling relations for stationary diffusional growth. *Europhysics Letters,* 17**,** 535.

BRENER, E., MÜLLER-KRUMBHAAR, H. & TEMKIN, D. 1996. Structure formation and the morphology diagram of possible structures in two-dimensional diffusional growth. *Physical Review E,* 54**,** 2714-2722.

BROWER, R. C., KESSLER, D. A., KOPLIK, J. & LEVINE, H. 1983. Geometrical Approach to Moving-Interface Dynamics. *Physical Review Letters,* 51**,** 1111-1114.

BROWER, R. C., KESSLER, D. A., KOPLIK, J. & LEVINE, H. 1984. Geometrical models of interface evolution. *Physical Review A,* 29**,** 1335-1342.

CAHN, R. W. & GREER, A. L. 1996. Metastable States of Alloys. *In:* CAHN, R. W. & HAASEN, P. (eds.) *Physical Metallurgy.* Fourth ed.: Elsevier Science BV.

CAO, L., COCHRANE, R. F. & MULLIS, A. M. 2013. Lamella structure formation in drop-tube processed Ni–25.3at.% Si alloy. *Journal of Alloys and Compounds*.

CHEN, Y. Z., LIU, F., YANG, G. C., LIU, N., YANG, C. L., XIE, H. & ZHOU, Y. H. 2008a. Grain refinement of $Fe_{75}Ni_{25}$ alloys at low undercooling. *Materials Characterization,* 59**,** 412-416.

CHEN, Z., LIU, F., WANG, H., YANG, W., YANG, G. & ZHOU, Y. 2008b. Formation of single-phase supersaturated solid solution upon solidification of highly undercooled Fe–Cu immiscible system. *Journal of Crystal Growth,* 310**,** 5385-5391.

CHENG, J.-J., APELIAN, D. & DOHERTY, R. 1986. Processing-structure characterization of rheocast IN-100 superalloy. *Metallurgical Transactions A,* 17**,** 2049-2062.

CHOPRA, M. A., GLICKSMAN, M. E. & SINGH, N. B. 1988. Dendritic solidification in binary alloys. *Metallurgical Transactions A,* 19**,** 3087-3096.

CLINE, H. E. 1971. Shape instabilities of eutectic composites at elevated temperatures. *Acta Metallurgica,* 19**,** 481-490.

COCHRANE, R. F., BATTERSBY, S. E. & MULLIS, A. M. 2001. The mechanisms for spontaneous grain refinement in undercooled Cu-O and Cu-Sn melts. *Materials Science and Engineering: A,* 304-306**,** 262-266.

COCHRANE, R. F., GREER, A. L., ECKLER, K. & HERLACH, D. M. 1991a. Dendrite growth velocities in undercooled Ni---Si alloys. *Materials Science and Engineering: A,* 133**,** 698-701.

COCHRANE, R. F. & HERLACH, D. M. 1989. *In:* 7th European symp on 'materials and fluid sciences under microgravity', Oxford. B H Kaldeich, 147-156.

COCHRANE, R. F., HERLACH, D. M. & FEUERBACHER, B. 1991b. Grain refinement in drop-tube-processed nickel-based alloys. *Materials Science and Engineering: A,* 133**,** 706-710.

COLLIGAN, G. A., SUPRENANT, V. A. & LEMKEY, F. D. 1961. *Journal of Metals,* 13**,** 691.

CONCORDIA-COLLEGE. 2013. Simultaneous determination of manganese and nickel in steel by inductively coupled plasma atomic emission spectrometry. *Analytical Chemistry Laboratory Manual* [Online]. Available: http://wwwp.cord.edu/dept/chemistry/analyticallabmanual/experiments/icpaes/intro.html [Accessed 01/09/2013].

CORIELL, S. R. & TURNBULL, D. 1982. Relative roles of heat transport and interface rearrangement rates in the rapid growth of crystals in undercooled melts. *Acta Metallurgica,* 30**,** 2135-2139.

CORRIGAN, D. P., KOSS, M. B., LACOMBE, J. C., DE JAGER, K. D., TENNENHOUSE, L. A. & GLICKSMAN, M. E. 1999. Experimental measurements of sidebranching in thermal dendrites under terrestrial-gravity and microgravity conditions. *Physical Review E,* 60**,** 7217.

CRYSTAL-TREASURE.COM. 2014. *Top perfect cyclic chrysoberyl crystal* [Online]. Available: http://www.crystal-treasure.com/product_info.php/info/p5376_Top-Perfekter-zyklischer-Chrysoberyl-Trilling.html [Accessed 23/01/2014].

DANTZIG, J. A., NAPOLI, P. D., FRIEDLI, J. & RAPPAZ, M. 2013. Dendritic growth morphologies in Al-Zn Alloys - Part II: Phase-field computations. *Metallurgical and Materials Transactions A,* 44.

DANTZIG, J. A. & RAPPAZ, M. 2009. *Solidification,* Boca Raton, CRC Press.

DEVAUD, G. & TURNBULL, D. 1987. Microstructures of undercooled Germanium droplets. *Acta Metallurgica,* 35**,** 765-769.

DMOWSKI, W., FAN, C., MORRISON, M. L., LIAW, P. K. & EGAMI, T. 2007. Structural changes in bulk metallic glass after annealing below the glass-transition temperature. *Materials Science and Engineering: A,* 471**,** 125-129.

DOHERTY, R. D., HUGHES, D. A., HUMPHREYS, F. J., JONAS, J. J., JENSEN, D. J., KASSNER, M. E., KING, W. E., MCNELLEY, T. R., MCQUEEN, H. J. & ROLLETT, A. D. 1997. Current issues in recrystallization: a review. *Materials Science and Engineering: A,* 238**,** 219-274.

DRAGNEVSKI, K. I. 2002. *Microstructural Evolution During Solidification into Undercooled Cu-based Melts.* Ph.D, University of Leeds.

DRAGNEVSKI, K. I., COCHRANE, R. F. & MULLIS, A. M. 2004a. The mechanism for spontaneous grain refinement in undercooled pure Cu melts. *Materials Science and Engineering A,* 375-377**,** 479-484.

DRAGNEVSKI, K. I., COCHRANE, R. F. & MULLIS, A. M. 2004b. The solidification of undercooled melts via twinned dendritic growth. *Metallurgical and Materials Transactions A,* 35**,** 3211-3220.

DUWEZ, P., WILLENS, R. H. & KLEMENT, W. 1960. *Journal of Applied Physics,* 31**,** 1136-7 & 1500.

ECKERT, J., MATTERN, N., ZINKEVITCH, M. & SEIDEL, M. 1998. Crystallization behavior and phase formation in Zr-Al-Cu-Ni metallic glass containing oxygen. *Materials Transactions, JIM,* 39**,** 623-632.

ECKLER, K., HERLACH, D. M., HAMERTON, R. G. & GREER, A. L. 1991a. Dendrite growth velocities in highly undercooled, dilute Ni–C melts. *In:* FREDRIKSSON, H. & SAVAGE, S. (eds.) *Rapidly Quenched Materials.* Oxford: Elsevier.

EDWARDS. 2013. *Edwards Vacuum Instruments* [Online]. Available: http://www.edwardsvacuum.com/Products/List.aspx?r=124 [Accessed].

EVANS, P. V., VITTA, S., HAMERTON, R. G., GREER, A. L. & TURNBULL, D. 1990. Solidification of germanium at high undercoolings: morphological stability and the development of grain structure. *Acta Metallurgica et Materialia,* 38**,** 233-242.

FLEMINGS, M. C. 1974. *Solidification Processing,* New York, NY, McGraw-Hill.

FMF. 2014. *Cyclic twinning* [Online]. Available: http://www.mineral-forum.com/message-board/viewtopic.php?p=26992 [Accessed].

GALENKO, P. K., PHANIKUMAR, G., FUNKE, O., CHERNOVA, L., REUTZEL, S., KOLBE, M. & HERLACH, D. M. 2007. Dendritic solidification and fragmentation in undercooled Ni-Zr alloys. *Materials Science and Engineering: A,* 449-451**,** 649-653.

GAO, J. & WEI, B. 1999. Containerless solidification of undercooled NdFeZrB alloy droplets in a drop tube. *Journal of Alloys and Compounds,* 285**,** 229-232.

GILL, W. N., JANG, J. & MOLLENDORF, J. C. 1981. Rapid Solidification of Subcooled Small Metallic Drops. *Chemical Engineering Communications,* 12**,** 3-31.

GLICKSMAN, M. E. 1965. Dynamic effects arising from high-speed solidification. *Acta Metallurgica,* 13**,** 1231-1246.

GLICKSMAN, M. E. & LUPULESCU, A. O. 2004. Dendritic crystal growth in pure materials. *Journal of Crystal Growth,* 264**,** 541-549.

GLICKSMAN, M. E., SCHAEFER, R. J. & AYERS, J. D. 1976. Dendritic growth-A test of theory. *Metallurgical Transactions A,* 7**,** 1747-1759.

GONZALES, F. & RAPPAZ, M. 2006. Dendrite growth directions in aluminum-zinc alloys. *Metallurgical and Materials Transactions A,* 37**,** 2797-2806.

GONZALES, F. & RAPPAZ, M. 2008. Grain Selection and Texture Evolution in Directionally Solidified Al-Zn Alloys. *Metallurgical and Materials Transactions A,* 39**,** 2148-2160.

GREER, A. L. 2009. Metallic glasses…on the threshold. *Materials Today,* 12**,** 14-22.

GRIER, D., BEN-JACOB, E., CLARKE, R. & SANDER, L. M. 1986. Morphology and Microstructure in Electrochemical Deposition of Zinc. *Physical Review Letters,* 56**,** 1264-1267.

GUDGEL, K. A. & JACKSON, K. A. 2001. Oscillatory growth of directionally solidified ammonium chloride dendrites. *Journal of Crystal Growth,* 225**,** 264-267.

GULYAEV, A. P. & TRUSOVA, E. F. 1950. *Zhur. Tekh. Fiz.,* 20**,** 66.

HALL, E. O. 1951. The deformation and ageing of mild steel: III Discussion of results. *Proceedings of the Physical Society,* 64**,** 747.

HAN, X. J., YANG, C., WEI, B., CHEN, M. & GUO, Z. Y. 2001. Rapid solidification of highly undercooled Ni-Cu alloys. *Materials Science and Engineering: A,* 307**,** 35-41.

HAXHIMALI, T., KARMA, A., GONZALES, F. & RAPPAZ, M. 2006. Orientation selection in dendritic evolution. *Nat Mater,* 5**,** 660-664.

HENRY, S., MINGHETTI, T. & RAPPAZ, M. 1998a. Dendrite growth morphologies in aluminium alloys. *Acta Materialia,* 46**,** 6431-6443.

HENRY, S., RAPPAZ, M. & JARRY, P. 1998b. 〈110〉 dendrite growth in aluminum feathery grains. *Metallurgical and Materials Transactions A,* 29**,** 2807-2817.

HENRY, S., RAPPAZ, M., JARRY, P. & JOUNEAU, P. H. 1997. Electron backscattered diffraction investigation of the texture of feathery crystals in aluminum alloys. *Metallurgical and Materials Transactions A,* 28**,** 207-213.

HERLACH, D. M. 1991. Containerless undercooling and solidification of pure metals. *Annual Review of Materials Science,* 21**,** 23-44.

HERLACH, D. M., COCHRANE, R. F., EGRY, I., FECHT, H. J. & GREER, A. L. 1993. Containerless processing in the study of metallic melts and their solidification. *International Materials Reviews,* 38**,** 273-347.

HERLACH, D. M., HOLLAND-MORITZ, D. & GALENKO, P. 2007. Metastable solids from undercooled melts.

HERRING, R. 2013. EM course - kikuchi diffraction. Canada Foundation for Innovation.

HOFMANN, P. 2013. *Ultra High Vacuum* [Online]. Available: http://www.philiphofmann.net/surflec3/surflec005.html [Accessed].

HOFMEISTER, H. 2004. Fivefold twinned nanoparticles. *In:* NALWA, H. S. (ed.) *Encyclopedia of Nanoscience and Nanotechnology.* Halle, Germany: Max Planck Institute of Microstructure Physics.

HOFMEISTER, W. H., BAYUZICK, R. J. & ROBINSON, M. B. 1989. Noncontact temperature measurement of a falling drop. *International Journal of Thermophysics,* 10**,** 279-292.

HONG, S., CHOI, I. & NAM, S. 1984. Anomalous creep behaviour of a Ni-22 at % Cu alloy and the miscibility gap. *Journal of Materials Science,* 19**,** 1672-1679.

HORVAY, G. 1965. The tension field created by a spherical nucleus freezing into its less dense undercooled melt. *International Journal of Heat and Mass Transfer,* 8**,** 195-243.

HYERS, R. W. 2005. Fluid flow effects in levitated droplets. *Measurement Science and Technology,* 16**,** 394.

IHLE, T. & MÜLLER-KRUMBHAAR, H. 1993. Diffusion-limited fractal growth morphology in thermodynamical two-phase systems. *Physical Review Letters,* 70**,** 3083-3086.

IHLE, T. & MÜLLER-KRUMBHAAR, H. 1994. Fractal and compact growth morphologies in phase transitions with diffusion transport. *Physical Review E,* 49**,** 2972-2991.

INOUE, A., FAN, C., SAIDA, J. & ZHANG, T. 2000. High-strength Zr-based bulk amorphous alloys containing nanocrystalline and nanoquasicrystalline particles. *Science and Technology of Advanced Materials,* 1**,** 73.

IVANTSOV, G. P. 1947. *Doklady Akademii Nauk SSSR,* 58:567.

JACKSON, K. A. 1958. *Liquid Metals and Solidification,* Cleveland.

JACKSON, K. A., HUNT, J. D., UHLMANN, D. R. & SEWARD, T. P. 1966. Lamellar and rod eutectic growth. *Trans. TMS-AIME,* 236**,** 149-58.

JONES, B. L. & WESTON, G. M. 1970. *Journal of the Australian Institute of Metals,* 15**,** 167.

JONES, H. 1982. *Rapid Solidification of Metals and Alloys, Monograph no.8,* London, The Institution of Metallurgists.

KAHLWEIT, M. 1970. On the dendritic growth of NH_4Cl crystals from aqueous solutions. *Journal of Crystal Growth,* 6**,** 125-129.

KAMIO, A. Year. Proc. Japan-US Cooperative Science Program Seminar on Solidification Processing of Advanced Materials. *In:* Oiso, Japan Society for the Promotion of Science and NSF, 1989 Kanagawa, Japan. 195.

KARMA, A. & RAPPEL, W.-J. 1996a. Numerical simulation of three-dimensional dendritic growth. *Physical Review Letters,* 77**,** 4050-4053.

KARMA, A. & RAPPEL, W.-J. 1996b. Phase-field method for computationally efficient modeling of solidification with arbitrary interface kinetics. *Physical Review E,* 53**,** R3017-R3020.

KARMA, A. & RAPPEL, W.-J. 1998. Quantitative phase-field modeling of dendritic growth in two and three dimensions. *Physical Review E,* 57**,** 4323.

KATTAMIS, T. Z. 1976. Mechanism of establishment of cast microstructure during solidification of highly undercooled melts. *Journal of Crystal Growth,* 34**,** 215-220.

KATTAMIS, T. Z. & FLEMINGS, M. C. 1966. *Transactions of the Metallurgical Society of AIME,* 236**,** 1523-1532.

KATTAMIS, T. Z. & FLEMINGS, M. C. 1967. *Mod. Casting,* 52.

KESSLER, D. A., KOPLIK, J. & LEVINE, H. 1984. Geometrical models of interface evolution. II. Numerical simulation. *Physical Review A,* 30**,** 3161-3174.

KESSLER, D. A., KOPLIK, J. & LEVINE, H. 1988. Pattern selection in fingered growth phenomena. *Advances in Physics,* 37**,** 255-339.

KIM, S. U. & KOO, Y. M. 2004. Nucleation modes of the drop tube processed $Nd_{70}Fe_{20}Al_{10}$ droplets. *Materials Letters,* 58**,** 975-979.

KIM, Y.-T., GOLDENFELD, N. & DANTZIG, J. 2000. Computation of dendritic microstructures using a level set method. *Physical Review E,* 62**,** 2471-2474.

KOBAYASHI, K. F. & SHINGU, P. H. 1988. The solidification process of highly undercooled bulk Cu-O melts. *Journal of Materials Science,* 23**,** 2157-2166.

KÖSTER, U., MEINHARDT, J., ROOS, S. & LIEBERTZ, H. 1996. Formation of quasicrystals in bulk glass forming Zr–Cu–Ni–Al alloys. *Applied Physics Letters,* 69**,** 179-181.

KOTLER, G. R. & TILLER, W. A. 1968. Stability of the needle crystal. *Journal of Crystal Growth,* 2**,** 287-307.

KUPFERMAN, R., KESSLER, D. A. & BEN-JACOB, E. 1995. Coexistence of symmetric and parity-broken dendrites in a channel. *Physica A: Statistical Mechanics and its Applications,* 213**,** 451-464.

KURZ, W. 1989. *Fundamentals of Solidification,* Aedermannsdorf Trans Tech Publications, Switzerland.

LAFFERTY, J. M. 1998. *Foundations of Vacuum Science and Technology,* New York, John Wiley & Sons, Inc. (US).

LANGER, J. S. 1980. Instabilities and pattern formation in crystal growth. *Reviews of Modern Physics,* 52**,** 1-28.

LANGER, J. S. 1986. Models of pattern formation in first-order phase transitions. *In:* GRINSTEIN, G. & MAZENKO, G. (eds.) *Directions in Condensed Matter Physics.* Singapore: World Scientific.

LANGER, J. S. 1987. Lectures in the Theory of Pattern Formation. *In:* SOULETIE, J., VANNIMENUS, J. & STORA, R (eds.) *Chance and Matter.* North Holland: Rev. Mod. Phys. 629-711.

LANGER, J. S. & MÜLLER-KRUMBHAAR, H. 1978. Theory of dendritic growth--I. Elements of a stability analysis. *Acta Metallurgica,* 26**,** 1681-1687.

LEHMAN, L. P., ATHAVALE, S. N., FULLEM, T. Z., GIAMIS, A. C., KINYANJUI, R. K., LOWENSTEIN, M., MATHER, K., PATEL, R., RAE, D., WANG, J., XING, Y., ZAVALIJ, L., BORGESEN, P. & COTTS, E. J. 2004. Growth of Sn and intermetallic compounds in Sn-Ag-Cu solder. *Journal of Electronic Materials,* 33**,** 1429-1439.

LEHMAN, L. P., XING, Y., BIELER, T. R. & COTTS, E. J. 2010. Cyclic twin nucleation in tin-based solder alloys. *Acta Materialia,* 58**,** 3546-3556.

LI, D., ECKLER, K. & HERLACH, D. M. 1996. Undercooling, crystal growth and grain structure of levitation melted pure Ge and Ge---Sn alloys. *Acta Materialia,* 44**,** 2437-2443.

LI, J. F., ZHOU, Y. H. & YANG, G. C. 2000. Solidification behavior of undercooled $Cu_{70}Ni_{30}$ alloy melt. *Materials Science and Engineering A,* 277**,** 161-168.

LI, Q. & BECKERMANN, C. 2002. Modeling of free dendritic growth of succinonitrile–acetone alloys with thermosolutal melt convection. *Journal of Crystal Growth,* 236**,** 482-498.

LIPTON, J., GLICKSMAN, M. E. & KURZ, W. 1984. Dendritic growth into undercooled alloy metals. *Materials Science and Engineering,* 65**,** 57-63.

LIPTON, J., KURZ, W. & TRIVEDI, R. 1987. Rapid dendrite growth in undercooled alloys. *Acta Metallurgica,* 35**,** 957-964.

LIU, L., LI, J. F. & ZHOU, Y. H. 2011. Solidification interface morphology pattern in the undercooled Co–24.0 at.% Sn eutectic melt. *Acta Materialia,* 59**,** 5558-5567.

LIU, L. X. & KIRKALDY, J. S. 1995. Thin film forced velocity cells and cellular dendrites—I. Experiments. *Acta Metallurgica et Materialia,* 43**,** 2891-2904.

LSM-ANALYTICAL-SERVICES. 2013a. *Carbon, Sulphur, Nitrogen, Oxygen and Hydrogen Analysers* [Online]. Available: http://www.lsmanalytical.com/gases.aspx [Accessed 10/09/2013].

LSM-ANALYTICAL-SERVICES 2013b. ICP Testing Information Document. *www.lsmanalytical.com.*

MATSON, D. 1998. *In:* TMS, Warrendale, Pa. Minerals, Metals & Materials Society, 233-244.

MONDOLFO, L. F. (ed.) 1983. *Grain refinement in casting and welds,* Warrendale, PA: Metallurgical society of AIME.

MULLINS, W. W. & SEKERKA, R. F. 1964. Stability of a Planar Interface During Solidification of a Dilute Binary Alloy. *Journal of Applied Physics,* 35**,** 444-451.

MULLIS, A. M. 2011. Prediction of the operating point of dendrites growing under coupled thermosolutal control at high growth velocity. *Physical Review E,* 83**,** 061601.

MULLIS, A. M. 2012. Phase-field modelling of rapid solidification in alloy systems: Spontaneous grain refinement effects. *IOP Conference Series: Materials Science and Engineering,* 33.

MULLIS, A. M. & COCHRANE, R. F. 2000. On the Karma Model for Spontaneous Grain Refinement at High Solid Fractions. *International Journal of Non-Equilibrium Processing,* 11**,** 283-297.

MULLIS, A. M., DRAGNEVSKI, K. I. & COCHRANE, R. F. 2004a. The solidification of undercooled melts via twinned dendritic growth. *Materials Science and Engineering A,* 375-377**,** 547-551.

MULLIS, A. M., DRAGNEVSKI, K. I. & COCHRANE, R. F. 2004b. The transition from the dendritic to the seaweed growth morphology during the solidification of deeply undercooled metallic melts. *Materials Science and Engineering A,* 375-377**,** 157-162.

MUSEUMWALES. 2014. *Mineralogy of Wales* [Online]. Available: http://www.museumwales.ac.uk/en/800/?mineral=73 [Accessed].

NELSON, D. R. & SPAEPEN, F. 1989. Polytetrahedral Order in Condensed Matter. *Solid State Physics.* San Diego, CA: Academic Press, 42, 1-90.

NORMAN, A. F., ECKLER, K., ZAMBON, A., GÄRTNER, F., MOIR, S. A., RAMOUS, E., HERLACH, D. M. & GREER, A. L. 1998. Application of microstructure-selection maps to droplet solidification: a case study of the Ni–Cu system. *Acta Materialia,* 46**,** 3355-3370.

OLDFIELD, W. 1973. Computer model studies of dendritic growth. *Materials Science and Engineering,* 11**,** 211-218.

OMEGA 2003. Transactions in Measurement and Control - Force-Related Measurements. *A Technical Reference Series Brought to You by OMEGA.* Omega.

OSHER, S. & SETHIAN, J. A. 1988. Fronts propagating with curvature-dependent speed: Algorithms based on Hamilton-Jacobi formulations. *Journal of Computational Physics,* 79**,** 12-49.

OVSIYENKO, D. E., MASLOV, V. V. & ALFINTSEV, G. A. 1974. *Journal of Russian Metallurgy***,** 1974, 66-69.

OVSIYENKO, D. E., MASLOV, V. V., ALFINTSEV, G. A. & OGANYAN, L. E. 1976. *Journal of Russian Metallurgy*, 1976, 92-94.

OXFORD-INSTRUMENTS. 2013. *EBSD - The Diffraction Pattern* [Online]. Available: http://www.ebsd.com/index.php/component/content/article/83-ebsd-for-beginners/111-the-diffraction-pattern [Accessed 17/09/2013].

OZAWA, S. & KURIBAYASHI, K. 2006. Microstructures of Fe_2RE (RE; Tb and Nd) alloys produced by drop tube processing. *Journal of Alloys and Compounds,* 415**,** 129-133.

PAPAPETROU, A. Z. 1935. *Z. f. Kristallograph,* 92**,** 89.

PEREPEZKO, J. H. 1984. Nucleation in undercooled liquids. *Materials Science and Engineering,* 65**,** 125.

PETCH, N. J. 1953. The cleavage strength of polycrystals. *Journal of Iron and Steel Institute,* 174**,** 25-8.

PORTER, D. A. & EASTERLING, K. E. 1992. *Phase Transformations in Metals and Alloys,* London, Chapman & Hall.

POWELL, G. L. F. & HOGAN, L. M. 1969. *Transactions of the Metallurgical Society of AIME,* 245**,** 407.

RAMIREZ, J. C. & BECKERMANN, C. 2005. Examination of binary alloy free dendritic growth theories with a phase-field model. *Acta Materialia,* 53**,** 1721-1736.

RAMIREZ, J. C., BECKERMANN, C., KARMA, A. & DIEPERS, H. J. 2004. Phase-field modeling of binary alloy solidification with coupled heat and solute diffusion. *Physical Review E,* 69**,** 051607.

REID, R. J. 2007. Vacuum Science and Technology in Accelerators. *Cockroft Institute Lectures.*

REY, C. A., MERKLEY, D. R., HAMPTON, S., DEVOS, J., MAPES-RIORDAN, D. & ZATARSKI, M. 1991. Containerless processing at high temperatures using acoustic levitation. *Advances in Space Research,* 11**,** 69-77.

ROSAM, J., JIMACK, P. K. & MULLIS, A. M. 2008. An adaptive, fully implicit multigrid phase-field model for the quantitative simulation of non-isothermal binary alloy solidification. *Acta Materialia,* 56**,** 4559-4569.

ROSAM, J., JIMACK, P. K. & MULLIS, A. M. 2009. Quantitative phase-field modeling of solidification at high Lewis number. *Physical Review E,* 79**,** 030601.

RUTTER, J. & CHALMERS, B. 1953. *Can. J. Phys.,* 31**,** 15.

SAIDA, J. & INOUE, A. 2003. Quasicrystals from glass devitrification. *Journal of Non-Crystalline Solids,* 317**,** 97-105.

SANDER, L. M., RAMANLAL, P. & BEN-JACOB, E. 1985. Diffusion-limited aggregation as a deterministic growth process. *Physical Review A,* 32**,** 3160-3163.

SATO, T., NAKAMURA, T. & OZAWA, F. 1975. Thermal decomposition of nickel hydroxide. *Journal of Applied Chemistry and Biotechnology,* 25**,** 583-590.

SAWADA, Y. 1986. Transition of growth form from dendrite to aggregate. *Physica A: Statistical Mechanics and its Applications,* 140**,** 134-141.

SAWADA, Y., DOUGHERTY, A. & GOLLUB, J. P. 1986. Dendritic and Fractal Patterns in Electrolytic Metal Deposits. *Physical Review Letters,* 56**,** 1260-1263.

SCHAEFER, R. J. & GLICKSMAN, M. E. 1967. Direct observation of dendrite remelting in metal alloys. *Trans. AIME,* 239**,** 257.

SCHLEIP, E., HERLACH, D. M. & FEUERBACHER, B. 1990. External seeding of a metastable metallic phase. *Europhysics Letters,* 11**,** 751.

SCHROERS, J. Year. Identifying bulk metallic glass compositions through combinatiorial strategies. *In:* ISMANAM2013, 2013 Turin, Italy. Journal of Alloys and Compounds.

SCHWARZ, M., KARMA, A., ECKLER, K. & HERLACH, D. M. 1994. Physical Mechanism of Grain Refinement in Solidification of Undercooled Melts. *Physical Review Letters,* 73**,** 1380.

SÉMOROZ, A., DURANDET, Y. & RAPPAZ, M. 2001. EBSD characterization of dendrite growth directions, texture and misorientations in hot-dipped Al–Zn–Si coatings. *Acta Materialia,* 49**,** 529-541.

SHECHTMAN, D., BLECH, I., GRATIAS, D. & CAHN, J. W. 1984. *Physical Review Letters,* 53**,** 1951-1953.

TAUB, A. L. & SPAEPEN, F. 1979. *Scripta Metallurgica,* 13**,** 195.

TELFORD, M. 2004. The case for bulk metallic glass. *Materials Today,* 7**,** 36-43.

TRIVEDI, R. & TILLER, W. A. 1978. Interface morphology during crystallization—I. Single filament, unconstrained growth from a pure melt. *Acta Metallurgica,* 26**,** 671-678.

TSAI, A. P., INOUE, A. & MASUMOTO, T. 1987. *Japanese Journal of Applied Physics,* 26**,** L1505-L1507.

TURNBULL, D. (ed.) 1987. Undercooled alloy phases*, In*: Metallurgical Society of AIME, Warrendale, PA.

UNIVERSITY-OF-WISCONSIN 2005. Standard Operation Procedure - Elemental Analysis of Solution Samples with Inductively Coupled Plasma Optical Emission Spectrometry. University of Wisconsin - Madison: University of Wisconsin.

VOLMER & WEBER 1926. *Physical Chemistry,* 119, 277.

WALKER, J. L. 1959. *The physical chemistry of process metallurgy, part 2,* ST PIERRE, G. S. (ed.) New York: Interscience, p.845.

WEISSLER, G. L. & CARLSON, R. W. 1979. *Methods of Experimental Physics Volume 14 - Vacuum Physics & Technology,* New York, Academic Press, Inc.

WHEELER, A. A., MURRAY, B. T. & SCHAEFER, R. J. 1993. Computation of dendrites using a phase field model. *Physica D: Nonlinear Phenomena,* 66**,** 243-262.

WILLNECKER, R., HERLACH, D. M. & FEUERBACHER, B. 1989. Evidence of nonequilibrium processes in rapid solidification of undercooled metals. *Physical Review Letters,* 62**,** 2707.

WILLNECKER, R., HERLACH, D. M. & FEUERBACHER, B. 1990. Grain refinement induced by a critical crystal growth velocity in undercooled melts. *Applied Physics Letters,* 56**,** 324-326.

XIAO, J. Z., LEUNG, K. K. & KUI, H. W. 1995. Mechanism of grain refinement in undercooled $Cu_{30}Ni_{70}$. *Applied Physics Letters,* 67**,** 3111-3113.

YU, J.-T., HWANG, J. G., TSAI, C.-C. & LII, K. H. 1989. Low-temperature EPR of some cupric compounds in the YBaCuO system. *Solid State Communications,* 70**,** 167-171.

ZHANG, T., LIU, F., WANG, H. F. & YANG, G. C. 2010. Grain refinement in highly undercooled solidification of $Ni_{85}Cu_{15}$ alloy melt: Direct evidence for recrystallization mechanism. *Scripta Materialia,* 63**,** 43-46.